Ting Wang

Modelling of Welded Thin-Walled Aluminium Structures

Doctoral thesis
for the degree of philosophiae doctor

Trondheim, April 2006

Norwegian University of Science and Technology
Faculty of Engineering Science and Technology
Department of Structural Engineering

NTNU
Innovation and Creativity

NTNU
Norwegian University of Science and Technology

Doctoral thesis
for the degree of philosophiae doctor

Faculty of Engineering Science and Technology
Department of Structural Engineering

ISBN 82-471-7907-5 (printed version)
ISBN 82-471-7906-7 (electronic version)
ISSN 1503-8181

Doctoral theses at NTNU, 2006:78

Printed by NTNU-trykk

Abstract

This thesis aims to develop a comprehensive methodology for capacity prediction of thin-walled welded aluminium structures. Through material testing, model choice and calibration, numerical simulations and experimental verification, a procedure and a combination of modelling techniques using shell elements were obtained for such structures.

Experimental and numerical studies were performed to investigate the structural capacity of quasi-statically loaded fillet-welded connections. The data of two other series of experiments were adopted from a previous study and were used to verify the modelling methodology developed in this study. These experiments are beam-to-column joints subjected to tension and welded members subjected to four-point bending.

In the numerical study, the yielding and work hardening parameters for the weld, HAZ and base material were identified through material tests in the current study and available data from previous experiments. Shell elements in LS-DYNA are used throughout this thesis. With relatively large elements, the numerical analyses were generally found efficient and accurate in prediction of ultimate load, but structural ductility was over-estimated. When using smaller elements, the results were seen to be mesh-dependent and fail to predict the structural performance properly. This problem was solved by introducing a nonlocal approach to plastic thinning in the HAZ and weld. Several case studies showed that mesh sensitivity was greatly reduced. Techniques of representing the thickness variation in fillet welds, contact between coarse and dense meshed regions were used and were shown to improve the analyses in terms of efficiency or accuracy.

A simple analytical method was introduced to compute the mechanical response of a welded aluminium sheet under uniaxial tensile loading. Despite certain limitations it predicts the performance of the sheet reasonably well. These analyses gave a rapid engineering assessment to the influence of HAZ modelling on prediction of the structural capacity of a welded connection, especially with respect to its ductility.

Acknowledgements

I would like to express my deepest gratitude to my supervisors Professors Odd Sture Hopperstand and Per Kristian Larsen and Dr.ing Odd-Geir Lademo. This thesis would not have been possible without their professional guidance and input, as well as the strength of a team work

I am grateful to Dr Arild Holm Clausen who provided patient support in the beginning of this study. Considerable assistance was received for numerical study from Dr Torodd Berstad that is highly appreciated. The assistance from Dr Miroslaw Matusiak for providing experimental data from his dissertation is gratefully acknowledged. A thank goes to Mr Trygve Meltzer who assisted with the experimental tests.

Mr Ragnar Lindstrom in Engineering Research Nordic provided efficient and patient support in using LS-DYNA.

Thanks also go to my fellow PhD students and colleagues in SIMLab for providing a stimulating and friendly working environment.

The present study was carried out as part of the Norlight Research Program, and the financial support from the Norwegian Research Council and Hydro Aluminium is gratefully acknowledged.

At last I would like to thank my friends and my family for their support, encouragement and having faith in me during these years.

Ting Wang
Trondheim, April 2006

Contents

Notations

$\boldsymbol{\sigma}$	Cauchy stress tensor
$\mathbf{D}$	rate-of-deformation tensor
$\hat{\boldsymbol{\sigma}}$	corotational Cauchy stress tensor
$\hat{\mathbf{D}}$	corotational rate-of-deformation tensor
$\mathbf{R}$	orthogonal rotation tensor
$\hat{\mathbf{D}}^{\mathrm{e}}$	corotational elastic rate-of-deformation tensor
$\hat{\mathbf{D}}^{\mathrm{p}}$	corotational plastic rate-of-deformation tensor
$\hat{\mathbf{C}}^{\sigma}_{\mathrm{el}}$	elastic moduli
$\hat{\mathbf{q}}$	collection of internal variables
$\hat{\mathbf{r}}$	plastic flow direction
$\hat{\mathbf{h}}$	tensor-valued function
$\mathbf{M}$	transformation matrix
A	cross section area
A_0	initial cross section area
a	material parameter; throat thickness of weld
B_e	width of element e
B_0	initial width of element e
C_i	strain hardening parameters, $i=1, 2$
c	material parameter
D	diameter
def	total deformation in simulation
e_l	engineering longitudinal strain
F	force
F_e	traction force in element e
$f, \hat{f}$	yield function
$f_{0.2}$	conventional strength at 0.2% permanent strain
f_u	ultimate strength in uniaxial tensile test
f_{wd}	design strength of the weld material
f_d	design strength
HV	Vickers hardness
h	material parameter
h_0^e	initial thickness of element e
L	total length of the plate; radius of nonlocal domain
L_e^0	initial length of element e
L_e	current length of element e

L_w	weld length
K_1, K_2	stress tensor invariants
M	material parameter
N_{wd}	maximum force that can be carried by a double fillet weld
N_d	force capacity
N_e	total number of elements
p	material parameter; parameter in nonlocal equation of LS-DYNA
Q_i	strain hardening parameters, i=1, 2
q	parameter in nonlocal equations of LS-DYNA
R_α	R-ratio in direction α relatively to a reference direction
R_b	balanced biaxial plastic flow ratio
r_α	flow stress ratio in direction α relatively to a reference direction
s	engineering stress
T	total duration time of loading
v	prescribed velocity
v_0	constant velocity
W^p	specific plastic work
$\dot{W}^p$	specific plastic work rate
W_{cr}	material parameter
w	actual width; imperfection
w_0	initial width; amplitude of imperfection
Y_0	yield stress
α	stress ratio; incremental strain ratio
β	strain ratio
β_e	strain ratio in element e
$\bar{\varepsilon}$	effective plastic strain
$\dot{\bar{\varepsilon}}$	effective plastic strain rate
ε_1, ε_2, ε_3	in-plane major and minor principal strains and thickness strain
$\dot{\varepsilon}_w^p$, $\dot{\varepsilon}_t^p$	plastic strain rate in width and thickness directions
ε_{xx}^p, ε_{yy}^p	plastic strain components
ε_{cr}	critical thickness strain
ε_α^p	plastic strain in direction α relatively to a reference direction
ε_l^p, ε_w^p, ε_t^p	plastic strain in longitudinal, transverse and thickness directions of a uniaxial tensile test
ε_l, ε_w, ε_t	strain in longitudinal, transverse and thickness directions
$\bar{\varepsilon}_e$	effective strain in element e
ε_1^e, ε_2^e, ε_3^e	in-plane major and minor principal strain and thickness strain in element e

$\bar{\varepsilon}_{tot}$	total effective strain
$\dot{\lambda}$	scalar plastic flow rate
$\sigma_{xx,}\ \sigma_{yy,}\ \sigma_{xy}$	stress components
σ_{α}	tension stress in direction α relative to a reference direction
σ_{Y}	yield strength in uniaxial tension
$\bar{\sigma}$	effective stress
$\sigma_1,\ \sigma_2,\ \sigma_3$	in-plane major and minor principal stresses and thickness stress
$\hat{\psi}$	flow potential
$\Re(\ )$	residual force

1. Introduction

1.1 Background

Welded thin-walled structures made from aluminium extrusions are used in several applications where there is a demand for reduced structural weight, increased payload, and in the case of transportation applications higher speed and reduced fuel consumption. Some applications are plate girders and bridge decks, living quarters on offshore installations, containers, high speed ferries and ship super-structures, automobiles, railways and aircrafts. The competitiveness of such structures is primarily due to modern extrusion technology, new joining technologies and efficient manufacturing processes. Further market penetration of these structures depends upon more efficient designs that fully utilize their structural capacity. However, at present this is impeded by the lack of suitable design rules in the ultimate limit state and in accidental load situations.

The localization of deformation in poorly designed welded structural details may cause significant problems and a loss of structural integrity, particularly when subjected to tensile forces. For welded components in for instance safety components of cars that are designed to absorb energy during a crash situation, the loss of ductility may be more severe than the loss of strength. It is thus important to be able to predict in a simple way the loss of structural ductility induced by welding.

At present welds are mostly designed according to interaction formulas given in design codes. Currently there is no unified approach to the problem of material failure in thin-walled aluminium structures, which considers the mechanical properties of the welds and the heat-affected-zones (HAZ), as well as the stress concentrations caused by the inhomogeneity of material properties in HAZ. Sufficiently accurate and computationally feasible models are not available for the prediction of ductile failure.

1.2 Previous works

Experimental studies on welded connections in aluminium structures up to the year of 1999 were reviewed in the doctoral thesis of Matusiak (1999). The most fundamental contribution is from the work of Soetens (1987). However, the thesis of Matusiak (Matusiak 1999) is also a major contribution within this field, and plays a major role in the present investigation. It comprises a comprehensive experimental database on the plastic deformation behaviour, ultimate capacity and failure modes of welded aluminium connections, which only to a very limited extent has been used for assessment of numerical predictions.

Numerically, attempts of predicting the deformation behaviour and ultimate strength of welded components have been done by Matusiak (1999) (aluminium), Mellor, Rainey and Kirk (1999) (steel), Chan and Porter Goff (2000) (aluminium) and Hildrum and Malo (2002) (aluminium) using solid elements and elasto-plastic constitutive models. Ødegard and Zhang (1996) successfully predicted the performance of welded aluminium nodes for car body applications using solid elements and a constitutive model of elasto-plasticity and ductile damage. More recently, Zhang et al. (2001) integrated a thermal-mechanical microstructure analysis with a load-deformation mechanical analysis to predict the fracture behaviour of aluminium joints, employing solid elements and a constitutive model of elasto-plasticity and ductile damage. Good agreement with test data was found.

The existing literature on the use of the shell elements in prediction of the capacity and failure of welded aluminium components is limited. Using a constitutive model of elasto-plasticity and ductile damage, Hildrum (2002) predicted the behaviour of butt-welded stiffened panels made of aluminium extrusions subjected to impact loading. Satisfactory agreement with experimental results was obtained. Hildrum and Hopperstad (2002) performed numerical simulations of welded structural components using shell elements, rigid body welds and elasto-plastic constitutive models. The results were encouraging, but it was concluded that a more extensive validation programme is needed before this methodology can be recommended for design purposes.

Currently it is not feasible to model thin-walled aluminium structures using solid elements, and shell elements have to be used in FEM-based design. Accordingly, a systematic study is required to achieve an accurate, efficient and robust shell modelling methodology for such structures.

1.3 Objective and scope

This thesis focuses on the development of a predictive methodology for welded thin-walled aluminium structures using shell elements with special emphasis on HAZ. The objective is to eventually provide a validated FEM-based procedure for large-scale analyses of such structures, which retain the safety level given by the design codes.

Experimental tests and numerical simulations are performed to investigate the mechanical performance of a series of fillet-welded connections in aluminium alloy EN AW 6082 T6 under tension loading. Figure 1.1 shows pictures of the investigated specimens. In the numerical study, the connections are modelled using shell elements in LS-DYNA (LSTC 2003). A material model called the Weak Texture Model 2D (WTM-2D) (Lademo et al. 2004; Lademo et al. 2004) is adopted throughout this thesis. The strength and hardening data for the weld, HAZ and base material are identified according to material tests and available experimental data in the literature. The performance of the connections under tension loading is further studied by a simple analytical method aiming for rapid information on the influence of the HAZ modelling on prediction of the structural performance, especially with respect to its ductility.

Experiments of beam-to-column joints subjected to tension and welded members under four-point bending (Figure 1.2) previously performed by Matusiak (1999) are used for further assessment of the FE models developed in the present study. Parametric and mesh convergence studies are performed with focus on the prediction of the structural strength and ductility. Nonlocal plastic thinning is introduced to the models of some of the investigated structures and is found to successfully reduce mesh-dependency.

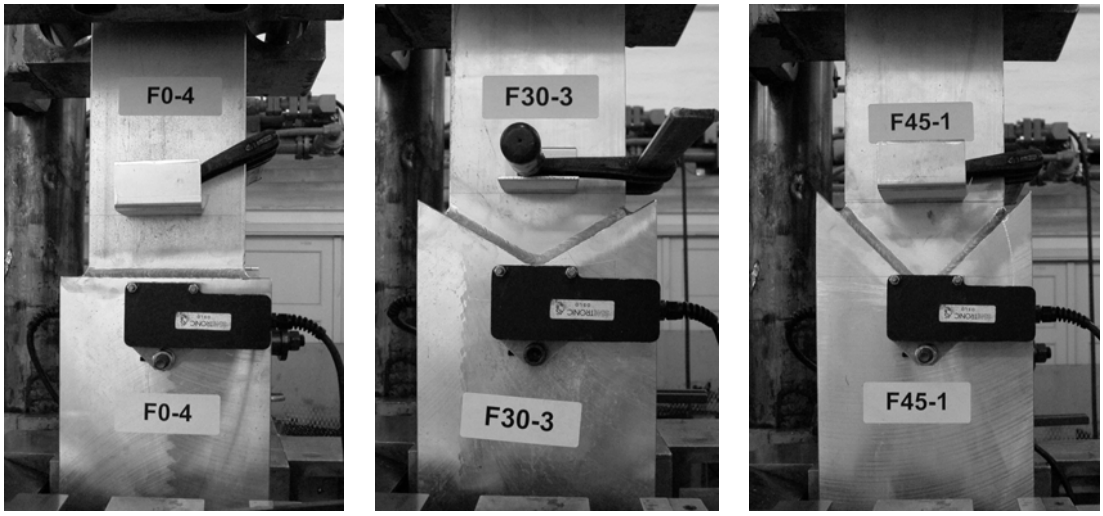

Figure 1.1. Experimental and numerical study of fillet-welded connections loaded in tension.

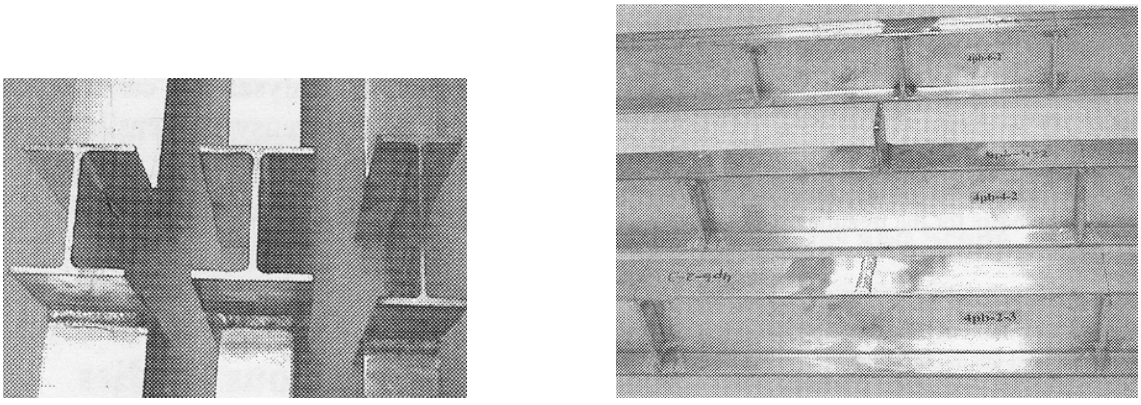

Figure 1.2. Numerical studies of welded joints subjected to tension and members under four-point bending, photos from Matusiak (1999).

2. Physical metallurgy

2.1 Introduction

The macroscopic performance of materials can usually be explained by their microscopic properties. Extruded aluminium sheets possess crystallographic texture that lead to anisotropy in their strength, plastic flow and ductility. For many loading situations the polycrystalline sheets can be assumed to be in a plane stress state. When subjected to welding, or generally, a thermal influence, their material properties can be changed dramatically. Here the microscopic properties of aluminium extrusions are briefly looked into in order to theoretically understand the physics behind their macroscopic performance.

2.2 Texture and anisotropy

Aluminium is a polycrystalline material with a face-centred cubic (f.c.c) packing structure. In a polycrystalline aggregate the individual grains have a crystallographic orientation different from those of its neighbours. Usually the orientations have certain preferred orientations which are called crystallographic textures.

Texture in aluminium profiles is developed during their manufacturing processes. The processes may involve numerous controlling parameters, such as deformation mode, tooling, geometry and interaction between tool and workpiece etc. Another reason for texture is subsequent annealing, or recrystallization. As Hatherly and Hutchinson (1979) described, the material may recrystallize after extrusion, i.e., in the elongated grains formed by the extrusion process nuclei are formed from where new grains are growing. The nuclei are formed at grain boundaries, shear bands and transition bands which all

have a non-random orientation. As a result, the recrystallized grain structure also has a certain preferred orientation. The recrystallization texture develops depending on the starting texture and also on the recrystallization kinetics. Thus it is affected by parameters such as annealing time, heating and cooling rates (Barlat and Richmond 1987). As Hatherly and Hutchinson (1979) stated "monocrystalline materials' physical, chemical and mechanical properties depend upon orientation, consequently wherever texture exists in polycrystalline material, directional dependency, or anisotropy, of these properties will result."

The aluminium extrusions investigated in this thesis possess anisotropy which is revealed by material tests presented in Chapter 5.

2.3 Orthotropy and planar stress

Owing to the symmetry of extrusion process, the anisotropy has certain symmetry planes. A common form of anisotropy in extruded aluminum profiles is the orthotropic anisotropy. That is, at each material point, there exist three mutually orthogonal planes of symmetry. The intersections of these planes are called the axes of orthotropy, which are the extrusion direction, the transverse direction, and the normal direction of the plate.

The polycrystalline sheets are assumed to be in a planar stress state, which is appropriate for many sheet loading situations (Barlat and Richmond 1987). Therefore, a tricomponent (σ_{xx}, σ_{yy} and σ_{xy}) yield surface is usually considered sufficient to predict the mechanical performance of an extruded profile or a rolled sheet.

2.4 Heat-treatable alloys and HAZs

The strength of aluminium may be increased by two methods, namely "alloy hardening" and "work hardening", and the two methods can be employed simultaneously (Altenpohl 1982).

Alloy hardening is based on the reaction of dislocation lines caused by foreign atoms. The foreign atoms have a different atomic diameter and electron structure from aluminium atoms. For this reason, the addition of such atoms creates a disturbance in the aluminium lattice. Different types of foreign atoms affect the lattice to different degrees. Moreover, the hardening depends on whether the foreign elements are in solution, or precipitate in a more or less fine distribution within the aluminium lattice. Depending on their distribution, the foreign atoms impede the movement of the

dislocations, and thereby, the progress of plastic deformation to widely differing degrees. For this reason Altenpohl (1982) divide alloy hardening into two kinds: first, solid solution hardening, which is used in non-heat-treatable alloys; and second, precipitation hardening or age hardening, produced by controlled precipitation of alloying elements previously in solution in heat-treatable alloy.

The material studied in this thesis is aluminium sheet of alloy EN AW 6082-T6 which is a heat-treatable AlMgSi alloy. It develops strength through thermal treatments that precipitate fine Mg_2Si particles. Alloy EN AW 6082-T6 is suitable for extrusion, has good formability, welding characteristics and corrosion resistance and has been extensively used in offshore structural applications.

When a heat treatable alloy is welded, annealing at a sufficiently high temperature removes the hardening effect of a previous heat treatment. Figure 2.1 shows the variation in hardness in the vicinity of a weld bead in pure aluminium and in heat-treatable alloys. A severe temperature gradient is created in the structure during welding as described by Altenpohl (1982). In the weld zone itself, the temperature is above the melting point, and decreases with distance away from the weld zone. Structural changes take place simultaneously in the vicinity of the weld. When welding a cold-worked, age-hardened alloy, six processes can be identified: melting in the weld zone, followed by solidification of a cast structure; in the hottest but not melted zone, recrystallization and solution treatment occur; after this comes the region where reversion, age hardening and softening by overaging (coarse precipitation) all overlap. The Figure 2.2 shows that the common origin of all of these processes is the increased mobility of the atoms for a short period of time. The various processes with their different effects occur through the migration or repositioning of the atoms at different temperatures.

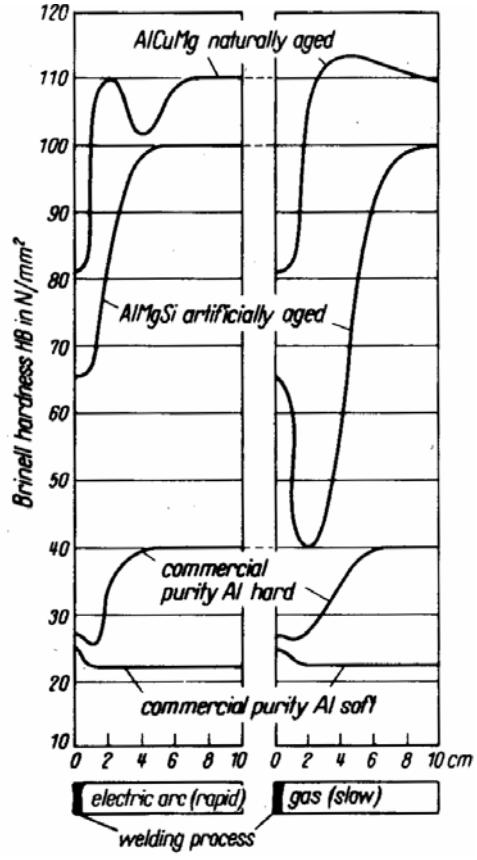

Figure 2.1. Variation in hardness in the vicinity of a weld bead (The weld bead consists mainly of non-age-hardening filler metal) (Altenpohl 1982).

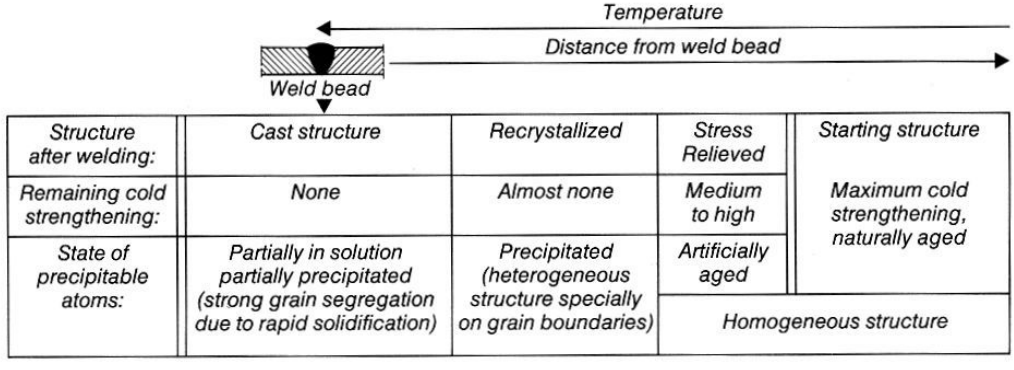

Figure 2.2. Structure of a weld bead and the adjacent areas (weld bead in age-hardened, cold-worked alloy). (Altenpohl 1982)

3. Design and modelling of welded connections

3.1 Introduction

Experimental testing and numerical analyses provide means to understand structural performances. One of the ultimate goals of the understanding would be to establish simple formulas (models) serving as guidance to structural design. The formulas should ensure that the designers can easily compute reliable and conservative predictions of the resistance. Eurocode 9 (CEN 2004) is such an assembly of up-to-date standards for design of aluminium structures established by European Committee for Standardization (CEN). In the first part of this Chapter (Section 3.2) the design codes of weld and HAZ in Eurocode 9 relevant to this thesis are reviewed. Other than guidance of design, the codes can also be used in conjunction with FE computing. In LS-DYNA the empirical formulas are used as the onset of weld failures, in the modelling of welds by introducing constraints between nodes/node sets. However, the modeling method of LS-DYNA is not suitable for more general cases of fillet welds. Therefore, a simple computing method for failure prediction of fillet welds is proposed based on the calculation according to the design rule in the second part of this Chapter (Section 3.3).

3.2 Structural design with welds and HAZs

Traditionally the fillet weld and butt weld account for 80% and 15%, respectively, of all weldments in construction industry. The reminder comprises plug, slot and spot welds (Patrick et al. 1988). Besides the electrical-arc welding method, friction stir welding and laser welding are also commonly used. The present study will focus on fillet and butt welds.

In the design of welded joints consideration should be given to the strength and ductility of welds and the important strength reduction in HAZs. For the following classes of alloys a HAZ has to be taken into account

- Heat-treatable alloys in any heat-treated condition above T4 (6xxx and 7xxx series)
- Non-heat-treatable alloys in any work-hardened condition (3xxx and 5xxx series)

3.2.1 Structural design with butt welds

For the design stress the following should be applied:

- normal stress in the cross section of weld, tension or compression, perpendicular to the weld axis, see Figure 3.1a

$$\sigma_{\perp} \leq \frac{f_w}{\gamma_{Mw}} \tag{3.1}$$

- shear stress, see Figure 3.1b

$$\tau \leq 0.6 \frac{f_w}{\gamma_{Mw}} \tag{3.2}$$

- combined normal and shear stresses

$$\sqrt{\sigma_{\perp}^2 + 3\tau^2} \leq \frac{f_w}{\gamma_{Mw}} \tag{3.3}$$

where:

f_w is the characteristic strength of weld metal;

$\sigma_{\perp}$ is the normal stress, perpendicular to the weld axis;

τ is the shear stress, parallel to the weld axis;

γ_{Mw} is the partial safety factor for welded joints.

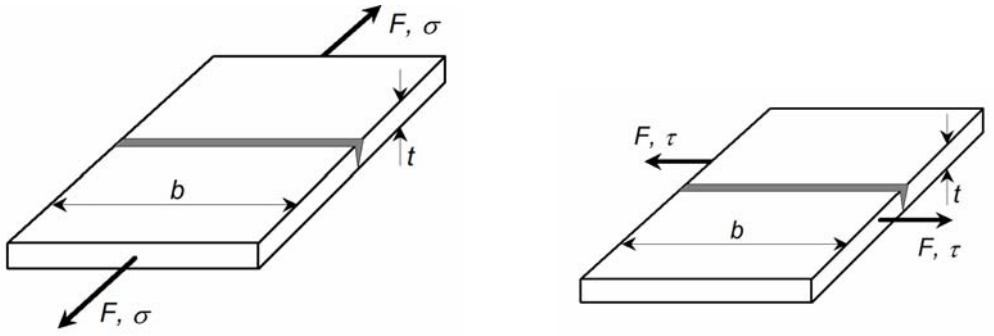

a) b)

Figure 3.1. a) Butt weld subject to normal stresses, and b) butt weld subject to shear stresses (CEN 2002).

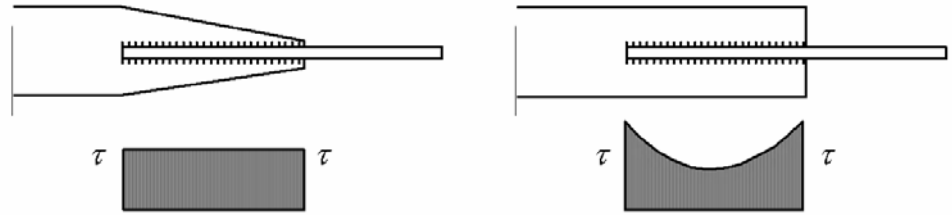

a) b)

Figure 3.2. a) Example of uniform stress distribution, and b) example of non-uniform distribution (CEN 2002).

3.2.2 Structural design with fillet welds

For the design of fillet welds the throat section shall be taken as the governing section. The area of the throat section shall be determined by the effective weld length and the effective throat thickness of the weld. The effective length shall be taken as the total length of the weld if

- the length of the weld is at least 8 times the throat thickness;
- the length of the weld does not exceed 100 times the throat thickness with a non-uniform stress distribution;
- the stress distribution along the length of the weld is constant, for instance in case of lap joints as shown in Figure 3.2.

If the stiffness of the connected members differs considerably from each other, the stresses may be non-uniform and a reduction of the effective weld length has to be taken into account. If the length of longitudinal fillet welds has to be reduced, the following shall be applied:

$$L_{W,eff} = (1.2 - 0.2L_W / 100a)L_W \quad \text{with} \quad L_W \geq 100a \tag{3.4}$$

where

$L_{W,eff}$ is the effective length of longitudinal fillet welds;

L_W is the total length of longitudinal fillet welds;

a is the effective throat thickness, see Figure 3.3.

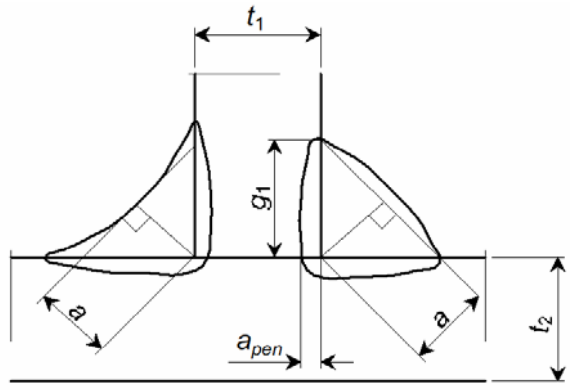

Figure 3.3. Effective throat thickness a; positive root penetration a_{pen} (CEN 2002).

The effective throat thickness a has to be determined as indicated in Figure 3.3, i.e. a is the height of the largest triangle which can be inscribed within the weld.

The forces that have to be transmitted by a fillet weld shall be resolved into stress components with respect to the throat section, see Figure 3.4. These components are:

- a normal stress $\sigma_{\perp}$, perpendicular to the throat section;
- a shear stress $\tau_{\perp}$, acting on the throat section perpendicular to the weld axis;
- a shear stress $\tau_{\parallel}$, acting on the throat section parallel to the weld axis.

Residual stresses and stresses not participating in the transfer of load need not be included when checking the resistance of a fillet weld. This applies specially to the normal stress $\sigma_{\parallel}$ acting parallel to the axis of a weld.

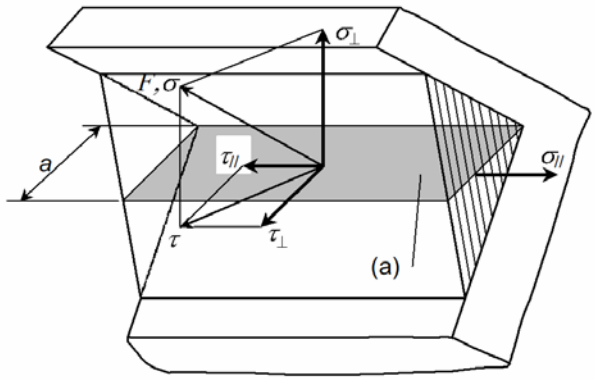

Figure 3.4. Stresses $\sigma_{\perp}$, $\tau_{\perp}$ and $\tau_{\square}$, acting on the throat section of a fillet weld (CEN 2002).

According to the failure criterion, the design resistance of a fillet weld shall be applied as:

$$\sqrt{\sigma_{\perp}^2 + 3(\tau_{\perp}^2 + \tau_{\square}^2)} \leq \frac{f_w}{\gamma_{Mw}} \tag{3.5}$$

where

f_w is the characteristic strength of weld metal;

γ_{Mw} is the partial safety factor for welded joints.

For two frequently occurring cases the following design formulas, derived from Equation (3.5), shall be applied:

- double fillet welded joint, loaded perpendicularly to the weld axis (see Figure 3.5). The throat thickness a should satisfy the following formula:

$$a \geq 0.7 \frac{F_{\perp}}{f_w / \gamma_{Mw}} \tag{3.6}$$

where

$F_{\perp}$ is the design load per unit length in the connected member, normal to the weld;

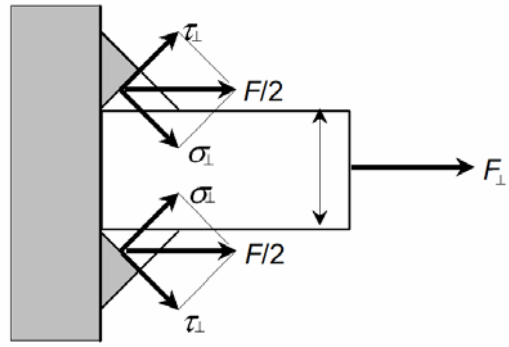

Figure 3.5. Double fillet welded joint loaded perpendicularly to the weld axis (CEN 2002).

- double fillet-welded connection, loaded parallel to the weld axis (see Figure 3.6). The throat thickness a shall be applied as:

$$a \geq 0.85 \frac{F_{\parallel}}{f_w / \gamma_{Mw}} \tag{3.7}$$

where

$F_{\parallel}$ is the load per unit length in the connected member, parallel to the weld.

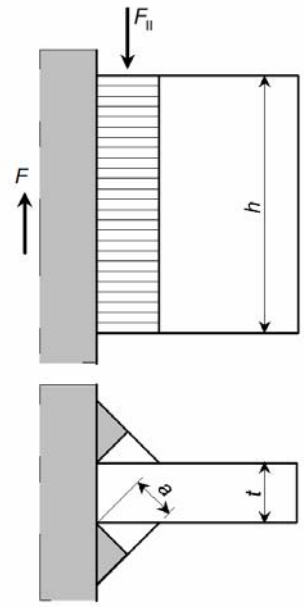

Figure 3.6. Double fillet welded joint loaded parallel to the weld axis (CEN 2002).

3.2.3 Structural design with HAZs

The design strength of a HAZ adjacent to a weld shall be taken as follows:

i) Tension force perpendicular to the failure plate (see Figure 3.7)

- HAZ butt welds:

$$\sigma_{haz} \le \frac{f_{u,\,haz}}{\gamma_{MW}} \text{ at the toe of the weld (full cross section)} \quad (3.8)$$

- HAZ fillet welds:

$$\sigma_{haz} \le \frac{f_{u,\,haz}}{\gamma_{MW}} \text{ at the fusion boundary and at the toe of the weld (full cross section)} \quad (3.9)$$

where:

σ_{haz} is the design normal stress perpendicular to the weld axis;

$f_{u,haz}$ is the characteristic ultimate strength of HAZ.

ii) Shear force in failure plate:

- HAZ butt welds:

$$\tau_{haz} \le \frac{f_{v,\,haz}}{\gamma_{MW}} \quad (3.10)$$

- HAZ fillet welds

$$\tau_{haz} \le \frac{f_{v,\,haz}}{\gamma_{MW}} \text{ at the toe of the weld (full cross section)} \quad (3.11)$$

where:

τ_{haz} shear stress parallel to the welds axis;

$f_{v,haz}$ characteristic ultimate shear strength of HAZ.

iii) Combined shear and tension:

- HAZ butt welds:

$$\sqrt{\sigma^2 + 3\tau^2} \le \frac{f_{\mathrm{u,\,haz}}}{\gamma_{\mathrm{MW}}} \text{ at the toe of the weld (full cross section)} \qquad (3.12)$$

- HAZ fillet welds:

$$\sqrt{\sigma^2 + 3\tau^2} \le \frac{f_{\mathrm{u,haz}}}{\gamma_{\mathrm{MW}}} \text{ at the toe of the weld (full cross section)} \qquad (3.13)$$

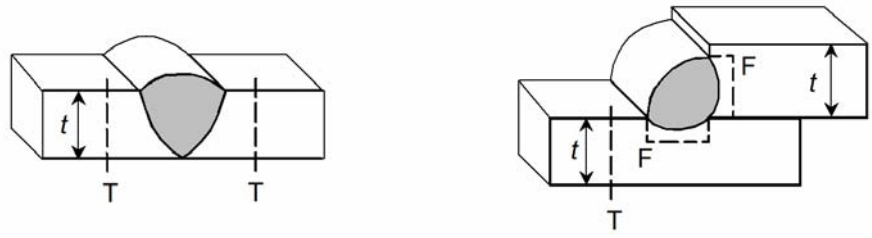

Figure 3.7. Failure plates in HAZ adjacent to a weld. The line F = HAZ in the fusion boundary; the line T = HAZ in toe of the weld, full cross section (CEN 2002).

3.3 A computation method for failure of fillet welds

3.3.1 Problem definition

In finite element modelling of welded connections, the weld material is commonly modelled by solid elements in the same way as the base material, by using different material parameters (Hildrum et al. 2002; Matusiak 1999; Ødegard and Zhang 1996, Zhang et al. 2001). However, using solid elements to represent the weld geometry can be quite complicated and CPU consuming and therefore not very practical for design purposes or for modelling complex structures with many welds.

LS-DYNA provides a simple method of representing welds by using constraints between nodes/node sets. This method can be used with shell elements for five weld options which are: spot, fillet, butt, cross-fillet and combined welds. The included ductile failure is governed by a critical plastic strain, while brittle failure is determined from a stress-based interaction criterion defining a critical stress at failure. Among these options, the nodal ordering of the fillet weld and butt weld are shown in Figure 3.8 and Figure 3.9, especially. These two options were used by Hildrum and Hopperstad (2002)

to represent the performance of welded aluminium joints. The analyses predicted the force level reasonably well for three structures and also to some extent the failure mode. It was found that the analyses were straightforward and cost effective to perform compared with the ones using solid elements. However, an extensive validation programme is required before one can recommend the use of this method.

Even so, the drawback of this feature would be that the weld models are limited to the five given sets of the nodes/node ordering, and are not applicable to any other cases. For instance the fillet weld option is only suitable for two perpendicular plates fillet-welded together, but not for one thinner sheet welded to another thicker plate which is the case of the fillet-welded connections to be presented in Chapter 7. Therefore a method capable of representing welds in more general cases is needed for shell modelling of aluminium structures. In this Section, a simple method for failure prediction of fillet welds is proposed based on the calculation procedure offered by Eurocode 9 (CEN, 2004).

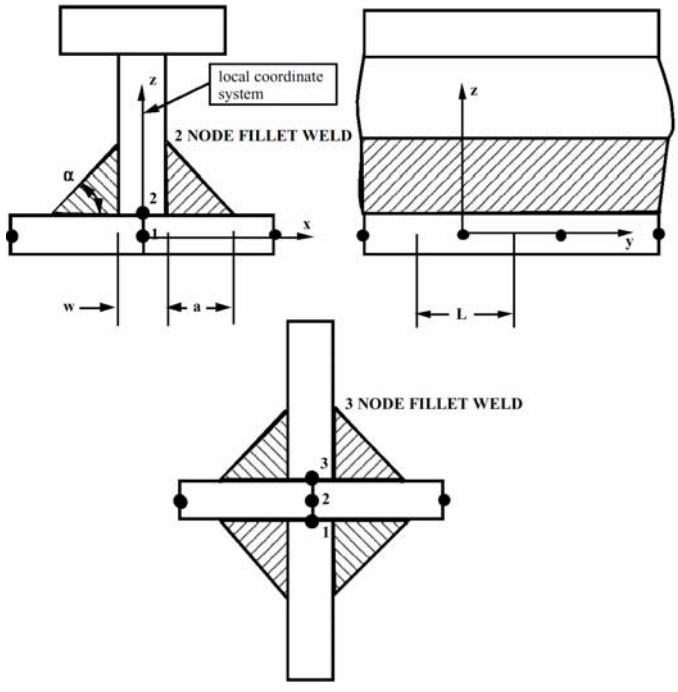

Figure 3.8. Fillet weld defined by nodal constraint in LS-DYNA (LSTC 2003).

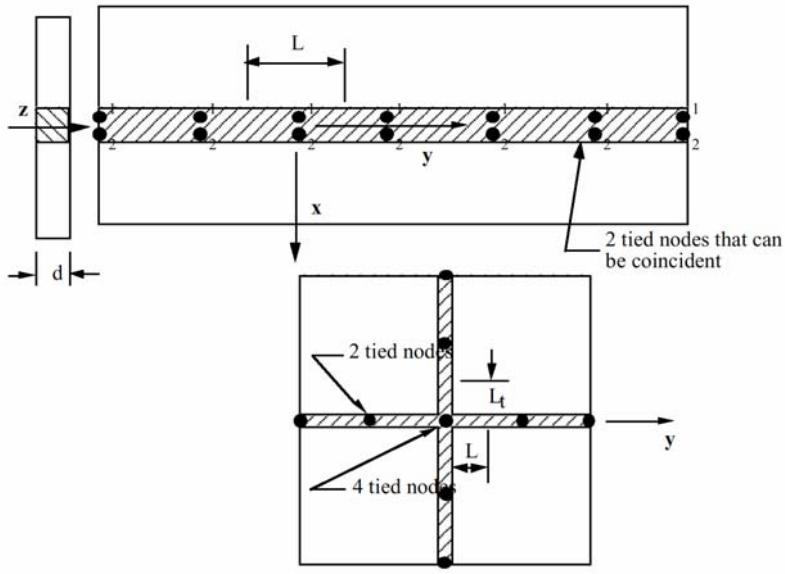

Figure 3.9. Butt weld defined by nodal constraint in LS-DYNA (LSTC 2003).

3.3.2 Calculation procedure

Eurocode 9 (CEN 2004) requires that the capacity of the weld shall be checked at the throat section and at the two fusion faces between the base material and the weld material. In a finite element context this requires that the element stresses in the plate to be connected must be transformed to a local coordinate system, from which the stresses in the weld may easily be determined.

This is most conveniently done by introducing a local $n-t$ system in the plane of the sheet, where t is parallel to and n is normal to the weld. In practice, neither a single nor a double fillet weld is used to transmit moments about an axis parallel to the weld, and only the membrane stresses in the element is therefore considered when computing the weld stresses $\sigma_{\perp}$, $\tau_{\perp}$, and $\tau_{\square}$.

In the current method a two-sided fillet weld is assumed. The array of weld and HAZ elements are as seen in Figure 3.10. Failure of the weld is calculated according to design codes based on the stress state of the HAZ element next to the weld, which is assumed to be constant throughout the element. The stresses in the throat section and fusion faces, $\sigma_{\perp}$, $\tau_{\perp}$ and $\tau_{\square}$, are calculated as following based on equilibrium considerations.

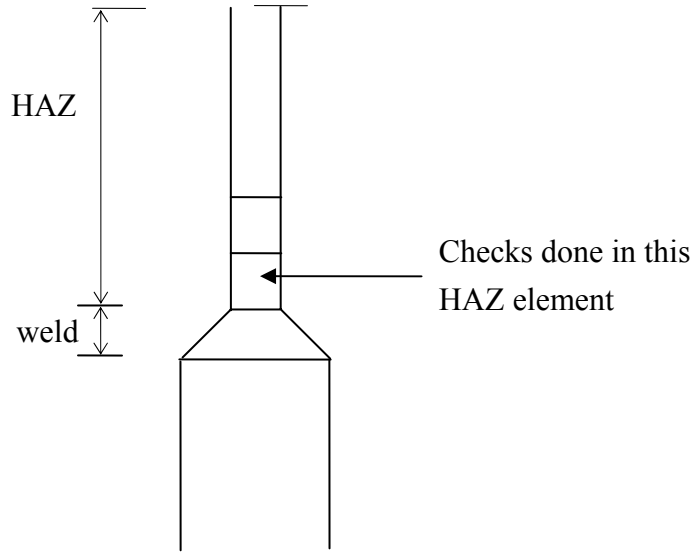

Figure 3.10. Weld and HAZ elements in a fillet-welded structure.

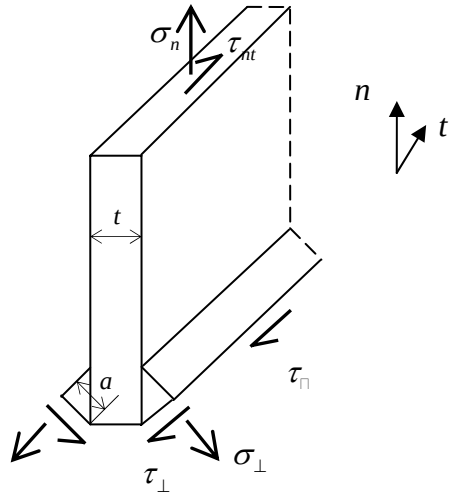

Figure 3.11. Stresses in weld.

i) Throat section

Calculate stresses in the throat section of weld, $\sigma_{\perp}$, $\tau_{\perp}$ and $\tau_{\perp}$, from HAZ element stresses σ_n and τ_{nt} in local system $n-t$, see Figure 3.11.

$$\sigma_{\perp} = \tau_{\perp} = \sigma_n \frac{t}{2a\sqrt{2}} \tag{3.14}$$

$$\tau_{\parallel} = \tau_{nt} \frac{t}{2a} \tag{3.15}$$

Check failure of weld according to

$$\sigma_c = \sqrt{\sigma_{\perp}^2 + 3\left(\tau_{\perp}^2 + \tau_{\parallel}^2\right)} \leq f_{dW} \tag{3.16}$$

where f_{dW} is the design strength of the weld material.

ii) First fusion face

Calculate stresses in the first fusion face between weld and base material (see Figure 3.12):

$$\sigma_{\perp} = \sigma_n \frac{t}{2a\sqrt{2}} \tag{3.17}$$

$$\tau_{\parallel} = \tau_{nt} \frac{t}{2a\sqrt{2}} \tag{3.18}$$

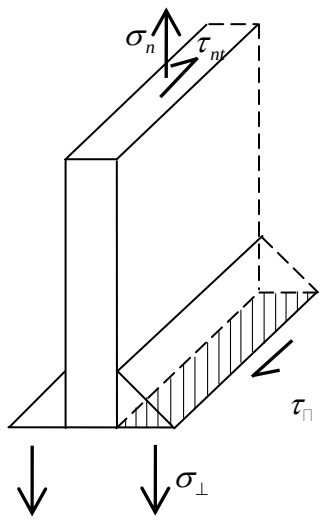

Figure 3.12. Stresses in the fusion surface between the weld and the base material.

Check failure of base material:

$$\sigma_c = \sqrt{\sigma_{\perp}^2 + 3\tau_{\parallel}^2} \le f_{d,HAZ} \tag{3.19}$$

where $f_{d,HAZ}$ is the design strength of the HAZ material.

iii) Second fusion face:

Calculate shear stresses in the second fusion face between the weld and base material (see Figure 3.13):

$$\tau_{\perp} = \sigma_n \frac{t}{2a\sqrt{2}} \tag{3.20}$$

$$\tau_{\parallel} = \tau_{nt} \frac{t}{2a\sqrt{2}} \tag{3.21}$$

Check failure of base material:

$$\sigma_c = \sqrt{3(\tau_{\perp}^2 + \tau_{\parallel}^2)} \le f_{d,HAZ} \tag{3.22}$$

iv) In addition to the checks of throat section and fusion faces between weld and the base material, it is necessary to check the material in the HAZ for plastic instability (i.e. strain localisation) and ductile fracture.

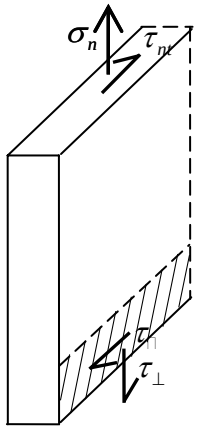

Figure 3.13. Stresses in surface between the weld and the base material.

3.3.3 Summary

A computation method is proposed to represent fillet welds in large-scale finite element modelling. The model calculates stress states through equilibrium between base material and weld, and uses the design formulas to check failure. It simplifies the shell modelling by representing the fillet weld by one or more elements along the weld height.

The emphasis of this thesis is on the modelling of the heat-affected-zone rather than on the weld. It is due to the fact that failure of the weld can be usually controlled by using more weld material, i.e. a larger value of throat thickness a. On the other hand the effect of HAZ on structural performance can be more severe and less predictable than the weld for aluminium structures. Therefore the above model is not further investigated in the present study. Nevertheless, as a simple computing method to represent fillet welds, more work is worth doing to further develop, implement and validate this model in finite element codes.

4. Constitutive models

4.1 Introduction

Both recrystallized and non-recrystallized extruded aluminium alloys typically have a strong crystallographic texture that lead to anisotropy in strength, plastic flow and ductility. Proper representation of the material's anisotropy is essential to capture several phenomena of prime industrial interest. For instance, plastic thinning which often is the prime phenomenon causing failure in sheet metals subjected to positive in-plane stresses and strains (Lademo et al. 2005). Correct prediction of thinning instability is dependent upon an accurate representation of anisotropy (Hopperstad and Lademo 2002; Lademo et al. 2004a; Lademo et al. 2004b; Marciniak and Kuczynski 1967; Marciniak et al. 1973).

An anisotropic plane stress yield function proposed by Barlat and Lian (1989) is considered suitable for modelling the aluminium extrusions. This yield function has been implemented in a model named the Weak Texture Model 2D (WTM-2D) in LS-DYNA by Lademo et al. (Lademo et.al. 2004; Lademo et al. 2004), and was validated as a suitable model for aluminium extrusions. The model adopts the five-parameter extended Voce rule to describe the isotropic work hardening relation of the aluminium alloy, and three failure criteria are included. This model is adopted in the numerical studies performed in this thesis. The constitutive equation and failure criteria of the WTM-2D are reviewed in the following.

4.2 Elastoplasticity framework

Hypoelastic-plastic models are typically used when elastic strains are small compared to plastic strains (Belytschko et al. 2000), which is the case for aluminium. The rate-of-deformation tensor, $\mathbf{D}$, and Cauchy stress tensor, $\boldsymbol{\sigma}$, are used for the strain rate measure and stress measure, respectively. In addition, a corotational formulation is adopted to simplify the formulation of plastic anisotropy. The corotational Cauchy stress and corotational rate-of-deformation tensors are defined by the relations

$$\hat{\boldsymbol{\sigma}} = \mathbf{R}^{\mathrm{T}} \cdot \boldsymbol{\sigma} \cdot \mathbf{R}; \quad \hat{\mathbf{D}} = \mathbf{R}^{\mathrm{T}} \cdot \mathbf{D} \cdot \mathbf{R} \tag{4.1}$$

where $\mathbf{R}$ is an orthogonal rotation tensor. The corotational Cauchy stress and corotational rate-of-deformation tensors are objective tensors, in the sense that they are invariant to superimposed rigid body rotations.

The corotational rate-of–deformation is decomposed into elastic and plastic parts:

$$\hat{\mathbf{D}} = \hat{\mathbf{D}}^{\mathrm{e}} + \hat{\mathbf{D}}^{\mathrm{p}} \tag{4.2}$$

where indices “e” and “p” denote elastic and plastic, respectively. The rate of the corotational stress is defined as a linear function of the elastic corotational rate-of-deformation:

$$\dot{\hat{\boldsymbol{\sigma}}} = \hat{\mathbf{C}}^{\sigma}_{\mathrm{el}} : \hat{\mathbf{D}}^{\mathrm{e}} = \hat{\mathbf{C}}^{\sigma}_{\mathrm{el}} : (\hat{\mathbf{D}} - \hat{\mathbf{D}}^{\mathrm{p}}) \tag{4.3}$$

where $\hat{\mathbf{C}}^{\sigma}_{\mathrm{el}}$ contains the elastic moduli.

It is postulated that there exists a domain in stress space, defined by a yield surface, in which the material response is elastic. Any yield surface is a postulated mathematical expression of the states of stress that will induce yielding or the onset of plastic deformation (Hosford and Caddell 2002). It is usually a function of some internal variables that account for the prior history of the material. The yield condition which defines the elastic domain of the material is stated as

$$\hat{f}(\hat{\boldsymbol{\sigma}}, \hat{\mathbf{q}}) = 0 \tag{4.4}$$

where $\hat{f}$ is the yield criterion, and $\hat{\mathbf{q}}$ is a collection of scalar internal variables. The material behaves elastic as long as $\hat{f} < 0$, while plastic strains are generated when the yield condition is satisfied during deformation.

The plastic rate-of-deformation is defined by a plastic flow rule in the form

$$\hat{\mathbf{D}}^{\mathrm{p}} = \dot{\lambda}\hat{\mathbf{r}}(\hat{\boldsymbol{\sigma}}, \hat{\mathbf{q}}) \tag{4.5}$$

where $\dot{\lambda}$ is a scalar plastic flow rate, and $\hat{\mathbf{r}}$ is the plastic flow direction, depending on stress $\hat{\boldsymbol{\sigma}}$ and internal variables $\hat{\mathbf{q}}$. The plastic flow direction $\hat{\mathbf{r}}$ is often defined in terms of a flow potential $\hat{\psi}$:

$$\hat{\mathbf{r}} = \frac{\partial \hat{\psi}}{\partial \hat{\boldsymbol{\sigma}}} \tag{4.6}$$

The plastic flow is said to be associated when the flow potential and the yield function are identical, $\hat{\psi} = \hat{f}$, and non-associated for all other cases. Experimental observations show that the plastic deformations of metals can be characterized quite well by the associated flow rule (Khan and Huang 1995).

The internal variables $\hat{\mathbf{q}}$ in Equation (4.5) are assumed to be a collection of scalar variables that describe strain hardening, damage evolution, strain aging etc. during plastic deformation. The evolution equation for the internal variables is defined by

$$\dot{\hat{\mathbf{q}}} = \dot{\lambda}\hat{\mathbf{h}}(\hat{\boldsymbol{\sigma}}, \hat{\mathbf{q}}) \tag{4.7}$$

where $\hat{\mathbf{h}}$ is a tensor-valued function that has to be determined from experimental data.

Assuming $\hat{\mathbf{q}}$ includes $\bar{\varepsilon}$ only, the yield criterion is now written in the form

$$\hat{f}(\hat{\boldsymbol{\sigma}},\ \bar{\varepsilon}) = \bar{\sigma}(\hat{\boldsymbol{\sigma}}) - \sigma_Y(\bar{\varepsilon}) \tag{4.8}$$

where $\sigma_Y(\bar{\varepsilon})$ is the yield strength in uniaxial tension and $\bar{\sigma}$ is the effective stress. The increase of the yield strength after initial yield is called work hardening or strain hardening. The hardening property of the material is generally a function of the prior history of plastic deformation. In metal plasticity, the history of plastic deformation is often characterized by the effective plastic strain which is given by (Belytschko, Liu and Moran 2000)

$$\bar{\varepsilon} = \int \dot{\bar{\varepsilon}} dt \tag{4.9}$$

where $\dot{\bar{\varepsilon}}$ is the effective plastic strain rate. It can be defined from the specific plastic work rate $\dot{W}^p$ as follows. The effective stress and strain rate and the Cauchy stress and the plastic rate-of-deformation are pairs of energy conjugate measures, i.e.

$$\dot{W}^P = \hat{\boldsymbol{\sigma}} : \hat{\mathbf{D}}^{\mathrm{p}} = \bar{\sigma} \cdot \dot{\bar{\varepsilon}} \tag{4.10}$$

The associated flow rule is adopted and the plastic rate-of-deformation is defined as

$$\hat{\mathbf{D}}^{\mathbf{p}} = \dot{\lambda} \frac{\partial \hat{f}}{\partial \hat{\boldsymbol{\sigma}}} \tag{4.11}$$

Thus, Equation (4.10) leads to

$$\dot{\bar{\varepsilon}} = \frac{\hat{\boldsymbol{\sigma}} : \hat{\mathbf{D}}^{\mathrm{p}}}{\bar{\sigma}} = \frac{\hat{\boldsymbol{\sigma}} : (\dot{\lambda} \frac{\partial \hat{f}}{\partial \hat{\boldsymbol{\sigma}}})}{\bar{\sigma}} = \frac{\dot{\lambda}}{\bar{\sigma}} \hat{\boldsymbol{\sigma}} : \frac{\partial \hat{f}}{\partial \hat{\boldsymbol{\sigma}}} \tag{4.12}$$

Using Euler's theorem for homogeneous functions and assuming $\hat{f}$ to be a positive homogeneous function of degree one, we get

$$\hat{\boldsymbol{\sigma}} : \frac{\partial \hat{f}}{\partial \hat{\boldsymbol{\sigma}}} = \bar{\sigma} \tag{4.13}$$

and it follows that

$$\dot{\bar{\varepsilon}} = \dot{\lambda} \tag{4.14}$$

The effective plastic strain $\bar{\varepsilon}$ is an example of an internal variable that is used to characterize the inelastic response of the material.

The conditions for plastic loading and elastic loading/unloading are expressed in Kuhn-Tucker form

$$\hat{f}(\hat{\boldsymbol{\sigma}}, \hat{\mathbf{q}}) \le 0; \quad \dot{\lambda} \ge 0; \quad \dot{\lambda} \hat{f} = 0 \tag{4.15}$$

The first of these conditions indicates that the stress state must lie on or within the yield surface, while the second indicates that the plastic rate parameter is non-negative. The last condition assures that the stress lies on the yield surface during plastic loading.

Assuming isotropic hardening, the reference hardening curve is modelled by the five-parameter extended Voce rule

$$\sigma_Y(\bar{\varepsilon}) = Y_0 + Q_1(1-\exp(-C_1\cdot\bar{\varepsilon})) + Q_2(1-\exp(-C_2\cdot\bar{\varepsilon})) \tag{4.16}$$

where Y_0 is yield stress, C_i and Q_i are strain hardening parameters. Clearly the curve includes three parts, one is the constant yield stress Y_0, and the other two parts are functions of the effective strain which represents the strain hardening, see Figure 4.1

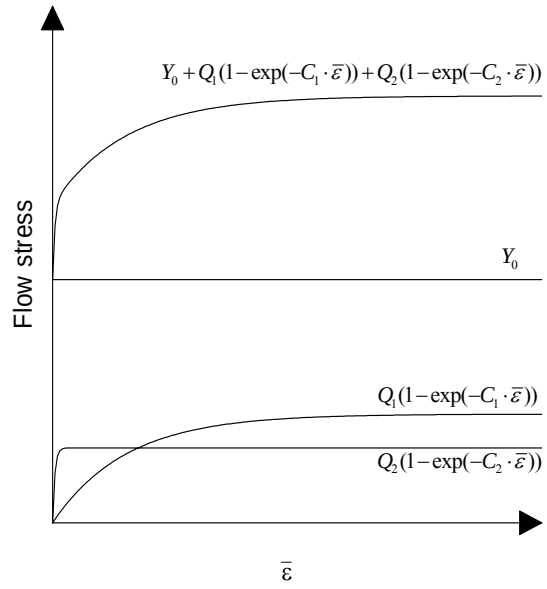

Figure 4.1. Decomposition of the work hardening curve by the extended Voce rule.

4.3 Yield function

To model the mechanical response and failure of extruded thin-walled aluminium, it is necessary to adopt a constitutive model with a sufficiently accurate yield criterion. Proper representation of the material's anisotropy is essential to capture several phenomena of prime interest.

The yield function proposed by Barlat and Lian (1989) is adopted in the present study. The criterion is based on a generalized isotropic yield criterion proposed by Hersey & Dahlgren (1954) and Hosford (1972). The original criterion takes the form

$$f = \sqrt[M]{\frac{1}{2}\left(\left|\sigma_1-\sigma_3\right|^M + \left|\sigma_3-\sigma_2\right|^M + \left|\sigma_2-\sigma_1\right|^M\right)} - \sigma_Y \le 0 \tag{4.17}$$

where σ_1 , σ_2 and σ_3 are principal stresses, and M is a material parameter. For simplicity, the symbol $(\hat{})$, signifying corotational variables is omitted in this section.

Barlat and Richmond (1987) expressed the function in a orthotropic reference frame x, y, z using the plane stress assumption

$$f = \sqrt[M]{\frac{1}{2}\left(\left|K_1+K_2\right|^M + \left|K_1-K_2\right|^M + \left|2K_2\right|^M\right)} - \sigma_Y \le 0 \tag{4.18}$$

where K_1 and K_2 are stress tensor invariants.

$$\begin{aligned} K_1 &= \frac{\sigma_{xx}+\sigma_{yy}}{2} \\ K_2 &= \sqrt{\left(\frac{\sigma_{xx}-\sigma_{yy}}{2}\right)^2 + \sigma_{xy}{}^2} \end{aligned} \tag{4.19}$$

Barlat and Lian (1989) further extended the formulation to the anisotropic case by adding some coefficients *a, b* and *c* that characterize the degree of the anisotropy:

$$f = \sqrt[M]{\frac{1}{2}\left(a\left|K_1+K_2\right|^M + b\left|K_1-K_2\right|^M + c\left|2K_2\right|\right)} - \sigma_Y \le 0 \tag{4.20}$$

K_1 and K_2 being unchanged, this equation can only describe planar isotropy unless *a, b* and *c* are functions themselves of the three stress components. For the sake of simplicity, *a, b* and *c* are taken as constants.

It has been shown that the plane stress yield surface of f.c.c. sheet metals can be roughly approximated by a dilatation of the normalized isotropic surface in one or both directions of $\sigma_{yy}/\bar{\sigma}$ and $\sigma_{xy}/\bar{\sigma}$ (Barlat and Lian 1989). Therefore, Barlat and Lian (1989) provided a simple yield function for planar anisotropy and plane stress states

$$f = \sqrt[M]{\frac{1}{2}(a\left|K_1+K_2\right|^M + a\left|K_1-K_2\right|^M + c\left|2K_2\right|^M)} - \sigma_Y \le 0$$

$$K_1 = \frac{\sigma_{xx} + h\sigma_{yy}}{2} \tag{4.21}$$

$$K_2 = \sqrt{(\frac{\sigma_{xx} - h\sigma_{yy}}{2})^2 + p^2\sigma_{xy}^2}$$

where *a*, *c*, *h* and *p* are material parameters. This criterion is obtained by inserting the principal stresses into the criterion of Hersey and Dahlgren (1954)/Hosford (1972), while weighing the normal stress in y-direction by a factor *h,* and the shear stress with a factor *p* in addition to the introduction of the factors *a* and *c* in Equation (4.20). The hydrostatic stresses are cancelled out as can be seen from Equation (4.17).

A typical yield surface for a textured aluminium alloy obtained by Equation (4.21) is showed in Figure 4.2, where *M* is equal to 14, and *a*, *c*, *h* and *p* are determined from the given R-ratios. It is seen that the contours of constant values of σ_{xy} change their shape

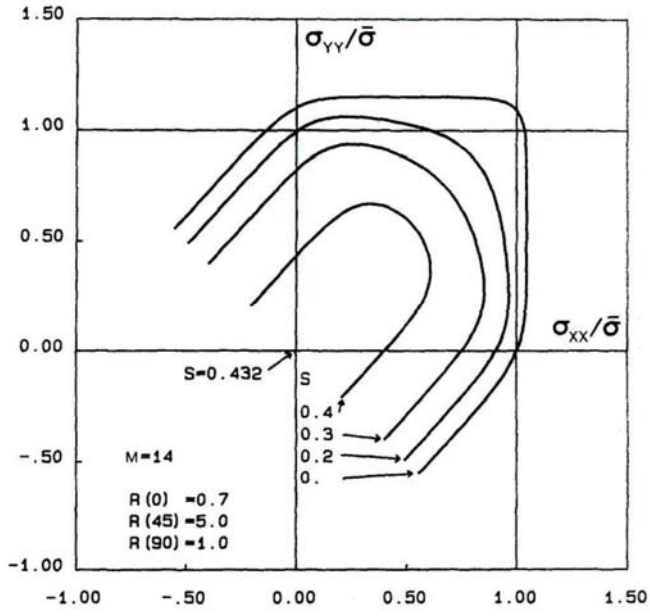

Figure 4.2. A tricomponent plane stress yield surface for a textured aluminium alloy obtained by Equation (4.21) (Barlat and Lian 1989).

for increasing values of shear stress, which indicates a coupling between shear and normal stress components (Barlat and Richmond 1987). The figure also indicates that the surface lies between the criteria of von Mises and Tresca. When M is equal to 2, and a, c, h and p are all equal to unity, the criterion is identical to the von Mises criterion. When M increases towards infinity, the criterion approaches the Tresca criterion.

4.4 Fracture criteria

Fracture is modelled by eroding elements when a fracture criterion is satisfied at an optional number of integration points through the shell thickness. Three fracture criteria were included in the WTM-2D. The first one is the critical-thickness-strain criterion which triggers fracture when the thickness strain reaches a critical value (Marciniak et al. 1973), ε_{cr} , i.e.

$$\varepsilon_3 = \varepsilon_{cr} \tag{4.22}$$

where it is noted that ε_{cr} is a negative number. Owing to plastic incompressibility and assuming negligible elastic strains, this criterion can also be expressed as

$$\varepsilon_1 + \varepsilon_2 = -\varepsilon_{cr} \tag{4.23}$$

which is the equation for the line in the $\varepsilon_1 - \varepsilon_2$ diagram that has a slope of -1 and intersects the ε_1 - axis at $-\varepsilon_{cr}$, as shown in Figure 4.3.

The second failure criterion is the so-called Cockcroft-Latham (CL) criterion (Cockcroft and Latham 1968). It is assumed that fracture is determined by

$$\int_0^{\bar{\varepsilon}} \max\left\{\sigma_1, 0\right\} d\bar{\varepsilon} = W_{cr} \tag{4.24}$$

where σ_1 is the major principal stress and W_{cr} is a material parameter which can be identified by material tests.

The last failure criterion is based on the work of Bressan and Williams (1982) which represents failure caused by localized through-thickness shear instability. Bressan and Willams (1982) assumed that shear instability occurs along a plane inclined through the

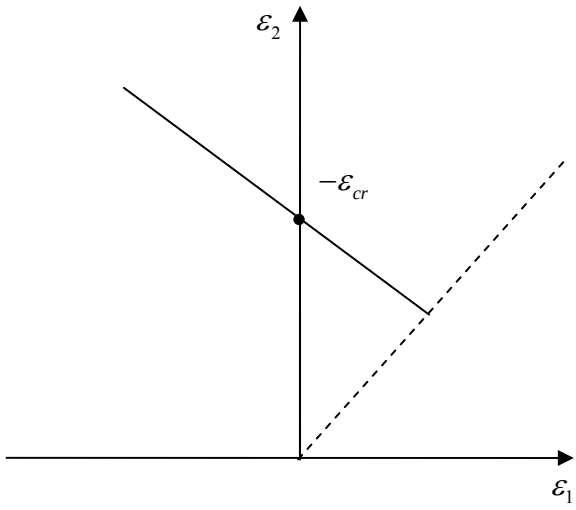

Figure 4.3. Critical thickness strain in ε_1 vs. ε_2 diagram.

thickness of the sheet that is parallel to the minor principal axis, and further that material elements which lie in the inclined plane and are normal to the minor principal direction, experience no change in length, see Figure 4.4. It is further assumed that instability occurs when the local shear stress on the plane reaches a critical value τ_{cr}. The value of τ_c is considered being a material characteristic and needs also to be deducted from experiments. In the case of planar isotropy the criterion can be expressed as (Bressan and Williams 1982)

$$\sigma_1 = \left| \frac{2\alpha + 1}{\sqrt{\alpha^2 + \alpha}} \right| \tau_{cr} \tag{4.25}$$

where $\alpha = d\varepsilon_2 / d\varepsilon_1$. Hopperstad et al. (2005) extended this criterion from isotropy to planar anisotropy. Without introducing more parameters, it can be simply expressed as

$$\sigma_1 \geq \frac{2\tau_{cr}}{\sin 2\varphi} \tag{4.26}$$

where σ_1 is the major principal stress, and φ defines the angle between the shear deformation plane and the major principal direction x_1. The angle can be determined by the compatibility condition.

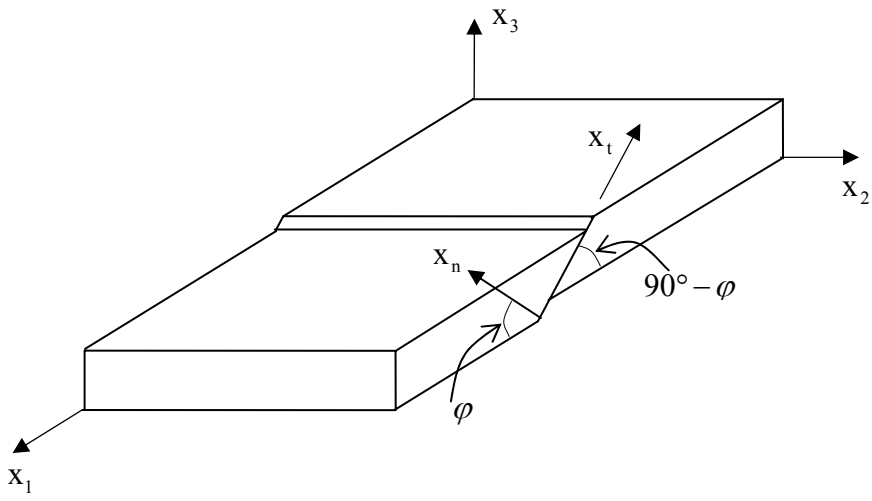

Figure 4.4. Local necking of sheet material through development of localised shear deformation at an angle φ with the major principal axis x_1.

5. Material tests

5.1 Introduction

This Chapter deals with mechanical properties of a 5 mm thick aluminium sheet which is the upper part of the fillet-welded connections presented in Chapter 7, see Figure 7.1. Uniaxial tensile tests, hardness tests and compression tests were performed to characterise the anisotropic strength, plastic flow and ductility of the material.

The investigated sheet is made of aluminium alloy EN AW-6082 and has been artificially heat-treated to obtain temper T6. The main alloying elements in EN AW-6082 are magnesium and silicon, and the minor alloying elements are manganese, iron, copper, chromium, zinc, and titanium, as listed in Table 5.1. The material specifications according to the certification from Hydro Aluminium are as follows: proof stress of 260 MPa, and tensile strength of 310 MPa.

5.2 Uniaxial tensile tests

The geometry of the uniaxial tensile test specimen is shown in Figure 5.1. Tests were performed in three directions, 0°, 45° and 90°, with reference to the extrusion direction. For each of the directions three specimens were cut from a piece of the extruded sheet, as shown in Figure 5.2. In addition, five compression test specimens in the form of 25 mm diameter discs were cut from the same sheet.

The tensile tests were carried out in a 100 kN Instron hydraulic tension/torsion machine with a logging frequency of 5 Hz. The strain was measured by a calibrated extensometer with 27 mm gauge length. The tests were carried out in displacement control mode at a nominal strain rate of approximately 2 mm/min.

Table 5.1. Chemical composition of aluminium alloy EN AW-6082.

	Si	Fe	Cu	Mn	Mg	Cr	Zn	Ti
Min (%)	0.7	0	0	0.4	0.6	0	0	0
Max (%)	1.3	0.5	0.1	1	1.2	0.2	0.2	0.1

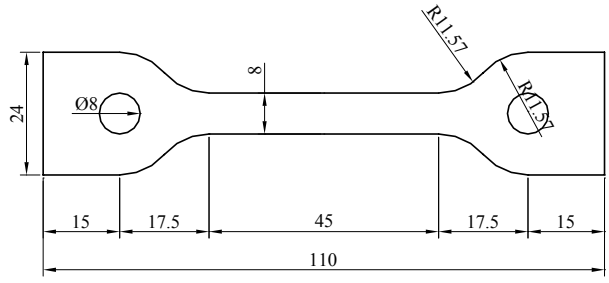

Figure 5.1. Geometry of the uniaxial tensile test specimen.

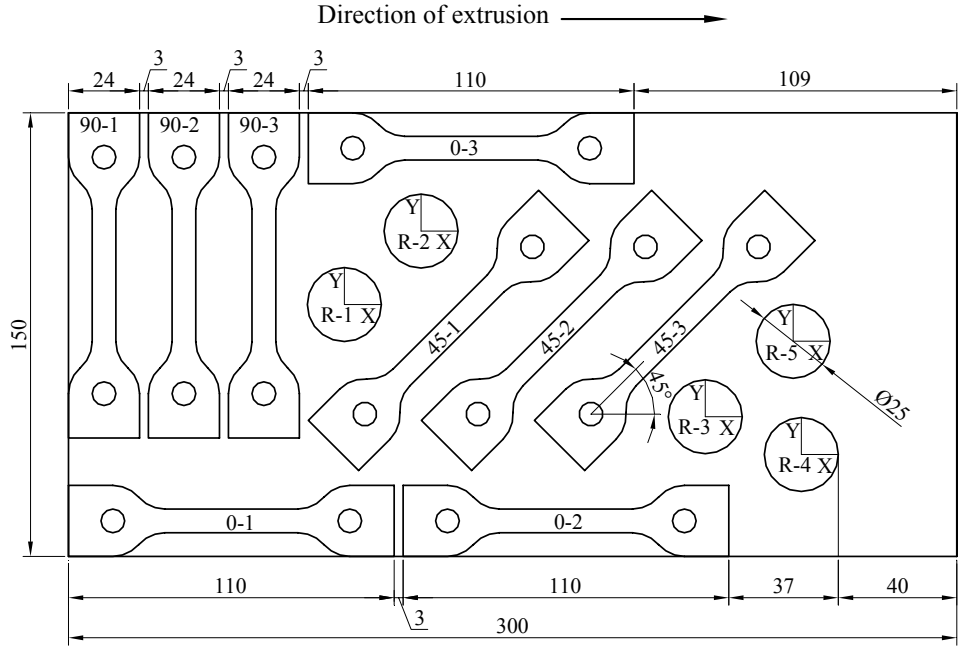

Figure 5.2. Specimens of uniaxial tensile tests and compression tests cut from the extruded sheet.

True stress and strain

The engineering stress, s, and engineering longitudinal strain, e_l, are defined as

$$s = \frac{F}{A_0}; \quad e_l = \frac{l - l_0}{l_0} \tag{5.1}$$

where F and A_0 are the force and initial cross section of the specimen, respectively, and l_0 and l are the initial gauge length and the actual length, respectively. The true stress, σ, and the true longitudinal strain, ε_l, were calculated from the nominal values as

$$\sigma = s(1 + e_l); \quad \varepsilon_l = \ln(1 + e_l) \tag{5.2}$$

The formulas for the transverse strain, ε_w, and the thickness strain ε_t, take the form

$$\varepsilon_w = \ln(\frac{w}{w_0}); \quad \varepsilon_t = \ln(\frac{t}{t_0}) \tag{5.3}$$

where w and w_0 are the actual and initial width, respectively, and t and t_0 are the actual and initial thickness, respectively. The true plastic strain in the longitudinal direction, ε_l^p, takes the form

$$\varepsilon_l^p = \varepsilon_l - \frac{\sigma}{E} \tag{5.4}$$

where E is Young's modulus.

Results from all tests are gathered in Appendix A. For the 0° and 90° specimens, some scatter was observed. Representative tests were chosen for the strength level obtained by most of the tests for each of the directions. Figure 5.3 shows the engineering stress vs. strain curves, and the representative tests are indicated with a dotted line for each direction. Figure 5.4 presents the results in terms of the true stress vs. strain curves in the three directions. Additionally, the true stresses vs. plastic strain curves in various directions are presented in the same figure. The figure clearly shows that the alloy has significant anisotropy in strength and ductility. The strength is about the same in the 0° and 90° directions, but significantly lower in the 45° direction.

For the representative 0° tensile test, the work hardening curve was calibrated according to the five-parameter extended Voce rule (Equation (4.16)) using a least-

square method in Microsoft Excel. The identified parameters are listed in Table 5.2, and will be used in the subsequent numerical analyses. The extended Voce rule was also used to obtain a parametric representation of all the other uniaxial tensile tests. The obtained parameters are listed in Table A-1 of Appendix A.

Table 5.2. Hardening parameters identified from a representative 0° tensile test.

Y_0 [MPa]	Q_1 [MPa]	C_1 [-]	Q_2 [MPa]	C_2 [-]	$Y_0+\sum Q_i$ [MPa]
256	52.3	4605	59.5	20.5	367.8

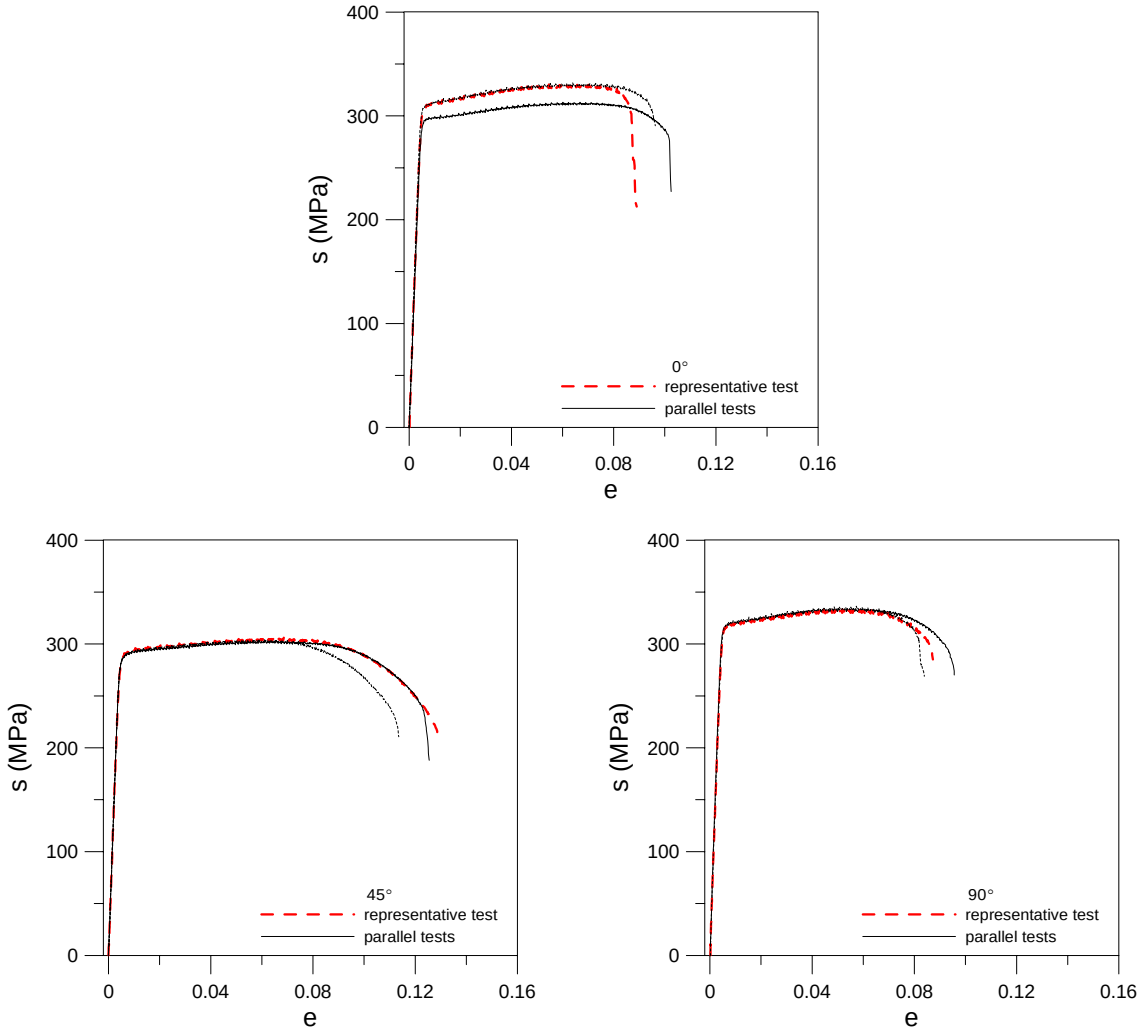

Figure 5.3. Engineering stress vs. strain curves of the uniaxial tensile tests for various directions.

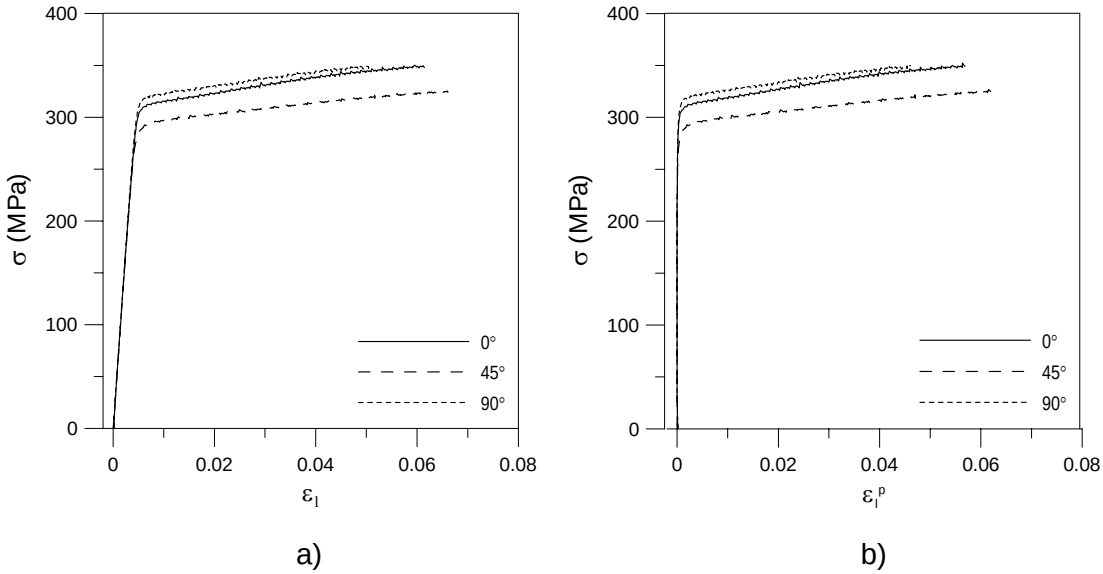

Figure 5.4. Representative test results: a) true stress vs. strain curves, and b) true stress vs. plastic strain curves.

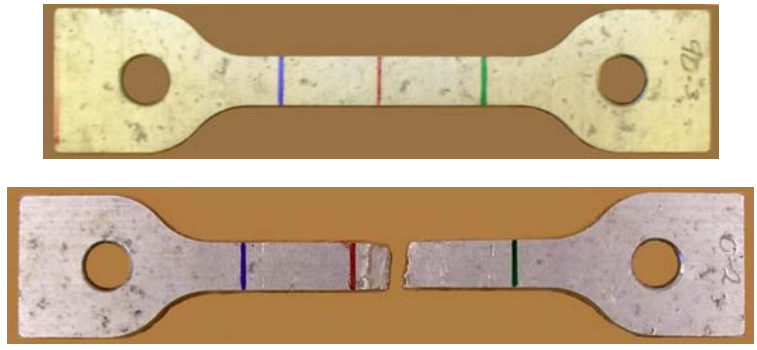

Figure 5.5. Tensile test specimen before and after testing.

Before testing the specimens were marked with colour lines across the width of the gauge length, as shown in Figure 5.5. The length of the lines before and after testing was measured, and the plastic transverse strain, ε_w^p, was calculated by Equation (5.3). Also the thickness at the position of the lines was measured, and the plastic thickness strain, ε_t^p, was calculated by Equation (5.3). The results are presented in Table A-2 and were used to obtain the R-ratio as explained in the following.

R-ratio

As a measure of the flow properties of the material, a specimen's R-ratio is defined as the ratio between the plastic strain rates in its width and thickness direction

$$R_\alpha = \left. \frac{\dot{\varepsilon}_w^p}{\dot{\varepsilon}_t^p} \right|_\alpha \tag{5.5}$$

where α denotes the specimen's direction relatively to the extrusion direction, see Figure 5.6.

Assuming proportional straining, which has found to be an acceptable assumption in various investigations, e.g. Lademo (1999), the R-ratio may alternatively be found from the accumulated strains as

$$R_\alpha = \left. \frac{\varepsilon_w^p}{\varepsilon_t^p} \right|_\alpha \tag{5.6}$$

The R-ratios obtained from the representative tests are presented in Table 5.3. It is seen that the extrusion exhibits significant anisotropy in plastic flow, with a strong tendency to thinning in the 0° direction. In this direction the R-ratio is as low as 0.37, while in the other two directions the R-ratios are much higher. Especially in the 45° direction the R-ratio has the maximum value of 1.19. R-ratios for all the specimens are gathered in Table A-2. The average and standard deviation of the R-ratio obtained from the tests can be seen in Table A-3.

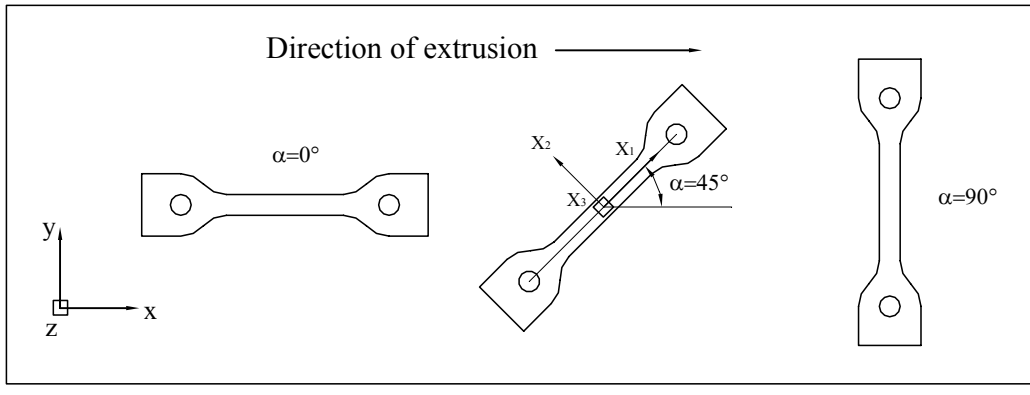

Figure 5.6. Uniaxial test specimens with various orientations.

Flow stress ratio r

The flow stress ratio is introduced to compare the hardening property in different directions, at the same value of the specific plastic work (Lademo 1999).

For a given value of plastic strain ε_α^p, the specific plastic work W^p in the tensile test in the direction α is defined as

$$W^p = \int_0^{\varepsilon_\alpha^p} \sigma_\alpha d\varepsilon_\alpha^p \qquad \text{(no sum)} \tag{5.7}$$

The flow stress ratio is calculated as

$$r_\alpha = \left.\frac{\sigma_\alpha}{\sigma_0}\right|_{W^p} \tag{5.8}$$

Figure 5.7 depicts the flow stress ratio computed for the representative tests of 45° and 90° specimens, respectively. The flow stress ratio in the 0° direction is equal to unity according to its definition. As can be seen, the ratio is nearly a constant at 0.93 for the 45° specimen, and 1.02 for the 90° specimen. The R-ratios and flow stress ratios from the representative tests are listed in Table 5.3.

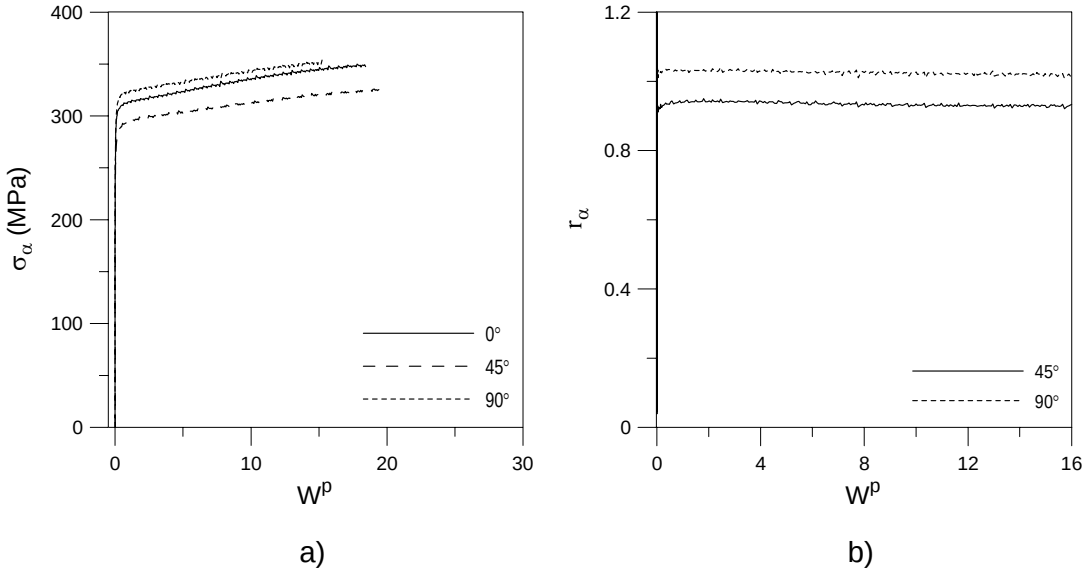

Figure 5.7. Representative test results: a) True stress vs. specific plastic work, and b) flow stress ratio vs. specific plastic work.

Table 5.3. Representative test results: the R-ratios and flow stress ratios.

R_0	R_{45}	R_{90}	r_0	r_{45}	r_{90}
0.37	1.19	0.87	1.00	0.93	1.02

Since the flow stress ratios are almost constant for all angles, it can be concluded that the material is quite well described by the assumption of isotropic hardening in the investigated uniaxial tension regime of the stress space.

5.3 Hardness tests

Indentation hardness is an easily measured and well-defined characteristic, and it can give the designer useful information about the strength and heat treatment of the metal. The test consists of pressing a pointed diamond or a hardened steel ball into the surface of the material to be examined. The further into the material the "indenter" sinks, the softer is the material and the lower is its strength.

An empirical correlation between the strength and hardness has been shown to give good agreement for several metals, Dieter (1988). Matusiak (1999) proposed a linear strength vs. hardness formula for the aluminium alloy EN AW-6082 based on Vickers hardness and uniaxial tensile tests. The relations are:

$$f_{0.2}(MPa) = 3.6HV - 81$$
$$f_u(MPa) = 2.6HV + 54 \tag{5.9}$$

where HV is Vickers hardness, $f_{0.2}$ is the yield stress and f_u is the ultimate stress.

In the present study, it is not possible to directly measure the strength properties of the weld and HAZ material, therefore hardness was measured instead. As Figure 5.8 shows, the specimens of the hardness test were cut from the region of the weld and HAZ from a 0°-welded component (The details of this welded component is given in Chapter 7). The specimens were located at one-third of the width from the left and right edges of the upper plate. Vickers hardness was measured using a load of 5 kg along the centre line of the cross-section, with 1 mm distance between the measuring points, as shown in Figure 5.9. The results are given in Figure 5.10.

It is seen that there is significant scatter between the two sets of measurements, but the trends are clear. The hardness has a minimum value in a narrow region of the HAZ

about 10 mm from the weld centre. This minimum value is about 65% of the hardness in the base material and approximately equal to the hardness of the weld material.

The hardness in the fillet weld was measured as well. Sample points were selected randomly as in seen Figure 5.11. The results are $HV = 77$ and 74 at the left side, and $HV = 72$ in all three points at the right side.

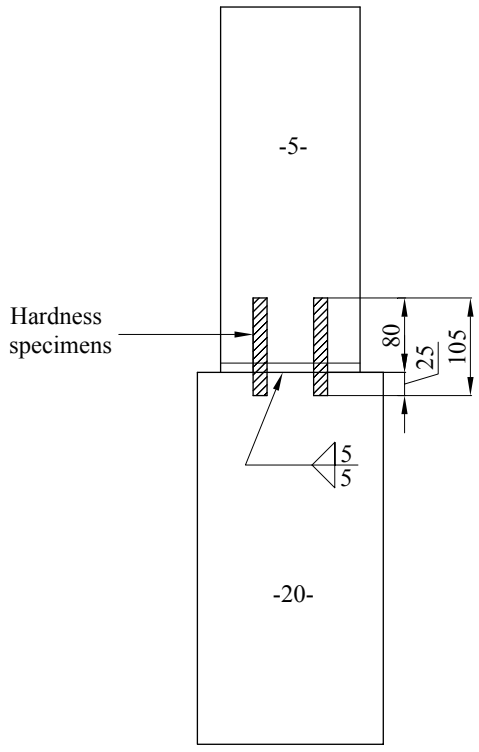

Figure 5.8. Hardness specimens cut from a 0° fillet-welded specimen.

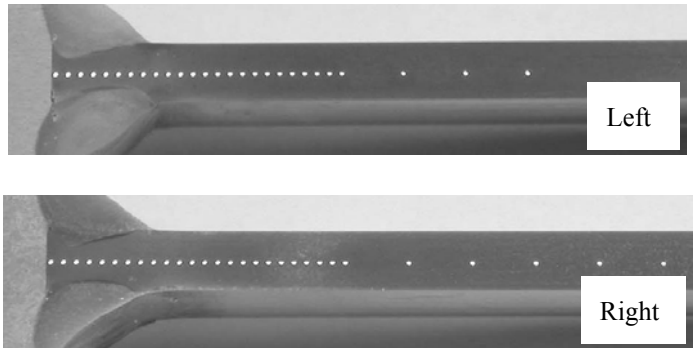

Figure 5.9. Measuring points in the HAZ.

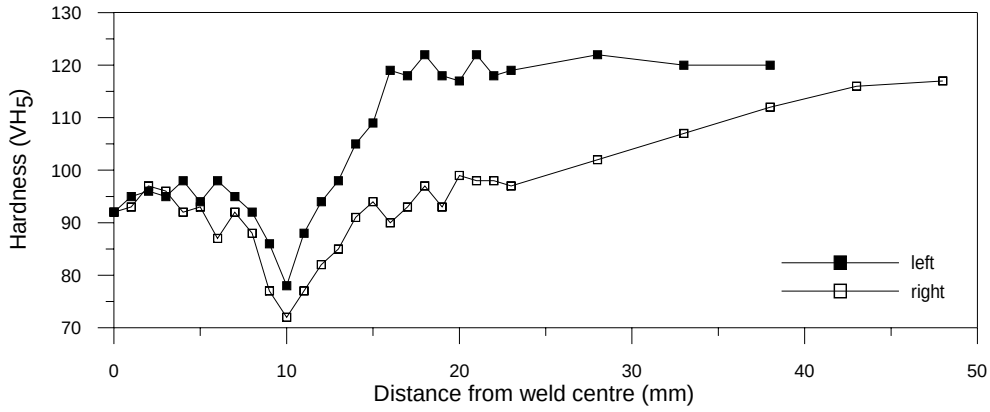

Figure 5.10. Results of hardness tests.

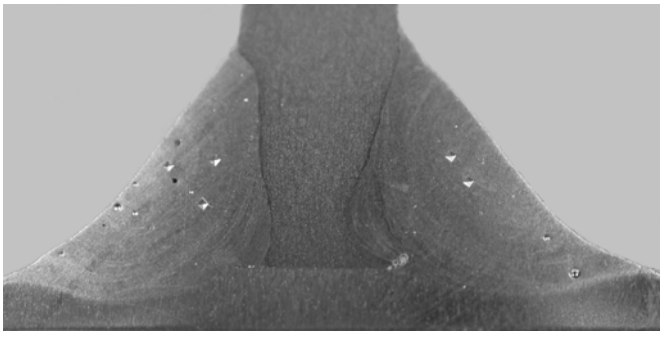

Figure 5.11. Measuring points in the weld material.

5.4 Compression tests

Since metals can be assumed to be plastically incompressible, any test may be considered as a combination of the testing condition and a hydrostatic pressure. Therefore, it is allowable to regard a through-thickness compression test as a combination of a uniaxial compressive stress and a hydrostatic tension stress with the same absolute value. As a result the loading can be considered equivalent to a balanced biaxial stress state, as indicated in Figure 5.12. The uniaxial compression test can thus give information about the material's plastic response in a balanced biaxial stress state.

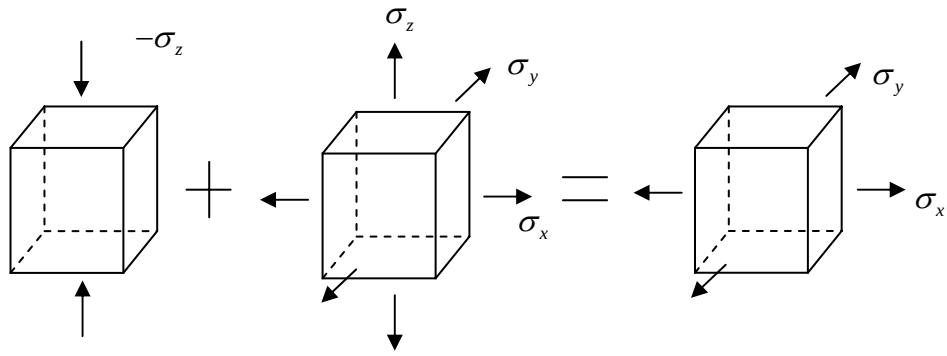

Figure 5.12. In a plastic state a combination of a uniaxial compressive stress and a hydrostatic tensile stress is equivalent to a balanced biaxial in-plane stress state.

Table 5.4. Results for compression tests

Specimen	Diameter before		Diameter after				
	D_{x0}	D_{y0}	D_x	D_y	ε_{xx}^p	ε_{yy}^p	$\varepsilon_{xx}^p / \varepsilon_{yy}^p$
	[mm]	[mm]	[mm]	[mm]			
1	24.73	24.80	29.71	27.46	0.18	0.10	1.80
2	24.83	24.81	27.48	26.60	0.10	0.07	1.46
3	24.87	24.87	29.40	27.59	0.17	0.10	1.61
4	24.83	24.85	28.18	27.19	0.13	0.09	1.41
5	24.81	24.82	28.26	26.92	0.13	0.08	1.60
Average							1.58
Stdeva							0.15

More specifically, the through-thickness compression tests were performed to obtain information about the plastic flow direction for the balanced biaxial stress state. Circular discs with a diameter of 25 mm were electro-eroded from the extruded sheet, as shown in Figure 5.2. The specimens were quasi-statically compressed between two well-aligned and lubricated steel plates in a servo hydraulic testing machine. After testing, the strains along and perpendicular to the extrusion direction were measured, and the balanced biaxial plastic flow ratio, R_b, was defined and calculated as

$$R_b = \frac{\varepsilon_{xx}^p}{\varepsilon_{yy}^p} = \frac{\ln(D_x / D_{x0})}{\ln(D_y / D_{y0})} \tag{5.10}$$

where x is the extrusion direction, and y is the transverse direction in the aluminium sheet. The diameter of the disc specimens is denoted as D_{x0} and D_{y0} before testing, and D_x and D_y after completion of the test. The measurement and computation results are provided in Table 5.4. It is evident that there is a strong directional dependence of the plastic strain and that the average plastic strain in the extrusion direction is much higher than in the transverse direction. However, the scatter in the results is significant.

6. Identification of material parameters

6.1 Introduction

Here the parameters of the WTM-2D are identified for the subsequent numerical simulations. The identification relies upon experimental data from the current study and the available results from open literature. The model parameters for the HAZ and weld are considered of prime importance for accurate prediction of the performance of the welded structures.

6.2 Work hardening parameters

The work hardening parameters for the weld, HAZ and base material were identified according to the current material tests and available experimental data by Matusiak (1999), on the basis that the previously studied aluminium plate has an identical thickness and chemical compositions as the one in the current study. The identification procedure is explained in the following.

6.2.1 Review of a previous study

In a previous investigation by Matusiak (1999), the variation of the mechanical properties in the vicinity of a weld bead was studied by means of uniaxial tensile tests and hardness measurements. Nineteen uniaxial tensile test specimens were cut at incremental distances of 4 mm from the weld centre, as depicted in Figure 6.1. The engineering stress vs. strain curves of the specimens are shown in Figure 6.2. The figure

demonstrates the effect of welding on the mechanical properties as: a) reduced yield stress and ultimate strength within a distance of 16 mm from weld centre, b) generally greater elongation and higher strain hardening in the HAZ than in the base material, and c) considerably greater elongation and strain hardening in the weld than in the base material.

Assuming isotropic hardening, the reference equivalent stress vs. strain relation is represented by the five-parameter extended Voce rule given by Equation (4.16). The model parameters, Y_0, Q_i and C_i $(i = 1,\ 2)$, were found by a least-square approach. The experimental and fitted true stress vs. plastic strain curves are presented respectively in Figure 6.3 a) and b). Since the test data are from the 90° direction, and not the extrusion direction, the obtained parameters can not be used to the WTM-2D directly. To obtain Y_0 in the reference direction, $Y_0(90°)$ in all curves are divided by r_{90}, owing to the definition of the flow stress ratio. The ratio was determined as $r_{90} = 1.02$ for the extruded sheet, see Section 5.2. Keeping Q_i and C_i unchanged, it is thus implicitly assumed that the strain hardening process is identical in the extrusion (0°) direction and in the transverse (90°) direction. This is a reasonable assumption owing to the observation that the flow stress ratio r_{90} is found to vary only slightly with plastic work. The weld is assumed to be isotropic, and Y_0 is taken as the value identical to the yield stress in the 90° direction. After adjustment the work hardening parameters (Y_0 (0°), Q_i, and C_i) in Table 6.1 were found.

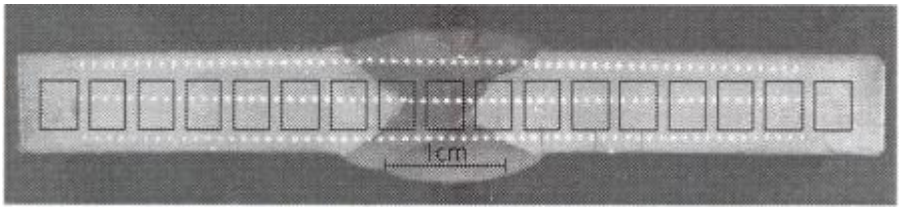

Figure 6.1. Hardness profiles and tensile test specimens cut from butt-welded plate (Matusiak 1999).

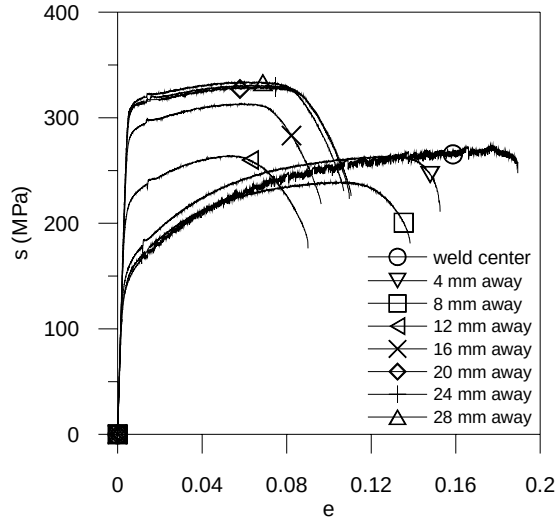

Figure 6.2. Engineering stress vs. strain curves for material in the vicinity of a butt weld. (Data from (Matusiak 1999)).

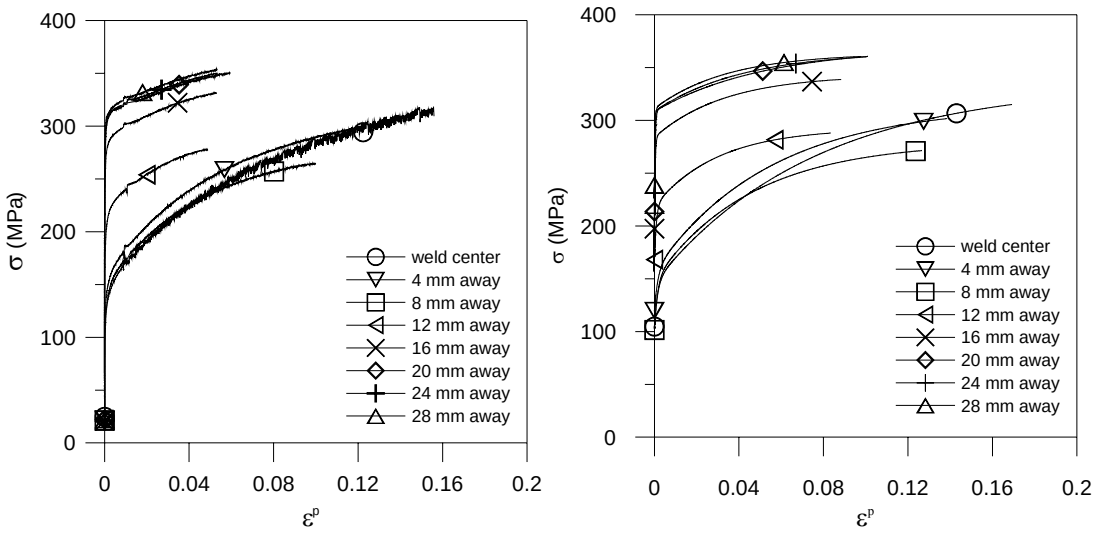

Figure 6.3. For material in the vicinity of a butt weld, a) the true stress vs. plastic strain curves and b) the fitted true stress vs. plastic strain curves. (Data from (Matusiak 1999)).

Table 6.1. Work hardening parameters for the weld, HAZ and base material Identified by tensile tests of a butt-welded plate.

Zone	Curve parameters						
	Y_0 (90°) [N/mm^2]	Y_0 (0°) [N/mm^2]	Q_1 [N/mm^2]	C_1 [-]	Q_2 [N/mm^2]	C_2 [-]	$\sigma_0+\Sigma Q$ [N/mm^2]
Weld	105	105	42	656	189	13	335
4 mm away	120	118	38	616	157	18	314
8 mm away	101	99	47	669	131	22	280
12 mm away	168	165	51	1091	74	33	293
16 mm away	200	196	84	2811	60	30	343
20 mm away	221	217	88	6095	61	19	369
24 mm away	209	205	100	2780	57	24	365
28 mm away	240	235	72	3196	52	29	364

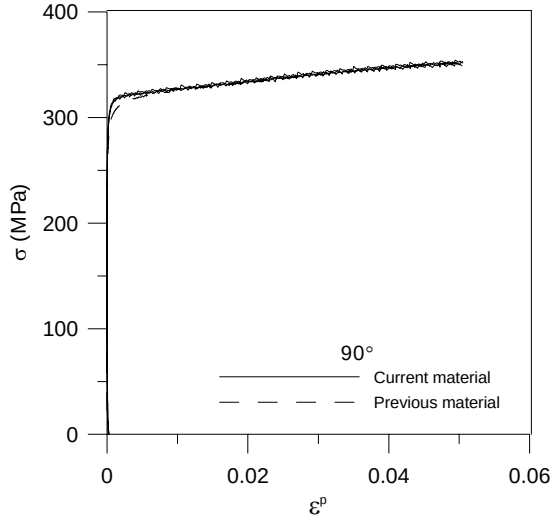

Figure 6.4. True stress vs. plastic strain curves of the 90° tensile tests of the materials in the current and previous studies.

6.2.2 Parameters for the present study

Figure 6.4 shows the true stress vs. plastic strain curves (90°) for the material in the present study and in the previous study by Matusiak (1999). Clearly the strength and hardening properties are identical for both materials. For simplicity, it is further assumed that both materials possess identical anisotropy.

Direct measurement of the inhomogeneous properties of the weld and HAZ is not feasible, at least not for the practical industrial purpose of this work. Therefore, hardness test results in these zones were used to provide information about the material strength. The tests were performed using the same procedure as in Matusiak's study and details of the tests are given in Section 5.3. The hardness results for the present tests were compared with the ones for the butt-welded plate investigated by Matusiak. For the parts possessing the same hardness, the parameters of the part in the butt-welded plate was chosen to be the parameters of the corresponding part in the present component, as illustrated in Table 6.2. The obtained parameters for the fillet-welded connections are listed in Table 6.3. Figure 6.5 shows the corresponding true stress vs. plastic strain curves.

Table 6.2. Identification procedure of work hardening properties by the hardness tests and previous tensile tests.

Zone in present study	Hardness				Representative hardness	Corresponding zone in previous study
	Distance [mm]	HV left	HV right	Average		
Weld (0-8 mm)		77	72			
		74	72	74		Weld
			72			
Sub-HAZ 1 (8-12 mm)	9	86	77	81.5		
	10	78	72	75	80	8 mm away
	11	88	77	82.5		
	12	94	82	88		
Sub-HAZ 2 (12-16 mm)	13	98	85	91.5		
	14	105	91	98	98	12 mm away
	15	109	94	101.5		
	16	119	90	104.5		
Sub-HAZ 3 (16-20 mm)	17	118	93	105.5		
	18	122	97	109.5	107	16 mm away
	19	118	93	105.5		
	20	117	99	108		
Sub-HAZ 4 (20-24 mm)	21	122	98	110		
	22	118	98	108	109	20 mm away
	23	119	97	108		
Sub-HAZ 5 (24-28 mm)	28	122	102	112	112	24 mm away
Sub-HAZ 6 (28-32 mm)	28	122	102	112	112	24 mm away
Base	33	120	107	113.5		
	38	120	112	116	116	Base
	43		116	116		
	48		117	117		

Table 6.3. Obtained hardening parameters for the fillet-welded connections.

Zone	Curve parameters							Corresponding zones in previous study
	Y_0 (90°) [N/mm^2]	Y_0 (0°) [N/mm^2]	Q_1 [N/mm^2]	C_1 [-]	Q_2 [N/mm^2]	C_2 [-]	$\sigma_0+\Sigma Q$ [N/mm^2]	
Weld	105	105	42	656	189	13	335	weld
Sub-HAZ 1	101	99	47	669	131	22	280	8 mm away
Sub-HAZ 2	168	165	51	1091	74	33	293	12 mm away
Sub-HAZ 3	200	196	84	2811	59	30	343	16 mm away
Sub-HAZ 4	221	217	88	6095	61	19	369	20 mm away
Sub-HAZ 5	209	205	100	2780	57	24	366	24 mm away
Sub-HAZ 6	209	205	100	2780	57	24	366	24 mm away
Base	240	235	72	3196	52	29	364	Base

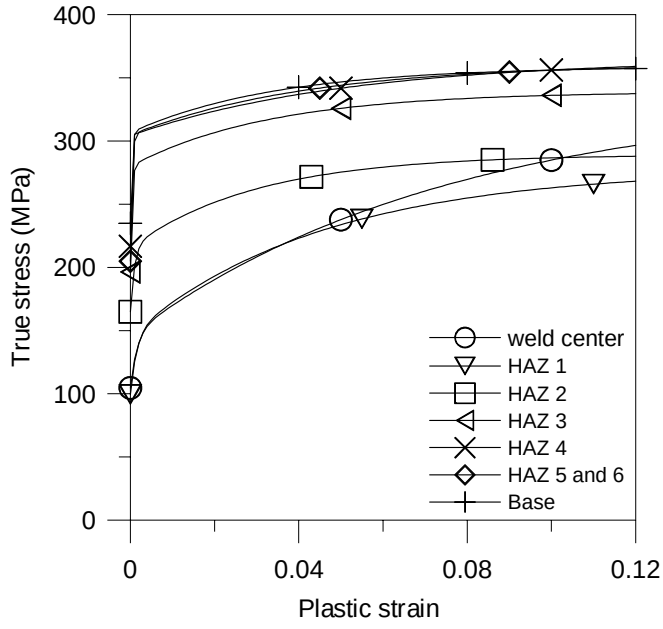

Figure 6.5. Obtained true stress vs. plastic strain curves for the fillet-welded connections.

6.3 Yield surface parameters

Assuming M is given, the yield surface parameters a, c, h, and p can be calibrated by various methods based on material tests. For the present study, only the uniaxial tensile tests reported in Chapter 4 are used.

6.3.1 Calibration methods

Analytical solution

Barlat and Lian (1989) provided the following method to identify the yield surface parameters by using yield stresses and R-ratios acquired from the uniaxial tensile tests. In an extruded sheet, specimens with various orientations are extracted as shown in Figure 5.6. A local coordinate system is defined as x_1, x_2, and x_3, with x_1 being the longitudinal direction of the specimen. A reference coordinate systems is defined as x, y, and z, with x being the extrusion direction. For the specimen at the direction inclined at θ from the extrusion direction, the stress tensor $\boldsymbol{\sigma}$ in the reference coordinate is written as

$$\boldsymbol{\sigma} = \mathbf{M}^{\mathrm{T}} \hat{\boldsymbol{\sigma}} \mathbf{M} \tag{6.1}$$

where $\mathbf{M}$ is a transformation matrix given by

$$\mathbf{M} = \begin{bmatrix} \cos\theta & \sin\theta & 0 \\ -\sin\theta & \cos\theta & 0 \\ 0 & 0 & 1 \end{bmatrix} \tag{6.2}$$

and $\hat{\boldsymbol{\sigma}}$ is the stress tensor in the local coordinate system (x_1, y_1 and z_1), i.e.,

$$\hat{\boldsymbol{\sigma}} = \begin{bmatrix} \sigma_\theta & 0 & 0 \\ 0 & 0 & 0 \\ 0 & 0 & 0 \end{bmatrix} \tag{6.3}$$

where σ_θ is the uniaxial stress in direction θ. This transformation leads to the components of $\boldsymbol{\sigma}$:

$$\begin{aligned} \sigma_{xx} &= \sigma_\theta \cos^2\theta \\ \sigma_{yy} &= \sigma_\theta \sin^2\theta \\ \sigma_{xy} &= \sigma_\theta \sin\theta\cos\theta \end{aligned} \tag{6.4}$$

When θ is equal to 0°, the uniaxial stress is equal to the effective stress $\bar{\sigma}$, i.e.

$$\begin{aligned}\sigma_{xx} &= Y_0(0°) = \bar{\sigma} \\ \sigma_{yy} &= \sigma_{xy} = 0\end{aligned} \tag{6.5}$$

where $Y_0(0°)$ is the yield stress in extrusion direction. By combination of Equations (4.21) and (6.4), the relationship between a and c is found as

$$c = 2 - a \tag{6.6}$$

When θ is equal to 90°, it follows that

$$\begin{aligned}\sigma_{yy} &= Y_0(90°) \\ \sigma_{xx} &= \sigma_{xy} = 0\end{aligned} \tag{6.7}$$

where $Y_0(90°)$ is the yield stress in 90° direction. Substituting (6.5) and (6.7) into the yield function (4.21), h is determined as

$$h = \frac{Y_0(0°)}{Y_0(90°)} \tag{6.8}$$

Assuming plastic incompressibility, the specimen's R-ratio takes the form

$$R_\theta = \frac{\dot{\varepsilon}_{22}^p}{\dot{\varepsilon}_{33}^p} = \frac{\dot{\varepsilon}_{11}^p}{\dot{\varepsilon}_{11}^p + \dot{\varepsilon}_{22}^p} - 1 = \frac{\dot{\varepsilon}_{11}^p}{\dot{\varepsilon}_{xx}^p + \dot{\varepsilon}_{yy}^p} - 1 \tag{6.9}$$

Assuming the associated flow rule, the rate of plastic strains given by yield function (4.21) are

$$\begin{aligned}\dot{\varepsilon}_{xx}^p = \dot{\lambda}\frac{\partial f}{\partial \sigma_{xx}} = \dot{\lambda}\frac{1}{M}\Bigg\{ & a\left(K_1 + K_2\right)\left|K_1 + K_2\right|^{M-2}\left(\frac{1}{2} + \frac{\sigma_{xx} - h\sigma_{yy}}{4K_2}\right) \\ & + a\left(K_1 - K_2\right)\left|K_1 - K_2\right|^{M-2}\left(\frac{1}{2} + \frac{\sigma_{xx} - h\sigma_{yy}}{4K_2}\right) \\ & + 2^M c K_2^{M-1}\frac{\sigma_{xx} - h\sigma_{yy}}{4K_2}\Bigg\} f^{\frac{1-M}{M}}\end{aligned} \tag{6.10}$$

$$\dot{\varepsilon}_{yy}^{p} = \dot{\lambda}\frac{\partial f}{\partial \sigma_{yy}} = \dot{\lambda}\frac{1}{M}\left\{a\left(K_1+K_2\right)\left|K_1+K_2\right|^{M\text{-}2}\left(\frac{h}{2}-h\frac{\sigma_{xx}-h\sigma_{yy}}{4K_2}\right)\right.$$
$$+a\left(K_1-K_2\right)\left|K_1-K_2\right|^{M-2}\left(\frac{h}{2}+h\frac{\sigma_{xx}-h\sigma_{yy}}{4K_2}\right) \tag{6.11}$$
$$\left.+2^M cK_2^{M-1}h\frac{\sigma_{xx}-h\sigma_{yy}}{4K_2}\right\} f^{\frac{1-M}{M}}$$

and

$$\dot{\varepsilon}_{xy}^{p} = \dot{\lambda}\frac{\partial f}{\partial \sigma_{xy}} = \dot{\lambda}\frac{1}{M}\left\{a\left(K_1+K_2\right)\left|K_1+K_2\right|^{M\text{-}2}-a\left(K_1-K_2\right)\left|K_1-K_2\right|^{M-2}\right.$$
$$\left.+2^M cK_2^{M-1}\right\} p^2\frac{\sigma_{xy}}{2K_2} f^{\frac{1-M}{M}} \tag{6.12}$$

The associated flow rule gives the plastic strain rate in the x_1-direction as

$$\dot{\varepsilon}_{11}^{p} = \dot{\lambda}\frac{\partial f}{\partial \sigma_{\theta}} = \dot{\lambda}\left(\frac{\partial f}{\partial \sigma_{xx}}\frac{\partial \sigma_{xx}}{\partial \sigma_{\theta}}+\frac{\partial f}{\partial \sigma_{yy}}\frac{\partial \sigma_{yy}}{\partial \sigma_{\theta}}+\frac{\partial f}{\partial \sigma_{xy}}\frac{\partial \sigma_{xy}}{\partial \sigma_{\theta}}\right)$$
$$=\dot{\lambda}\left(\frac{\partial f}{\partial \sigma_{xx}}\cos^2\theta+\frac{\partial f}{\partial \sigma_{yy}}\sin^2\theta+\frac{\partial f}{\partial \sigma_{xy}}\sin\theta\cos\theta\right) \tag{6.13}$$

Substituting (6.13) into (6.9), it follows that

$$R_{\theta} = -\frac{\frac{\partial f}{\partial \sigma_{xx}}\sin^2\theta+\frac{\partial f}{\partial \sigma_{yy}}\cos^2\theta-\frac{\partial f}{\partial \sigma_{xy}}\sin\theta\cos\theta}{\frac{\partial f}{\partial \sigma_{xx}}+\frac{\partial f}{\partial \sigma_{yy}}} \tag{6.14}$$

Based on yield function (4.21) and the associated flow rule, the R-ratio can thus be calculated for any orientation of a specimen. Particularly, for θ is equal to 0°, the expression for the R-ratio takes the form

$$R_0 = \frac{2}{2-ch}-1 \tag{6.15}$$

For θ equal to 90° , the R-ratio takes the form

$$R_{90} = \frac{2h}{2h-c} - 1 \tag{6.16}$$

Combination of Equations (6.6), (6.15), and (6.16) gives the expression of a and h in terms of R_0 and R_{90}

$$a = 2 - c = 2 - 2\sqrt{\frac{R_0 R_{90}}{(1+R_0)(1+R_0)}} \tag{6.17}$$

$$h = \sqrt{\frac{R_0(1+R_{90})}{(1+R_0)R_{90}}} \tag{6.18}$$

Having obtained a, c and h, the only unknown parameter p can be determined by using the expression of R_{45}. Using the same method as above, an implicit equation in terms of p can be found taking into account of σ_0, σ_{45} and R_{45}. The nonlinear equation can be solved numerically. Instead of R_{45}, the R-ratio in any other direction can also be used to identify the parameter p.

General weighted least-square approach

Using the Solver function in Microsoft Excel, it is also possible to identify the parameters through weighted least-square approach, by minimizing the sum of squares between the model representation and the experimental data of R-ratios and flow stress ratios.

From the yield function (4.20) and the stress components in (6.4), the flow stress ratio in a general direction is found as

$$r_\theta^{\text{model}} = \frac{\sigma_\theta}{\bar{\sigma}} = \frac{1}{\left[\frac{1}{2}\left(a\left|k_1+k_2\right|^M\right) + a\left|k_1-k_2\right|^M + c\left|2k_2\right|^M\right]^{\frac{1}{M}}} \tag{6.19}$$

where $\bar{\sigma}$ is the effective stress in yield function (4.21), and

$$k_1 = \frac{\cos^2\theta + h\sin^2\theta}{2}$$
$$k_2 = \sqrt{\left(\frac{\cos^2\theta - h\sin^2\theta}{2}\right)^2 + \left(p\sin\theta\cos\theta\right)^2} \tag{6.20}$$

The minimizing of the sum of the square between the model and the experimental data can be written as

$$\sum_\theta \left(R_\theta^{\exp} - R_\theta^{\text{model}}\right)^2 + \sum_\theta \left(r_\theta^{\exp} - r_\theta^{\text{model}}\right)^2 = \min \tag{6.21}$$

where θ = 0°, 45° and 90° for the present study. R_θ^{model} can be obtained from Equation (6.14).

Equation (6.21) is not the only choice of minimizing the difference between the model and experimental data. Considering that the R-ratios are less accurate than the flow stress ratios, it is desirable to give the flow stress ratios more weight than the R-ratios in the sum of squares. An approach is to raise the R-ratios to the power of $1/(M-1)$ in the minimising equation, i.e.,

$$\sum_\theta \left(\left(R_\theta^{\exp}\right)^{\frac{1}{M-1}} - \left(R_\theta^{\text{model}}\right)^{\frac{1}{M-1}}\right)^2 + \sum_\theta \left(r_\theta^{\exp} - r_\theta^{\text{model}}\right)^2 = \min \tag{6.22}$$

There are certainly many other ways to obtain a similar weighting of the contribution from flow stress ratios and R-ratios.

6.3.2 Results

The parameter M in yield function (4.21) was recommended to be equal to 8 for f.c.c. materials such as aluminium (Barlat and Lian 1989). However, $M = 14$ is also studied to investigate the influence of the yield function identification. The methods described in Section 6.3.1 are used to calibrate the parameters a, c, h and p. The method proposed by Barlat and Lian (Barlat and Lian 1989) using R_0 and R_{90} in Equations (6.17) and (6.18), and R_{45} from Equation (6.14) is named the Analytical method. Calibration based on Equation (6.21) is named the Simple method, and calibration based on Equation (6.22) is called the Power method.

Table 6.4. Yield function parameters.

No.	Method	Yield surface parameters					Predicted R_b (measured as: 1.58)
		M	a	c	h	p	
1.	Analytical	8	1.291	0.709	0.762	1.046	8.80
2.	Simple	8	1.234	0.765	0.856	1.069	3.38
3.	Power	8	1.255	0.745	0.96	1.122	1.39
4.	Analytical	14	1.291	0.709	0.762	0.978	44.9
5.	Simple	14	1.234	0.766	0.863	1.015	7.89
6.	Power	14	1.281	0.713	0.976	1.102	1.40

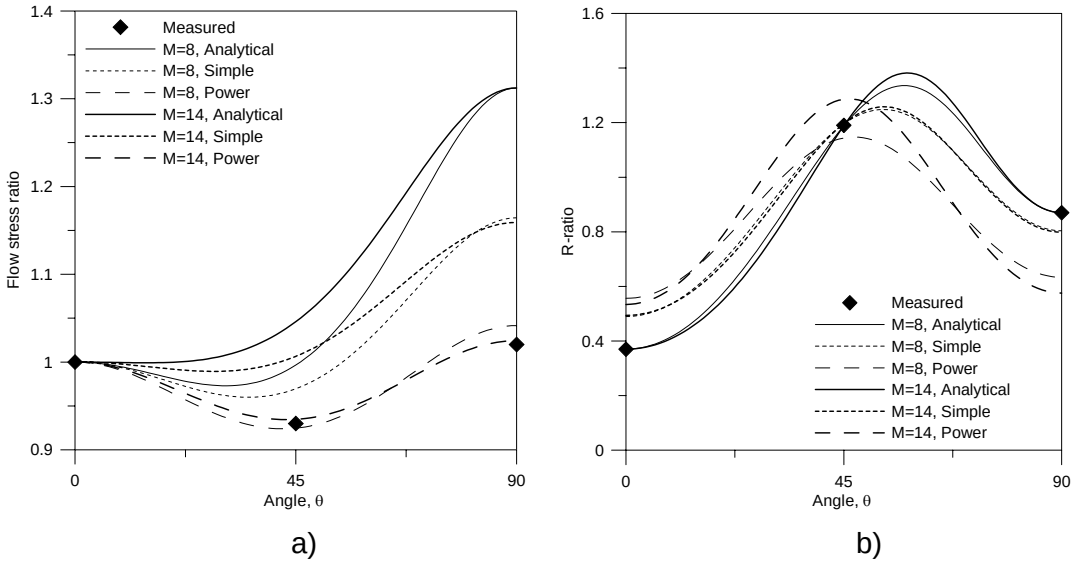

Figure 6.6. Measured and predicted a) flow stress ratios, and b) R-ratios.

The calibration methods and results are summarized in Table 6.4. Figure 6.6 shows the predicted curves and measured values of the R-ratios and flow stress ratios. It can be seen that the Analytical method represents the R-ratios accurately for the given angles as expected from its input, but not the corresponding stress ratios. The Simple method predicts the R-ratios relatively well. However, the Power method is much more accurate in predicting the flow stress ratios. This is expected since the weight of the R-ratios was reduced in Equation (6.22), consequently it predicts the flow stress ratios more accurately and the R-ratios less accurately, compared with the Simple method. In addition, the biaxial plastic strain ratio predicted by the yield functions is listed in Table 6.4 (It was measured as $R_b = 1.58$ in Section 5.4). It shows that the Power method

predicts the biaxial plastic strain ratio very well. The predictions are found affected by a variation of M when using the Analytical method and the Simple method.

The identified yield surfaces for $M = 8$ and $M = 14$ are presented in respectively Figure 6.7 and Figure 6.8. The contours in the figures represent levels of constant normalized shear stress with a contour distance of $0.03\sigma_0$. A smaller radius of curvature near balanced biaxial stress conditions is given by the $M = 14$ surfaces. The obtained normalized yield stress for pure shear is about $0.5\sigma_{xy}/\sigma_0$ with small deviations for various identification methods. It is the greatest for the Analytical method and the smallest for the Power method.

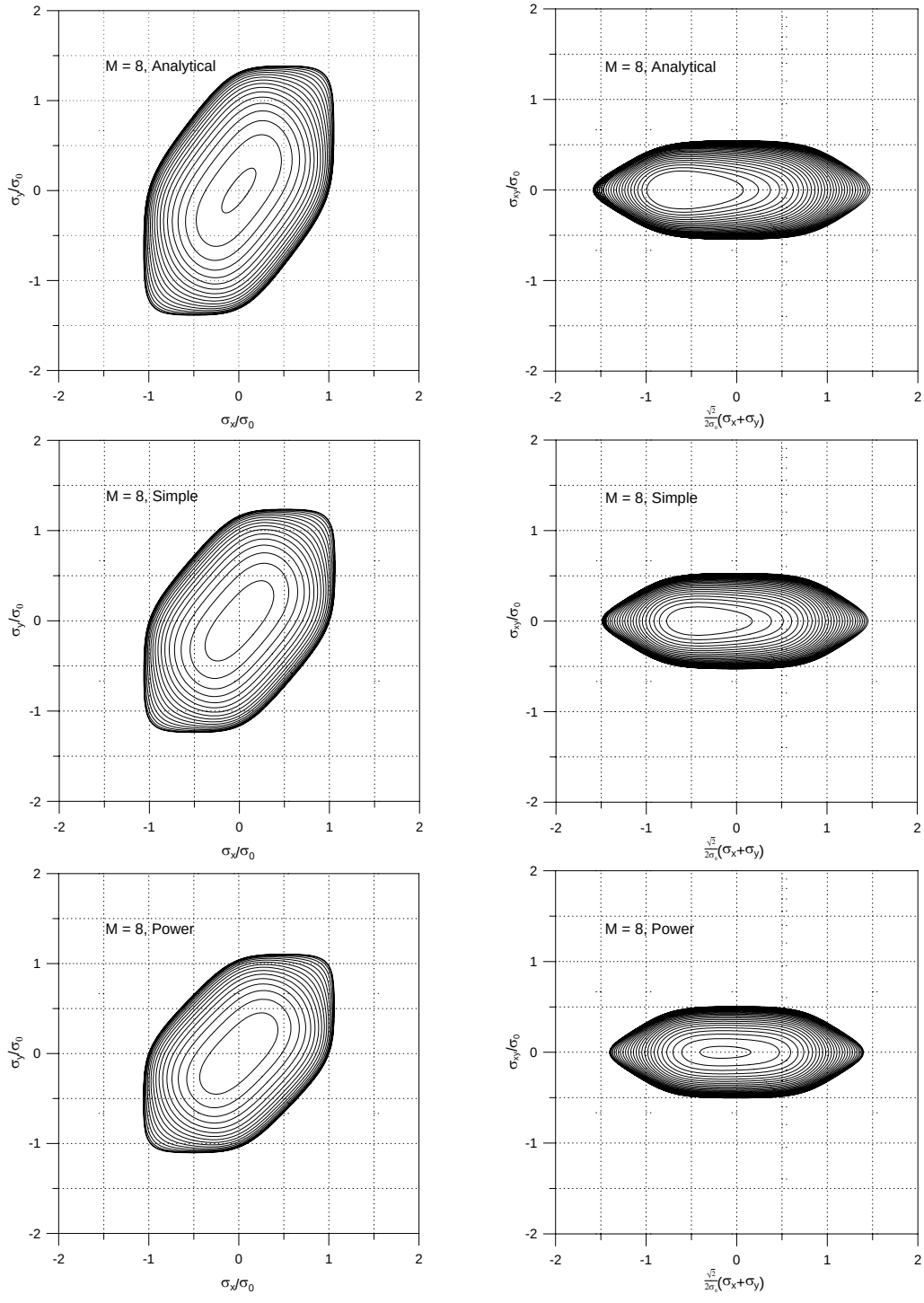

Figure 6.7. Identified yield surfaces with $M = 8$: a) in the space of σ_x, σ_y and σ_{xy} and b) Intersections of yield surfaces along the axis where $\sigma_x = \sigma_y$ and the σ_{xy} -axis.

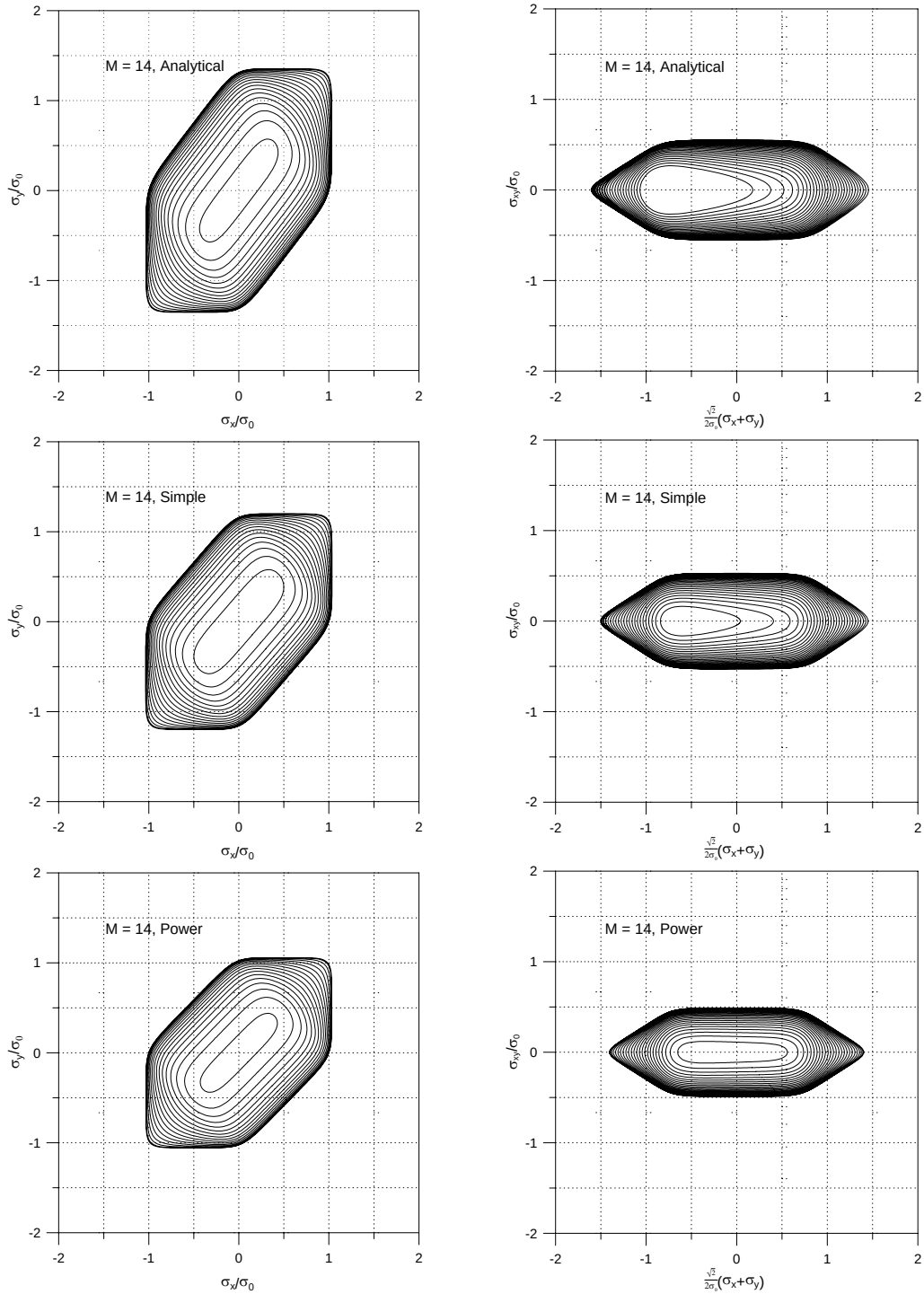

Figure 6.8. Identified yield surfaces with $M=14$: a) in the space of σ_x, σ_y and σ_{xy} and b) Intersections of yield surfaces along the axis where $\sigma_x = \sigma_y$ and the σ_{xy} -axis.

6.4 Verification of model parameters

6.4.1 Finite element model of uniaxial tensile tests

To verify the parameters obtained above, the uniaxial tensile tests described in Section 5.2 were modelled and analysed with the WTM-2D in LS-DYNA.

The geometry of the specimen is shown in Figure 5.1. Its FE model is depicted in Figure 6.9, which consists of 3648 Belytschko-Tsay shell elements. Each of the elements has one point reduced in-plane integration and two integration points through the thickness. The bolts were modelled as rigid bodies. Viscous hourglass control was used and found to give less hourglass energy and better predictions compared with the stiffness based one. Node-to-surface contact algorithm was used between the bolts and the specimen.

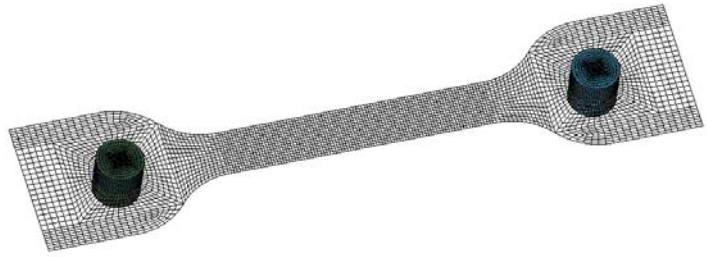

Figure 6.9. Finite element model of the tensile test specimen.

Loading was applied through the right bolt, while the left bolt was constrained. It is important in quasi-static analysis using the explicit solver of LS-DYNA to apply the loading smoothly to avoid introducing spurious high frequency components into the solution. The prescribed velocity of the right bolt was given as a function of time

$$v = \frac{v_0}{2}\left(1-\cos\left(\min\left(\frac{\pi t}{t_r},\pi\right)\right)\right) \tag{6.23}$$

where t_r is the duration for the velocity to smoothly ramp up to a constant level v_0 which depends on the desired final deformation $d_{\max}$. The velocity also depends on T, the total duration of the loading. Integrating v from $t=0$ to T, $d_{\max}$ comes out as

$$d_{\max} = \int_0^T v dt = \int_0^T \frac{v_0}{2}\left(1-\cos\left(\min\left(\frac{\pi t}{t_r}, \pi\right)\right)\right) dt$$
$$= \frac{v_0}{2}\left(2T - t_r\right) \tag{6.24}$$

Substituting (6.24) into (6.23), the loading velocity is written as

$$v = \frac{d_{\max}}{\left(2T - t_r\right)}\left(1-\cos\left(\min\left(\frac{\pi t}{t_r}, \pi\right)\right)\right) \tag{6.25}$$

The duration T is a fictive time period in the explicit simulation, and is chosen as $T = 7$ ms. Using this duration time and a deformation of about 7 mm, the kinetic energy was found negligible compared with the total energy, which is essential for an explicit quasi-static simulation to be valid. A loading curve with $d_{\max} = 7$ mm, $T = 7$ ms and $t_r = T/4$ is shown in Figure 6.10.

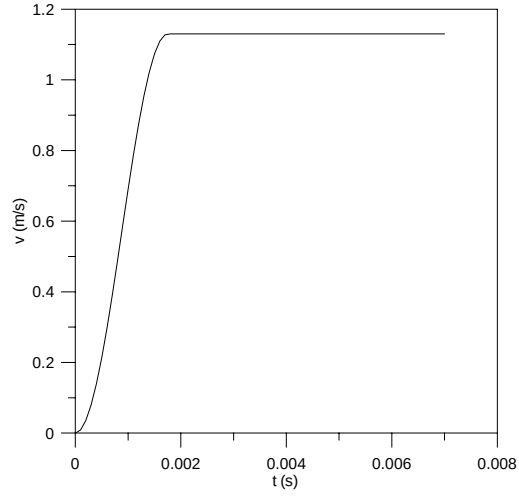

Figure 6.10. A loading curve with $d_{\max} = 7$ mm and $T = 7$ ms and $t_r = T/4$.

6.4.2 Results

The work hardening parameters used in the simulations are as listed in Table 5.2, and the various yield surface parameters identified in Section 6.3 were adopted. Fracture was modelled using the simple Critical-Thickness-Strain criterion with critical value of

$\varepsilon_{cr} = -0.5$. Its absolute value is greater than the experimental value in order to have a complete observation of the necking process. In the various simulations the fracture modes were similar to each other, see Figure 6.11 for a typical evolution of the thickness reduction. Clearly the fracture occurs after onset of a diffuse neck. The localized neck and fracture make an angle to the load axis as should be expected from classical theory (Marciniak et al. 2002). For various identification methods with $M = 8$, thickness reduction before and after fracture of a 0° specimen are presented in Figure 6.12. For the 0° specimen, the localized neck inclined 60° to the longitudinal direction, for the 45° and 90° specimens the inclination is respectively 56° and 61°. Figure 6.13 shows the fracture of the 0° specimen with $M = 14$, by comparison with Figure 6.12 it can be seen that a variation of M does not affect the fracture mode. The engineering stress vs. strain curves for the representative tests and various analyses are presented in Figure 6.14 to Figure 6.19. These figures confirm that the power method predicts both strength and ductility better than the other two methods. The variation of M is not found to affect the predictions significantly.

The fracture criterion is expected to affect only the onset of fracture and not any other mechanical performance since it has no effect on the constitutive relations. To assess this assumption, one set of analyses was performed with $\varepsilon_{cr} = -0.3$. The yield surface parameters used are those of the Power method and $M = 8$. In these analyses fracture occurred somewhat earlier, but the fracture mode was identical to the simulation with $\varepsilon_{cr} = -0.5$. Particularly the images of the 0° analysis are shown in Figure 6.20. The engineering strain vs. stress curves of these analyses are presented in Figure 6.21, as expected the responses are identical to the basic analysis except the earlier onset of fracture.

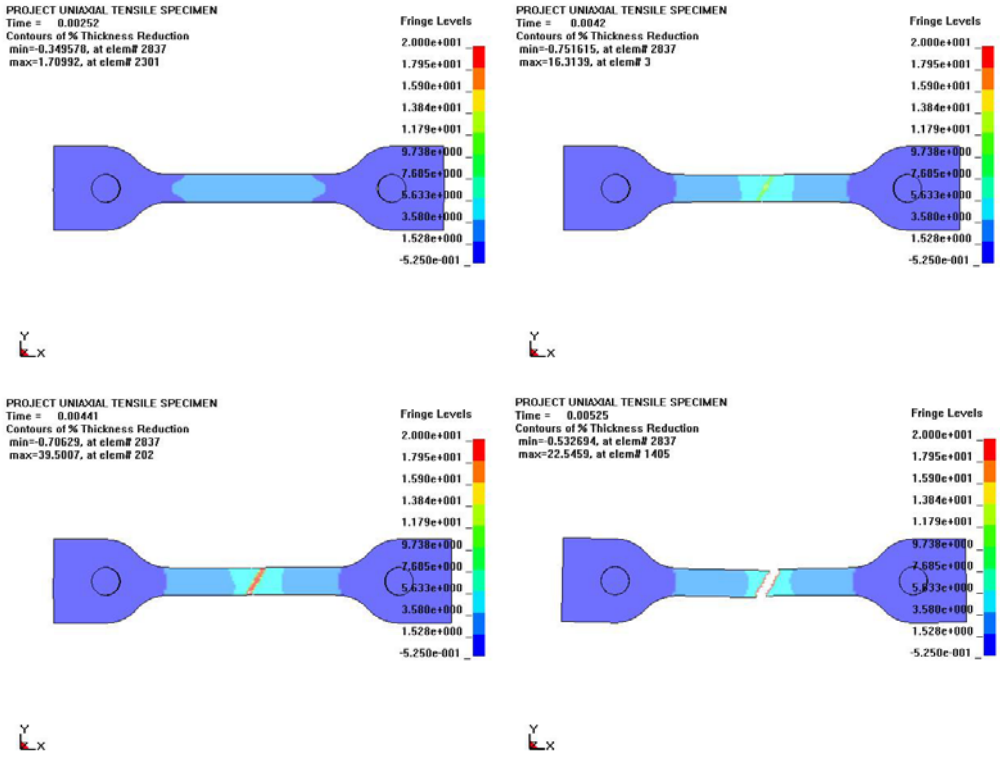

Figure 6.11. Typical evolution of thickness reduction.

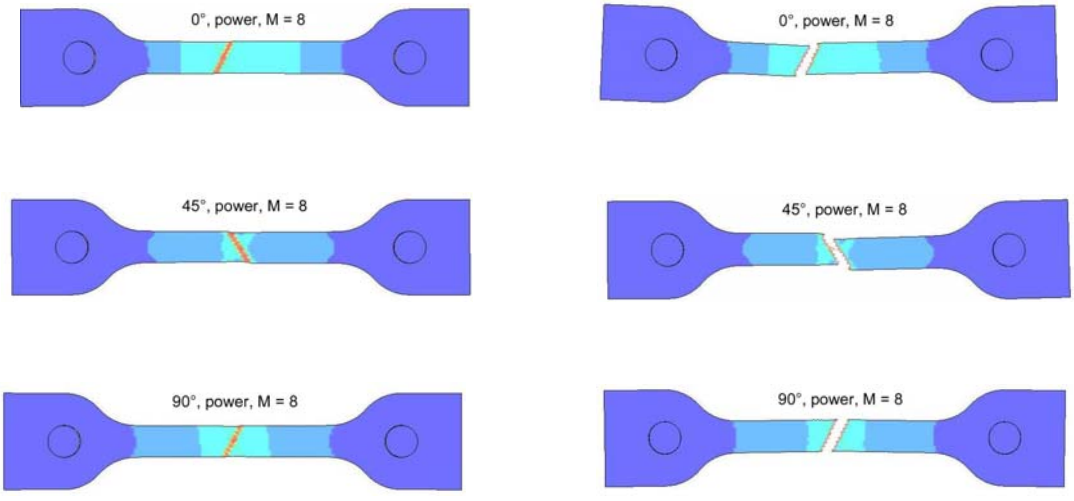

Figure 6.12. Thickness reduction before and after fracture for the simulations with $M = 8$, and yield surface parameters obtained by the Power method.

Figure 6.13. Thickness reduction before and after fracture for the 0° simulation with $M = 14$.

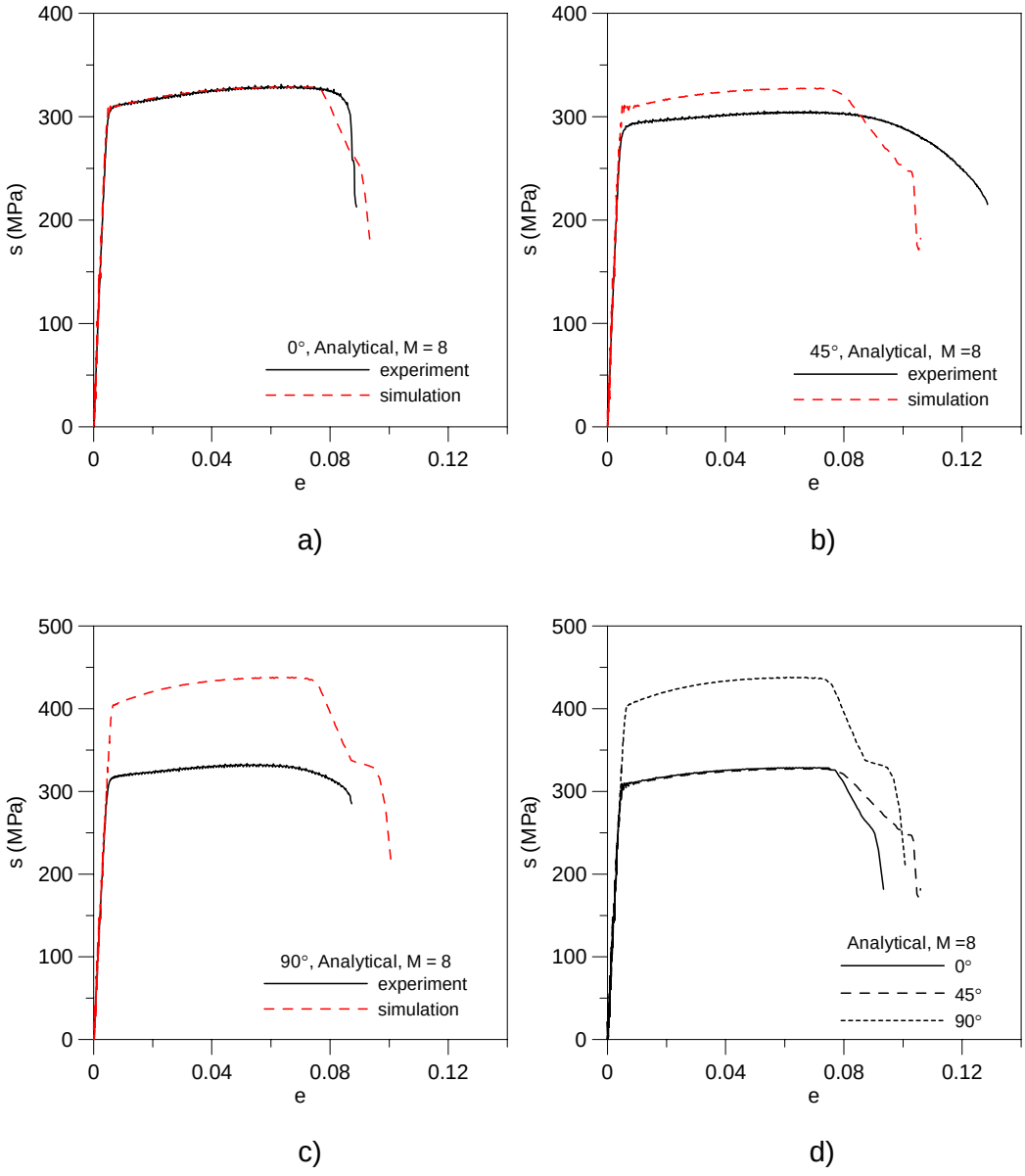

Figure 6.14. Experiment and simulation results by yield surface parameters obtained by the Analytical method and $M = 8$. a), b) and c), engineering stress vs. strain curves for the 0°, 45° and 90° specimens, and d) comparison of simulations.

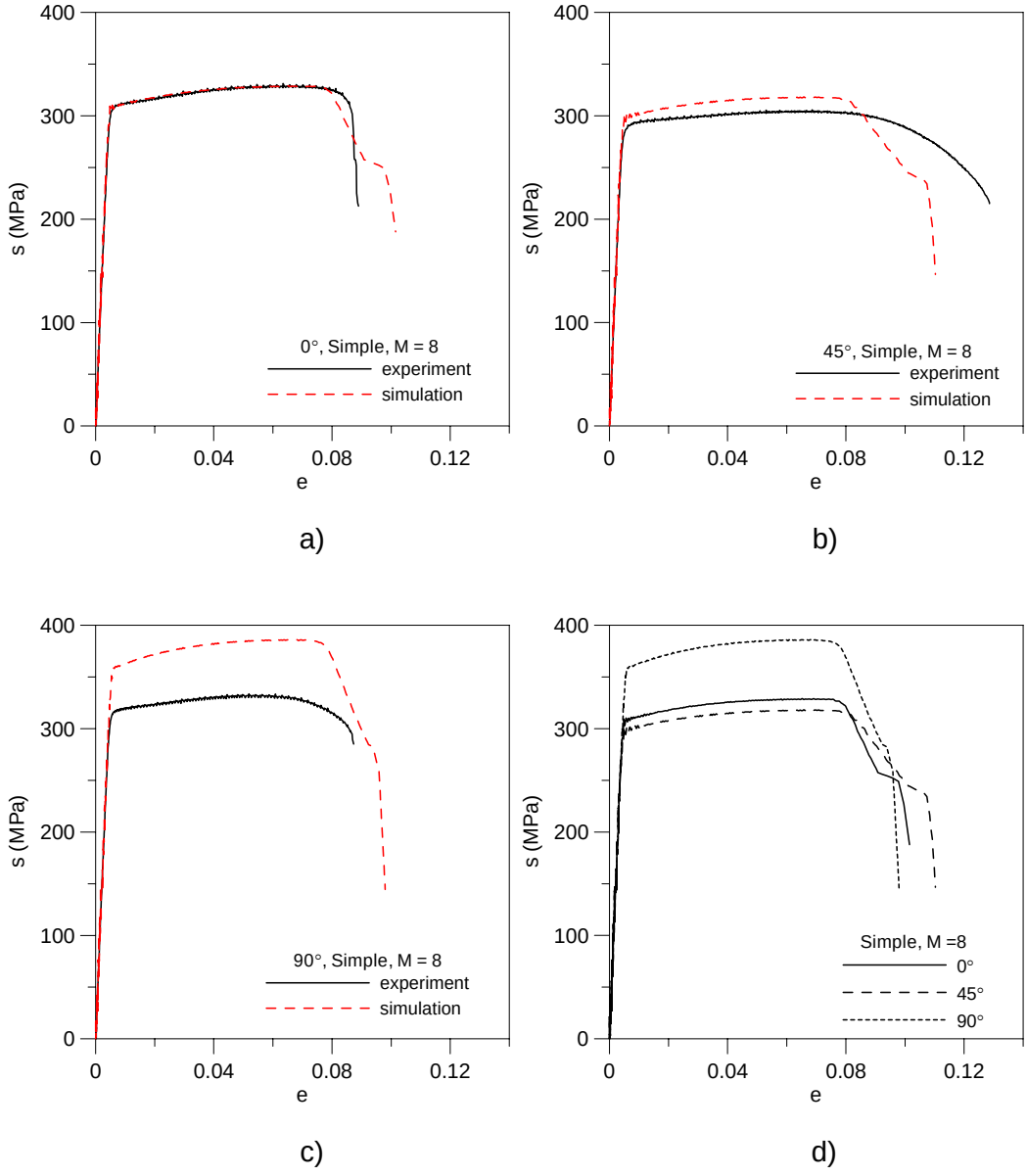

Figure 6.15. Experiment and simulation results by yield surface parameters obtained by the Simple method and $M = 8$. a), b) and c), engineering stress vs. strain curves for the 0°, 45° and 90° specimens, and d) comparison of simulations.

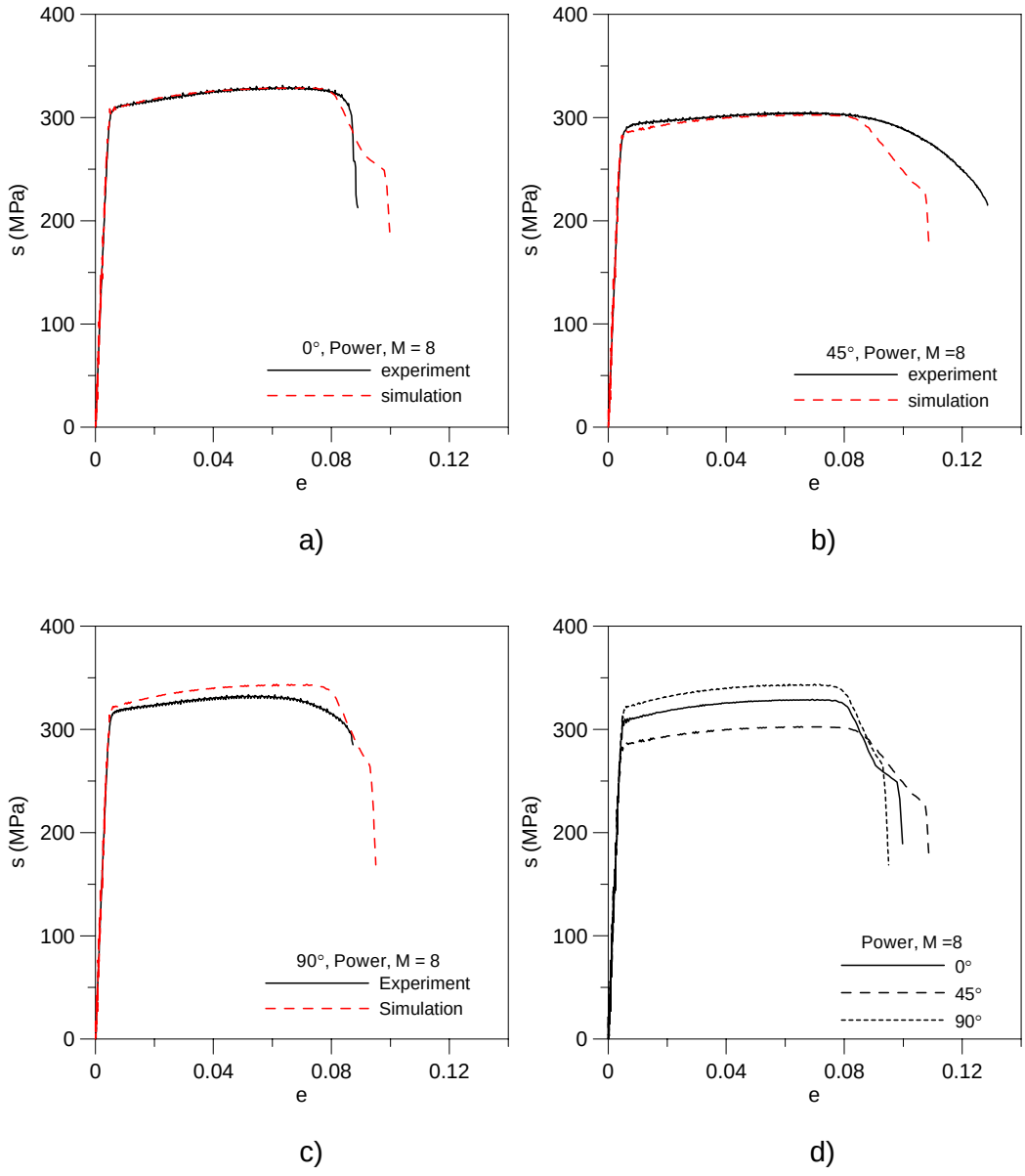

Figure 6.16. Experiment and simulation results by the yield surface parameters obtained by the Power method and $M = 8$. a), b) and c), engineering stress vs. strain curves for the 0°, 45° and 90° specimens, and d) comparison of simulations.

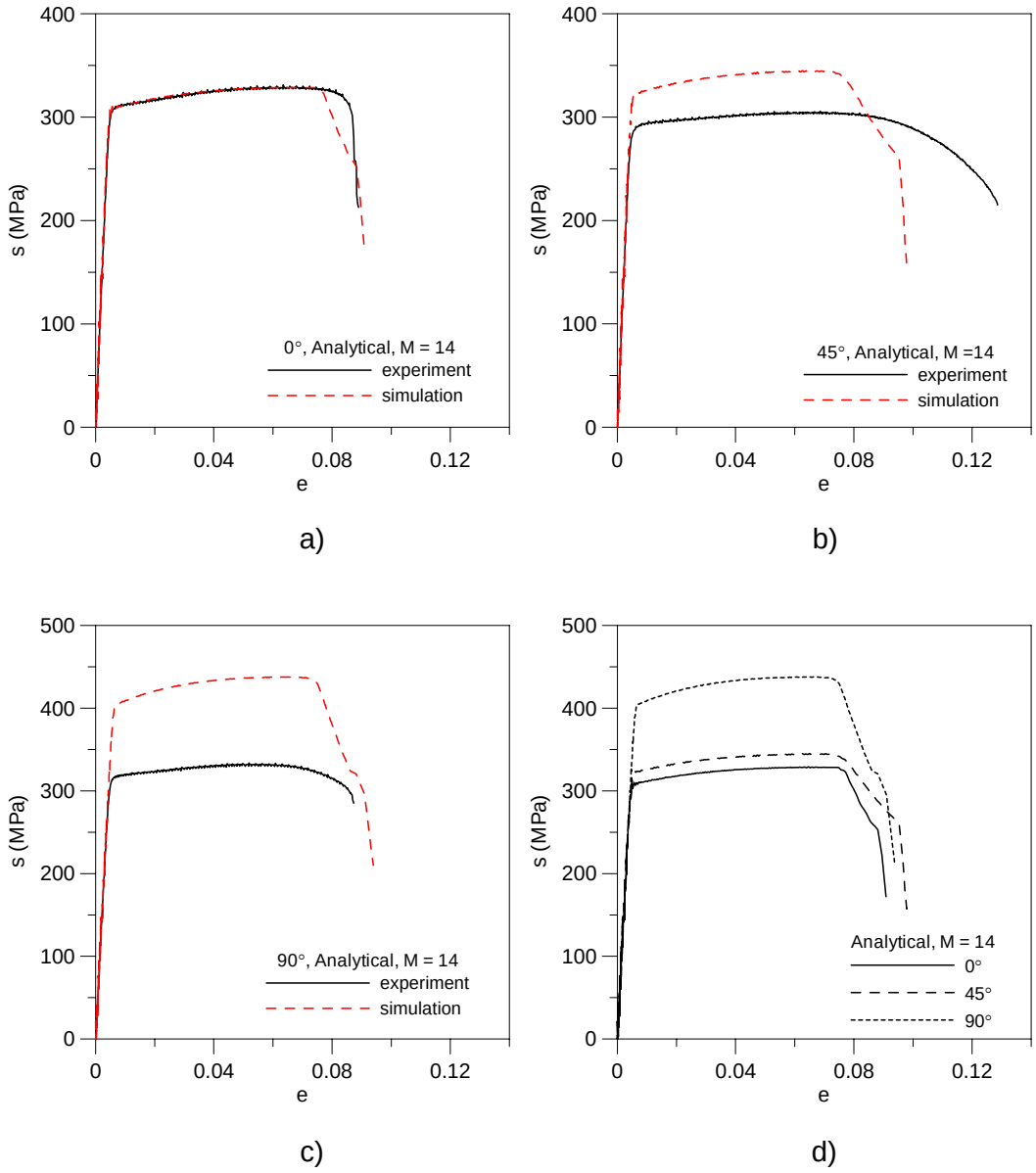

Figure 6.17. Experiment and simulation results by yield surface parameters obtained by the Analytical method and $M = 14$. a), b) and c), engineering stress vs. strain curves for the 0°, 45° and 90° specimens, and d) comparison of simulations.

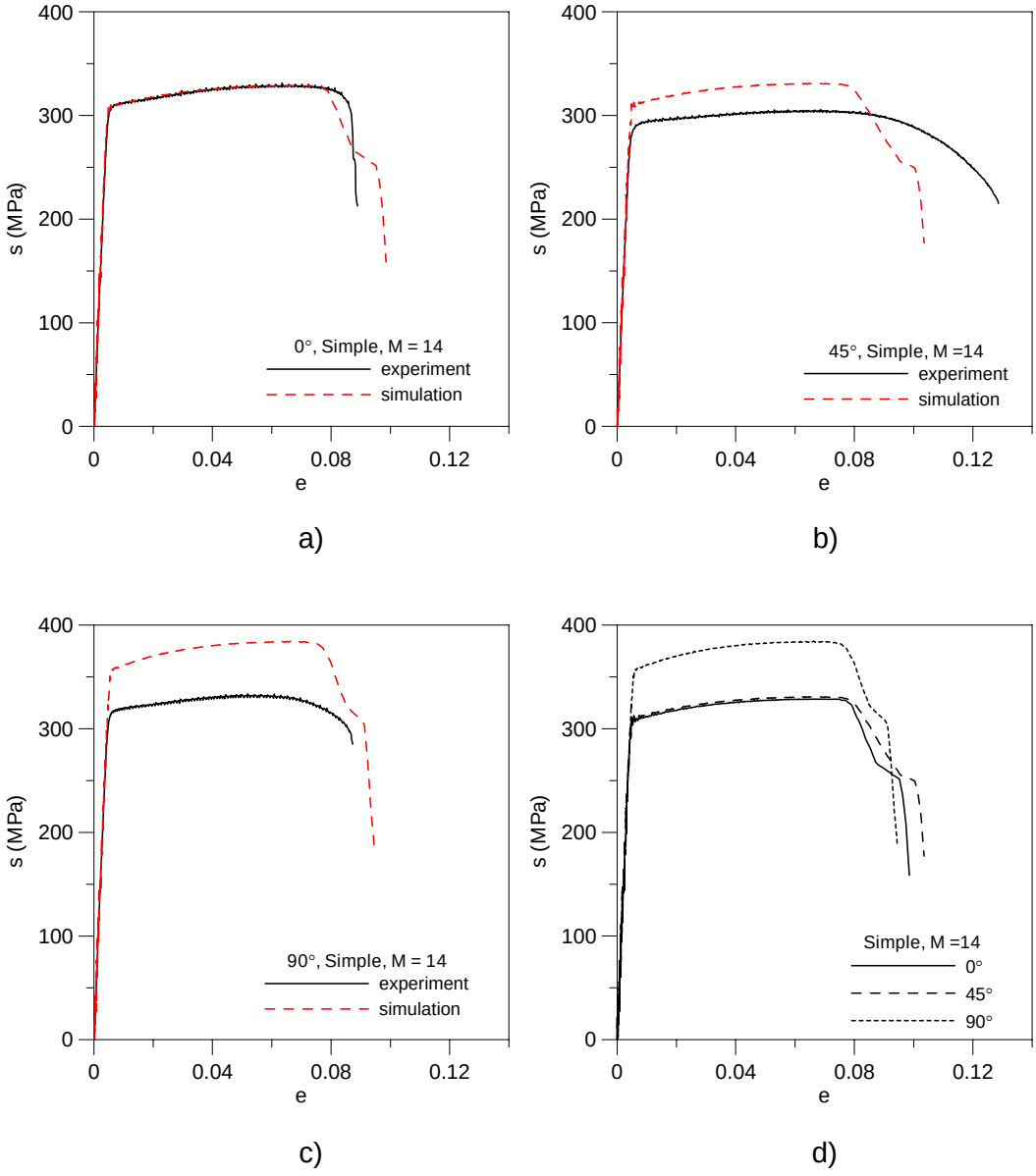

Figure 6.18. Experiment and simulation results by yield surface parameters obtained by the Simple method and $M = 14$. a), b) and c), engineering stress vs. strain curves for the 0°, 45° and 90° specimens, and d) comparison of simulations.

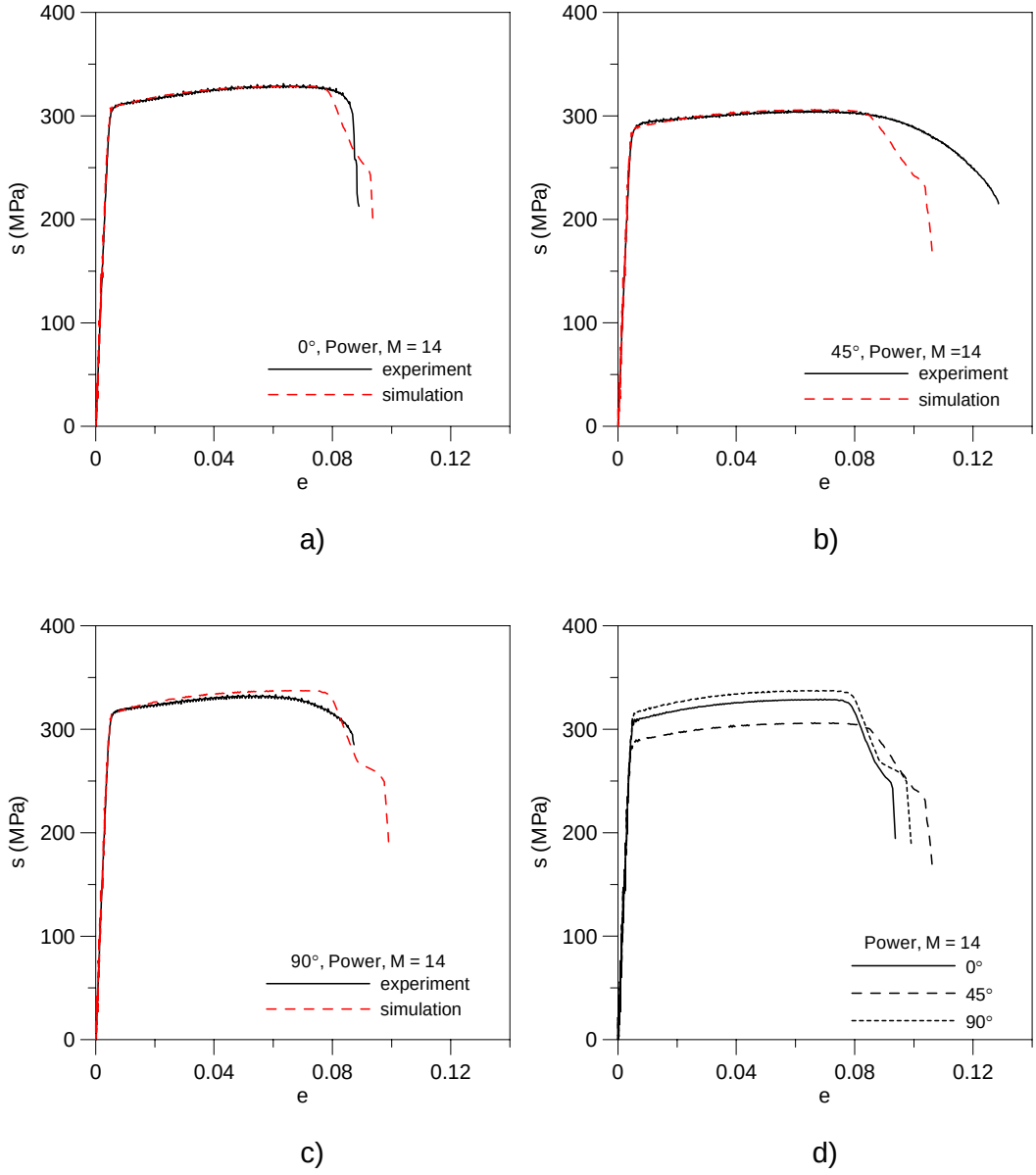

Figure 6.19. Experiment and simulation results by yield surface parameters obtained by the Power method and $M=14$. a), b) and c), engineering stress vs. strain curves for the 0°, 45° and 90° specimens, and d) comparison of simulations.

Figure 6.20. Images before and after fracture from the 0° simulation with $\varepsilon_{cr} = -0.3$.

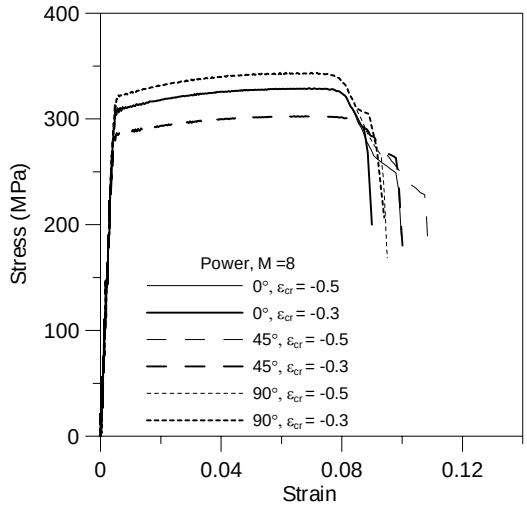

Figure 6.21. Simulation results with various Critical-Thickness-Strains.

7. Experiments and simulations of fillet-welded connections in tension

7.1 Introduction

Fillet welds are extensively used in various fields. For instance in construction industry they account for 80% of all weldments (Patrick et.al 1988), it is therefore important to be able to represent the mechanical capacity of fillet-welded structures in numerical analyses for design purposes. Here an experimental and numerical investigation was undertaken on the performance of a series of fillet-welded connections in aluminium. A simple connection relevant to for instance multi-stiffened panels is considered. The accuracy, efficiency and robustness of a shell modelling approach for prediction of the strength and ductility of the connections was assessed.

7.2 Test specimens

A sketch of the investigated fillet-welded connections is given in Figure 7.1. The connections consist of two plates of different thickness and width, which are connected using double fillet-welds. With reference to this figure the investigated weld angles θ are 0°, 30° and 45°. The upper plates are made of EN AW 6082 T6 and have a thickness of 5 mm. The lower plates are made of EN AW 5083 and have a thickness of 20 mm. The throat thickness of the fillet welds is 5 mm. The filler metal NORWELD 5283 was used. To give fracture in the HAZ for all the weld angles, the adopted throat thickness was chosen as following.

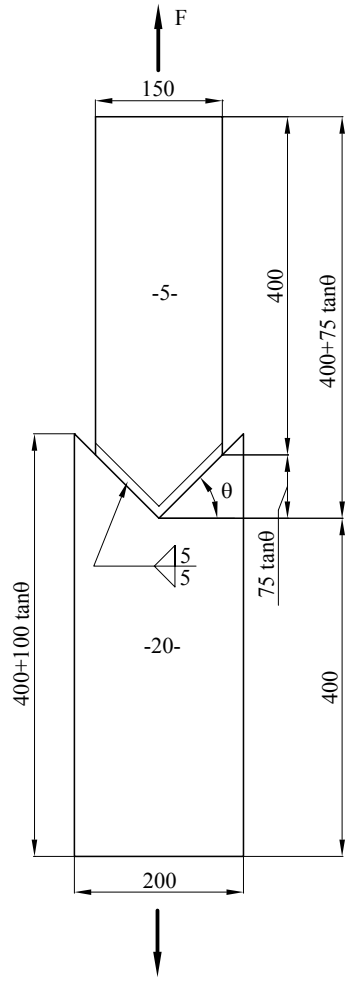

Figure 7.1. Geometry of the fillet-welded connection.

According to Eurocode 9 (CEN 2002), for sheets, strips and plates of wrought aluminium alloys, the nominal yield and ultimate strength are respectively 260 MPa and 310 MPa for plates up to 6 mm thickness of alloy EN AW 6082 T6. In the HAZ for plates of thickness up to 15 mm, the nominal yield and ultimate strengths of this alloy are 125 MPa and 185 MPa, respectively.

Based on Equation (3.5), the maximum force that can be carried by a double fillet weld with arbitrary orientation of the weld relative to the direction of the force is given as

$$N_{wd} = \frac{f_{wd} 2aL_w}{\sqrt{2 + \cos^2 \beta}} \tag{7.1}$$

where $\beta = 90^\circ - \theta$, f_{wd} is the design strength of the weld material, L_w is the weld length on one side of the plate and a is the throat thickness. The tensile capacity of the upper plate is given by

$$N_d = f_d L t \tag{7.2}$$

where f_d is the design strength of the base material, L is the width of the plate and t is the plate thickness. From the geometry of the component, we have the relation

$$L_w = \frac{L}{\sin\beta} \tag{7.3}$$

The necessary throat thickness is then obtained by equating the maximum force in the weld with the capacity of the upper plate, i.e.

$$N_{wd} = N_d \Rightarrow 2a = \frac{f_d}{f_{wd}} t \sin\beta \sqrt{2 + \cos^2\beta} \tag{7.4}$$

Assuming the same partial safety factor for the base material and the filler material, e.g. $\gamma_M = 1$, we get $f_d = 260$ MPa for the base material and $f_{wd} = 210$ MPa for the weld. Since the HAZ is neglected, this would lead to a conservative result. Inserting $t = 5$ mm gives $2a$ = 9 mm, 8 mm and 7 mm for θ equal to 0°, 30° and 45°, respectively. Accordingly, to be on the conservative side the throat thickness is taken equal to 5 mm for all values of θ.

7.3 Test set-up

Quasi-static tensile tests of the components were performed at ambient temperature in an UHS-100 testing machine. The applied force and the crosshead displacement were recorded. The displacement rate was 0.6 mm/min for one of the tests with 0° weld angle, while for the rest of the tests it was 0.06 mm/min. Three parallel tests were performed for the 0° weld angle, and for the 30° and 45° weld angles four parallel tests were done. An elongation measurement was obtained from an ODS-70 optical displacement transducer that was fixed to the lower plate. The displacement was recorded between the transducer and an additional clamp that was fixed to the upper plate. The transducer and the clamp were placed approximately 70 mm apart. Figure 7.2 shows the components

with various weld angles mounted in the machine before testing. The test set-up and the achieved maximum loads and deformations are summarized in Table 7.1.

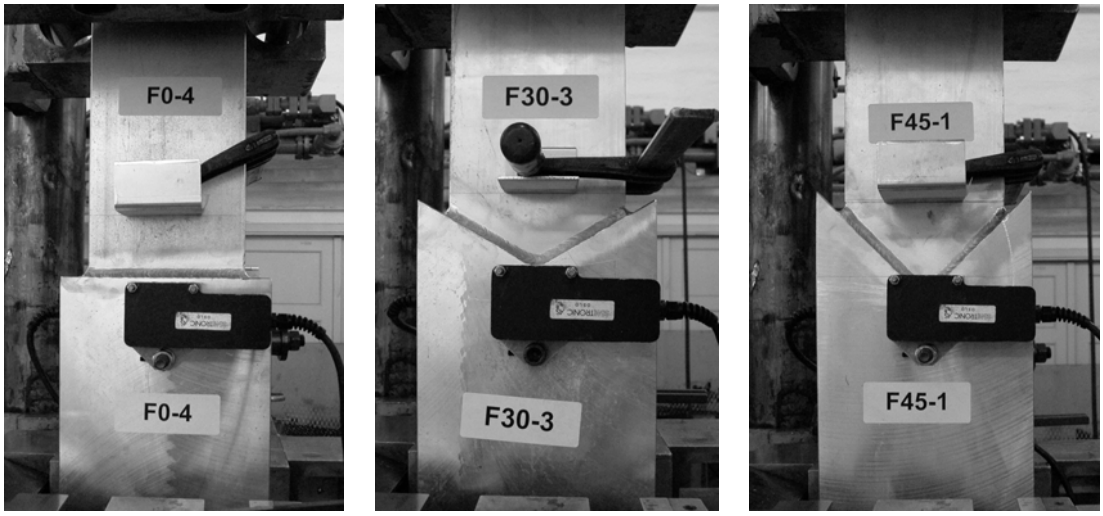

Figure 7.2. Test set-up.

Table 7.1. Test set-up and results.

Specimens	Weld angle [°]	Displacement rate [mm/min]	Logging frequency [Hz]	Max load [kN]	Max deformation [mm]	Fracture location
F0-1	0	0.6	1	172	1.07	HAZ
F0-3	0	0.06	4	165.6	1.53	HAZ
F0-4	0	0.06	4	167.8	1.55	HAZ
F30-1	30	0.06	4	175.8	1.45	HAZ
F30-2	30	0.06	4	186.8	1.45	HAZ
F30-3	30	0.06	4	190.6	1.76	HAZ
F30-4	30	0.06	4	182.6	1.56	HAZ
F45-1	45	0.06	4	176.6	3.02	HAZ
F45-2	45	0.06	4	184.2	2.74	HAZ
F45-3	45	0.06	4	192.4	2.56	HAZ
F45-4	45	0.06	4	194	2.64	HAZ

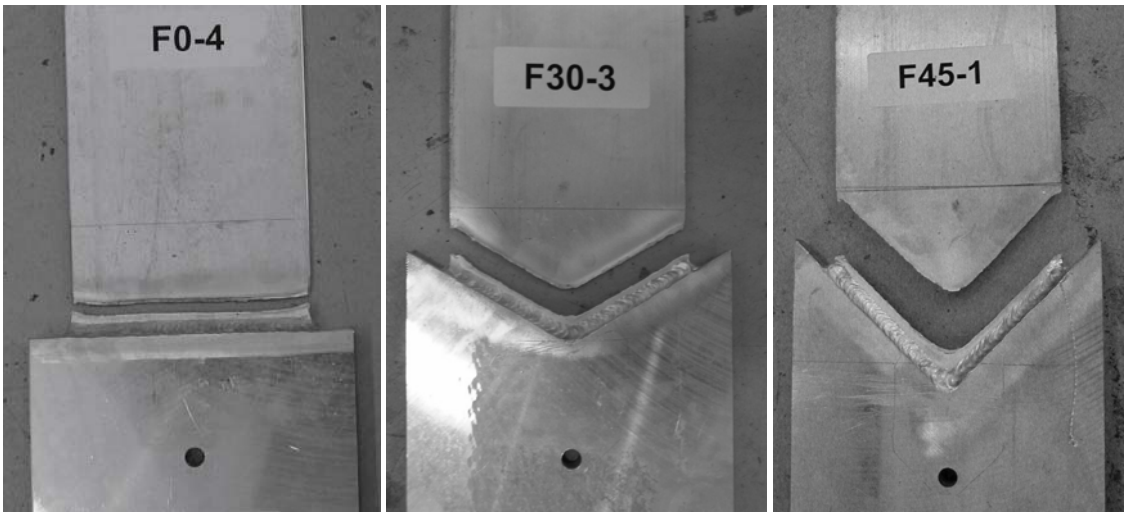

Figure 7.3. Specimens after testing.

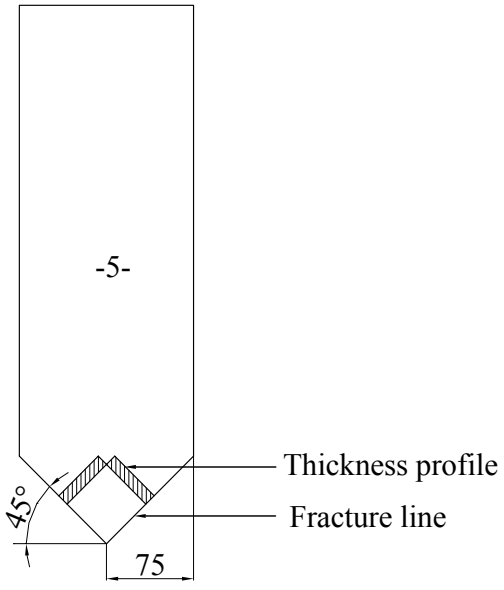

Figure 7.4. Thickness profiles cut from the fractured upper plate of the specimen.

7.4 Test results

All connections failed in the HAZ as shown in Figure 7.3, owing to strong localization of the plastic deformation. For one of the parallel specimens of every type, the thickness of the fractured upper plate was measured to reveal the strain localisation. As shown in Figure 7.4, the profiles were cut perpendicular to the fracture lines from the connections. Pictures of these profiles are presented in Figure 7.5. The thickness strain of the specimens is defined by

$$\varepsilon_t = \ln(\frac{t}{t_0}) \tag{7.5}$$

where t_0 is the thickness before testing and t is the thickness after testing. The results are plotted in Figure 7.6. It can be seen that the thickness strain in the various components is highly localized.

The force vs. displacement curves are presented in Figure 7.7. In the curves the force value was averaged in neighbour sampling points to eliminate noise oscillations. It reveals that the 45° connections have the highest ductility, while both the 0° and 30° connections have significantly lower ductility. The average maximum load reached for the 30° and 45° connections was about 10% higher than for the 0° connections. For each of the specimen types the observed scatter may be due to the manufacturing process.

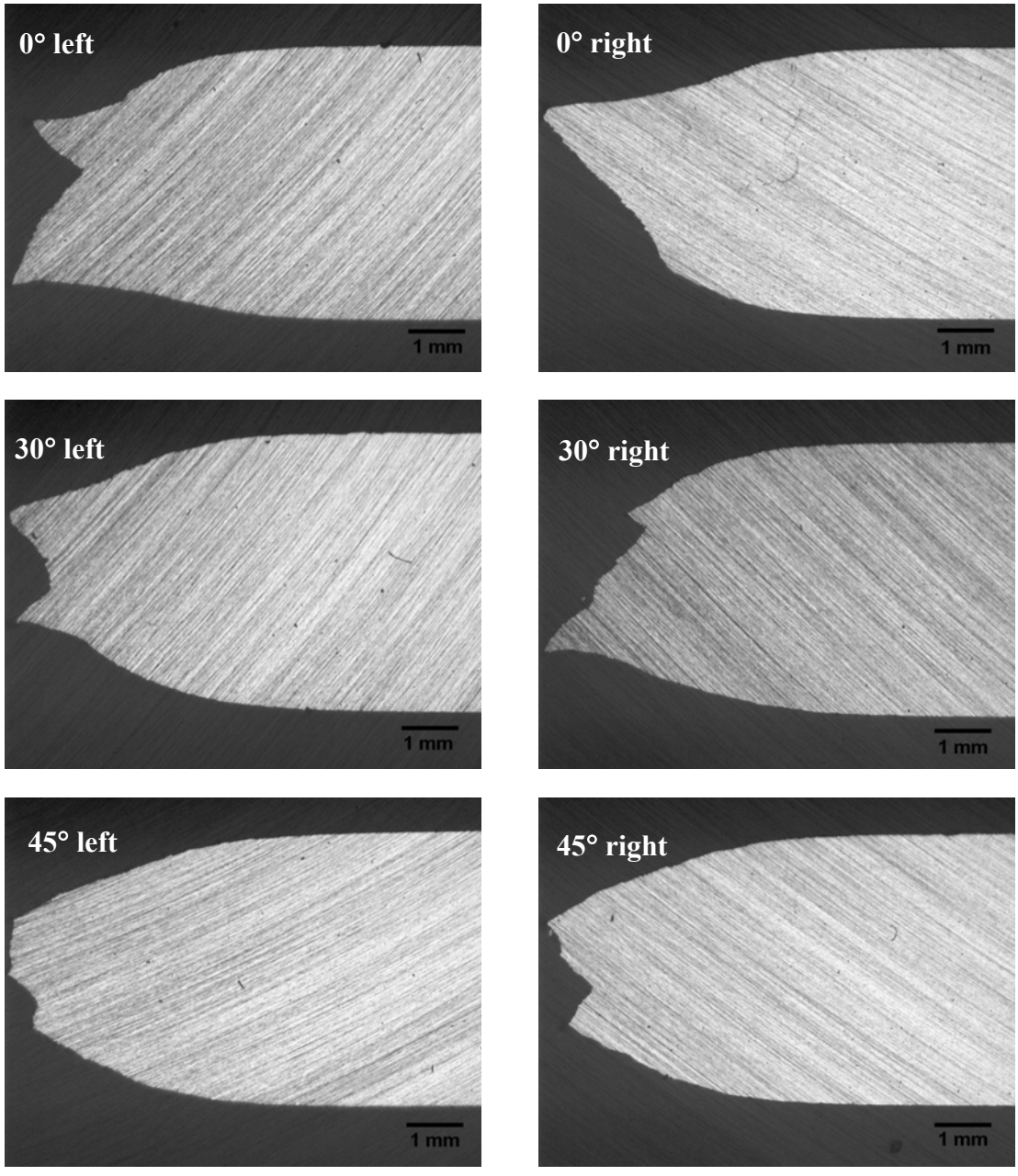

Figure 7.5. Thickness profiles for the specimens with various weld orientations.

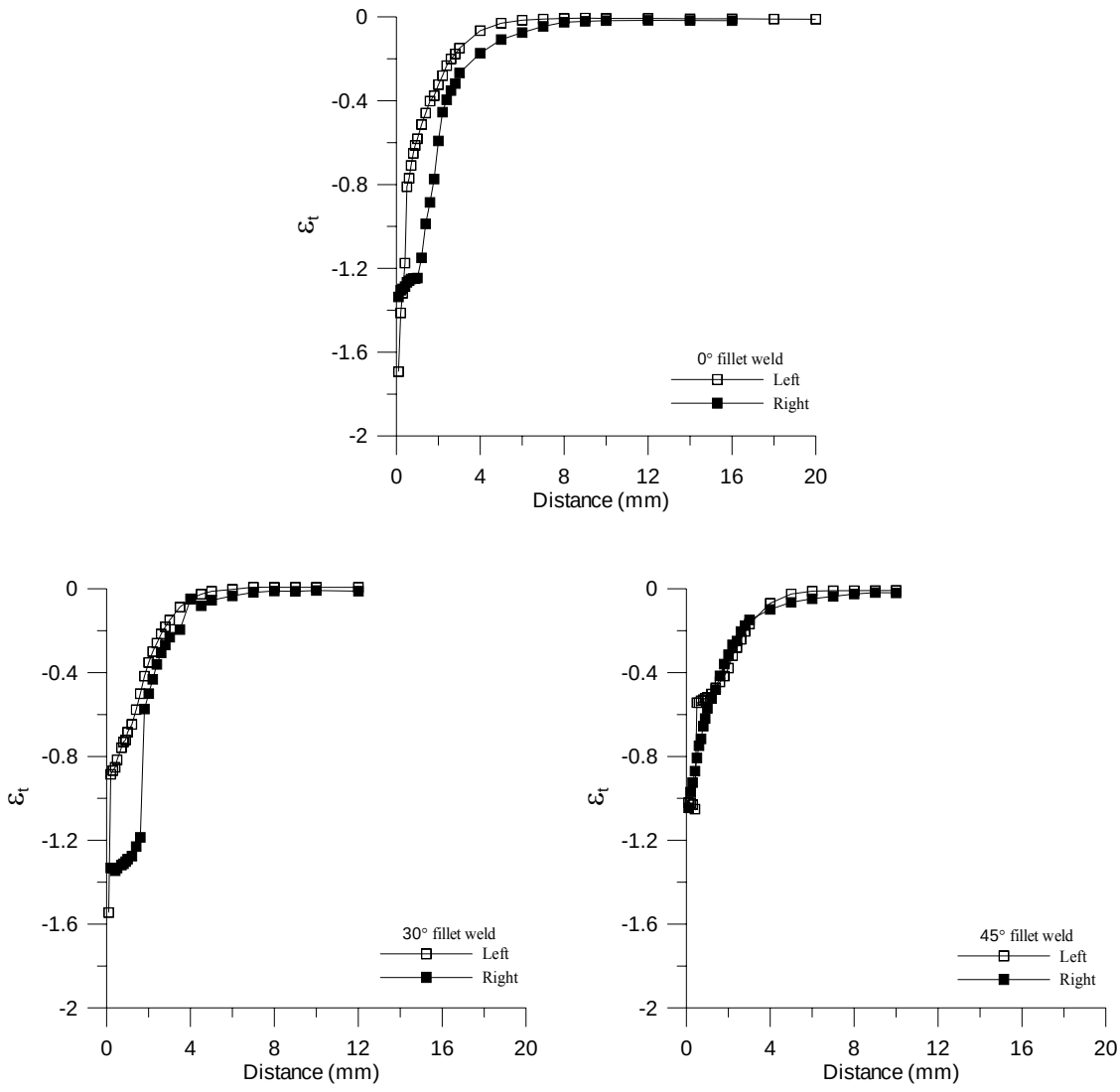

Figure 7.6. Thickness strain of the profiles from specimens with various weld orientations.

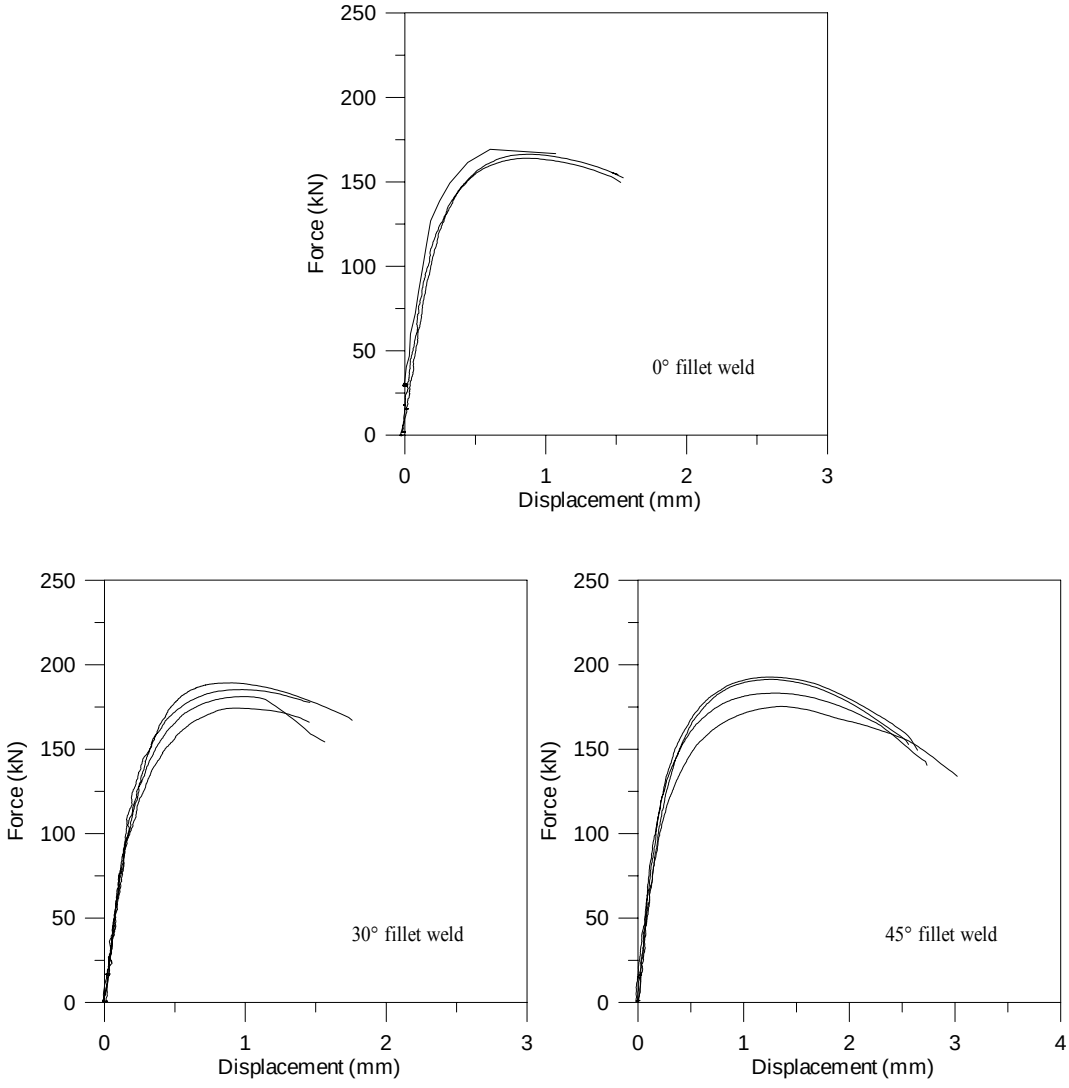

Figure 7.7. Force vs. displacement curves for fillet-welded connections with various weld orientations.

7.5 Finite element models

Numerical analyses were performed using the explicit solver of LS-DYNA (LSTC 2003). The connections were modelled with Belytschko-Tsay shell elements. The whole component was subdivided into eleven material IDs using three material models, see Figure 7.9 for the model of a 45° fillet-welded connection. The upper and lower clamped zones were modelled as rigid bodies, while the weld, upper plate and the HAZ were modelled using the WTM-2D. The rest of the lower plate was modelled using an

elasto-plastic model of *MAT_PIECEWISE_LINEAR_PLASTICITY. Thickness variation in weld elements was introduced to account for the actual weld geometry, as shown in Figure 7.10.

The HAZ is sub-divided into 6 sub-HAZs, sub-HAZ 1 to sub-HAZ 6. The work hardening parameters of these zones are adopted from Table 6.3 as explained in Section 6.2. The critical thickness strain for fracture was chosen as $\varepsilon_{cr} = -0.7$, based on measurement of the specimens after testing. The yield surface parameters were those obtained by the Power method and $M = 8$ in Table 6.4. Identical anisotropic properties have been assumed within the HAZ, since the main contributor to anisotropy is crystallographic texture that is not changed within the heat affected zone, as shown in Figure 7.8.

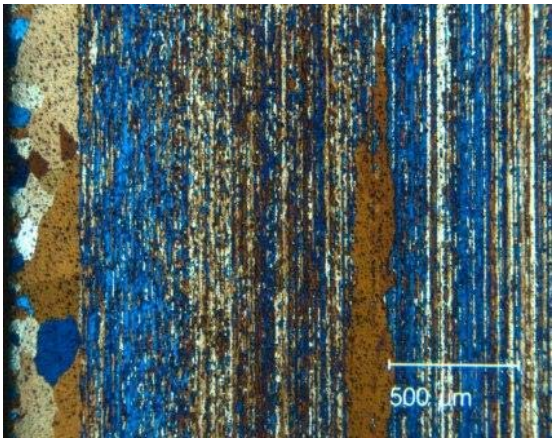

a)

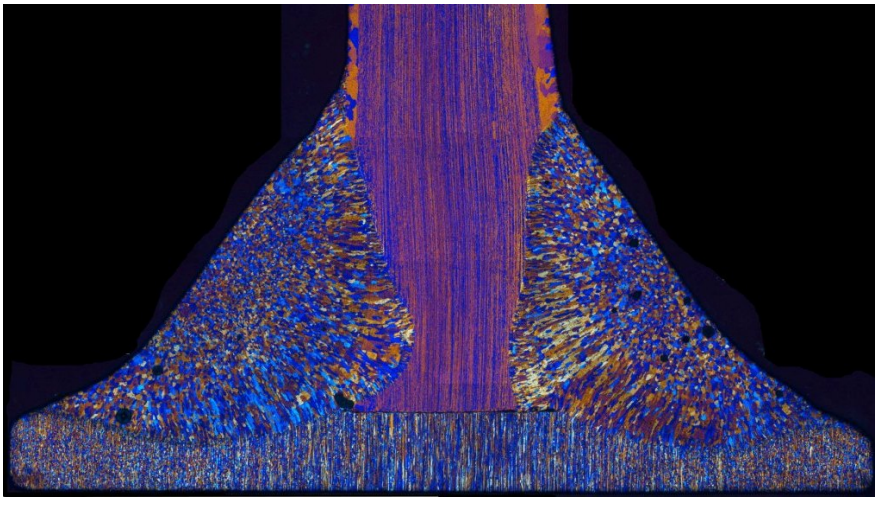

b)

Figure 7.8. Crystallographic textures in a) parent material, and b) HAZ.

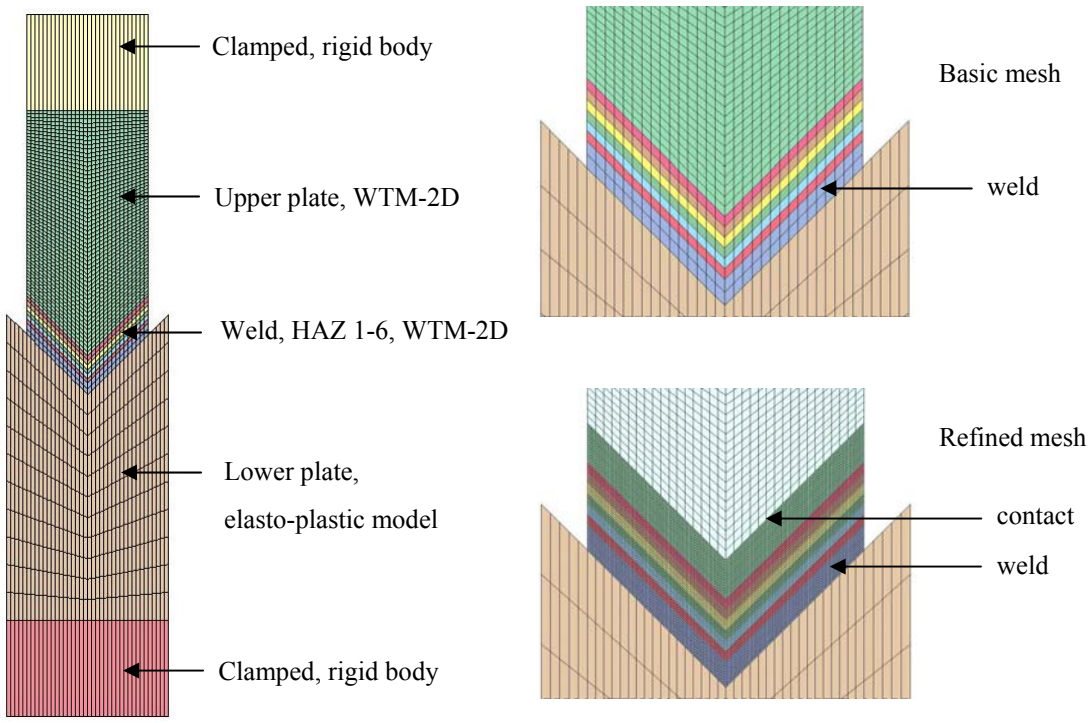

Figure 7.9. Model of the 45° fillet-welded connection.

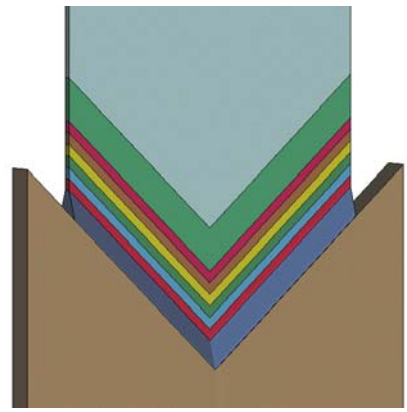

Figure 7.10. Thickness variation in the fillet-welded connection.

Additionally, the von Mises yield criterion was adopted to investigate the effect of yield criterion on the predicted response. For the von Mises yield criterion the parameters *a, c, h*, and *p* in Equation (4.21) were chosen equal to unity. To assess mesh convergence, analyses with a refined mesh in the weld and HAZ were performed. The

basic mesh has an element size of 4×4 mm^2 in the upper plate, the weld and HAZ. For the refined mesh, elements with size of 1×1 mm^2 were used for these parts.

Loading was applied through the upper clamped zone by assigning a time dependent velocity given as Equation (6.25), as explained in Section 6.4. The lower clamped zone was restrained from all displacements and rotations.

7.6 Numerical results

Fracture modes similar to the experiments were obtained in the numerical analyses as shown in Figure 7.11, i.e. the failures occurred in sub-HAZ 1 next to the weld for all the connections. Figure 7.12 presents the numerical and experimental force vs. deformation curves. All simulations appear to over-estimate the stiffness of the connections. In all simulations, the strength of the connections was over-predicted. The peak loads are seen to be influenced by the yield criterion. The results with the anisotropic criterion are closer to the tests than the ones with a von Mises yield criterion. The mesh was found to have little effect on the predicted peak force. The refined mesh resulted in peak loads almost identical to those obtained by the basic mesh. The over-estimation of the peak forces by the anisotropic criterion is up to 15%, while it is about 20% by the von Mises criterion.

Elongation of the connections was over-estimated by the basic mesh. The basic meshes resulted in elongations three times longer than those obtained by the refined mesh using the same fracture criterion as the refined mesh. The points of fracture are not shown in the figures for the basic mesh. The strain localisation was predicted well with the refined mesh, and relatively accurate estimates of the elongation were obtained. However, the evolution of the plastic thinning (as seen in the shape of the force vs. deformation curves) appeared mesh-dependent.

The simulations were found to be computational efficient, especially with the basic mesh, with an element size of 4×4 mm^2 in the upper plate, weld and HAZ. The CPU time is less than 6 minutes with a 0.02 s duration of the loading process. With the refined mesh in the weld and HAZ, element size being 1×1 mm^2, the simulations took about 3 hours.

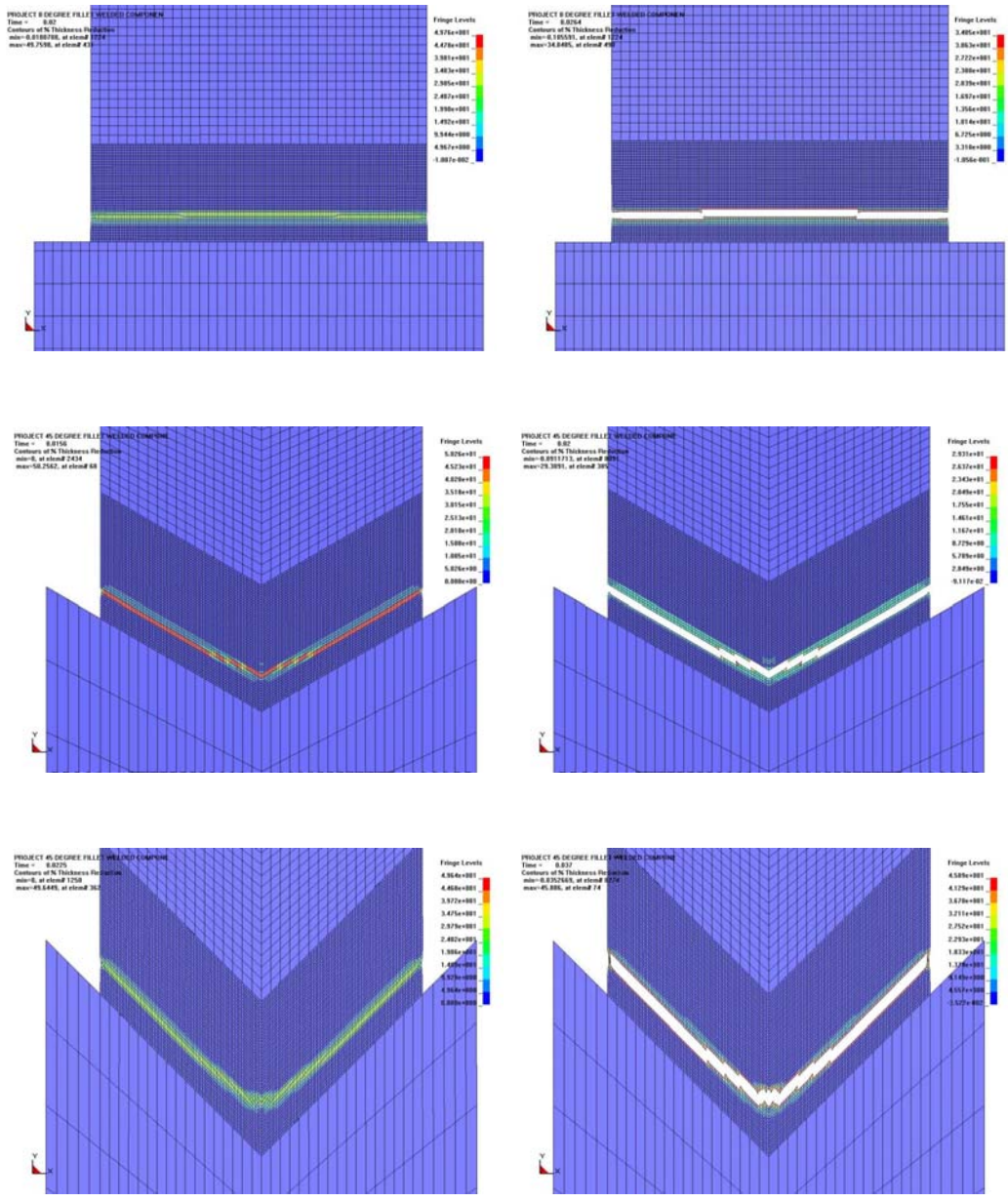

Figure 7.11. Thickness reduction before and after fracture.

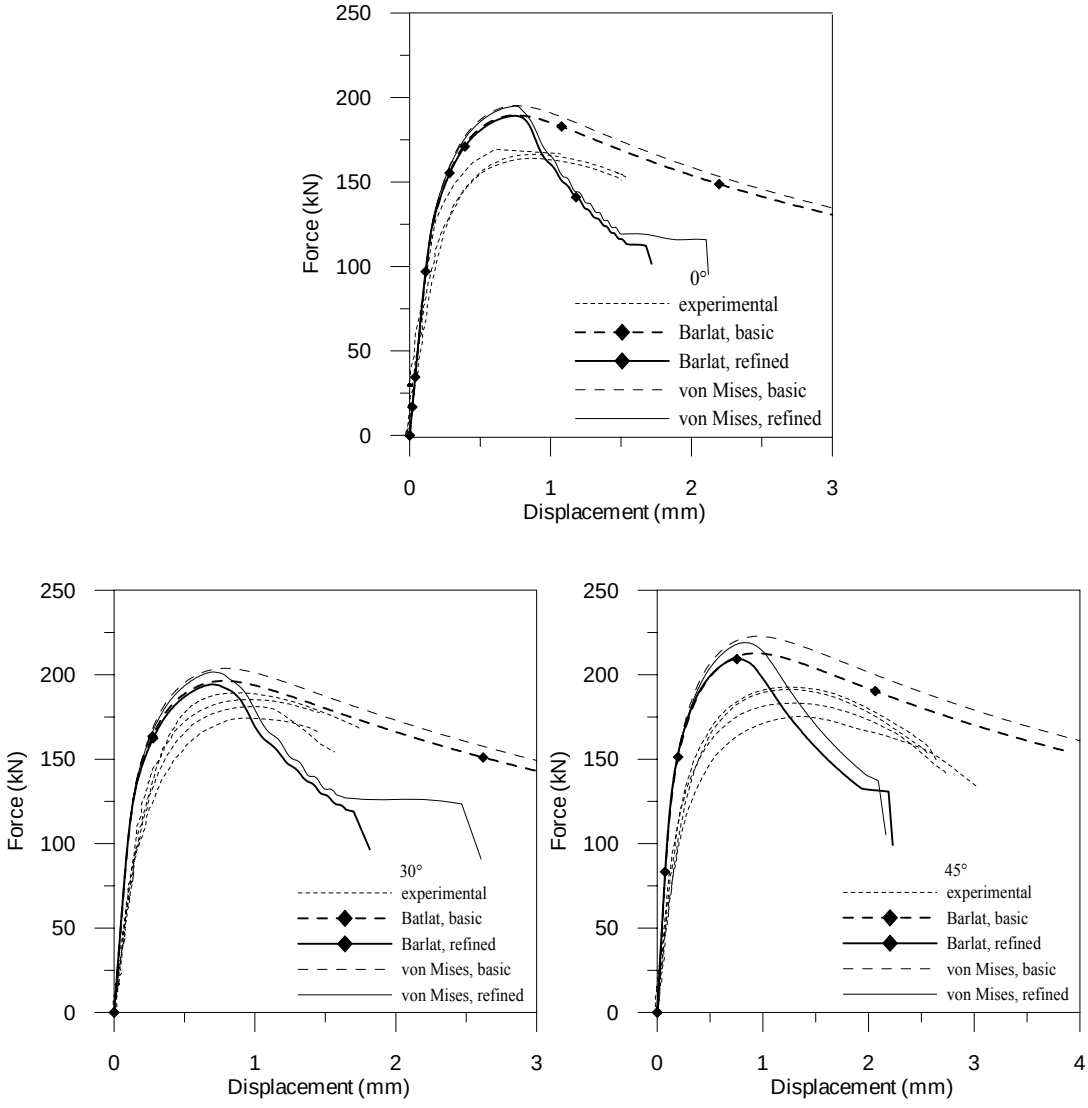

Figure 7.12. Force vs. displacement curves from the experiments and simulations for the connections with various weld orientations.

7.7 Conclusions

Experimental data on the structural performance of fillet-welded connections were provided by a series of quasi-static tensile tests. The tests were carried out with generally good repeatability, and fracture occurred in the HAZ as expected due to strong strain localization. The strength and ductility of the connections were found to depend upon the weld orientation.

The WTM-2D was calibrated by a series of uniaxial tensile tests in different directions. The strength and hardening data for the weld, HAZ and base material were identified according to material tests and available experimental data in the literature.

Shell elements were found to be convenient and efficient to model the connections. The numerical simulations generally predicted the structural strength reasonably well. However, the stiffness and peak load were over-estimated. The anisotropic yield criterion gives better results than the von Mises yield criterion. Mesh density was found to have little influence on the prediction of strength. As for structural ductility, relatively accurate predictions of elongation were obtained by the refined mesh, while it was three times over-estimated by the basic mesh compared with the refined mesh. Significant mesh-sensitivity was experienced with respect to the prediction of plastic thinning. Element size of $1\times1\,\mathrm{mm}^2$ was found to be able to predict the strain localisation, but the predicted evolution of the plastic thinning is not in good agreement with experiments. Moreover, the CPU-cost of the analyses with refined mesh is 30 times more expensive than the ones with basic mesh.

8. An analytical study of strain localization in HAZ

8.1 Introduction

As previously discussed, structural aluminium alloys are typically strengthened by heat treatment to obtain the peak hardness condition – or temper T6 (artificial aging at elevated temperature to peak hardness). The strengthening leads to reduced strain hardening and ductility. The high strength of alloys in temper T6 is advantageous in most structural applications, but leads to problems when structural components are welded. The heat induced by the welding process softens the alloy, and the strength of the material in the HAZ close to the weld may be reduced to only 50 % of the virgin strength.

In structural design codes, the strength loss in the HAZ is taken into account by using a reduced strength in a specified region in the neighbourhood of the weld. The strength reduction depends on the alloy and temper. For instance, an alloy in temper T4 (natural ageing in room temperature) will only lose a small percentage of its strength compared with an alloy in temper T6. In addition to the loss of strength, the HAZ leads to reduced ductility of a welded structural detail compared with an un-welded one. The reason is that owing to the reduced strength in the HAZ, strains localize readily in the softest part of the HAZ, and this leads to premature failure of the welded components. Hence, for welded structures in for instance safety components of cars that are designed to absorb energy during a crash situation, the loss of ductility may be more severe than the loss of strength. It is thus important to be able to predict in a simple way the loss of ductility induced by welding.

In this Chapter, an analytical study is carried out with a welded aluminium sheet. The intention with this work is to obtain a simple analytical method to provide rapid

information on the influence of the HAZ modelling on prediction of the structural performance, especially with respect to ductility

Here a welded rectangular sheet is analysed. Assuming a given variation of material properties, thickness and strain ratio along the sheet, the force vs. deformation curve were calculated and assessed according to the HAZ modelling method. It is noted that the analysis does not fulfil all compatibility conditions of the continuum sheet, but it is believed that the analyses are able to provide certain information about the influence of HAZ modelling on prediction of the structural performance, especially with respect to ductility. Further in order to obtain simple analytical expressions, only the use of von Mises yield criterion was investigated.

8.2 Rigid plasticity in plane stress

We consider plane stress states defined by

$$\sigma_1 > 0, \quad \sigma_2 = \alpha\sigma_1; \quad \sigma_3 = 0 \tag{8.1}$$

where σ_1 and σ_2 are the major and minor principal stresses in the plane of the sheet, respectively, α is a stress ratio, and σ_3 is the principal stress in the thickness direction. The incremental plastic strains are given by

$$d\varepsilon_1 > 0, \quad d\varepsilon_2 = \beta d\varepsilon_1; \quad d\varepsilon_3 = -(1+\beta)d\varepsilon_1 \tag{8.2}$$

where $d\varepsilon_1$ and $d\varepsilon_2$ are respectively the in-plane major and minor principal strain increments, $d\varepsilon_3$ is the through-thickness strain increment, and β is a strain ratio. Elastic strains are assumed small compared with plastic strains, and are thus neglected in the analysis. Plastic incompressibility has been assumed to obtain Equation (8.2), i.e.

$$d\varepsilon_1 + d\varepsilon_2 + d\varepsilon_3 = 0 \tag{8.3}$$

For proportional strain paths, the following relationships are valid

$$\varepsilon_1 > 0, \quad \varepsilon_2 = \beta\varepsilon_1; \quad \varepsilon_3 = -(1+\beta)\varepsilon_1 \tag{8.4}$$

Here we are concerned with local necking of a thin sheet with a HAZ. Thus plane stress states in which both σ_1 and σ_2 are compressive (less than zero) are not important,

since in this region local buckling will limit the deformation. Hence, we will assume that σ_1 is always positive.

For plane stress states the equivalent von Mises stress may be expressed in terms of the major principal stress and the stress ratio (Marciniak et al. 2002)

$$\bar{\sigma} = \sqrt{\sigma_1^2 - \sigma_1\sigma_2 + \sigma_2^2} = \sigma_1\sqrt{1-\alpha+\alpha^2} \tag{8.5}$$

while the inverse relation reads

$$\sigma_1 = \frac{\bar{\sigma}}{\sqrt{1-\alpha+\alpha^2}} \tag{8.6}$$

For plane stress state, the associated flow rule

$$d\varepsilon_i = d\lambda \frac{\partial \bar{\sigma}}{\partial \sigma_i}, \quad i = 1,2,3 \tag{8.7}$$

takes the simple form

$$\frac{d\varepsilon_1}{2-\alpha} = \frac{d\varepsilon_2}{2\alpha-1} = \frac{d\varepsilon_3}{-(1+\alpha)} \tag{8.8}$$

Using Equations (8.2) and (8.8), the relation between the stress and strain ratio is obtained by (Marciniak, Duncan and Hu 2002)

$$\alpha = \frac{2\beta+1}{2+\beta}, \quad \beta = \frac{2\alpha-1}{2-\alpha} \tag{8.9}$$

where it is noted that the strain ratio is in the range of $-2 < \beta \le 1$. It is then possible to express σ_1 in terms of $\bar{\sigma}$ and β, i.e.

$$\sigma_1 = \frac{2+\beta}{\sqrt{3}\sqrt{1+\beta+\beta^2}}\bar{\sigma} \tag{8.10}$$

The equivalent plastic strain $\bar{\varepsilon}$ is defined by

$$\sigma_1 d\varepsilon_1 + \sigma_2 d\varepsilon_2 + \sigma_3 d\varepsilon_3 = \bar{\sigma} d\bar{\varepsilon} \tag{8.11}$$

and for plane stress it may be expressed in terms of the major principal strain increment and the strain ratio (Marciniak et al. 2002)

$$d\bar{\varepsilon} = d\varepsilon_1 \sqrt{\frac{4}{3}\left\{1+\beta+\beta^2\right\}} \tag{8.12}$$

For constant strain ratios Equation (8.12) may be integrated to give

$$\bar{\varepsilon} = \varepsilon_1 \sqrt{\frac{4}{3}\left\{1+\beta+\beta^2\right\}} \tag{8.13}$$

8.3 Analysis of strain localization

Consider a welded rectangular sheet made of an aluminium alloy, see Figure 8.1. The sheet is considered fixed at one edge and loaded uniformly in uniaxial tension at the opposite side. The other two edges are free to move and without stress. It is assumed that the fixed one is next to the weld, so that the strength is reduced in a narrow region near the edge. B_0 and L_0 are the initial width and length of the sheet, respectively. The initial thickness h_0 of the sheet is assumed to be a function of x_1, while it is taken as constant in the x_2 direction. Further, the material properties are assumed to vary in the x_1 direction only. The sheet is fixed at the edge $\mathrm{x}_1 = 0$ and loaded by a uniform traction T along the edge $\mathrm{x}_1 = L_0$. The edges $\mathrm{x}_2 = \pm B_0/2$ are free to move and free of stress.

The sheet is discretized into a number of elements for which the material properties, thickness, strain ratio and deformation are all assumed constant, see Figure 8.2. The total number of elements are denoted N_e. The initial thickness of element *e* is denoted as h_0^e, while its strain ratio is β_e. Note that the strain ratio is assumed constant during straining of the sheet. It is deemed reasonable to take $\beta = 0$ for element 1 and $\beta = -1/2$ for element N_e. The variation of β from element to element has to be assumed by the analyst.

It is further assumed that the strain hardening of the material depends on the x_1 coordinate only, and for element *e* the effective stress is given by

$$\bar{\sigma}_e = Y_0^e + \sum_{i=1}^{2} Q_i^e \left(1 - \exp\left(-C_i^e \bar{\varepsilon}_e\right)\right) \tag{8.14}$$

where $\bar{\varepsilon}_e$ is the effective plastic strain in element e. The strain hardening parameters Y_0^e, Q_i^e and C_i^e all depend on the element's location in the sheet.

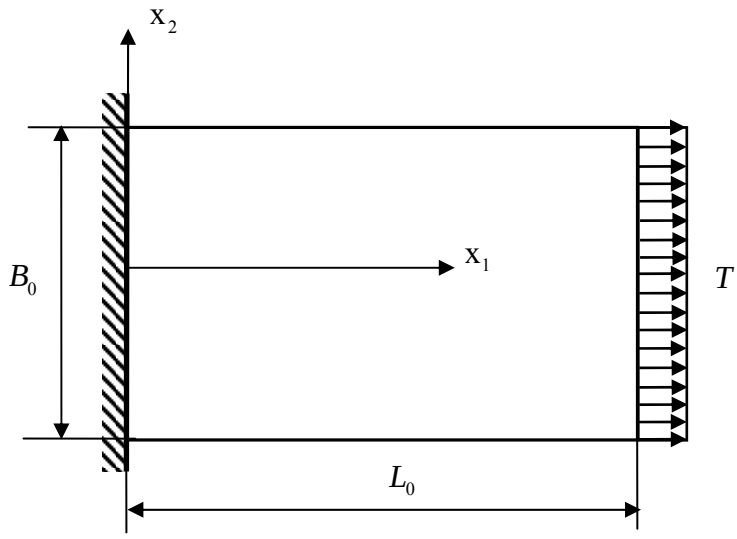

Figure 8.1. Geometry, boundary condition and loading of the rectangular sheet.

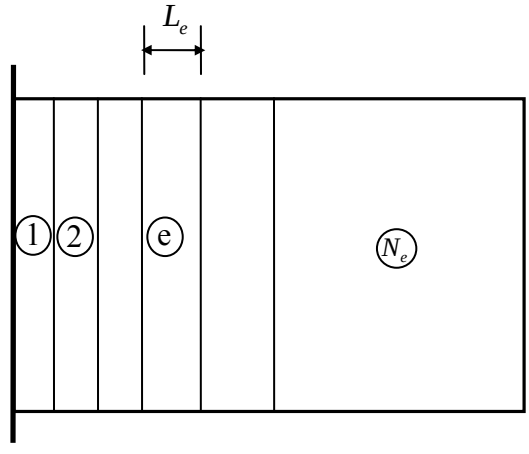

Figure 8.2. Discretization of the sheet.

Equilibrium in the x_1 direction requires that the applied force F equals

$$F = F_e = \sigma_1^e h_e B_e \quad \text{for } e = 1,...,N_e \tag{8.15}$$

where

$$\sigma_1^e = \frac{2+\beta_e}{\sqrt{3}\sqrt{1+\beta_e+\beta_e^2}}\left[Y_0^e + \sum_{i=1}^{2} Q_i^e \left(1-\exp\left(-C_i^e \bar{\varepsilon}_e\right)\right)\right] \tag{8.16}$$

The element width and thickness are

$$B_e = B_0 \exp\left(\frac{\bar{\varepsilon}_e \beta_e}{\sqrt{\frac{4}{3}\left(1+\beta_e+\beta_e^2\right)}} \right) \tag{8.17}$$

$$h_e = h_0^e \exp\left(\frac{-\bar{\varepsilon}_e \left(1+\beta_e\right)}{\sqrt{\frac{4}{3}\left(1+\beta_e+\beta_e^2\right)}} \right) \tag{8.18}$$

Equation (8.16) follows from Equations (8.10) and (8.14), while Equations (8.17) and (8.18) are derived from the definitions $\varepsilon_2^e = \ln\left(B_e / B_0\right)$ and $\varepsilon_3^e = \ln\left(h_e / h_0^e\right)$ using Equations (8.4) and (8.13).

Let the initial and current lengths of an element be given by L_e^0 and L_e, respectively. Using the definition $\varepsilon_1^e = \ln\left(L_e / L_0^e\right)$ together with Equation (8.13), the current length of element *e* is readily obtained as

$$L_e = L_e^0 \exp\left(\frac{\bar{\varepsilon}_e}{\sqrt{\frac{4}{3}\left(1+\beta_e+\beta_e^2\right)}} \right) \tag{8.19}$$

Finally, the total length of the plate is

$$L = \sum_{e=1}^{N_e} L_e \tag{8.20}$$

Hence the effective plastic strains $\bar{\varepsilon}_e$ in each element are the only free variable that determines the force versus elongation relationship of the plate.

The response of the sheet as a function of the applied traction T is found by determining a spatial distribution of the effective plastic strain $\bar{\varepsilon}_e$ that satisfies both internal and external equilibrium and the constitutive equations. This is done by assigning a numerical value to the strain $\bar{\varepsilon}_1$ of the weakest element, which is assumed as element 1, i.e. the element next to the weld. By means of the $N_e - 1$ inter-element equilibrium equations the strains $\bar{\varepsilon}_e$ in the remaining $N_e - 1$ elements are computed. The external traction T that is in equilibrium with this strain field is equal to the inter-element force F, which is constant for all elements. By incrementally (n=1, 2, …, N) increasing the strain in element 1, a sequence of strain fields $\bar{\varepsilon}_{e,n}$ and corresponding traction T_n and sheet length L_n are determined.

Assuming that the effective plastic strain in element 1 is prescribed, i.e. $\bar{\varepsilon}_1$ is input data, it follows that the number of unknown variables is $N_e - 1$, which can be solved from the $N_e - 1$ non-linear equilibrium equations on the boundary between the elements. The $N_e - 1$ unknown strain values $\bar{\varepsilon}_{e,n}$ for increment n are found from the $N_e - 1$ uncoupled nonlinear equilibrium equations. On residual form the set of equations read

$$\Re\left(\bar{\varepsilon}_e\right) = F_e\left(\bar{\varepsilon}_e\right) - F_{e-1}\left(\bar{\varepsilon}_{e-1}\right) = 0 \quad \text{for} \quad e = 2,3,...,N_e \tag{8.21}$$

The equations are uncoupled and are readily solved sequentially by using Newton's method for each element. At increment n, the force residual for element e reads

$$\Re\left(\bar{\varepsilon}_{e,n}^{k+1}\right) = \Re\left(\bar{\varepsilon}_{e,n}^{k}\right) + \frac{d\Re\left(\bar{\varepsilon}_{e,n}^{k}\right)}{d\bar{\varepsilon}_{e,n}^{k}} d\bar{\varepsilon}_{e,n}^{k+1} = 0 \tag{8.22}$$

where k is an iteration counter. Furthermore

$$\bar{\varepsilon}_{e,n}^{k+1} = \bar{\varepsilon}_{e,n}^{k} + d\bar{\varepsilon}_{e,n}^{k+1} = \bar{\varepsilon}_{e,n}^{k} - \frac{\Re\left(\bar{\varepsilon}_{e,n}^{k}\right)}{\dfrac{d\Re\left(\bar{\varepsilon}_{e,n}^{k}\right)}{d\bar{\varepsilon}_{e,n}^{k}}} \tag{8.23}$$

The Jacobian is approximated by

$$\frac{d\Re\left(\bar{\varepsilon}_{e,n}^{k}\right)}{d\bar{\varepsilon}_{e,n}^{k}} \approx \frac{\Re\left(\bar{\varepsilon}_{e,n}^{k}\right) - \Re\left(\bar{\varepsilon}_{e,n}^{k-1}\right)}{\bar{\varepsilon}_{e,n}^{k} - \bar{\varepsilon}_{e,n}^{k-1}} \tag{8.24}$$

For increment n the initial value of the strain field $\bar{\varepsilon}_{e,n}$ is assigned the converged value of the previous field $\bar{\varepsilon}_{e,n-1}$. For the iteration, the starting values $\bar{\varepsilon}^1_{e,n}$ are assigned the convergent values $\bar{\varepsilon}_{e-1,n}$ from the previous increment.

The above analytical scheme was programmed using Visual Basic and the flow chart of the routine is listed in Table 8.1.

Table 8.1. Flow chart for strain localization analysis.

1. Initial condition and initialization:
   Dimension of the sheet: length L_0 and width B_0.
   Dimension of element e: thickness h_e and length L_e.
   Hardening parameters of element e: Y_0^e, Q_1^e, Q_2^e, C_1^e and C_2^e.
   Strain ratio of element e: β_e
   For $\bar{\varepsilon}_1 = 0$, compute the initial traction force when yielding initiates: F_{int}.
2. Loop over increment n.
   i. For $\bar{\varepsilon}_1 = n\Delta\bar{\varepsilon}$, compute force at increment n, F^n.
   ii. Loop over elements.
      (1). Compute stress σ_n^e at element e.
      (2). Check yielding. If $\sigma_n^e \le Y_0^e$, $L_e^n = L_e$, go to next element.
      (3). Check maximum force. If $F^n < F^{n-1}$, $L_e^n = L_e^{n-1}$, go to next element.
      (4). Start Newton iteration to compute $\bar{\varepsilon}_{e,n}$ and L_e^n.
   iii. End loop over elements.
3. End loop over increments.
4. Output of F^n and L_e^n.

8.4 Validation study

The width of the rectangular sheet is chosen as $B_0 = 150$ mm, which is identical to the width of the upper sheet in the fillet-welded connections in Chapter 7. The length of the sheet is set as $L_0 = 58$ mm, the same as the distance between the weld toe and the transducer in the tests. By using $\Delta\bar{\varepsilon} = 0.0025$ and 200 increments, the total effective

plastic strain for Element 1 is $\bar{\varepsilon}_{tot} = 0.5$. Initially the HAZ is sub-divided into sub-HAZ elements, each of them has a length of 4 mm. The assumed strain ratios and hardening properties for the six sub-HAZ elements and the base material are listed in Table 8.2. The adopted hardening parameters are the ones found in Section 6.2.2

As previously stated yielding initiates in element 1, and the force associated with the prescribed strain is determined. Due to inter-element equilibrium this force acts on all elements, and the plastic strain that satisfies both equilibrium and the material law is computed. Based on these strains the plastic elongations in the elements are added up to determine the total displacement of the sheet.

The obtained force vs. displacement curve is shown in Figure 8.3, in comparison with the test results. It can be seen that the curve obtained by the present method (labelled as "6×4 mm HAZ") has a similar shape as the test curves, but the predicted ultimate load exceeds the tests by about 25%. It should be noted that the analytical solution only includes the plastic deformation, while the tests include the total deformation.

To assess the possibility of using this method for design purpose, the nominal material properties given by Eurocode 9 (CEN 2002) are used. For fillet welds in 6xxx aluminium sheets with thickness less than or equal to 6 mm, the code stipulates the extent of the HAZ to be $b_{haz} = 20\ mm.$ For alloy 6082 plates with thickness less than or equal to 5 mm, the reduction factor of the ultimate strength is $\rho_{u,\,haz} = 0.64$. Therefore the strength properties Y_0, Q_1, and Q_2 of element 7 in Table 8.2 were multiplied with $\rho_{u,\,haz} = 0.64$ and the parameters listed in Table 8.3 are obtained. Parameters C_1 and C_2 remained the values as element 1 in Table 8.2 to keep the same work hardening trend as the previous HAZ material. Using these parameters and total effective strains $\bar{\varepsilon}_{tot} = 0.5$, the force vs. deformation curve in Figure 8.3 is obtained. The analysis gave a conservative ultimate load which is 7% lower than the tests. However the ductility is much greater than obtained by the tests and the previous analysis.

The analyses using the material data in Table 8.2 predicted the loading process reasonably well, even though it over-estimated the ultimate load. The reason might lie in the inherent limitations of the method, and the uncertainty of the material properties. As discussed in the previous Section, the method violates compatibility in the width direction, and it also excludes the elastic deformation. Thus the area of the sheet cross section is not represented accurately, which might have an effect on the force level. Another limitation of this method is that the current calculations rely upon the isotropic von Mises equivalent stress, while the extruded aluminium sheet possesses anisotropic

properties. In previous finite elements simulations, the isotropic yield criterion was found to over-estimate the ultimate load by 5% compared with the anisotropic yield criterion. Furthermore, the material properties of the HAZ might not be sufficiently accurate. It should be noted that the previous FE simulations with the same material properties also over-estimated the ultimate load by 10%.

Table 8.2. Material parameters and assumed strain ratios of the elements.

Element	Length [mm]	Strain ratio [-]	Y_0 [N/mm^2]	Q_1 [N/mm^2]	C_1 [-]	Q_2 [N/mm^2]	C_2 [-]	$Y_0 + \sum Q_i$ [N/mm^2]
1 (HAZ)	4	0	99	47	669	131	22	277
2 (HAZ)	4	-0.1	165	51	1091	74	33	290
3 (HAZ)	4	-0.2	196	84	2811	59	30	339
4 (HAZ)	4	-0.3	217	88	6095	61	19	366
5 (HAZ)	4	-0.4	205	100	2780	57	24	362
6 (HAZ)	4	-0.4	205	100	2780	57	24	362
7 (Base)	34	-0.5	235	72	3196	52	29	359

Table 8.3. Material parameters derived from Eurocode 9 (CEN, 2002) and assumed strain ratios.

Element	Length [mm]	Strain ratio [-]	Y_0 [N/mm^2]	Q_1 [N/mm^2]	C_1 [-]	Q_2 [N/mm^2]	C_2 [-]	$Y_0 + \sum Q_i$ [N/mm^2]
1 (HAZ)	20	0	120	45	669	20	22	185
2 (Base)	38	-0.5	235	72	3196	52	29	359

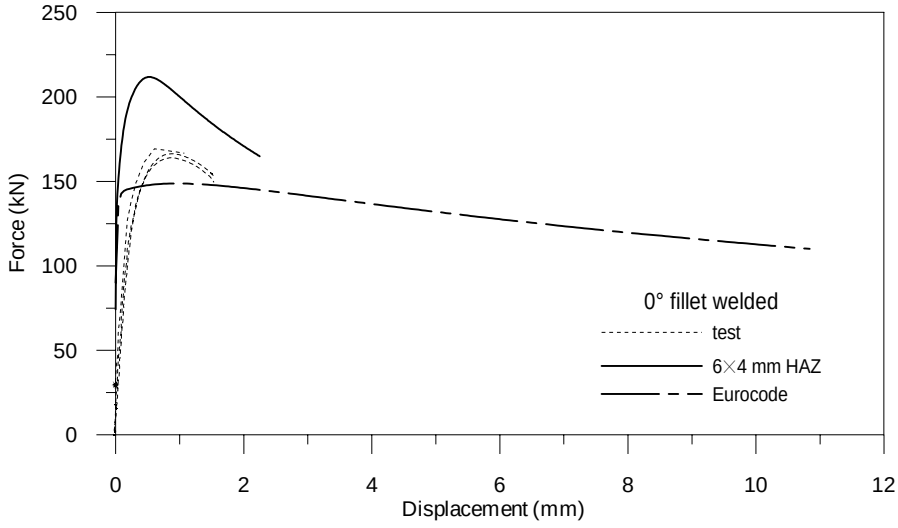

Figure 8.3. Force vs. deformation curves from the analytical method and the tests.

In conclusion, this simple analytical method is seen to predict the performance of the welded aluminium sheet under uniaxial tensile loading reasonably well. It is a simple and efficient method to study the performance of an inhomogeneous welded sheet, though it can not replace FE analyses in the cases of more complicated geometries.

8.5 Parametric study

Parametric study was performed to assess the effect of HAZ modelling on the predicted performance of the welded sheet under tensile loading. The seven-element analysis presented in Section 8.4 was used as a baseline calculation. The investigated parameters include HAZ discretization, the strain ratio and the material properties. In all analyses, the sheet length is $L_0 = 58$ mm, and the total effective plastic strain of Element 1 is $\bar{\varepsilon}_{tot} = 0.5$.

8.5.1 HAZ discretization

The HAZ is given lengths of 12 mm, 24 mm and 36 mm, respectively. For each of the lengths, the HAZ is sub-divided into 1, 2, 3, 4 and 6 sub-HAZs. The dimensions of each of the HAZ and sub-HAZs in the different discretization methods are listed in Table 8.4. The material parameters used in all the analyses are given in Table 8.5 to Table 8.9. The last element in every analysis is always the base material. For each of the analyses, the material properties of element 1 and the element of the base material remain the same as those in the baseline analysis.

Figure 8.4 shows the response curves of the analyses. For each of the investigated HAZ lengths, the ductility is seen to decrease with the increasing number of the sub-HAZs. The most homogeneous division, the one with a single sub-HAZ, predicted the greatest elongation; and the most inhomogeneous division, the one with six sub-HAZs, gave the smallest elongation. The ultimate force is not affected by the inhomogeneity given the material properties of element 1 being the same for all the analyses. Comparing the three figures, it can be further concluded that the elongation rises with an increase of the total length of the HAZ.

Table 8.4. Dimensions of HAZ and sub-HAZs in different discretization methods.

Length of HAZ [mm]	1 sub-HAZ	2 sub-HAZs	3 sub-HAZs	4 sub-HAZs	6 sub-HAZs
12	1×12 mm	2×6 mm	3×4 mm	4×3 mm	6×2 mm
24	1×24 mm	2×12 mm	3×8 mm	4×6 mm	6×4 mm
36	1×36 mm	2×18 mm	3×12 mm	4×9 mm	6×6 mm

Table 8.5. Hardening properties and assumed strain ratios for 1 sub-HAZ analysis.

Element	Strain ratio [-]	Y_0 [N/mm^2]	Q_1 [N/mm^2]	C_1 [-]	Q_2 [N/mm^2]	C_2 [-]	$Y_0 + \sum Q_i$ [N/mm^2]
1 (HAZ)	0	99	47	669	131	22	277
2 (Base)	-0.5	235	72	3196	52	29	359

Table 8.6. Hardening properties and assumed strain ratios for 2 sub-HAZs analysis.

Element	Strain ratio [-]	Y_0 [N/mm^2]	Q_1 [N/mm^2]	C_1 [-]	Q_2 [N/mm^2]	C_2 [-]	$Y_0 + \sum Q_i$ [N/mm^2]
1 (HAZ)	0	99	47	669	131	22	277
2 (HAZ)	-0.1	205	100	2780	57	24	362
3 (Base)	-0.5	235	72	3196	52	29	359

Table 8.7. Hardening properties and assumed strain ratios for 3 sub-HAZs analysis.

Element	Strain ratio [-]	Y_0 [N/mm^2]	Q_1 [N/mm^2]	C_1 [-]	Q_2 [N/mm^2]	C_2 [-]	$Y_0 + \sum Q_i$ [N/mm^2]
1 (HAZ)	0	99	47	669	131	22	277
2 (HAZ)	-0.1	196	84	2811	59	30	339
3 (HAZ)	-0.2	205	100	2780	57	24	362
4 (Base)	-0.5	235	72	3196	52	29	359

Table 8.8. Hardening properties and assumed strain ratios for 4 sub-HAZs analysis.

Element	Strain ratio [-]	Y_0 [N/mm^2]	Q_1 [N/mm^2]	C_1 [-]	Q_2 [N/mm^2]	C_2 [-]	$Y_0 + \sum Q_i$ [N/mm^2]
1 (HAZ)	0	99	47	669	131	22	277
2 (HAZ)	-0.1	165	51	1091	74	33	290
3 (HAZ)	-0.2	196	84	2811	59	30	339
4 (HAZ)	-0.3	205	100	2780	57	24	362
5 (Base)	-0.5	235	72	3196	52	29	359

Table 8.9. Hardening properties and assumed strain ratios for 6 sub-HAZs analysis.

Element	Strain ratio [-]	Y_0 [N/mm^2]	Q_1 [N/mm^2]	C_1 [-]	Q_2 [N/mm^2]	C_2 [-]	$Y_0 + \sum Q_i$ [N/mm^2]
1 (HAZ)	0	99	47	669	131	22	277
2 (HAZ)	-0.1	165	51	1091	74	33	290
3 (HAZ)	-0.2	196	84	2811	59	30	339
4 (HAZ)	-0.3	217	88	6095	61	19	366
5 (HAZ)	-0.4	205	100	2780	57	24	362
6 (HAZ)	-0.4	205	100	2780	57	24	362
7 (Base)	-0.5	235	72	3196	52	29	359

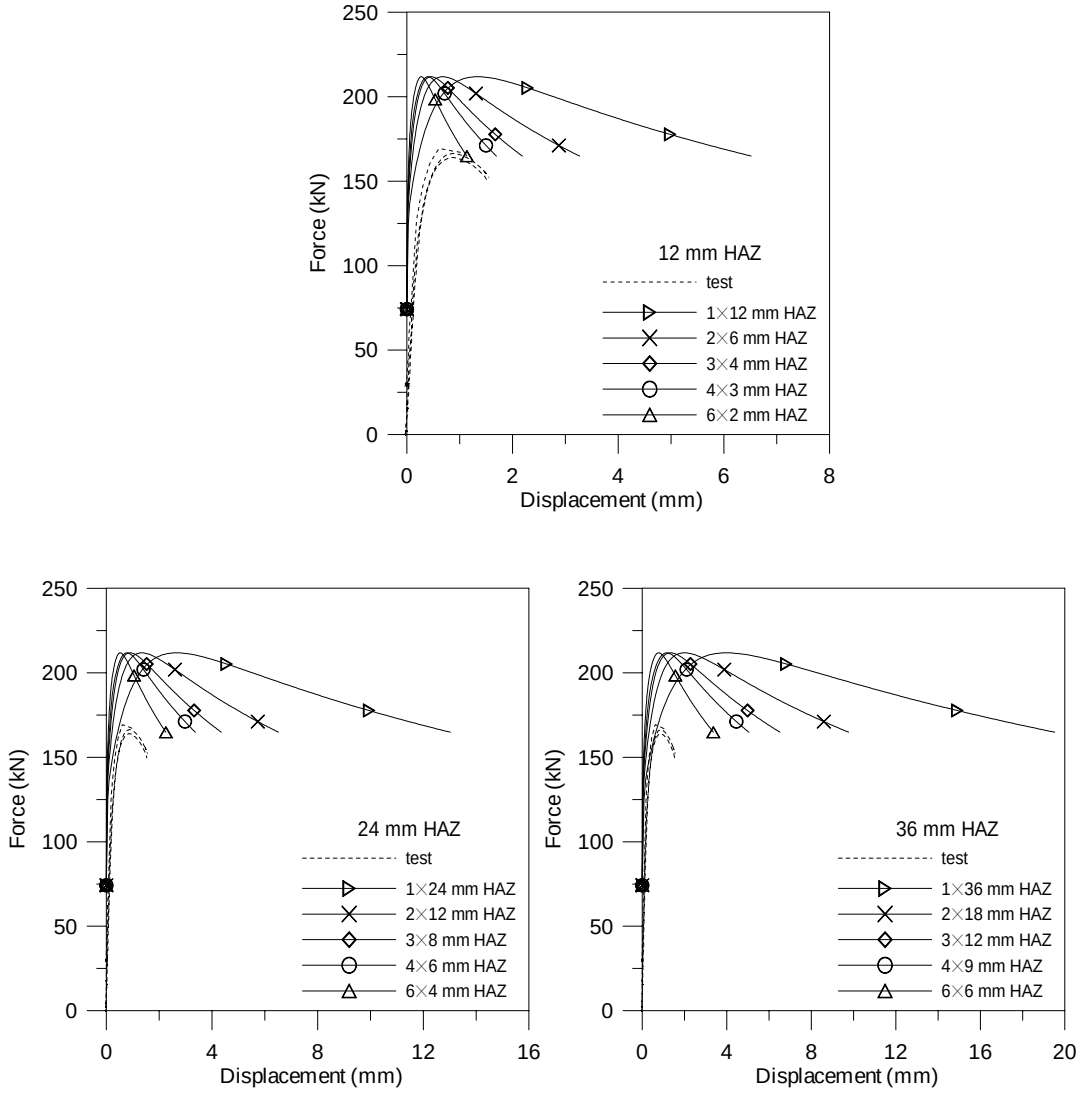

Figure 8.4. Analysis results with 12 mm, 24 mm and 36 mm HAZ.

8.5.2 Strain ratio

The effect of the assumed strain ratios on the ultimate load and ductility is studied using a model with two 10 mm Sub-HAZs. The strain ratio of element 1 varies from $\beta = -0.4$ to $\beta = 0$, while the strain ratio of element 2 is constant as $\beta = -0.4$. The material properties are listed in Table 8.10.

The response curves from the analyses are shown in Figure 8.4. The ultimate load is found to increase with decreasing absolute value of the strain ratio. The highest ultimate load is obtained by $\beta = 0$, while the lowest is by $\beta = -0.4$. Elongation is seen to rise with increasing absolute value of the strain ratio, i.e., $\beta = 0$ gave the smallest elongation and $\beta = -0.4$ gave the greatest.

Table 8.10. Material properties of 2×10 mm HAZ analysis.

Element	Y_0 [N/mm^2]	Q_1 [N/mm^2]	C_1 [-]	Q_2 [N/mm^2]	C_2 [-]	$Y_0 + \sum Q_i$ [N/mm^2]
1 (HAZ)	99	47	669	131	22	277
2 (HAZ)	205	100	2780	57	24	362
3 (Base)	235	72	3196	52	29	359

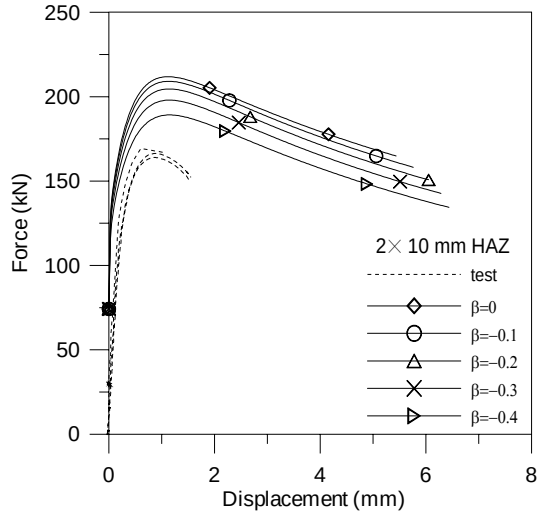

Figure 8.5. Analysis results with various strain ratios in Element 1.

8.5.3 Material strength

So far material strength in Element 1 has been kept constant, consequently the ultimate load for all the analyses are identical given the strain ratios being the same. In this Section, the material strength is varied to investigate its influence on the prediction of ultimate load and ductility. The method is that for the baseline analysis, i.e. the model with 6×4 mm HAZ and material properties as in Table 8.2, the strength related material parameters, Y_0, Q_1 and Q_2 in HAZ 1, are multiplied by a factor of 0.9, 0.8, 0.7, 0.6 and 0.5, respectively.

Figure 8.6 shows the obtained response curves in comparison with the tests and the baseline analysis. The ultimate load appears to rise proportionally with increasing material strength. Hence, the predicted force level depends strongly on the lowest strength within the HAZ.

8.5.4 Length of sub-HAZ 1

Here the result of the baseline analysis (4 mm sub-HAZ 1) is compared with calculations with sub-HAZ 1 lengths of 2 mm, 1 mm, 0.5 mm, and 0.1 mm. The length of sub-HAZ 2 was increased to 6 mm, 7 mm, 7.5 mm and 7.9 mm, so that the extent of the total HAZ remains 24 mm.

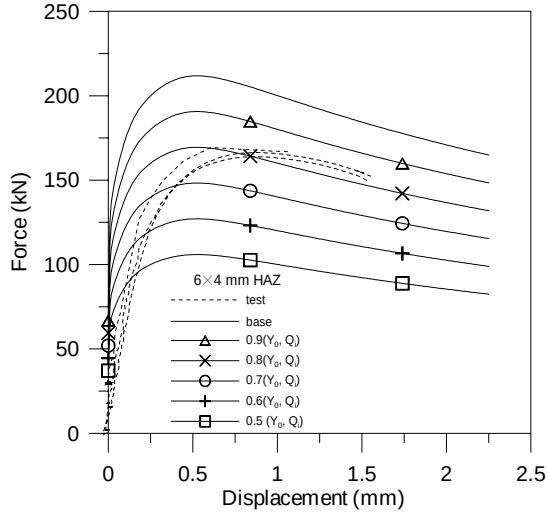

Figure 8.6. Analysis results with various material strengths.

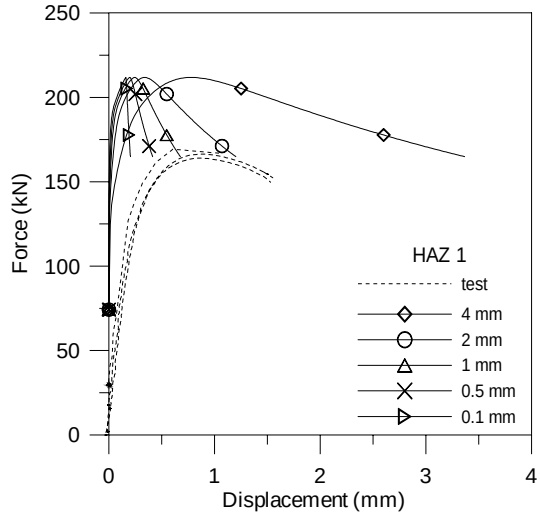

Figure 8.7. Analysis results with various lengths of the sub-HAZ 1.

The predicted force vs. displacement curves are shown in Figure 8.7. It can be seen that the ductility decreases with the length of Sub-HAZ 1. The shape of the curve by the analysis with 4 mm Sub-HAZ 1 resembles the tests most.

8.5.5 Inhomogeneity of Sub-HAZ 1

It has been shown that the predicted ultimate load depends on the material properties of sub-HAZ 1. In the previous analyses the material properties of sub-HAZ 1 was assumed homogeneous. However in a real structure, the material properties of the HAZ can be more inhomogeneous. Uniaxial tensile tests provide average material properties along the width of the specimens so that they are not able to describe the variation of the material properties within the specimens.

To assess the effect of this ignored inhomogeneity on the predicted ultimate load, analyses were carried out by sub-dividing the sub-HAZ 1 into 2 elements. The strength (Y_0, Q_1 and Q_2) of one of them was raised 5% and the other one was decreased 5%, so that the whole region possess an average strength similar to sub-HAZ 1 in the baseline analysis. The obtained result is shown in Figure 8.8. It can be seen that the ultimate load was decreased by the increased inhomogeneity. The ductility decreased also as expected in view of the results presented in Section 8.5.1.

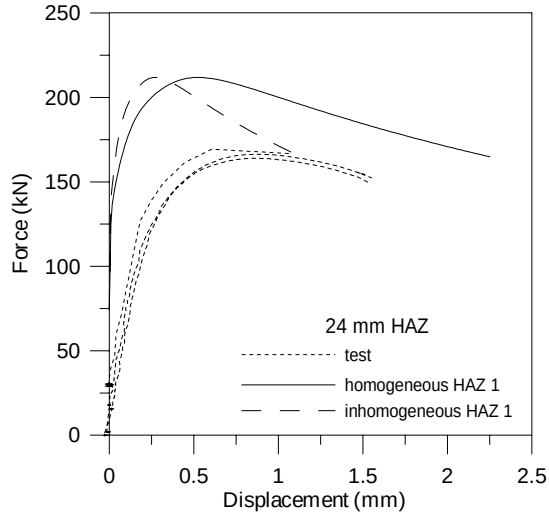

Figure 8.8. Analysis results with inhomogeneous Sub-HAZ 1.

8.6 Conclusions

A simple analytical method is introduced to compute the mechanical performance of a welded aluminium sheet under uniaxial tensile loading. The analysis does not fulfil all compatibility conditions of the continuum sheet, and it assumes that the extruded sheet possesses isotropic material properties. Despite these limitations it efficiently predicts the performance of the sheet within reasonable accuracy. The method is valid for the given welded geometry, and can not replace FE analysis of more complex structures. However, similar to an FE analysis, it is able to provide information on the influence of HAZ modelling on prediction of the structural performance, especially with respect to ductility. The results are clearly beneficial for FE modelling of welded structures.

Parametric studies were carried out to study the influence of the HAZ length, HAZ discretization, strain ratio, material strength, and properties of the weakest element (sub-HAZ 1) on prediction of the structural performance. It is found that the predicted ductility is affected by the length of the sub-HAZs, especially the length of the weakest element, and the total HAZ length. Generally speaking, the structural ductility increases when the material properties in the HAZ are more homogenous. The strain ratio appears to affect the ultimate load, and to slightly affect the structural ductility. The material strength of the weakest sub-HAZ was found to influence the predicted ultimate load proportionally.

Comparing the analysis results with the experiments, it can be concluded that a very detailed representation of the variation of the material properties in the HAZ does not ensure a correct prediction of the structural ductility. When yielding starts, strain localizes in the zone which possesses the lowest strength. A very short length of this zone would mean a very short base of stretching, which may be not enough to get the elongation as much as in the tests. According to metal forming theory, the width of the localized neck is typically of the order of the sheet thickness (Hosford and Caddell 2002). Thus, characteristic sub-HAZ-length similar to or of the same order of the thickness could be recommended to obtain a correct representation of the structural ductility.

9. Simulations of beam-to-column joints subjected to tension

9.1 Introduction

The case of a tensile force acting transversely on an unstiffened column flange through a flat plate constitutes a generic component of beam-to-column connections or other structural details, and is often incorporated in more complex joints, e.g. a beam-to column semi-rigid joint. For design purposes, the total force that can be transmitted from the tensile flange of the beam to the column is of interest. Previously, Matusiak (1999) carried out a series of tests to investigate the mechanical properties of aluminium joints. He found that the structural performance of aluminium joints with a transverse force on an unstiffened I-section depends on the joint's geometry. Material softening due to welding decreases significantly both the strength and ductility of the component. The failure modes are similar to those of joints in mild structural steel.

Numerical analyses have been performed by Matusiak (1999) for these beam-to-column joints using the FE-code ABAQUS and three-dimensional solid elements, namely an 8-node linear solid element with reduced integration. By a trial and error procedure of determining the spatial distribution of the material parameters, a good agreement between the experimental and numerical results was achieved. However, 3D modelling is usually time-consuming and therefore not feasible for large-scale analysis of structures. In this Chapter, these beam-to-column joints are modelled with a strategy similar to the one established in Chapter 7 aiming to a more efficient numerical methodology.

9.2 Review of the tests

9.2.1 Component tests

The experiments described in this Section were previously carried out by Matusiak (1999). In these tests, a tensile force was subjected to an unstiffened I-column flange through a plate which was fillet-welded to the column. Figure 9.1 shows the geometry of the specimen. The I-sections are denoted I-100 and I-80, with profile height $h = 100$ mm and $h = 80$ mm, respectively. Two plate widths and two cross sections of the profile gave three component geometries, denoted A, B and C in Table 9.1. Extruded flat plates with a thickness of 6 mm were fillet-welded in single passes to the flanges. The chemical composition of the alloy is the same as for the aluminium plate in the previous Chapters, as listed in Table 5.1.

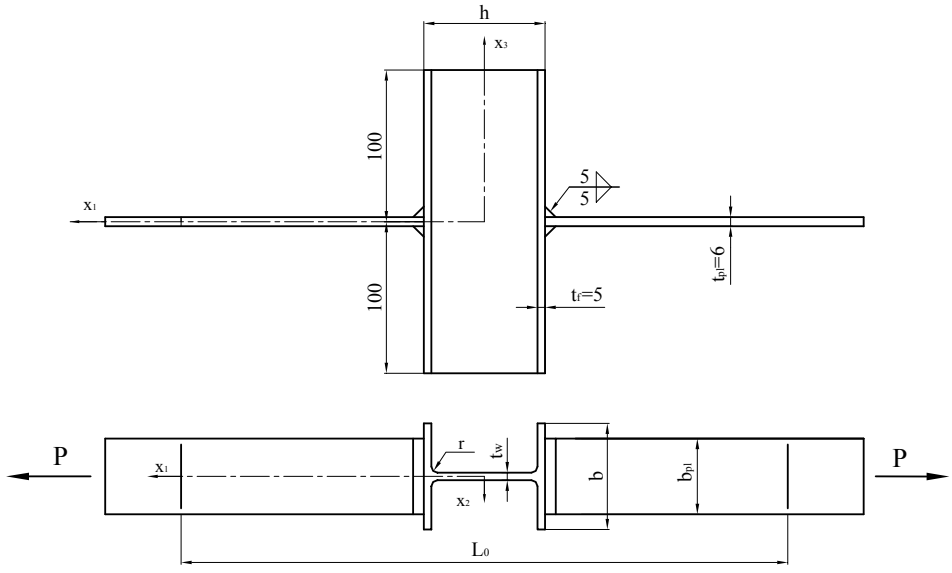

Figure 9.1. Geometry of the beam-to-column joint (Matusiak 1999).

Table 9.1. Nominal specimen dimensions (mm) (Matusiak 1999).

Joint type	I-profile				Plate b_{pl} [mm]	Gauge length L_0 [mm]
	h [mm]	b [mm]	r [mm]	t_w [mm]		
A	100	50	4	3.5	50	400
B	80	70	5	5	50	380
C	80	70	5	5	70	380

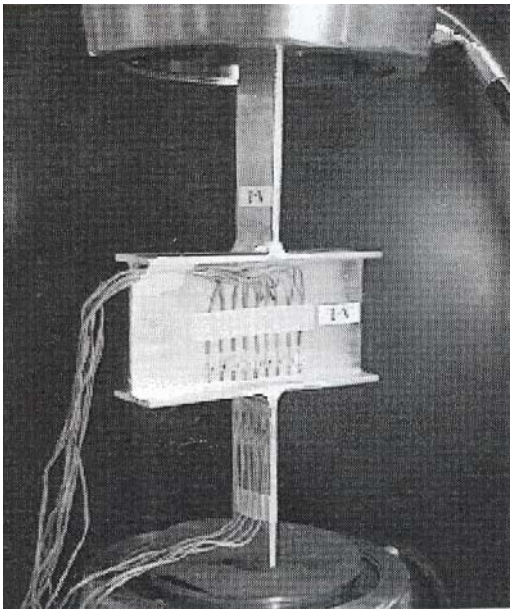

Figure 9.2. Test set-up (Matusiak 1999).

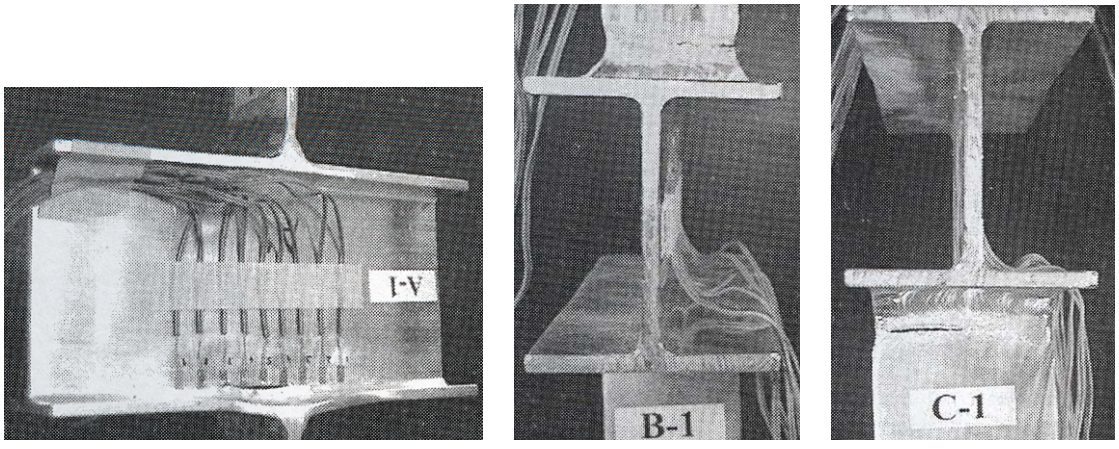

Figure 9.3. Specimens after testing (Matusiak 1999).

Three parallel tests were performed for each configuration using an Instron 100 kN universal testing machine, see Figure 9.2 for the test set-up. Monotonic loading until failure was applied under displacement control with a rate of 0.02 mm/s. The plate ends were clamped in the machine and the stroke was used as the displacement measure. In the tests, joints A failed due to web tearing while rupture of the plate was the failure mode of joints B and C. For one specimen of joint C fracture occurred between the flange and weld. The tearing of the web of joint A occurred very close to the flange, i.e.

in the HAZ within the web. For both joints B and C rupture occurred in the HAZ of the plate, a few millimetres away from the weld toe. Several areas of strain localisation occurred for all joints. Pictures of typical components after testing are presented in Figure 9.3.

9.2.2 Material tests

Unaxial tensile tests were performed to obtain the mechanical properties of the base material in the joints by Matusiak (1999). The specimens taken from the plate and the flange of the I-profile were tested parallel to the extrusion direction, while the specimens from the web were normal to the extrusion direction.

The obtained yield strength and ultimate strength of the various materials are listed in Table 9.2. In Table 9.3, the value of f_u (90°) for the plate and flange were obtained as the product of f_u (0°) and $r_{90} = 1.02$, which was obtained in Section 5.2. This implies that similar anisotropy was assumed to the aluminium sheets investigated in both the current and previous studies. It is seen that there are considerable differences in strength between the various parts of the specimens due to the extrusion process. The reaction of the extrusion billet with the container and die results in high compressive stresses and temperature change which might not be uniform at an irregular cross section of the profiles.

9.3 Identification of material parameters

Even if the anisotropy of the profile geometries in question might be different from the one found in the plates characterised in Section 6.3, the current study relies upon these parameters in lack of other data.

With respect to hardening properties, Matusiak (1999) has characterised the material in the vicinity of a *butt weld* by uniaxial tensile tests. In Chapter 6 these data were used to calibrate the five-parameter extended Voce rule, and were further scaled to the extrusion direction by use of $r_{90} = 1.02$. The obtained hardening parameters for the weld, sub-HAZs and base material are given in Table 6.1 in terms of distance to the weld centre. The ultimate strength of the base material in the butt-welded plate is $f_{\mathrm{u,butt}} = 336$ MPa , and it is compared with the ultimate strength of the base materials of the beam-to-column joints ($f_{\mathrm{u,joint}}$) in Table 9.3.

To obtain the hardening parameters for the web, flange and plate of the joints for use in the current numerical study, the parameters Y_0, Q_1 and Q_2 in Table 6.1 were multiplied by the factor of $f_{\mathrm{u,joint}} / f_{\mathrm{u,butt}}$ (90°) in Table 9.3. The obtained values for the plate are listed in Table 9.4. For profile I-80, the obtained parameters are listed in Table 9.5. For profile I-100, Table 9.6 and Table 9.7 provide the parameters for web and flange, respectively. Note that the values of the multiplier, $f_{\mathrm{u,joint}} / f_{\mathrm{u,butt}}$ (90°), are identical for the web and flange of I-80, and therefore uniform parameters are obtained for all parts of the I-beam. It should be noted that there are many uncertainties related to the chosen procedure in parameter identification.

Table 9.2. Average values of material parameters (Matusiak 1999).

Joint component	Direction	$f_{0.2}$ [N/mm^2]	f_u [N/mm^2]	$f_u / f_{0.2}$ [-]	ε_u [-]
Plate	$\parallel$	304.5	313.5	1.03	0.064
Profile I-100, web	$\perp$	262.7	281.6	1.07	0.068
Profile I-100, flange	$\parallel$	268.9	283.4	1.05	0.061
Profile I-80, web	$\perp$	300.2	315.6	1.05	0.074
Profile I-80, flange	$\parallel$	302.1	308.5	1.02	0.072

Table 9.3. Material strength in comparison with the base material of the butt-welded specimen (cf. Chapter 6).

Joint component	f_u (0°) [N/mm^2]	f_u (90°) [N/mm^2]	$f_{\mathrm{u,joint}} / f_{\mathrm{u,butt}}$ (90°) [-]
Plate	313.5	319.8*	0.95
Profile I-100, web		281.6	0.84
Profile I-100, flange	283.4	289.1*	0.86
Profile I-80, web		315.6	0.94
Profile I-80, flange	308.5	314.7*	0.94

* Data scaled from f_u (0°) by using the flow stress ratio.

Table 9.4. Assumed work hardening parameters for plate.

Zones	Y_0 (0°) [N/mm^2]	Q_1 [N/mm^2]	C_1 [-]	Q_2 [N/mm^2]	C_2 [-]	$Y_0 + \Sigma Q_i$ [N/mm^2]
Weld	105	42	656	189	13	329
HAZ 1	112	36	616	157	18	305
HAZ 2	94	45	669	131	22	270
HAZ 3	157	48	1091	74	33	279
HAZ 4	186	80	2811	60	30	326
HAZ 5	206	84	6095	61	19	351
HAZ 6	195	95	2780	57	24	347
Base	223	68	3196	52	29	344

Table 9.5. Assumed work hardening parameters for I-80.

Zones	Y_0 (0°) [N/mm^2]	Q_1 [N/mm^2]	C_1 [-]	Q_2 [N/mm^2]	C_2 [-]	$Y_0 + \Sigma Q_i$ [N/mm^2]
HAZ 1	111	36	616	157	18	304
HAZ 2	93	44	669	131	22	268
HAZ 3	155	48	1091	74	33	277
HAZ 4	184	79	2811	60	30	323
HAZ 5	204	83	6095	61	19	348
HAZ 6	193	94	2780	57	24	344
Base	221	68	3196	52	29	341

Table 9.6. Assumed work hardening parameters for web of I-100.

Zones	Y_0 (0°) [N/mm^2]	Q_1 [N/mm^2]	C_1 [-]	Q_2 [N/mm^2]	C_2 [-]	$Y_0 + \Sigma Q_i$ [N/mm^2]
HAZ 1	99	32	616	157	18	288
HAZ 2	83	39	669	131	22	254
HAZ 3	139	43	1091	74	33	255
HAZ 4	165	71	2811	60	30	295
HAZ 5	182	74	6095	61	19	317
HAZ 6	172	84	2780	57	24	313
Base	197	60	3196	52	29	310

Table 9.7. Assumed work hardening parameters for flange of I-100.

Zones	$Y(0°)$ [N/mm^2]	Q_1 [N/mm^2]	C_1 [-]	Q_2 [N/mm^2]	C_2 [-]	$Y_0 + \Sigma Q_i$ [N/mm^2]
HAZ 1	101	33	616	157	18	291
HAZ 2	85	40	669	131	22	257
HAZ 3	142	44	1091	74	33	260
HAZ 4	169	72	2811	60	30	301
HAZ 5	187	76	6095	61	19	323
HAZ 6	176	86	2780	57	24	319
Base	202	62	3196	52	29	316

9.4 Baseline finite element models

Having obtained the hardening parameters in the previous Section, numerical analyses were carried out with a modelling strategy similar to the one established in Chapter 7. A basic mesh of joint A is presented in Figure 9.4. The clamped zones in the plate were modelled as rigid bodies, while the rest of the specimen used the WTM-2D adopting the yield surface parameters obtained by the Power method and $M = 8$ (see Table 6.4). For each part of the specimen (web, flange and plate), six sub-HAZs were used, and the length of each sub-HAZ is 4 mm. The extent of the HAZ approximately agrees with that given by Eurocode 9 (CEN 2002). For the basic mesh, an initial element size of approximately 4×4 mm^2 was used. The refined mesh in Figure 9.5 is identical to the basic mesh, except that the element size in the central part of the web, flange and plate is approximately one quarter of the size outside this central part. In the refined mesh, tied_nodes_to_surface contact algorithm was used at the intersection of the coarse and dense meshed regions. The thickness modelling of the junction between web and flange for the I-profile is shown in Figure 9.6. In order to represent the geometry as accurately as possible, a non-constant thickness of the shell elements in various parts was used. The weld material is associated with the plate as shown in Figure 9.6b (in which the central flange is not shown) and is also associated with the flange in the central part (Figure 9.6a). The reason is that the material is considered to come into effect both in the flange and plate when the joint is subjected to loading. Five integration points were used through the thickness of the flange. For the web and plate only two through-thickness integration points were used through the thickness since no bending occurred there. The critical thickness strain for fracture is set to $\varepsilon_{cr} = -0.6$.

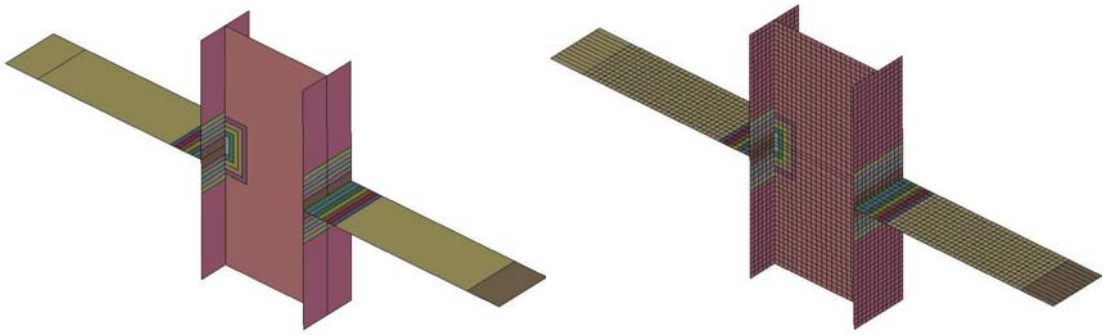

a) b)

Figure 9.4. Basic mesh of Joint A: a) parts, and b) mesh.

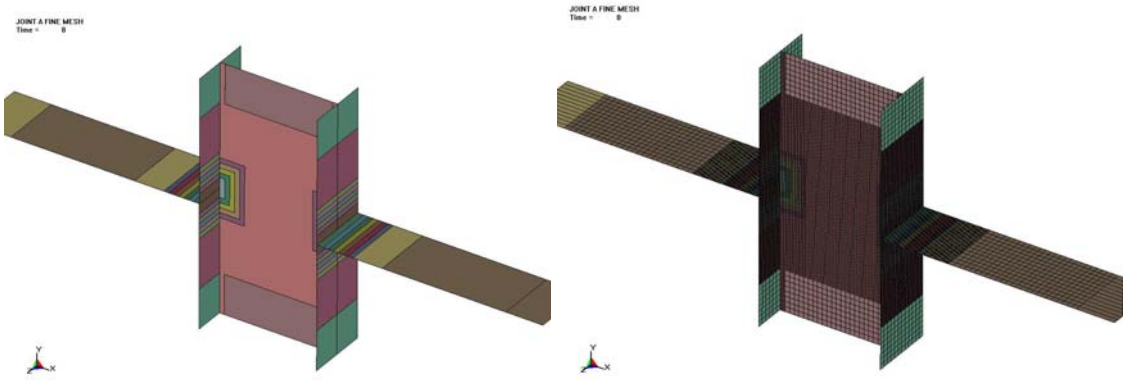

a) b)

Figure 9.5. Refined mesh of Joint A: a) parts, and b) mesh

Loading was applied smoothly using Equation (6.23) through the right clamped plate, while the left clamped plate was constrained. For the basic mesh, a total deformation of about 20 mm was imposed within a solution time of 12 ms. For the refined mesh, a total deformation of 6 mm within a 20 ms duration time was found CPU-optimized. The choices of deformations for both the basic and refined meshes are based on the different response from the various meshes. For any cases it was ensured that the response was quasi-static.

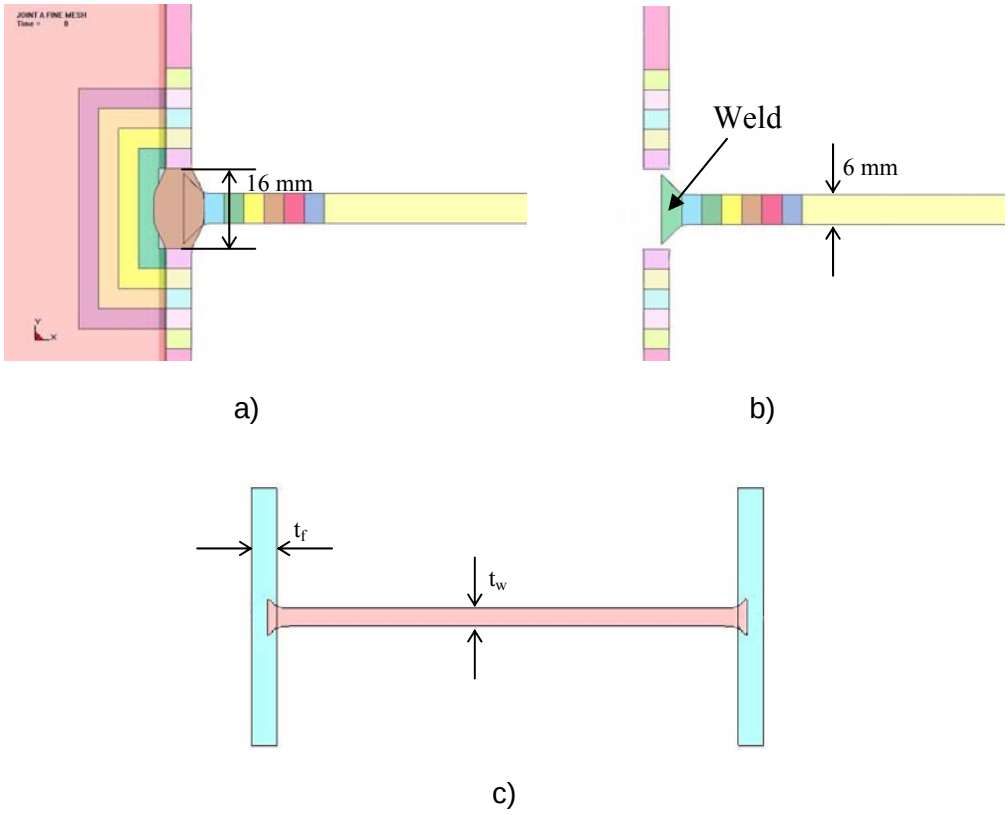

Figure 9.6. Thickness modelling in a) flange and plate, b) weld and c) I-beam profile.

9.5 Numerical results

9.5.1 Baseline models

Some results from the numerical simulations, in the form of thickness reduction, strain localization and response curves, are given in the following. Figure 9.7 depicts the predicted thickness reduction throughout the simulation process for joint A (basic mesh). In image a) plastic deformation occurs in both flange and web, followed by strain localization in sub-HAZ 2 in the web in images b) and c). At last elements reach the failure criterion in image d). The predicted location of the plastic deformation agrees with Matusiak's test results. The predicted fracture locations, however, do not correspond that well with all the experiments. In all simulations, fracture occurred in the web, except for the basic mesh of joint B, which failed in the plate. Fracture locations in the tests and simulations are summarized in Table 9.8. Fractures in the plate of the basic

model for joint B and in the web of the refined model for joint A are shown in Figure 9.8 and Figure 9.9.

Experimental and numerical results for joint A, B and C are presented in Figure 9.10. The basic mesh analyses for the three joints gave good predictions of stiffness and strength. The elongation was over-estimated, but it is noted that it depends very much on the assumed criterion and parameters. For the refined mesh, good agreement between the experimental and numerical results is achieved for joint B in terms of stiffness, ultimate strength and ductility. With the refined mesh, the simulations under-estimated the ultimate strength by about 10% with joint A and B, while it was under-estimated by 20% with joint C. Both of the analyses with a refined mesh of joint A and C under-estimated the ductility.

The fracture location was accurately predicted with both the basic and refined meshes of joint A, and with the basic mesh of joint B, but not with any mesh of joint C. Particularly for joint C, different localization modes were observed in the simulations and in the experiments. In the tests the strain localisation occurred in both the plate and the web (Matusiak 1999), while in the simulations it occurred only in the web. Naturally the simulation results were affected dramatically by these localization modes. To achieve more accurate predictions of the fracture location and the ultimate loads, specific studies of the actual components may needed concerning the material properties, the range of HAZ and the weld quality.

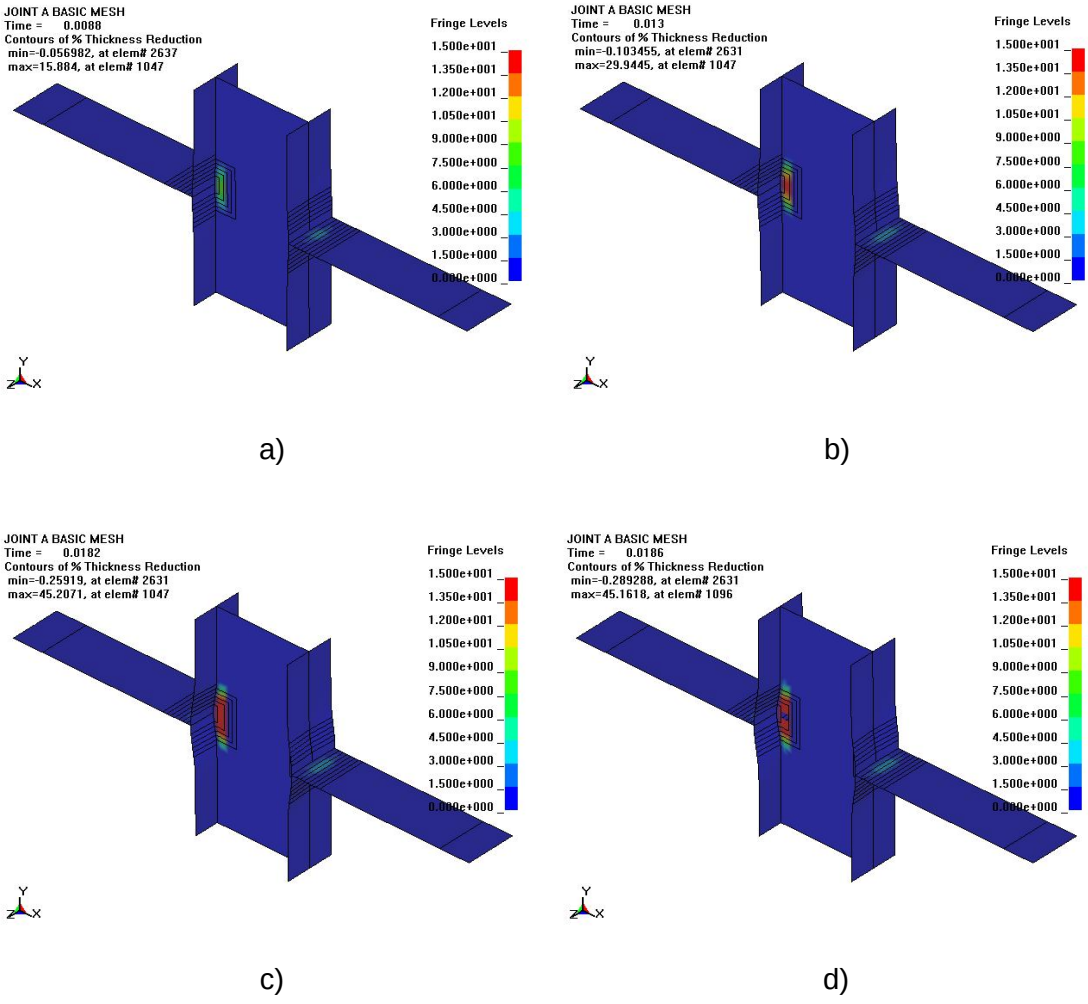

Figure 9.7. Typical evolution of thickness reduction with a basic mesh of joint A.

Table 9.8. Fracture location.

Joint type	Test	Simulation	
		Basic mesh	Refined mesh
A	Web	Web sub-HAZ 2	Web sub-HAZ 1
B	Plate	Plate sub -HAZ 1	Web sub -HAZ 1
C	Plate	Web sub -HAZ 2	Web sub -HAZ 1

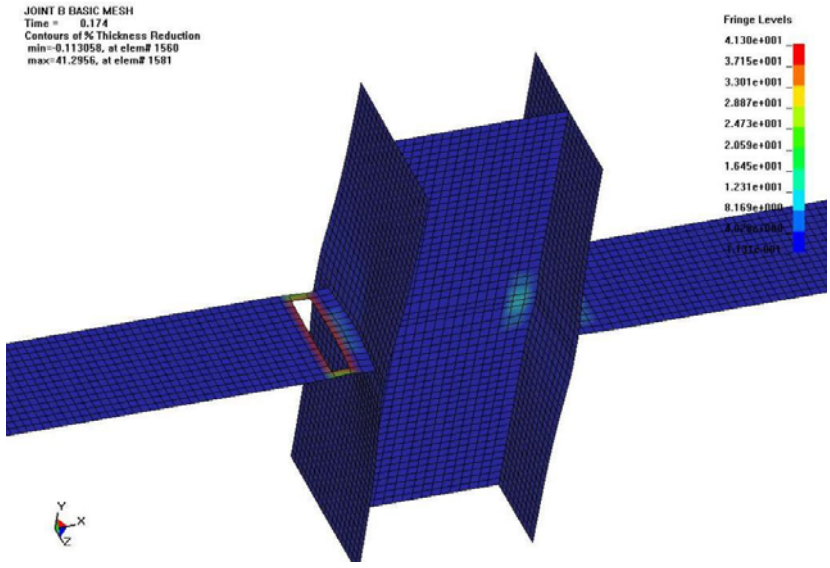

Figure 9.8. Fracture in plate with basic mesh of joint B.

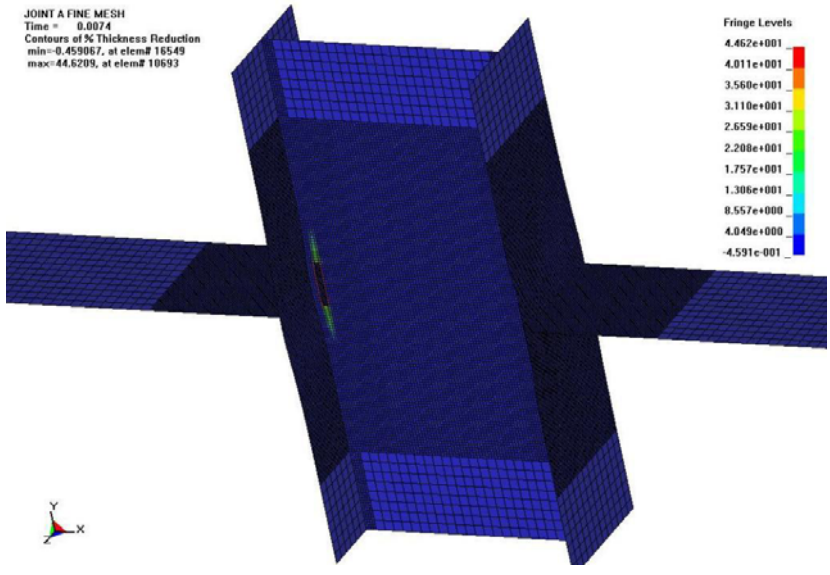

Figure 9.9. Fracture in web with refined mesh of joint A.

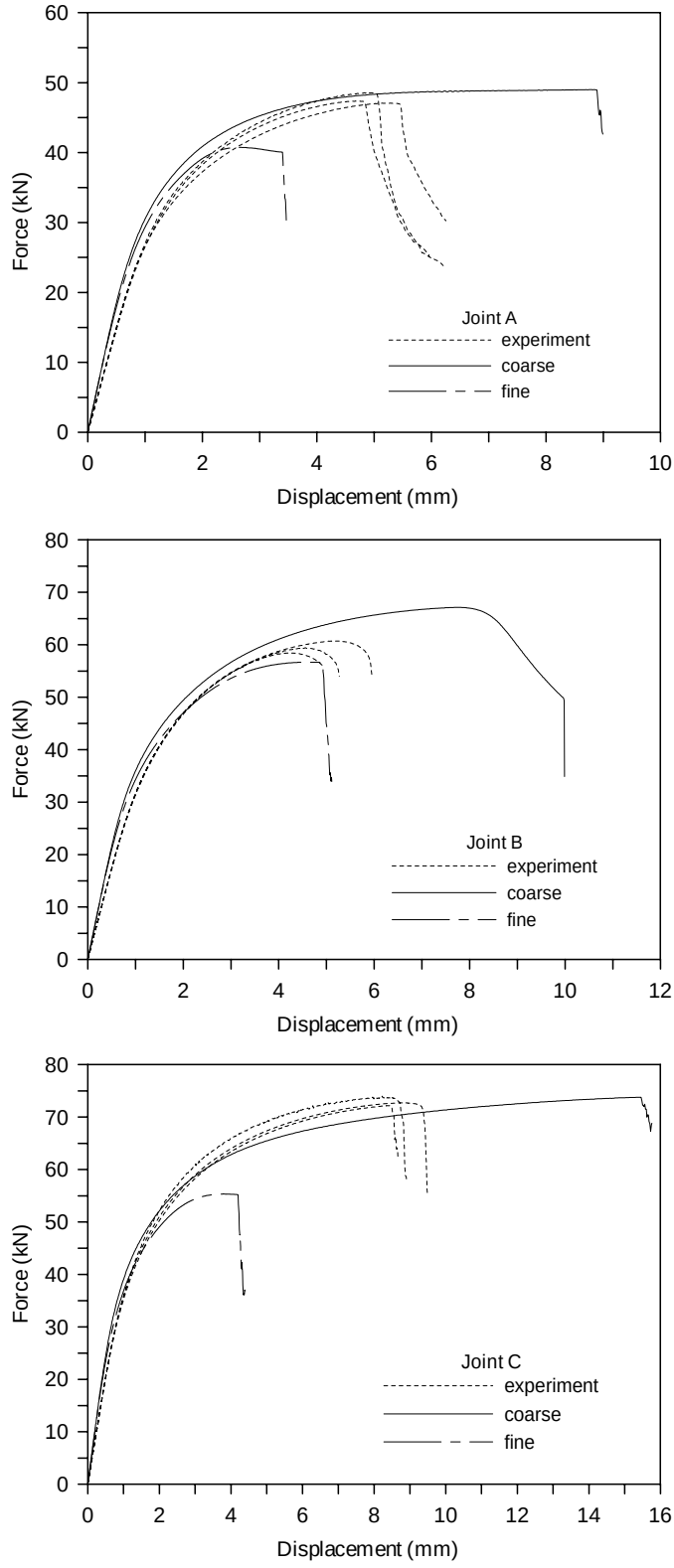

Figure 9.10. Experimental and numerical force vs. deformation curves for the joints

9.5.2 Parametric study

The response of the joints is governed by many factors, for instance the extent of the HAZ and the modelling of the thickness. It is therefore desirable to carry out a parametric study to investigate the influence of these factors on prediction. Based on the refined mesh of joint A, three additional analyses were performed where

- the thickness of the central part of the flange was increased;
- the HAZ in the web was ignored;
- the von Mises yield criterion was used instead of the Barlat and Lian yield criterion.

The resulting response curves are shown in Figure 9.11. It can be seen that the increase in the flange thickness caused a 5% increase in the ultimate load, while disregarding the HAZ and using the von Mises criterion resulted in a 10% increase. However, the predicted elongation and fracture location were not affected by these modifications in the model.

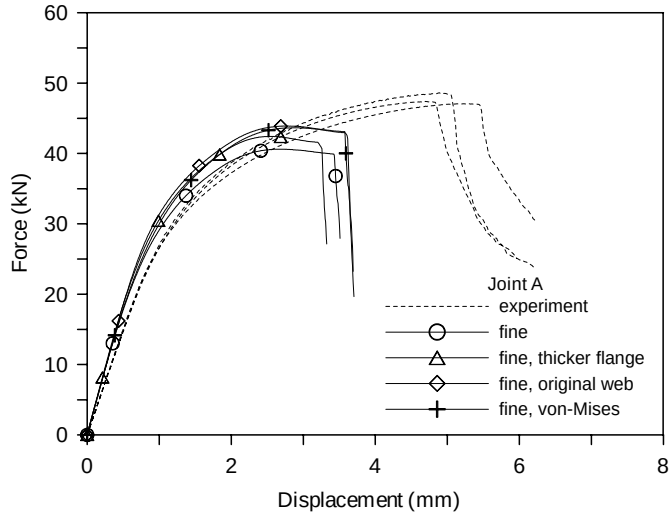

Figure 9.11. Force vs. deformation curves for parametric study.

9.6 Mesh convergence study

It is seen in the previous Section that the basic mesh predicted the structural performance better than the refined mesh except with respect to structural ductility. It is therefore uncertain whether a convergent result has been obtained by the refined mesh and even how it can be obtained. In this Section even finer meshes were used to model the joints in order to study the mesh effect.

Elements with characteristic length of 2 mm, 1 mm and 0.5 mm were used in the fine-meshed regions of the models. Instead of using the contact algorithm at the interface between dense and coarse meshed regions, all the elements were connected node to node as shown in Figure 9.12. This was done to avoid potential sliding energy which can violate the energy conservation. For the model with 2 mm elements the element size was almost uniform across the whole component, except in the central part of the flange and web, where slightly smaller elements were used in order to represent the thickness more precisely. For the models with 1.0 mm and 0.5 mm elements, larger elements were used in the regions where the deformations are less severe. Table 9.9 presents the solution time, total deformation and the CPU time of the simulations. All the simulations are valid in terms of energy ratio and kinetic energy, i.e., the energy ratio is close to unity and the kinetic energy is only a very small fraction of the internal energy. A shorter solution time was used for the 0.5 mm mesh to be CPU-optimised. The effect of solution time on prediction of the ultimate load and ductility was also studied, but no effect was observed as long as the simulations are valid.

The force vs. deformation curves are presented in Figure 9.13. It clearly shows that the predicted response is mesh-dependent and a convergent solution was not achieved. This is explained by the fact that strain tends to localize randomly with mesh refinement leading to results which can change significantly from mesh to mesh. Finer mesh was seen to represent the position of strain localisation very well, however not the evolution of the plastic thinning, this is also the case in the study of the fillet-welded connections in Chapter 7. When strain localisation is not represented well in the present welded specimens, interaction effects result in inaccurate predictions. With these discussions in mind, Chapter 11 is devoted to a potential remedy to regularise the situation so as to obtain mesh convergence.

In the previous Section, a contact algorithm was used between the dense and coarse meshed zones. Compared with the 1 mm model in the current Section, see Figure 9.14, it transpires that the two models give almost identical results, and thus shows that the use of contact algorithm also gives acceptable prediction.

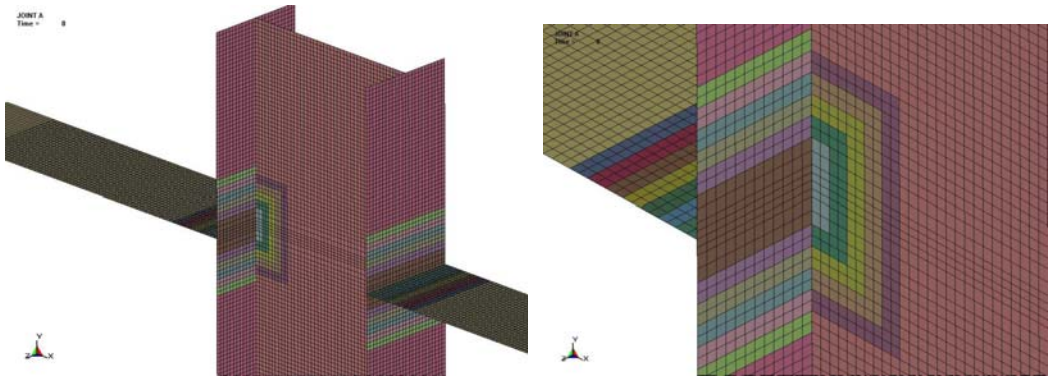

a)

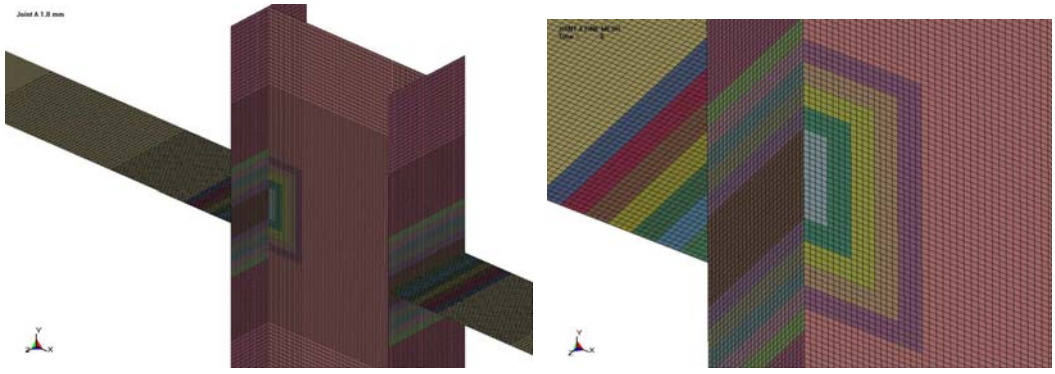

b)

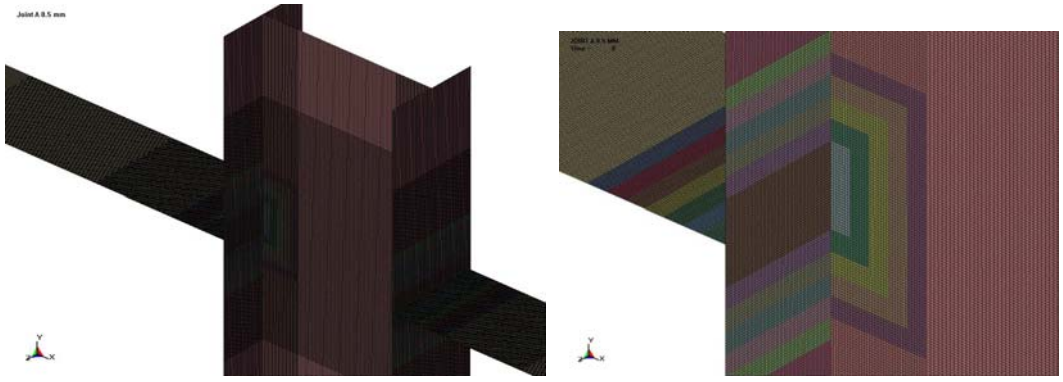

c)

Figure 9.12. Models with element size of a) 2 mm, b) 1 mm and c) 0.5 mm.

Table 9.9. Simulations with different element size.

Element size [mm]	Solution time [s]	Total deformation [mm]	CPU time [hour]
2	0.01	6	3
1	0.01	5	15
0.5	0.008	4	102

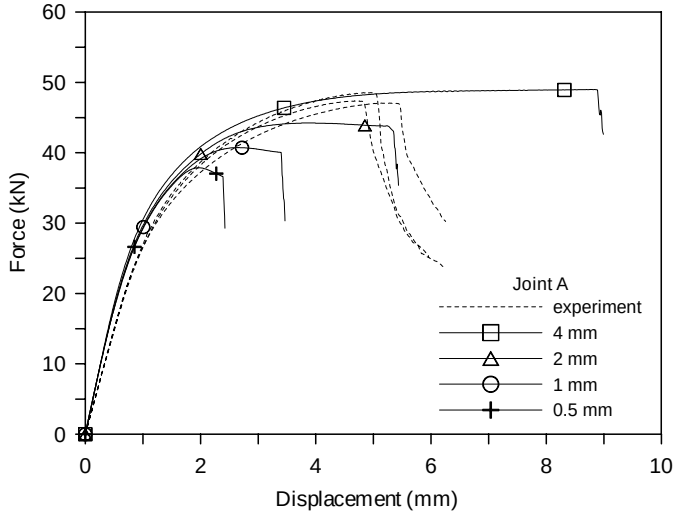

Figure 9.13. Force vs. deformation curves for various meshes.

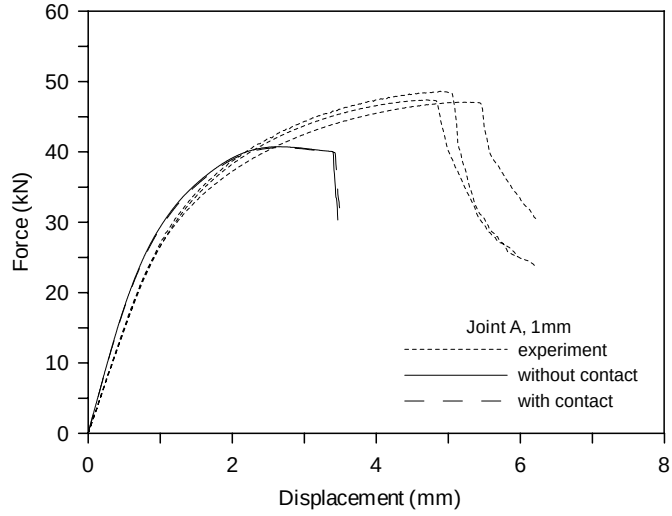

Figure 9.14. Force vs. deformation curves with and without contact algorithm. Element size is 1 mm.

9.7 Conclusions

Shell elements were used to discretize the welded beam-to-column joints. The material was modelled using the WTM-2D. In order to represent the geometry as accurately as possible, a non-constant thickness of the shell elements in various parts was used. Material properties of the weld, HAZ and base material in the plate and the I-profile were identified according to material tests and available experimental data. The established models with basic meshes were found to be able to represent the mechanical performance of the joints with reasonable accuracy, except that ductility was over-estimated. However, the models with refined meshes under-estimated the ultimate loads and elongations of the joints. Factors such as the range of the HAZ, thickness of the elements and the yield criterion were found to affect the predicted ultimate load with the refined models, but not the elongation.

The mesh sensitivity study indicates that the current problem is very mesh-dependent, and no convergent solution was obtained when reducing the element size. In Chapter 11, nonlocal plastic thinning is introduced as a remedy attempting to regularise the calculations and to obtain mesh convergent results.

The introduction of contact algorithm between dense and coarse meshed zones was found to have little effect on the prediction. This type of modelling can ensure regular (square) shape of the elements and for many cases it can simplify the pre-processing of the models.

10. Simulations of welded members subjected to bending

10.1 Introduction

In the earlier Chapters numerical analyses have been carried out for fillet-welded connections and beam-to-column joints subjected to tension. In this Chapter, structures with even more complex geometries under a different loading mode are studied numerically.

Previously Matusiak (1999) carried out a series of four-point bending tests with simple support beams containing welded details. The experimental data are used to further validate the established shell modelling methodology in predicting the structural performance of the welded thin-walled aluminium members. Explicit analyses were first performed with a basic mesh. Secondly implicit analyses were performed with both basic and refined meshes. Results from explicit and implicit solvers, basic and refined meshes, perfect and imperfect geometries are compared and discussed.

10.2 Review of the tests

The experiments described in this Section were previously carried out by Matusiak (1999). Four-point bending testes with simply supported beams were performed for an I-section containing a chosen set of welded details, see Figure 10.1 for the test set-up. Pictures of some of the components are shown in Figure B-1 of Appendix B. Except for the virgin material specimens, each of the I-section beams contains a chosen set of welded details. The weld details are a single butt weld in the tension or compression flange, a bracket welded to the tension or compression flange and welded stiffeners, as listed and indicated in Table 10.1. As shown in Figure 10.2, a 1000 mm span width and

a 400 mm distance between the two central point loads were used. The geometry of the virgin material specimen (4pb-1) is the same as the welded specimens except that it contains no weld in 4pb-1. The nominal dimensions of the cross section of the beam are given in Figure 10.3. The chemical composition of the alloy is the same as for the aluminium sheets in the previous Chapters, as listed in Table 5.1. The welds were made using MIG pulsed arc with filler alloy 5183 by a commercial fabricator, Marine Aluminium AS. Butt welds with a groove angle of 60° were made with one pass on each side, and fillet welds were made in a single pass. All the welded specimens were left to age naturally for more than 8 weeks before testing.

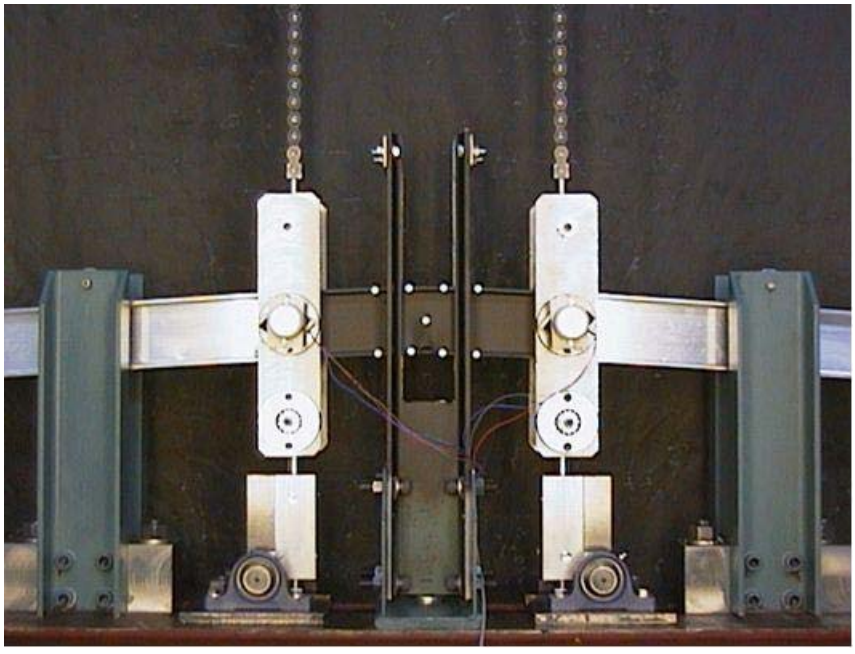

Figure 10.1 Test set-up (Matusiak 1999).

Table 10.1 Weld details of the specimens.

Specimen	Weld detail
4pb-1	Virgin material (no weld)
4pb-2	Butt weld in tension flange
4pb-3	Butt weld in compression flange
4pb-4	Bracket welded to tension flange
4pb-5	Bracket welded to compression flange
4pb-6	Welded stiffeners

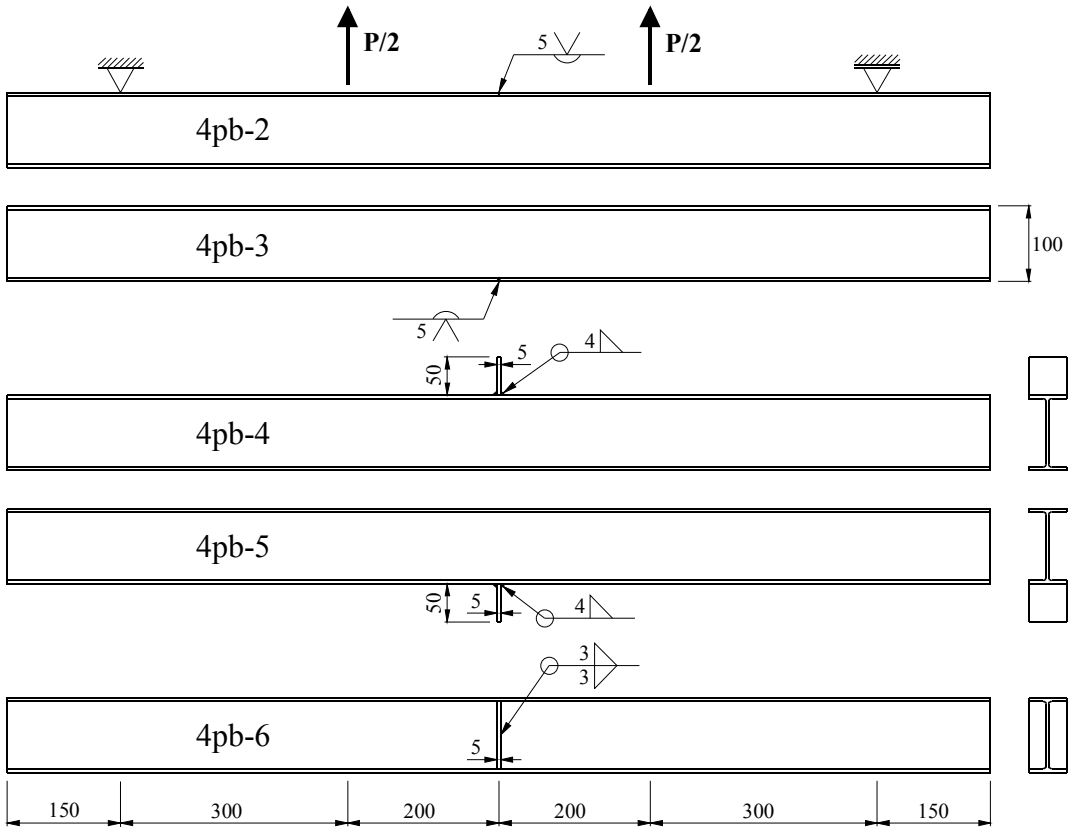

Figure 10.2. Geometry of the welded members (Matusiak 1999).

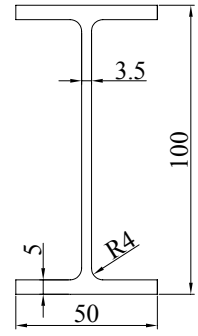

Figure 10.3. Geometry of the cross section.

The test rig is a standard vertical loading frame consisting of two supporting columns, a transverse beam and a hydraulic actuator. At the support points the vertical upward displacement and lateral movement, i.e. out-of-plane displacement and rotation

about the longitudinal axis, were prevented using roller bearings. The support and loading for the tests are depicted in Figure B-2.

For all tests optical targets in the centre of the web were used for measuring the vertical displacement by a video extensometer. Four targets were attached on both of the tension and compression flange at distances of 25 mm and 75 mm from the symmetry axis. For additional details of the test set-up and instrumentation it is referred to Matusiak's thesis (1999).

10.3 Identification of material parameters

The hardening parameters were identified using a similar method as for the joints in Chapter 9, by shifting the hardening data in the butt weld vicinity according to the tension properties of the base material characterised in Section 6.2. Table 10.2 provides the mechanical properties of the web and the flange of the I-beam, and consequently the factor of $f_{u,\,mem}/f_{u,\,butt}$. To obtain the hardening parameters for the current welded beam, the parameters Y_0, Q_1 and Q_2 in Table 6.1 were multiplied by the factor of $f_{\mathrm{u,\,mem}}/f_{\mathrm{u,\,butt}}$ in Table 10.2, and the resulting parameters for the flange and web are listed in Table 10.3 and Table 10.4, respectively. Recall that there are uncertainties related to the chosen procedure for parameter identification.

10.4 Explicit simulations

10.4.1 Finite element models

Explicit simulations were performed for all the six cases. The specimens were discretized using Belytschko-Tsay shell elements with a characteristic element size of 4×4 mm^2 for the central 400 mm (basic mesh). The general view of the model is presented in Figure 10.4. The roller bearings (constraints) were modelled as rigid bodies using solid elements. The beams were modelled using the WTM-2D adopting the yield surface parameters obtained by the power method in Section 6.3 (see Table 6.4). Model details of the weld and the HAZ are shown in Figure 10.5. In particular Figure 10.5a shows the FE model of the members with a butt weld in the compression flange (4pb-3). The length of the weld is 8 mm while it is 4 mm for each of the six sub-HAZs. The members with a butt weld in the tension flange (4pb-2) were modelled in the same way, except that the weld and the HAZ are at the upper flange. Figure 10.5b shows the FE

model of the members with a bracket welded to the tension flange (4pb-4). The bracket consists of weld (8 mm), six sub-HAZs (4 mm each) and the base material. The welded flanges consist of a 8 mm sub-HAZ in the centre, five 4 mm sub-HAZs and the base material on each side of the center line. The members with the bracket welded to the compression flange (4pb-5) were modelled in the same way, except that the weld and the HAZ are at the lower flange. The FE model of the members with welded stiffeners (4pb-6) is shown in Figure 10.5c. Weld materials was used only in the stiffener, and the HAZ was included in the flange, web and stiffeners.

Table 10.2. Average values of parameters of the base material in I-100 beam (Matusiak 1999).

Component	Direction	$f_{0.2}$ [N/mm^2]	f_u [N/mm^2]	$f_u / f_{0.2}$ [-]	ε_u [-]	$f_{u,mem} / f_{u,butt}$ ($\|\|$)
Beam, I-100, web	$\|\|$	279.2	289.3	1.04	0.066	0.89
Beam, I-100, flange	$\|\|$	277.6	290.4	1.05	0.065	0.88

Table 10.3. Assumed work hardening parameters for the flange of the I-100 beam.

Zone	Y_0 [N/mm^2]	Q_1 [N/mm^2]	C_1 [-]	Q_2 [N/mm^2]	C_2 [-]	$Y_0+\Sigma Q$ [N/mm^2]
Weld	105	42	656	189	13	336
HAZ 1	104	33	616	138	18	275
HAZ 2	87	41	669	115	22	244
HAZ 3	145	45	1091	65	33	255
HAZ 4	172	74	2811	53	30	299
HAZ 5	191	77	6095	54	19	322
HAZ 6	180	88	2780	50	24	319
Base	206.8	63	3196	46	29	316

Table 10.4. Assumed work hardening parameters for the web of the I-100 beam.

Zone	Y_0 [N/mm^2]	Q_1 [N/mm^2]	C_1 [-]	Q_2 [N/mm^2]	C_2 [-]	$Y_0+\Sigma Q$ [N/mm^2]
Weld	105	42	656	189	13	336
HAZ 1	105	34	616	140	18	279
HAZ 2	88	42	669	117	22	247
HAZ 3	147	45	1091	66	33	258
HAZ 4	174	75	2811	53	30	303
HAZ 5	193	78	6095	54	19	326
HAZ 6	182	89	2780	51	24	322
Base	209	64	3196	46	29	320

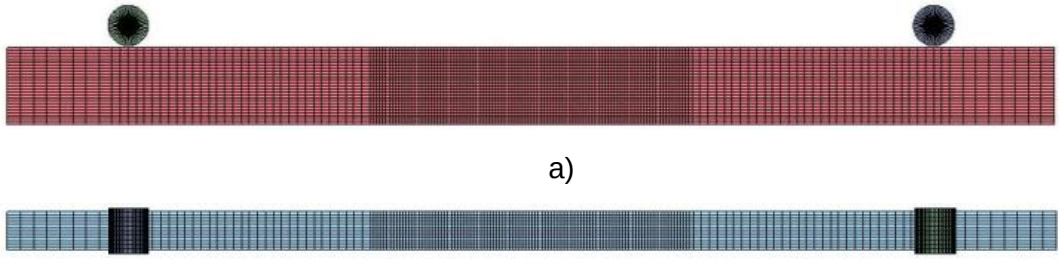

a)

b)

Figure 10.4. General view of the FE model of the I-beam: a) side view, and b) top view.

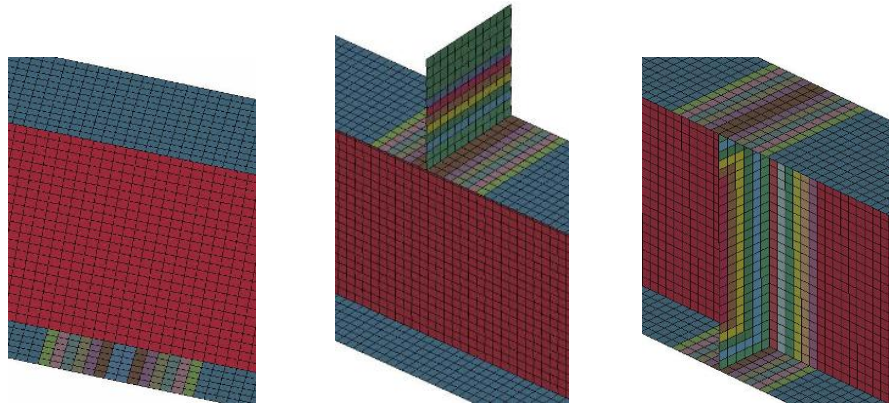

a) b) c)

Figure 10.5. Details of the FE mesh of the I-beam with a) butt weld in compression flange (4pb-3), b) bracket welded to the tension flange (4pb-4) and c) welded stiffener (4pb-6).

As Figure 10.6 illustrates, boundary constraints were applied to selected parts of one side of the flanges to represent the experimental condition. Loading was applied through Equation (6.25) to the vertically middle rows of the nodes in the stiffeners as shown in Figure 10.7. The duration time was chosen as $T = 5$ ms, and the total deformation is $d_{\max} = 50$ mm. The critical thickness strain for fracture was set as $\varepsilon_{cr} = -0.6$.

To study the influence of geometrical imperfections on the accuracy and instability, simulations were also performed with an imperfect geometry and compared with the simulations with idealised, perfect geometry. The initial imperfections were introduced to the central 400 mm of the compression flanges points through the equation

$$w(x, y) = w_0 \sin\left(\frac{2\pi x}{l}\right)\sin\left(\frac{\pi y}{b}\right) \tag{10.1}$$

where the amplitude of the imperfection was chose as $w_0 = 0.1$ mm. Two half-sine waves were included along the mid-span l, while one is included along the width of the flange. Figure 10.8 illustrates the imperfection with amplitude of 5 mm which is 50 times the actual one in analysis.

10.4.2 Results

Figure 10.9 depicts the deformations obtained with the perfect geometry at a late stage of the solution time. The legend indicates the thickness reduction (%). In similar way the deformations obtained with the imperfect geometry are shown in Figure 10.10. In the analyses with imperfection, local buckling occurred earlier than in the analyses with a perfect geometry for the components 4pb-1, 4pb-3 and 4pb-5, i.e., the ones that did

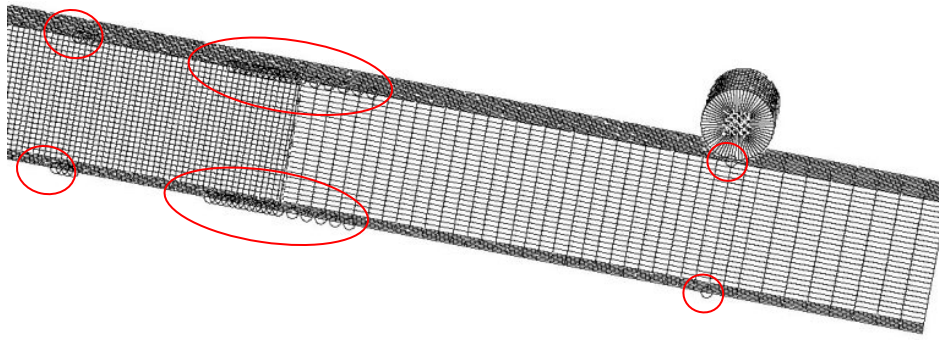

Figure 10.6. Lateral constraints on selected parts of one side of the flange.

not fracture in the tests. For these no-fracture tests, more tension was generated in the upper flange as shown in the figures. Especially for 4pb-1, two local buckles were observed in the compression flange with perfect geometry, while only one for the imperfect geometry. For the components with fracture, the fracture was seen to occur first in the welded flange, then in the web. The fracture mode is the same as observed in the experiments, details of the tests are however not available.

Experimental and numerically predicted force vs. deformations curves are shown in Figure 10.11. Generally, very good agreement was obtained between the analyses and experiments. Again the figures indicate that earlier local buckling occurred with a imperfect geometry for the components without fracture. The analyses with a perfect geometry provided response curves closer to the experiments. For the components with fracture (weld in tension flange), no significant difference is found between the analyses with and without imperfection.

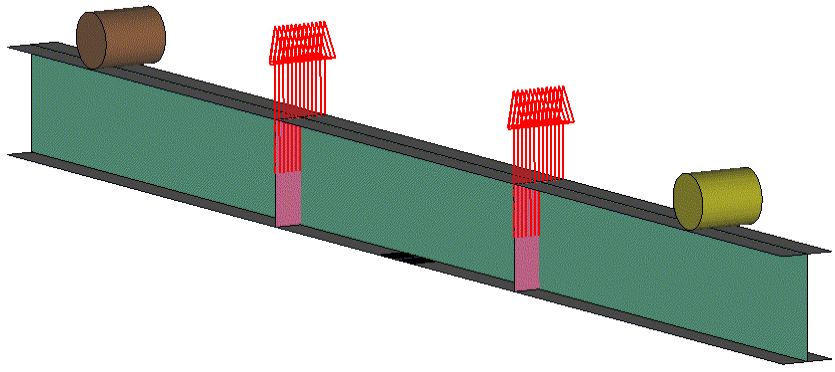

Figure 10.7. Loading applied to the vertically middle rows of the nodes in the stiffeners.

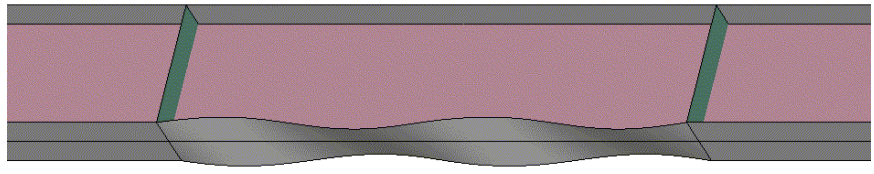

Figure 10.8 imperfection in the compression flange with an amplitude 50 times the actual one in the analyses.

The analyses with 4×4 mm^2 elements appear robust and efficient, with CPU time requirement of about 1 to 2 hours. Explicit analyses with 2×2 mm^2 elements were next performed to investigate the mesh effect. However, the explicit simulations with LS-DYNA were not numerically stable regardless of the use of a very small time step. The reason for the numerical instability is unclear, and is beyond the scope of the present study to resolve the problem. Analyses using another material model (*MAT_ANISOTROPIC_VISCOPLASTIC) were performed and found numerically stable. Implicit simulations were therefore carried out to study the mesh effect instead.

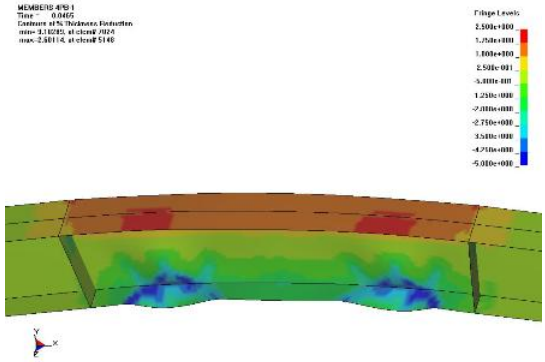

Unwelded (4pb-1)

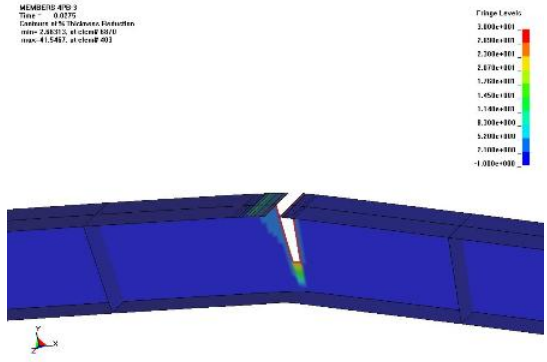

Butt weld in tension flange (4pb-2)

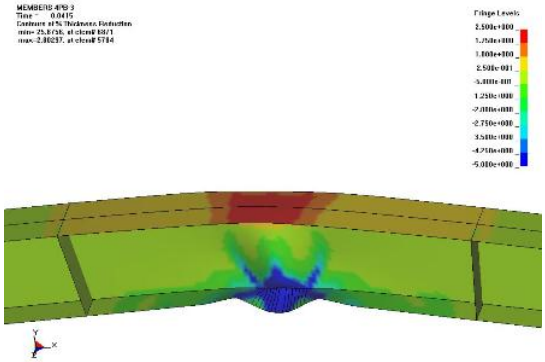

Butt weld in compression flange (4pb-3)

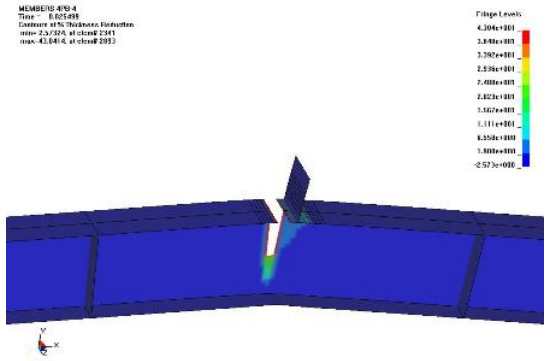

Bracket welded to tension flange (4pb-4)

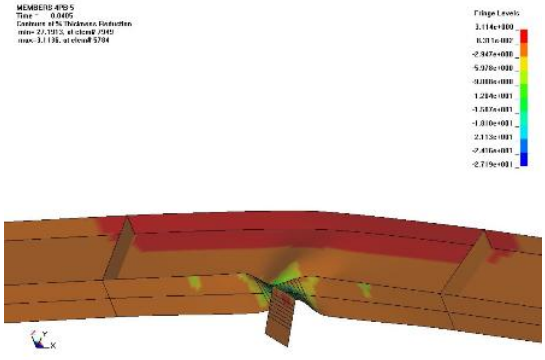

Bracket welded to compression flange (4pb-5)

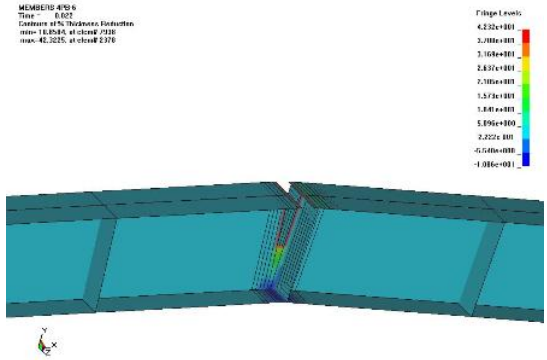

Welded stiffener (4pb-6)

Figure 10.9. Thickness reduction in *explicit* simulations *without imperfection*. Element size is 4×4 mm^2.

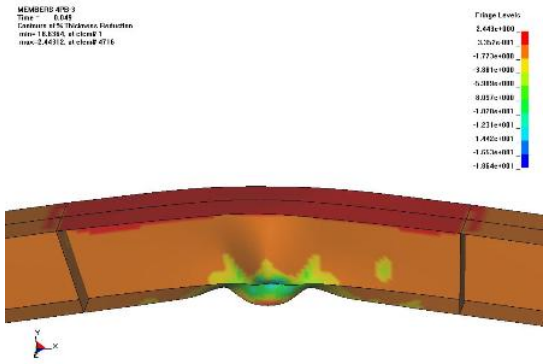

Unwelded (4pb-1)

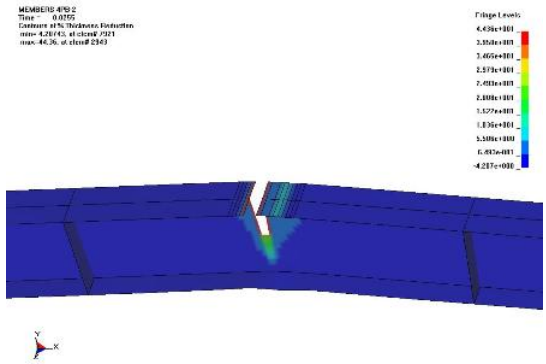

Butt weld in tension flange (4pb-2)

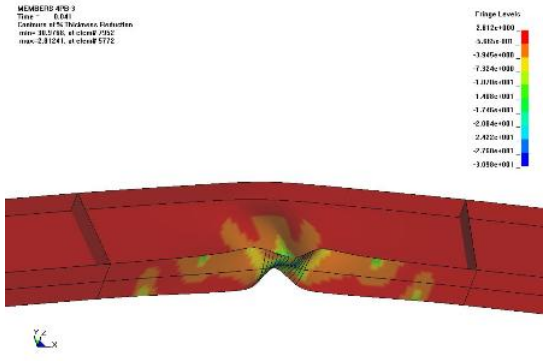

Butt weld in compression flange (4pb-3)

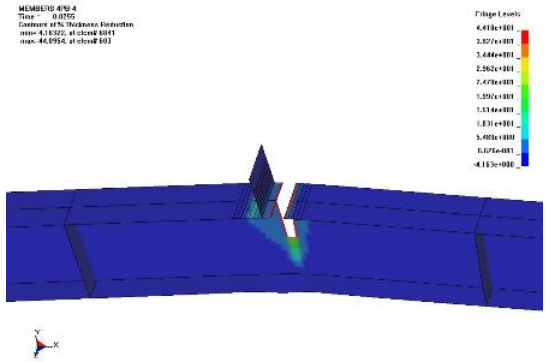

Bracket welded to tension flange (4pb-4)

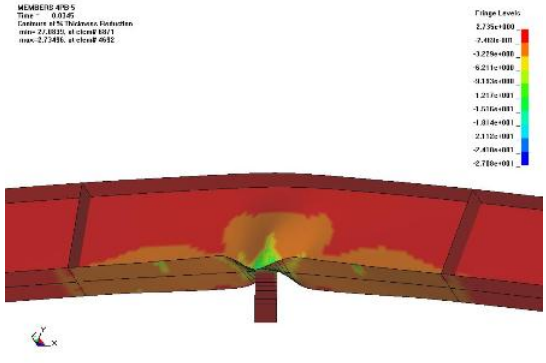

Bracket welded to compression flange (4pb-5)

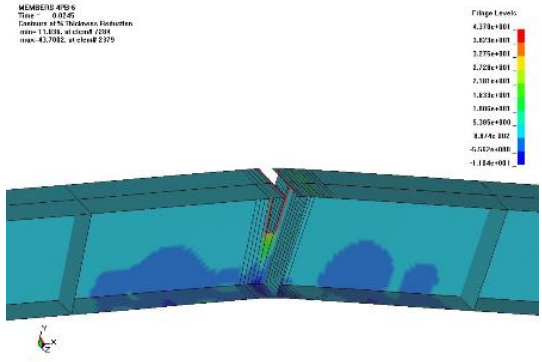

Welded stiffener (4pb-6)

Figure 10.10. Thickness reduction in *explicit* simulations *with imperfection*. Element size is 4×4 mm^2.

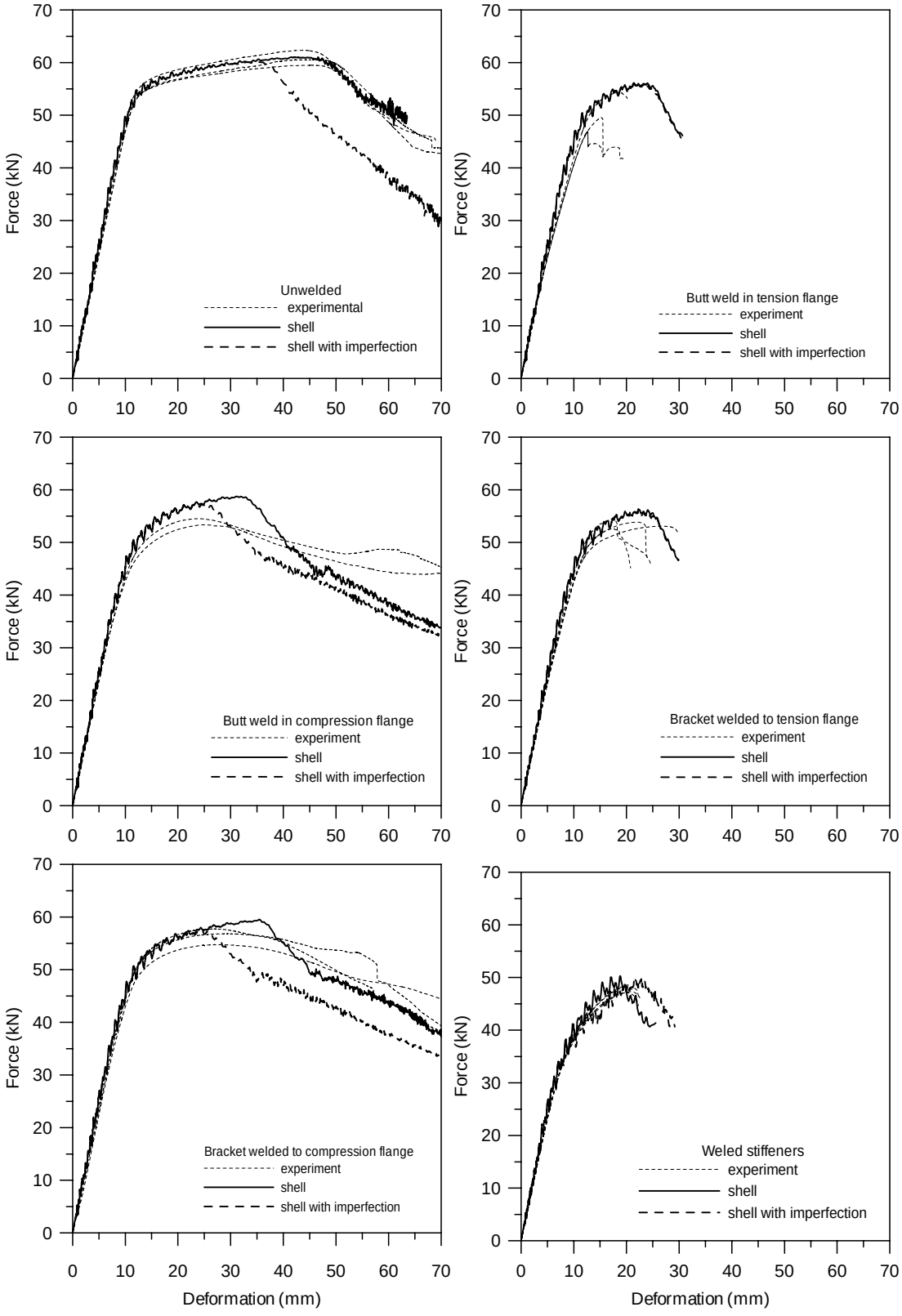

Figure 10.11. Experimental and *explicit* simulation results. Element size is 4×4 mm^2.

10.5 Implicit simulations

Implicit analyses were performed using the implicit solver of LS-DYNA both for the models with basic and refined mesh. For both models, perfect and imperfect geometries were also studied. In the implicit simulations, fracture was not accounted for, and thus the numerical results for tests experiencing fracture in the HAZ are reliable only up to the point at which fracture initiated in the tests.

For the analyses with basic mesh, the deformations obtained with perfect and imperfect geometries are presented in Figure 10.11 and Figure 10.12, respectively. Similar to the explicit analyses, local buckling occurred earlier when the geometric imperfection was introduced for the components that did not experience fracture. Further, compared with the explicit simulations, the implicit analyses predicted the local buckling to occur later and the tension flanges deformed more severely. Especially for 4pb-1 (unwelded component) which has homogeneous material properties in web and flange, local buckling was hardly observed for the analysis with perfect geometry. Figure 10.14 presents the load vs. deformation curves of the basic mesh analyses, showing very good agreement between the experimental and numerical results. Unlike the explicit analyses, the imperfect geometry provided a better prediction of experimentally observed characteristics. For the tests in which fracture occurred (i.e. 4pb-2, 4pb-4 and 4pb-6), the implicit analyses have problems to reach convergent solutions after the moment when fracture occurs in tests.

For the analyses with refined mesh, the deformations obtained with perfect and imperfect geometries are presented in Figure 10.15 and Figure 10.16, respectively. Load vs. deformation curves are presented in Figure 10.17. Both the deformations and the response curves are similar to those of the analyses with the basic mesh. The implicit analyses with the basic mesh took about 1 to 4 hours. The CPU time for the implicit analyses with the refined mesh varies from 4 to 70 hours.

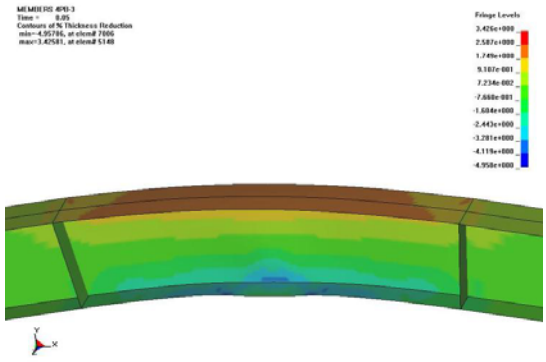

Unwelded (4pb-1)

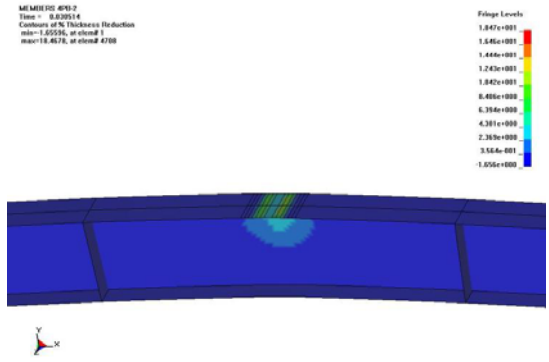

Butt weld in tension flange (4pb-2)

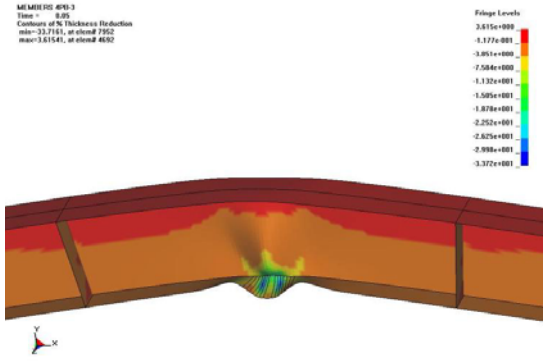

Butt weld in compression flange (4pb-3)

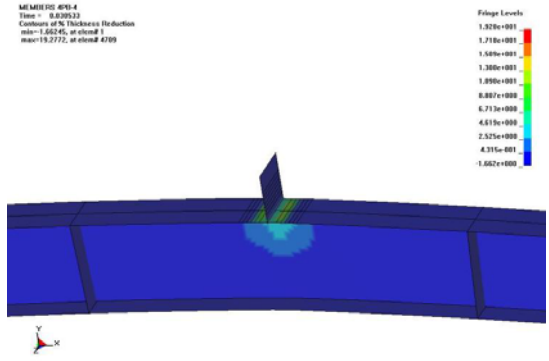

Bracket welded to tension flange (4pb-4)

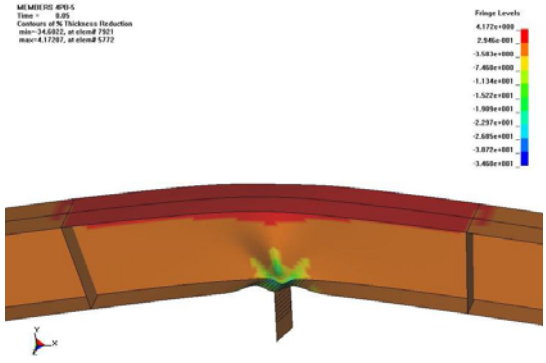

Bracket welded to compression flange (4pb-5)

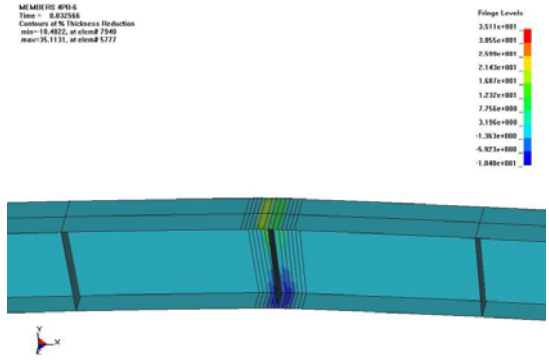

Welded stiffener (4pb-6)

Figure 10.12. Thickness reduction in *implicit* simulations *without imperfection*. Element size is 4×4 mm^2.

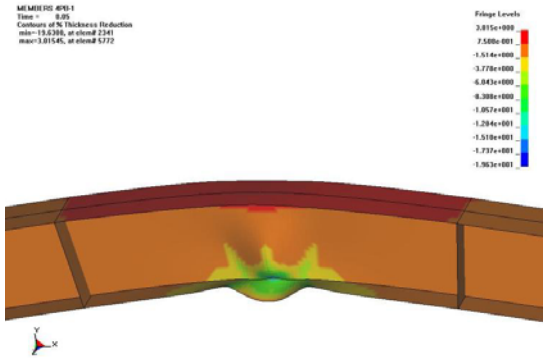

Unwelded (4pb-1)

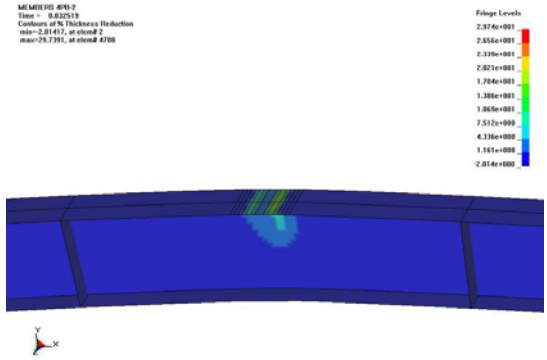

Butt weld in tension flange (4pb-2)

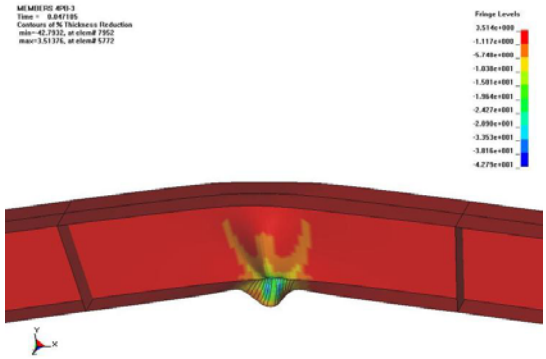

Butt weld in compression flange (4pb-3)

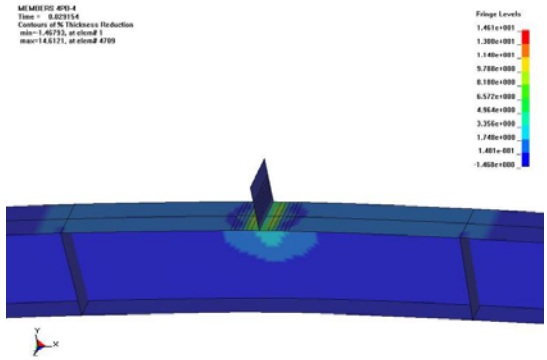

Bracket welded to tension flange (4pb-4)

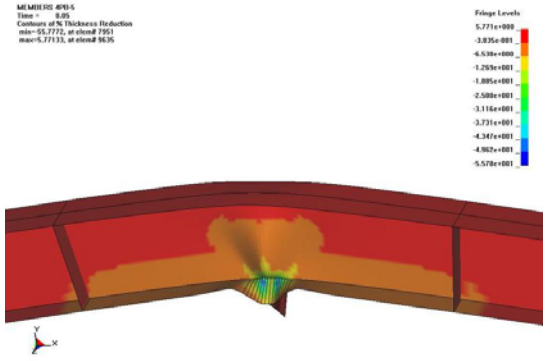

Bracket welded to compression flange (4pb-5)

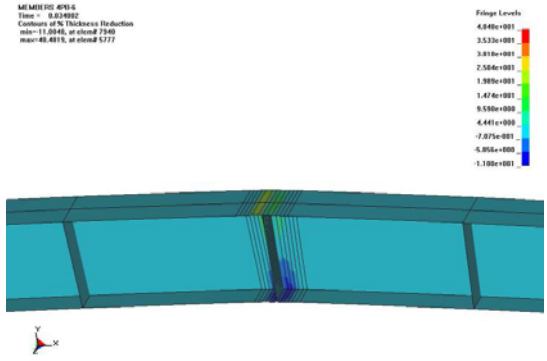

Welded stiffener (4pb-6)

Figure 10.13. Thickness reduction in *implicit* simulations *with imperfection*. Element size is 4×4 mm^2.

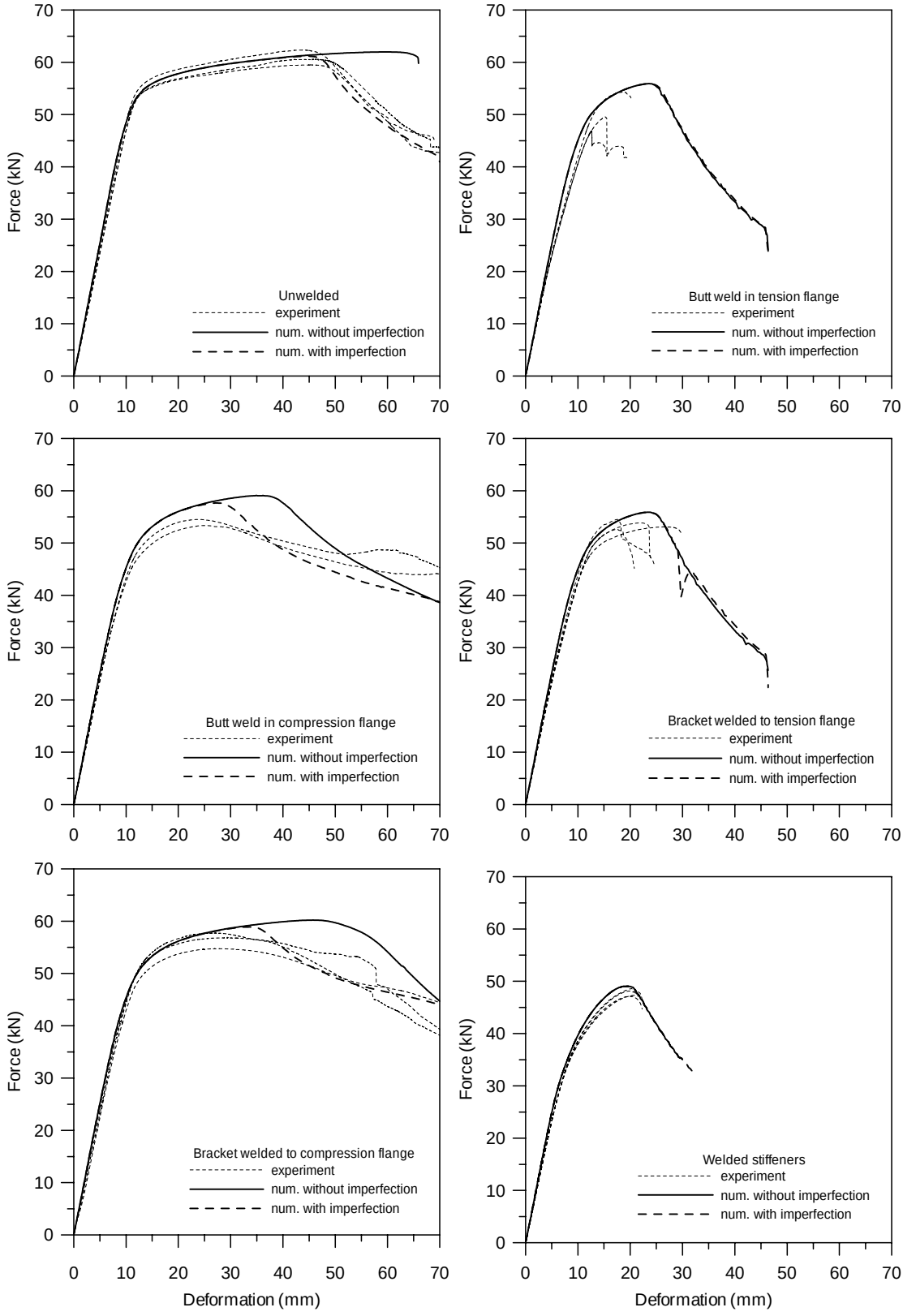

Figure 10.14. Experimental and *implicit* simulation results. Element size is 4×4 mm^2.

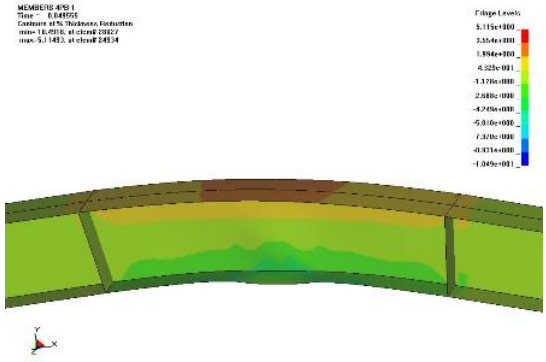

Unwelded (4pb-1)

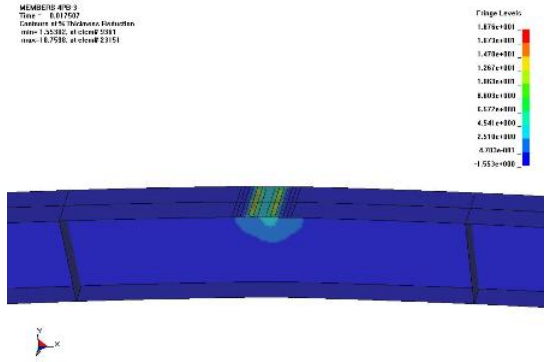

Butt weld in tension flange (4pb-2)

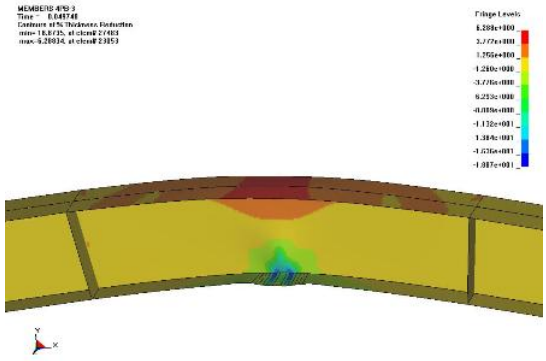

Butt weld in compression flange (4pb-3)

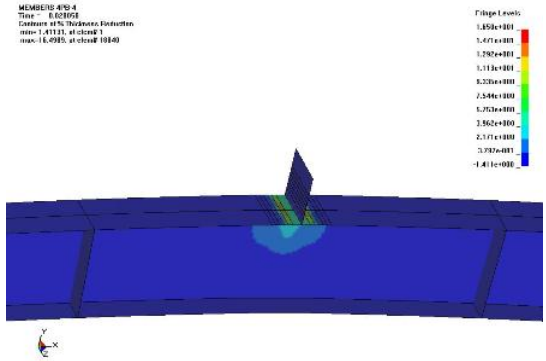

Bracket welded to tension flange (4pb-4)

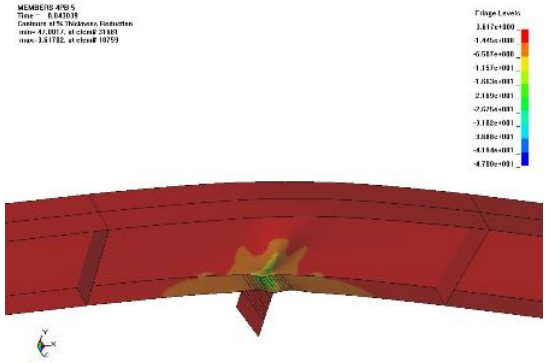

Bracket welded to compression flange (4pb-5)

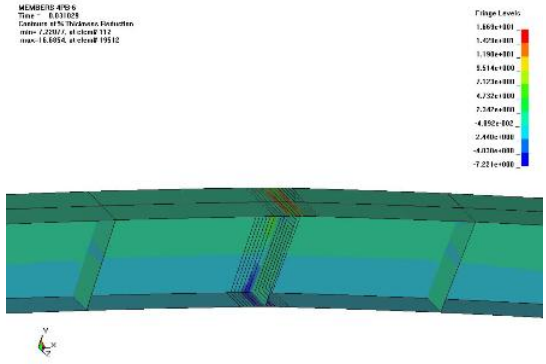

Welded stiffener (4pb-6)

Figure 10.15. Thickness reduction in *implicit* simulations *without imperfection*. Element size is 2×2 mm^2.

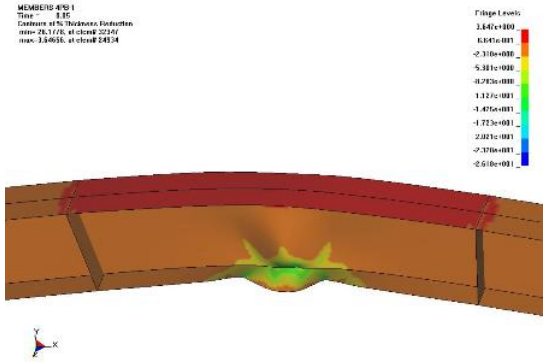

Unwelded (4pb-1)

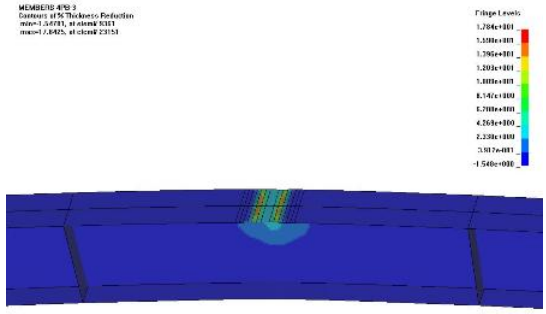

Butt weld in tension flange (4pb-2)

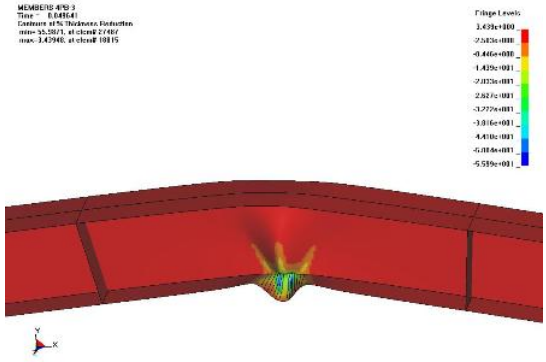

Butt weld in compression flange (4pb-3)

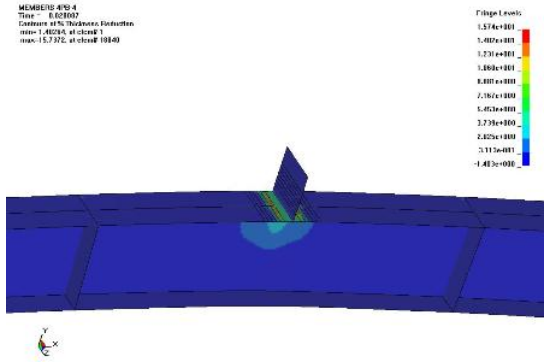

Bracket welded to tension flange (4pb-4)

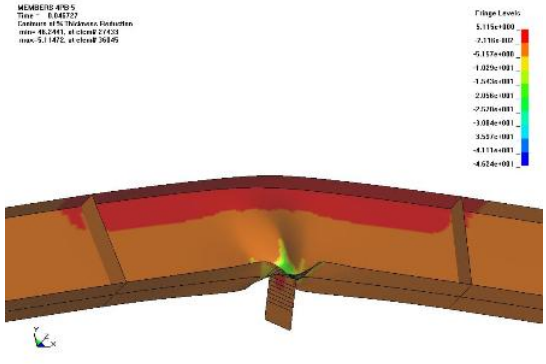

Bracket welded to compression flange (4pb-5)

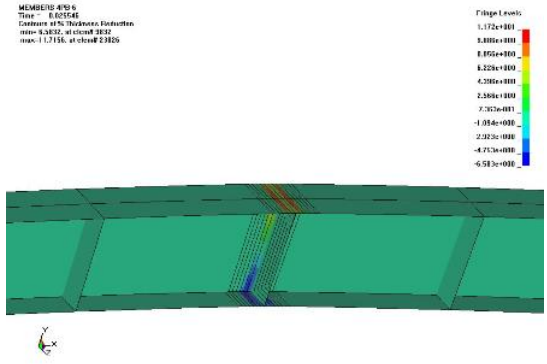

Welded stiffener (4pb-6)

Figure 10.16. Thickness reduction in *implicit* simulations *with imperfection*. Element size is 2×2 mm^2.

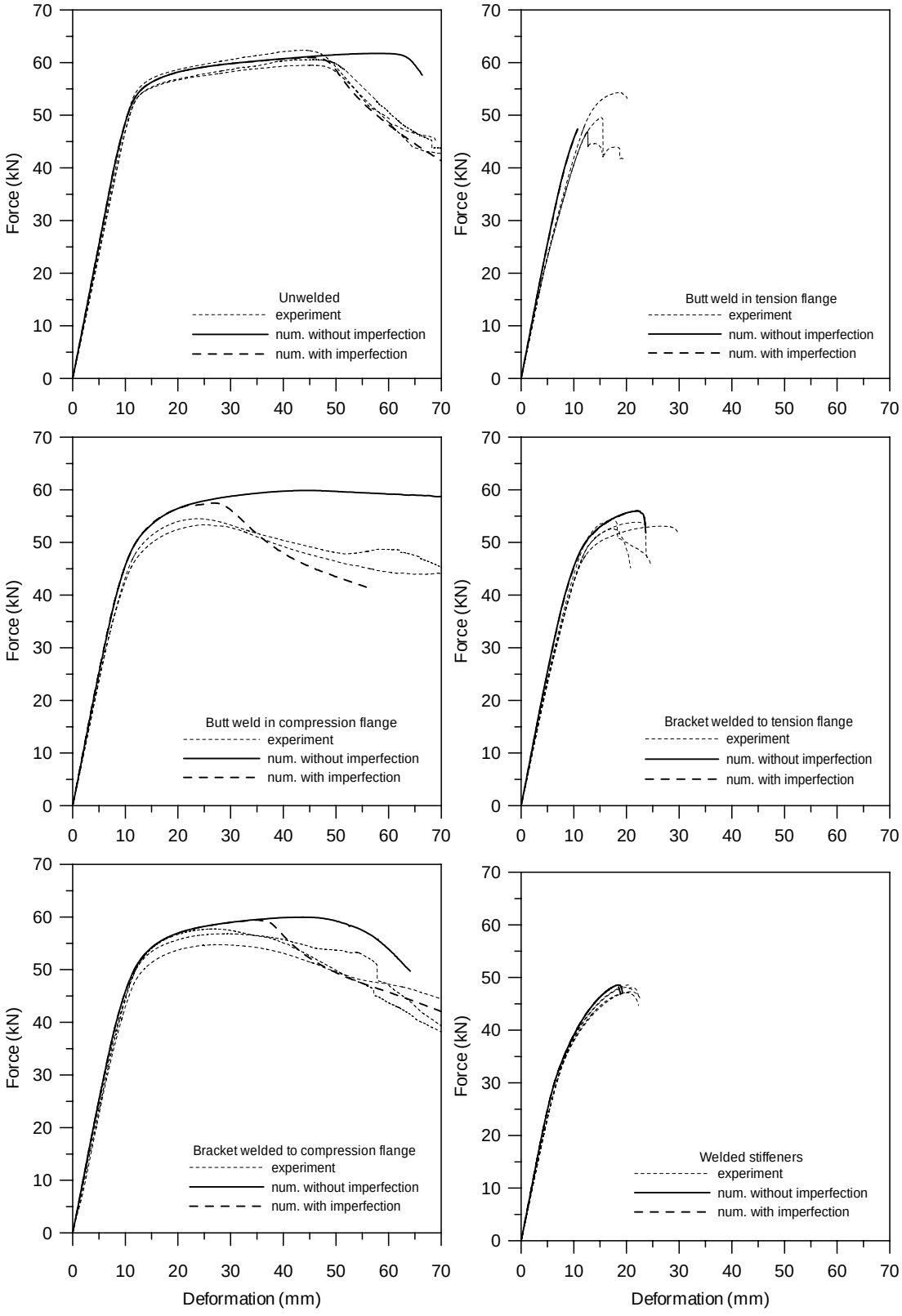

Figure 10.17. Experimental and *implicit* simulation results. Element size is 2×2 mm^2.

10.6 Conclusions

Numerical analyses were carried out by various methods to represent the mechanical performance of the welded and un-welded I-sections under four-point bending. The study is summarised and concluded as follows.

Using explicit and implicit solvers, the predicted force vs. deformation curves are in good agreement with the experimental results for all six cases of the members.

For both the explicit and the implicit analyses, simulations with element size of 4×4 mm^2 appear to be accurate, robust and efficient in predicting the mechanical response of the members. With the WTM-2D, the explicit analyses with the refined mesh were unsuccessful. Using the implicit solver, no significant difference was found between the analyses by coarse and refined meshes. It can therefore be concluded that a relatively coarse mesh (element size approximate to thickness) is sufficient for predicting the mechanical performance of this type of welded and unwelded structures.

Inhomogeneous material property and geometric imperfection were seen to cause local buckling to occur earlier. It can be concluded that for explicit analyses, geometric imperfections were not necessary for reasonable predictions for the current cases. Meanwhile for implicit analyses when the numerical accuracy needs to be high, geometric imperfection or material inhomogenity are essential for the predictions to be correct, since imperfection does exist in the actual components.

11. Nonlocal plastic thinning

11.1 Introduction

In Chapter 7 and 9 the numerical predictions appeared mesh-dependent due to the nature of the shell formulation. As discussed by Lademo et al. (2005): “In reality plastic thinning develops gradually in a non-local sense due to the development of stabilizing through-thickness stress components that are not represented in the shell element formulation. A shell element that experiences thinning is only confined to the neighbouring shell elements with in-plane compatibility and the respective in-plane stress components. It experiences no support by the neighbour elements when it comes to through-thickness deformations as it would have done if solid elements were used.” In Chapter 7, the refined mesh led to over-localised deformation in certain sub-HAZ and under-estimated the ductility of the fillet-welded connections. In Chapter 9, the models with 1 mm elements failed to represent the strength and ductility of the welded beam-to-column joints.

In this Chapter, a nonlocal approach to calculate plastic thinning is introduced to amend the overly localised deformation in the HAZ when relatively refined mesh is used. The aim is to establish a nonlocal modelling method capable of representing the mechanical performance of the welded thin-walled aluminium structures regardless of the element size. The studied components are the fillet-welded connections and the welded beam-to-column joints described previously.

11.2 Nonlocal equations

The nonlocal approach was originally proposed by Bazant and Pijaudier-Gabot (1988) in order to solve the mesh-dependence problem in softening materials, e.g., when using coupled damage theories. In nonlocal failure theories the failure criterion depends on the material within a radius of influence which surrounds the integration point. With a nonlocal criterion, the mesh sensitivity on failure is greatly reduced leading to results that converge to a unique solution as the mesh is refined.

In LS-DYNA (LSTC 2003) a non-local treatment of history variables is defined by the keyword *MAT_NONLOCAL. This option can be used with two and three-dimensional solid elements, and three-dimensional shell elements. The implementation is available for under-integrated elements, which have one integration point at their centre. In applying the nonlocal equations to shell elements, integration points lying in the same plane within the radius determined by the characteristic length are considered. As illustrated in Figure 11.1, the nonlocal domain Ω_r is the neighbourhood within radius L of element e_r, while e_i (i=1, 2, …, N_r) are the elements included in Ω_r. Shell elements are assumed to have multiple integration points through their thickness. The implemented equations are (LSTC 2003):

$$\dot{f}_r = \dot{f}(x_r) = \frac{1}{W_r}\int_{\Omega_r} \dot{f}_{local}\, w(x_r - y)dy \approx \frac{1}{W_r}\sum_{i=1}^{N_r} \dot{f}^{\,i}_{local}\, w_{ri} V_i \tag{11.1}$$

where

$$W_r = W(x_r) = \int w(x_r - y)dy \approx \sum_{i=1}^{N_r} w_{ri} V_i \tag{11.2}$$

$$w_{ri} = w(x_r - y_i) = \frac{1}{\left[1 + \left(\frac{\|x_r - y_i\|}{L}\right)^p\right]^q} \tag{11.3}$$

Here $\dot{f}_r$ and x_r are respectively the nonlocal rate of increase of damage parameter in softening material and the center of the element e_r, and $\dot{f}^{\,i}_{total}$, V_i and y_i are respectively

the local rate of increase of damage, the volume and the coordinate of the centre of element e_i. The parameters p and q determine the weight of the elements as a function of the distance between e_r and e_i.

The present study adopts the nonlocal plastic thinning concept, which was first introduced by Lademo et al. (2005). In this approach, the plastic thickness strain ratio $\dot{\varepsilon}_t^p$ is the variable subjected to the nonlocal equation. Any other variables in the constitutive relations remain unchanged. The parameters p and q were chosen as $p = q = 0$, so that equal weight was given to the integration points within the nonlocal domain. The nonlocal equation is thus given as

$$\dot{\varepsilon}_t^p(r) = \frac{1}{W_r} \int_{\Omega_r} \dot{\varepsilon}_{t,local}^p dy \approx \frac{1}{W_r} \sum_{i=1}^{N_r} V_i \dot{\varepsilon}_{t,local}^p \tag{11.4}$$

where

$$W_r = \int_{\Omega_r} dy \approx \sum_{i=1}^{N_r} V_i \tag{11.5}$$

When elements within Ω_r have the same size, the equation takes the form

$$\dot{\varepsilon}_t^p(r) = \frac{1}{N_r} \sum_{i=1}^{N_r} \dot{\varepsilon}_{t,local}^p(i) \tag{11.6}$$

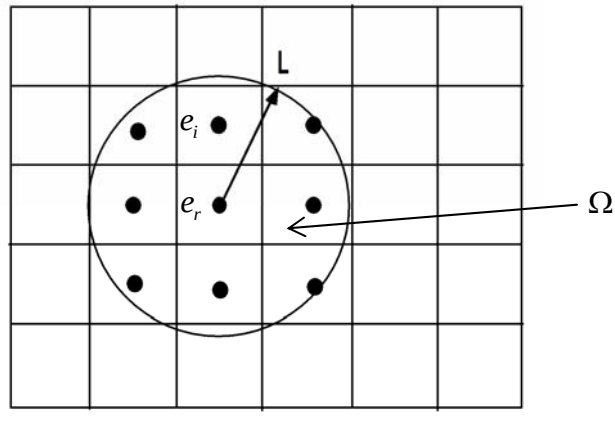

Figure 11.1. Nonlocal domain with radius L (LSTC, 2003).

The radius of the nonlocal domain was chosen as half of the thickness of the plate, in view of the observation that the width of the strain localisation in physical experiments is often in the same order of the material/plate thickness

11.3 Nonlocal plastic thinning within sub-HAZs

11.3.1 Fillet-welded connections

The refined mesh of the 0° fillet-welded connections in Chapter 7 is used for an initial case study. Currently in LS-DYNA, up to two material parts can be assigned the nonlocal feature and the feature can not be used across several material IDs. The nonlocal Equation (11.6) was first introduced to the sub-HAZ where the thinning instability occurred in the previous simulation with the same mesh. Secondly, two sub-HAZs, i.e. sub-HAZ 1 and 2 were assigned the nonlocal treatment simultaneously as shown in Figure 11.2. The radius of the nonlocal domain was chosen as half of the plate thickness, i.e. $L = 2.5$ mm.

The images of the instability predicted in the simulations are presented in Figure 11.3 and Figure 11.4 for nonlocal thinning in sub-HAZ 1 and in sub-HAZ 1 and 2, respectively. Figure 11.8 shows the corresponding force vs. deformation curves in comparison with the experiment and the previous simulation (indicated as “local”). It can be seen that the prediction of ductility was improved by the nonlocal approach, and that the results from the two analyses are similar to each other.

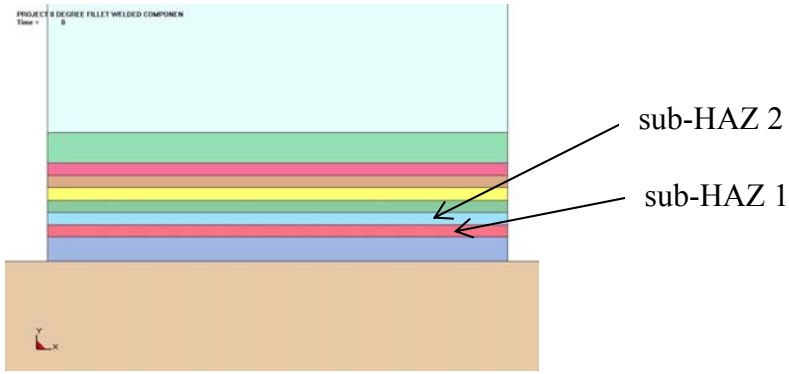

Figure 11.2. Nonlocal thinning introduced to sub-HAZ 1 and 2, separately.

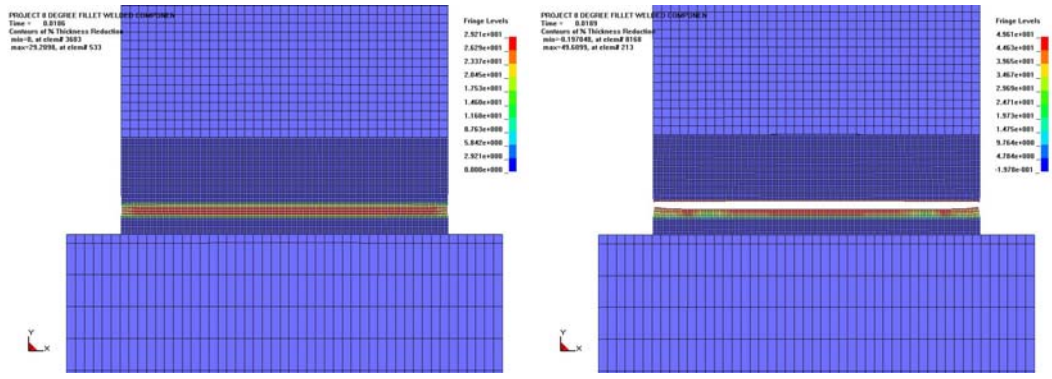

Figure 11.3. Thickness reduction before and after fracture with nonlocal plastic thinning introduced to sub-HAZ 1.

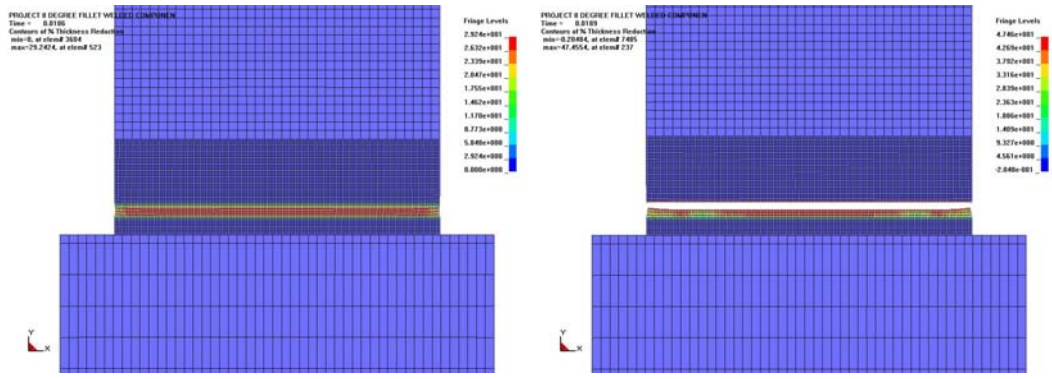

Figure 11.4. Thickness reduction before and after fracture with nonlocal plastic thinning introduced to sub-HAZ 1 and 2.

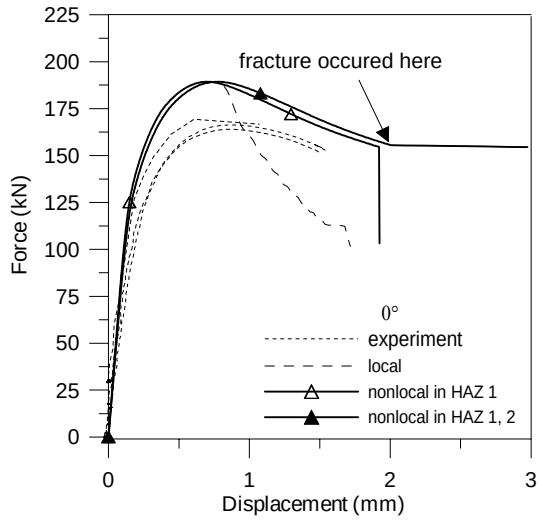

Figure 11.5. Force vs. deformation curves with nonlocal plastic thinning introduced to sub-HAZs separately.

11.3.2 Beam-to-column joints

In view of the improved prediction of the fillet-welded connections with the non-local feature, the same approach is introduced to the analyses of the welded beam-to-column joints presented in Chapter 9. The adopted FE model is the one with 1×1 mm^2 element size in Section 9.6. The nonlocal feature was first introduced to the sub-HAZ 1 of the web, where instability occurred in the previous simulation with the same mesh. Secondly two sub-HAZs, i.e. sub-HAZ 1 and sub-HAZ 2 in the web were modelled using the nonlocal feature simultaneously, see Figure 11.6. These two sub-HAZs were the ones experiencing the largest plastic strain in the previous simulation. The radius of the nonlocal domain was chosen as $L = 3$ mm.

Similar fracture mode and response curves were obtained for the two analyses, as shown in Figure 11.7 and Figure 11.8, respectively. The curves are seen to be almost identical to the one obtained by the previous analysis (indicated as “local”).

In conclusion, the analyses for the fillet-welded connections (Section 11.3.1) were improved by the nonlocal approach in one or two sub-HAZs. However, for the components with more complex geometry, e.g., the welded beam-to-column joints (Section 11.3.2), the prediction was not improved. It is thus desirable to modify this feature and to obtain a more robust and accurate modelling methodology.

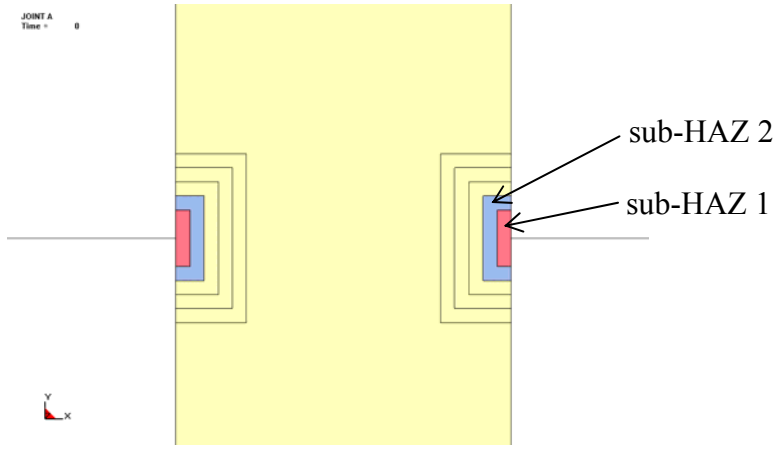

Figure 11.6. Nonlocal thinning introduced to web sub-HAZ 1 and 2.

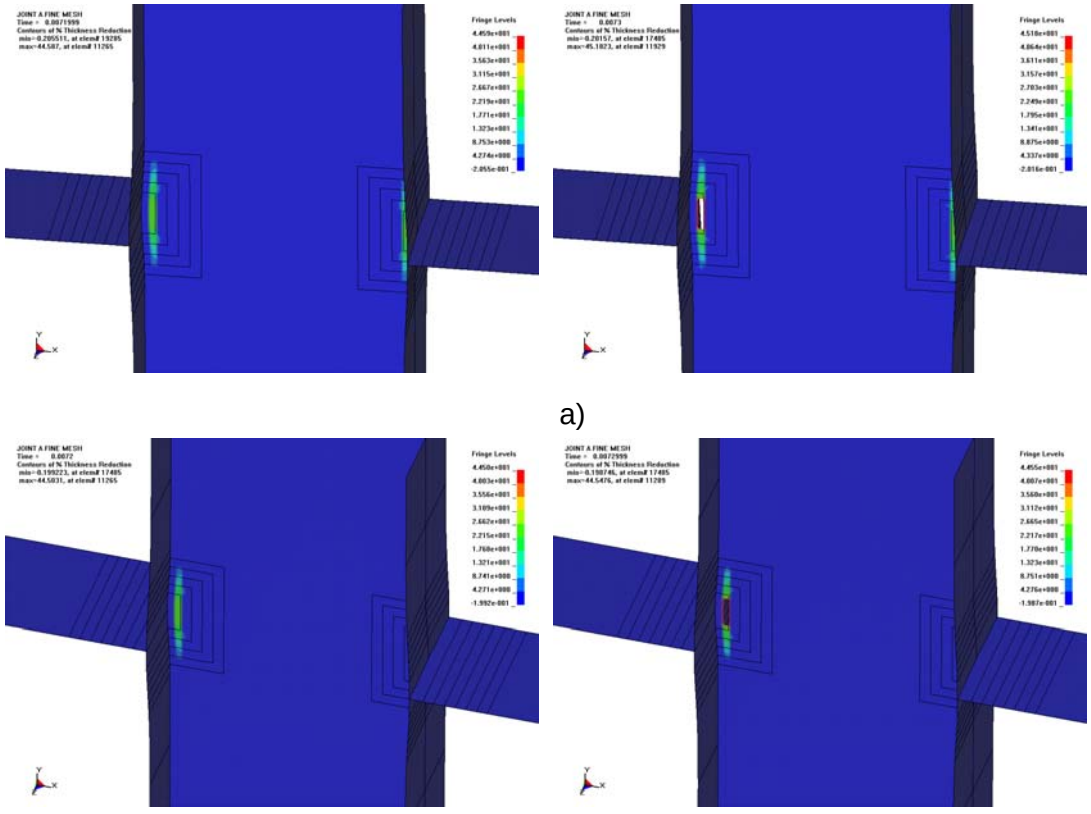

a)

b)

Figure 11.7. Thickness reduction before and after fracture with nonlocal plastic thinning introduced to a) web SUB-HAZ 1, and b) web SUB-HAZ 1 and 2.

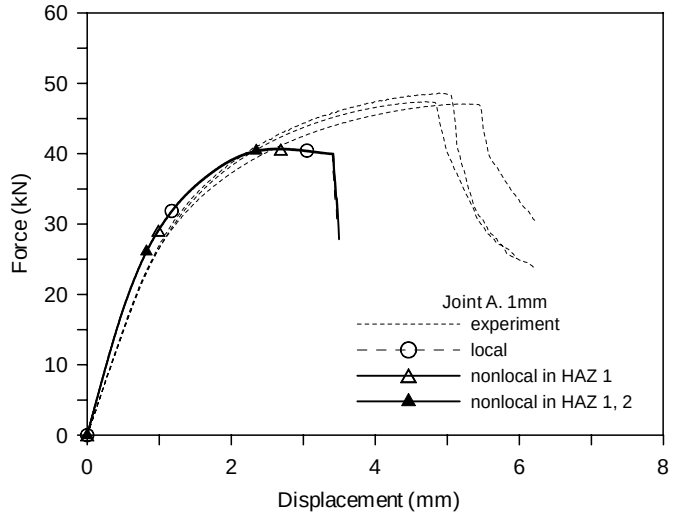

Figure 11.8. Force vs. deformation curves with nonlocal plastic thinning introduced to the sub-HAZs in web.

11.4 Nonlocal thinning in whole HAZ and weld

Above nonlocal thinning was introduced to sub-HAZs separately, i.e. averaging of plastic thinning is restrained within individual sub-HAZ zones, and the elements at the neighbourhood of the sub-HAZs do not have a nonlocal interaction with each other. Another problem is that the nonlocal treatment is limited to one or two sub-HAZs only, thus their portion in the whole HAZ can be too small to amend the over-localisation problem. To remedy these drawbacks, here nonlocal thinning is further introduced across the whole HAZ.

The feature of nonlocal domains extending over several material IDs is currently not available in standard LS-DYNA. The HAZ (so far modelled with six material IDs and corresponding parameters) needs therefore to be represented by a single material ID, meanwhile with spatially dependent material parameters. This is achieved through the use of one particular feature of WTM-2D which originally was intended used for "process-based" numerical analyses. Such analyses are of interest when the inhomogeneity caused by various thermo-mechanical processes can be predicted and after that a "process-based" functionality analysis is performed. This feature allows the definition of separate work hardening curves for various pre-strain levels within one material ID. For additional details of this feature it is referred to Lademo et al. (2004c).

11.4.1 Fillet-welded connections

For the components in this thesis, no thermo-mechanical process data is available, and consequently the inhomogeneity can not be assigned through a "process-based" analysis. However, the LS-DYNA keyword *INITIAL_STRESS_SHELL, which is usually written from the process analysis, still provides a method of initializing an analysis with a history effect. According to the HAZ discretization, the keyword file containing *INITIAL_STRESS_SHELL of the HAZ and weld elements was pre-written by Visual Basic. In the LS-DYNA input file, the whole HAZ and weld are included in one material ID, as seen in Figure 11.9a for the fillet-welded connections. For each of the elements, the five-parameters extended Voce rule is given by the pre-defined curves which are linked to the elements through the keyword *INITIAL_STRESS_SHELL. The legend in Figure 11.9b illustrates *fictive initial plastic strain* assigned to the sub-HAZs and weld. The assigned initial plastic strains correspond to the working hardening properties of the sub-HAZs in the previous models. Note that this fictive initial plastic

strain is only used to enable specification of spatially properties and that the effective strain was initialized to zero through the model.

Figure 11.10 presents the force vs. deformation curves that are highly improved compared with the analyses without the nonlocal approach and the ones where the nonlocal approach was introduced to separate sub-HAZs. Images before and after fracture for the connections with varying weld angles are presented in Figure 10.11. Compared with the analysis in Chapter 7, the fracture modes are seen to be closer to the experiments (Figure 7.3).

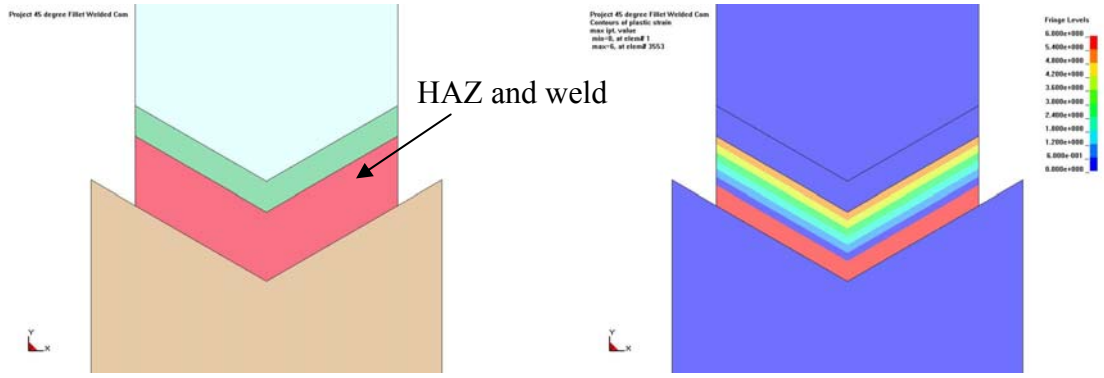

Figure 11.9. Fictive initial plastic strain in the HAZ of the fillet-welded connection using the “process-based” modelling feature of the WTM-2D. a) The material of HAZ and weld, and b) distribution of the fictive initial plastic strain in the HAZ and weld.

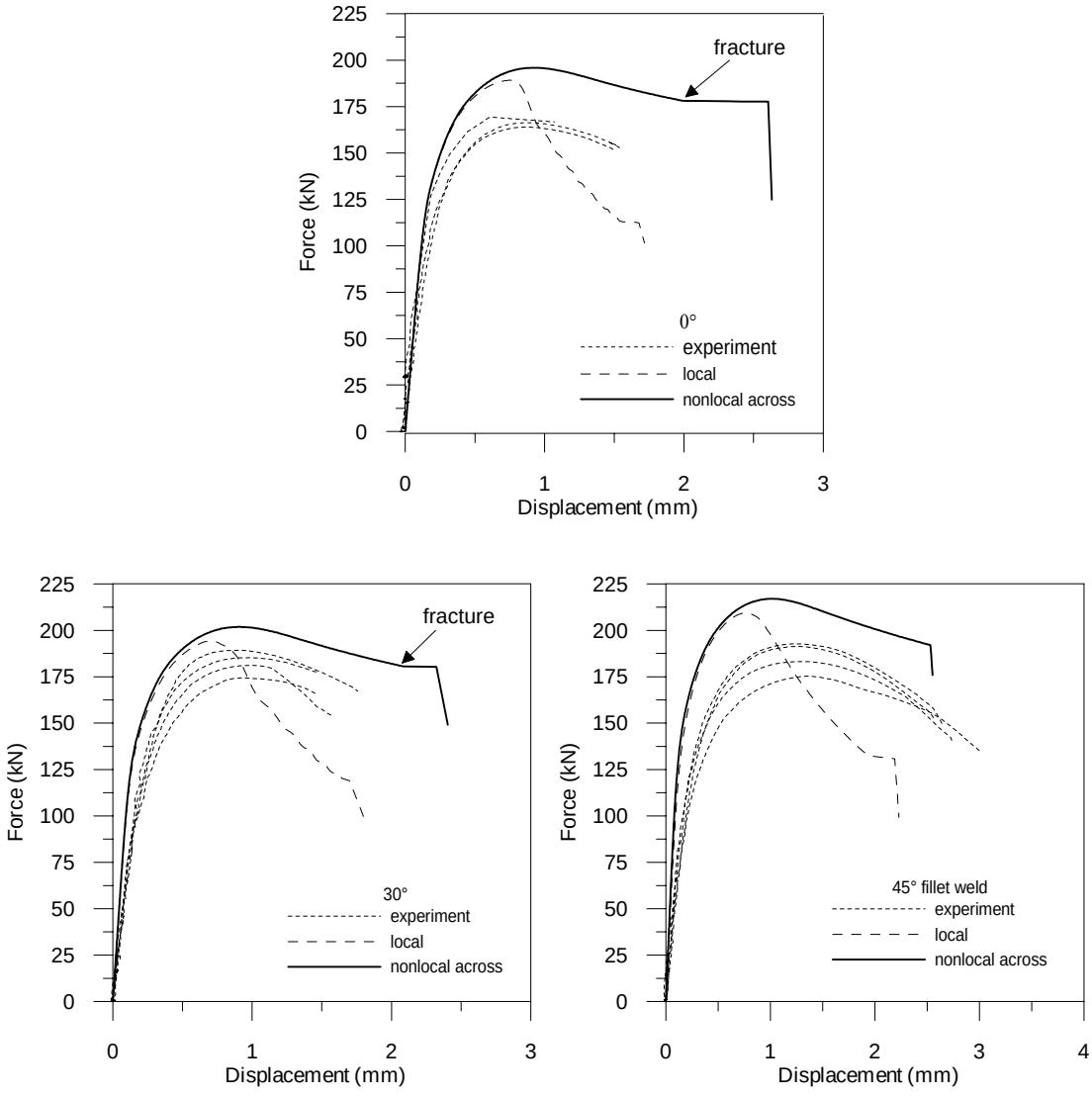

Figure 11.10. Force vs. deformation curves for the fillet-welded connections using nonlocal plastic thinning introduced to the whole HAZ and weld.

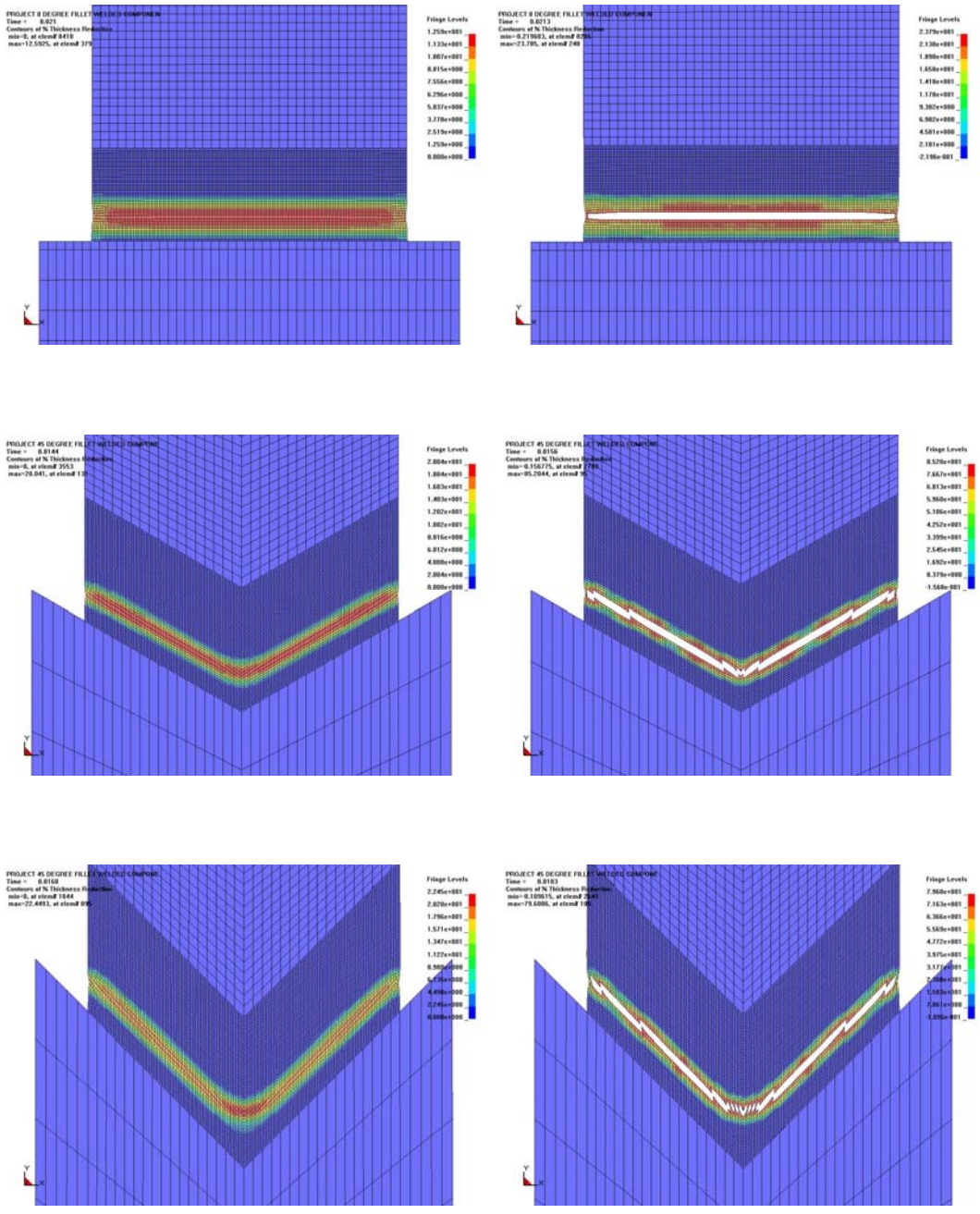

Figure 11.11. Thickness reduction before and after fracture with nonlocal plastic thinning introduced to the whole HAZ and weld.

11.4.2 Beam-to-column joints

Ideally the nonlocal plastic thinning approach should be applied to all the HAZs in the joints, i.e. to the HAZ in web, plate and flange. However, as mentioned LS-DYNA supports at the moment only two material parts with the nonlocal feature, so that only two of the three parts (web, plate and flange) can be assigned to this feature. Here nonlocal plastic thinning was first introduced to the web, secondly to the web and plate simultaneously. Figure 11.12 shows the pre-defined fictive initial plastic strain when nonlocal thinning was introduced to the HAZ in web. For the nonlocal plastic thinning introduced to the web and plate simultaneously, the initial plastic strain is shown in Figure 11.13.

In the analyses with nonlocal thinning introduced to the web only, fracture occurred in the web for joint A as shown in Figure 11.14a. For joint B and C, fracture occurred in plate as seen in Figure 11.14b and Figure 11.14c. In the analyses with nonlocal plastic thinning introduced to the web and plate, the fracture occurred in the web for all cases as shown in Figure 11.15. Figure 11.16 shows the obtained force vs. deformation curves. The correlation between experiments and analyses is much improved by introducing nonlocal plastic thinning to the whole HAZs, even when it is introduced only to the web. The predictions of fracture location and elongation are closer to the experiments. The predicted elongation depends, however, highly on the value of the critical thickness strain, which was assumed as $\varepsilon_{cr} = -0.6$ with no available experimental details. For the same reason, it is not possible to draw conclusions of which analysis gave better prediction of fracture region since it may depend on many factors in physical experiments.

To assess mesh convergence, the nonlocal approach was further applied to the 0.5×0.5 mm^2 model of joint A. The images of plastic strain before and after fracture are shown in Figure 11.17. Compared with the 1×1 mm^2 analyses, strain was seen to localize in a smaller area in the HAZ which is due to the element size. The force vs. deformation curve is presented in Figure 11.18. Very good agreement was obtained between the experiment and simulation. The predicted elongation was however slightly under-estimated compared with the test and the 1×1 mm^2 analysis. Anyhow, it can be concluded that the mesh-dependence was greatly reduced with nonlocal plastic thinning introduced to the whole HAZ and weld.

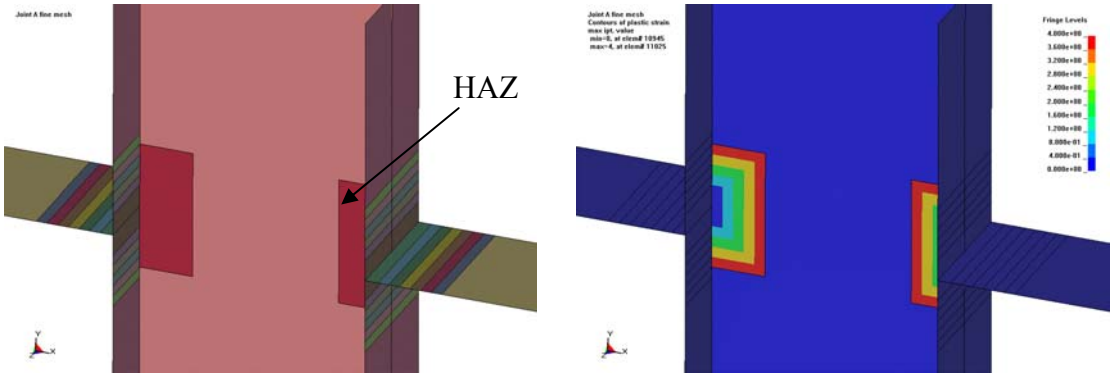

a) b)

Figure 11.12. Fictive initial plastic strain in the HAZ of the beam-to-column joints using the “process-based” modelling feature of the WTM-2D. a) The HAZ material, and b) distribution of the fictive initial plastic strain in the web HAZ .

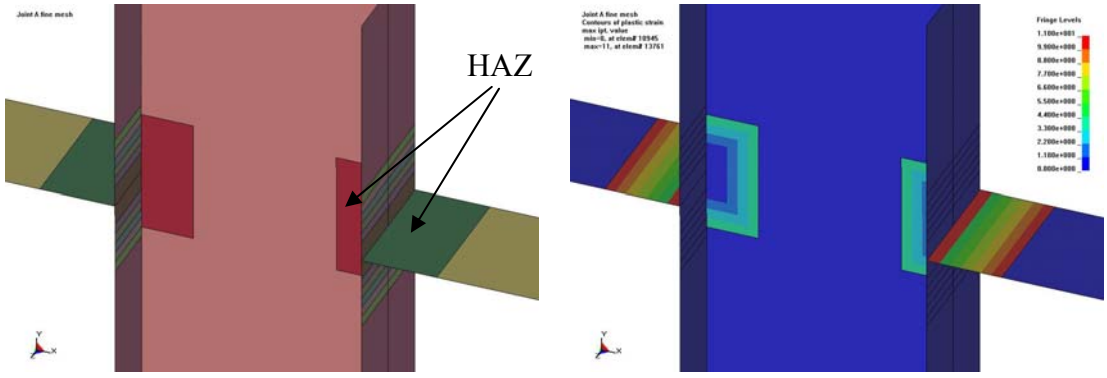

a) b)

Figure 11.13. Fictive initial plastic strain in the HAZ of the beam-to-column joints using the “process-based” modelling feature of the WTM-2D. a) The HAZ material, and b) distribution of the fictive initial plastic strain in the web HAZ, and the weld and HAZ in the flange.

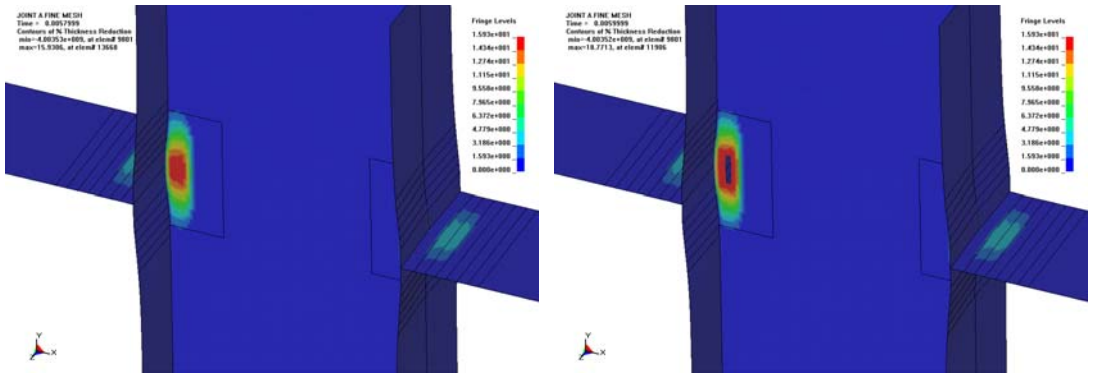

a)

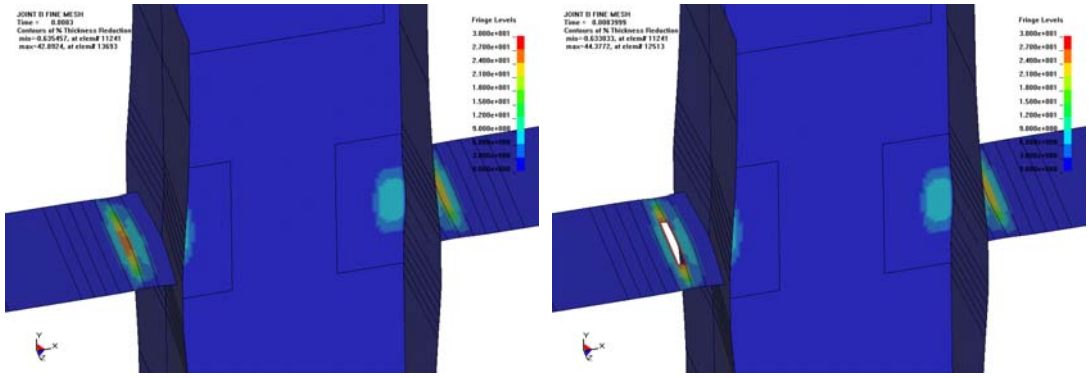

b)

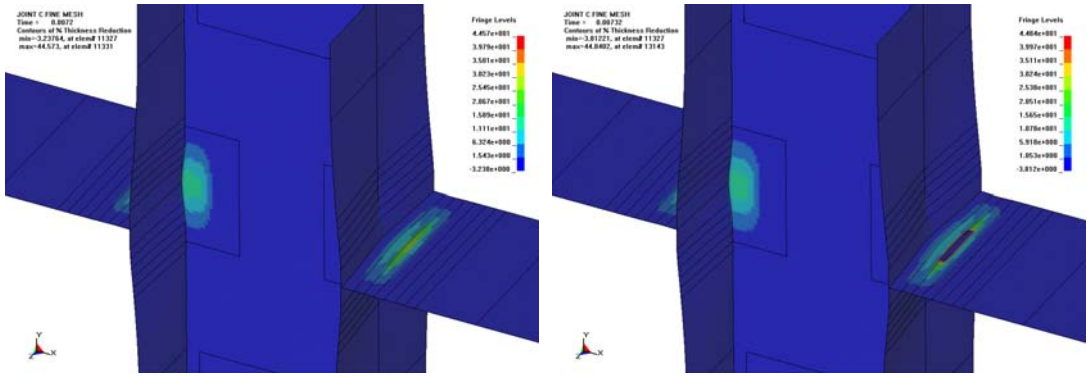

c)

Figure 11.14. Thickness reduction before and after fracture for a) joint A, b) joint B, and c) joint C with nonlocal plastic thinning introduced to the web HAZ. Element size is $1\times1\text{mm}^2$.

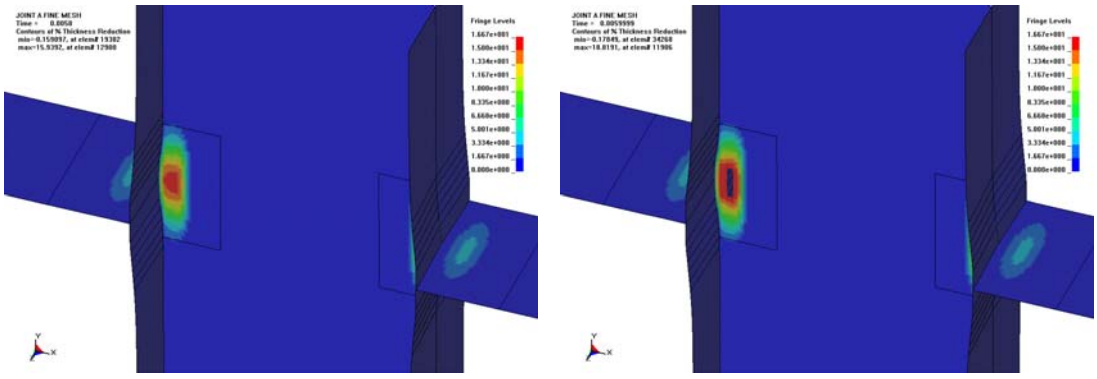

a)

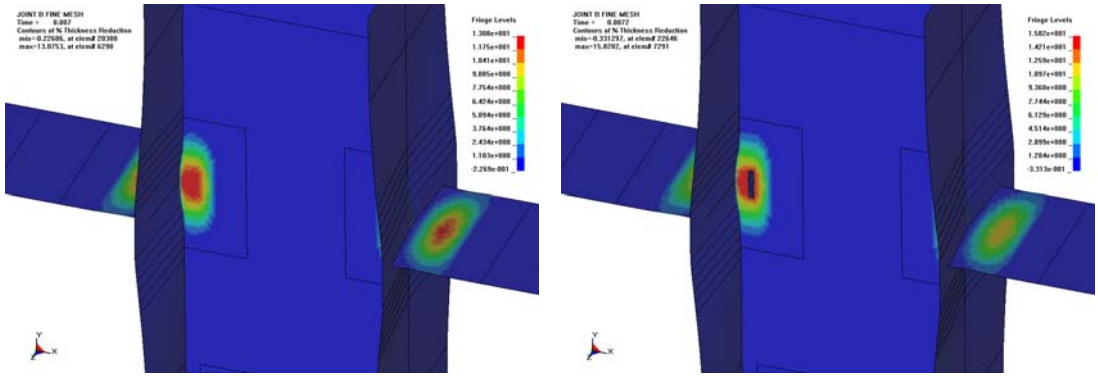

b)

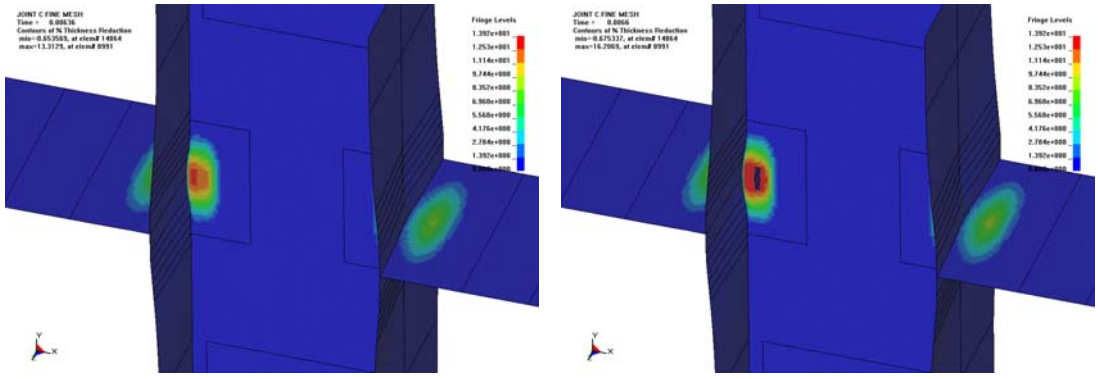

c)

Figure 11.15. Thickness reduction before and after fracture for a) joint A, b) joint B, and c) joint C with nonlocal thinning introduced to the web HAZ, and the weld and HAZ in the flange. Element size is $1\times1\text{mm}^2$.

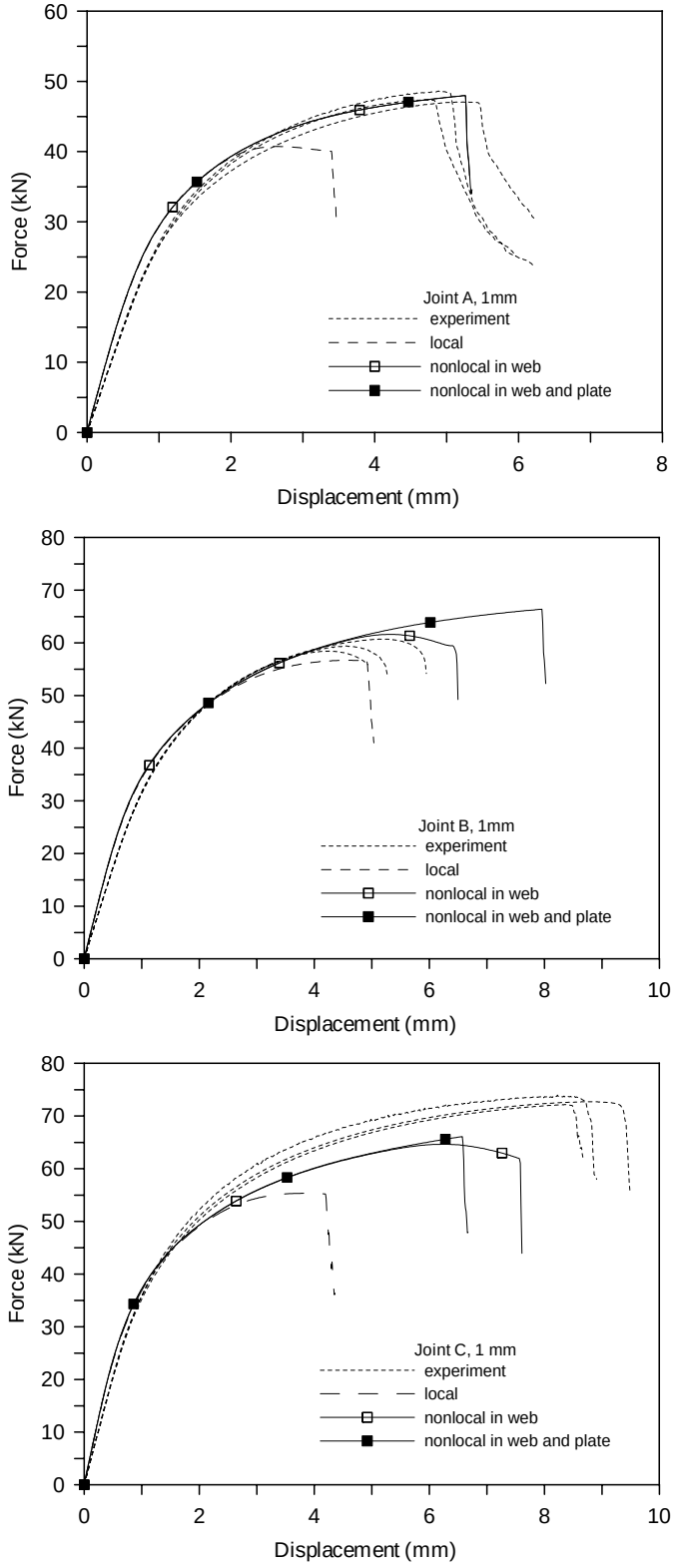

Figure 11.16. Force vs. deformation curves with nonlocal plastic thinning introduced to the whole HAZ materials. Element size is $1\times1\text{mm}^2$.

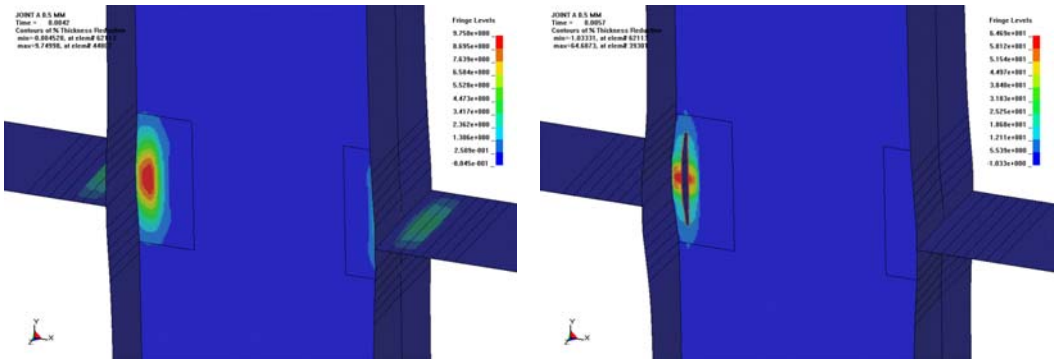

Figure 11.17. Thickness reduction before and after fracture with nonlocal thinning introduced to the whole HAZ in *web* for joint A with $0.5 \times 0.5\,\text{mm}^2$ elements

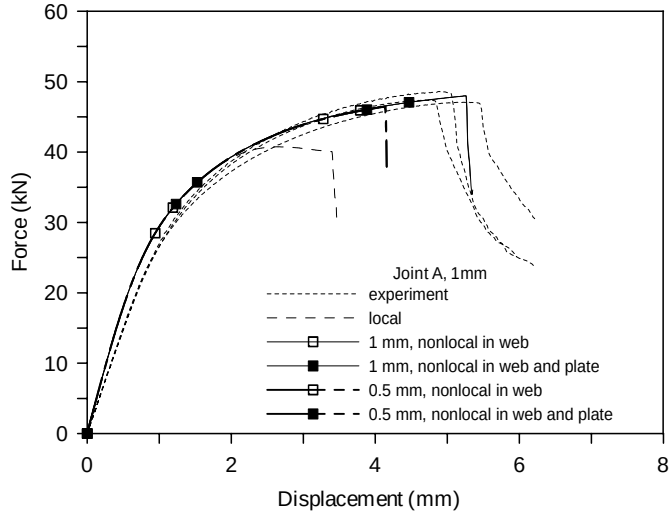

Figure 11.18. Force vs. deformation curves with nonlocal plastic thinning introduced to the whole HAZ and weld.

11.5 Conclusions

To overcome the mesh-dependence problem in the previous analyses, the remedy of nonlocal plastic thinning was introduced to the analyses of the fillet-welded connections and beam-to-column joints using the keywords of *MAT_NONLOCAL and *INITIAL_STRESS_SHELL in LS-DYNA. The following conclusions can be drawn from this study:

With nonlocal plastic thinning applied to one or two sub-HAZs *separately*, the predictions were found improved for the 2D fillet-welded connections. However, for the 3D beam-to-column joints it did not influence the prediction significantly.

With nonlocal plastic thinning applied across the whole HAZ and weld materials the numerical results were much improved, compared with any other analysis for both of the fillet-welded connections and the joints. Inhomogeneous work hardening property in the HAZ and weld was provided through a process-based feature that the WTM-2D incorporated in LS-DYNA. The results obtained by the 1 mm and 0.5 mm element meshes showed that mesh sensitivity is greatly reduced. This method is thus proved rather accurate, efficient and robust.

With adding one parameter, the radius of the nonlocal domain, the analyses with nonlocal feature were simple and efficient to perform.

12. Conclusions

12.1 Results

This thesis focuses on the development of accurate, robust and efficient predictive methodology for welded thin-walled aluminium structures with special emphasis on the HAZ. Through experiments, analytical calculations and numerical analyses, the mechanical performance of three series of typical welded thin-walled structures were well understood and predicted. A procedure and a combination of modelling techniques using shell elements were established for the modelling of HAZ and weld. The results of this study are summarized as follows.

Material tests and model calibration

The materials tests showed that the investigated aluminium extrusion possesses anisotropy in strength, plastic flow and ductility, which should be properly represented in the constitutive relations. It was shown that the relatively sophisticated material model WTM-2D was able to represent the mechanical response of the investigated material. However, the parameters of the anisotropic yield surface need to be properly identified. A verification study showed that the power weighted least-square approach led to a very accurate representation of the material anisotropy.

Component tests

The fillet-welded component tests and the hardness measurements showed how the extruded plate was weakened by the heat input during the welding process. Another important phenomenon is that the structural ductility was severely decreased owing to the highly localised strain in the HAZ. This is also the case in the previous experiments by Matusiak (1999).

Simulations

The simulations using shell elements were found generally efficient and accurate with relatively large elements, except that the structural ductility was over-estimated. While using smaller elements, the problem of mesh-dependence was experienced. Introducing a remedy, the feature of nonlocal plastic thinning in the HAZ and weld was shown to resolve this problem. Inhomogeneous work hardening property in the HAZ and weld materials was provided through a process-based feature of the WTM-2D. Several case studies showed that mesh sensitivity was greatly reduced by this technique. This method is thus proved rather accurate, efficient and robust.

The failure criterion of Critical-Thickness-Strain was shown to predict failure relatively well using a fine mesh given a pre-determined value. However accuracy of the failure predictions is highly dependent on mesh density, and it was shown not suitable for relatively coarse mesh.

Several modelling techniques were adopted in the numerical analyses including thickness variation in shell elements to account for the actual weld geometry, contact algorithm between dense and coarse meshed zones and the use of a nonlocal plastic thinning approach in the HAZ and weld to obtain mesh convergence. These techniques were shown to improve the efficiency and accuracy of the numerical analyses, and are recommended to shell modelling of aluminium thin-walled structures.

Even if most of the analyses were performed using the explicit solver of LS-DYNA, the implicit solver was applied to one of the test series. The limitations of the implicit solutions are that it does not include failure prediction, and geometry imperfections need to be introduced to obtain realistic predictions when bucking is important.

Analytical work

A computational method was proposed to represent fillet welds in FE modelling. However, in the current study emphasis was on the modelling of the HAZ rather than the weld, and this method was therefore not further investigated. Nevertheless, as a simple computing method to represent fillet welds, more work is worth doing to further develop and to implement this model in finite element codes.

A simple analytical method is introduced to compute the mechanical performance of a welded aluminium sheet under uniaxial tensile loading. Despite certain limitations it predicts the performance of the sheet reasonably well, and is much more efficient compared with an FE analysis. However, the method is only valid for the given geometry, and can not replace FE analyses for more complex structures. The method is able to provide information on the influence of HAZ modelling on prediction of the

structural performance, especially with respect to ductility. The results are clearly beneficial for FE modelling of welded structures and a rapid engineering assessment of the governing physics.

12.2 Future research

While this thesis has focused on the development and validation of a predictive methodology for welded thin-walled aluminium structures, a number of key topics remain unsolved and await further research.

First, there are uncertainties related to the procedure of work hardening parameter identification in the HAZ and weld. A more sophisticated method would be highly desirable. Welding process simulations, using e.g. the Weldsim code might provide means of estimating the distribution of the materials' work hardening through micro-structural analyses. However, sufficient verification is needed before these simulations can be used to determine the material properties in HAZ and weld.

Second, the material model showed numerical robustness problem for the four-point bending simulations using small elements and the explicit solver of LS-DYNA. To solve this problem, additional effort is needed to investigate the numerical algorithms.

Third, fracture criteria other than thickness strain need more attention and further investigation.

Fourth, the nonlocal approach is currently available for two material parts in LS-DYNA, which is not enough for structures with complex geometry, or components with several welds. Implementation work is needed for this feature to be easily used.

Fifth, the established methodology has not been looked into with respect to safety level given by design codes. Further work is needed to investigate its applications for design purposes.

At last, a suitable way is needed to transfer the present technical knowledge to manufacturers of extruded aluminium structures.

References

Altenpohl D. (1982): *Aluminium viewed from within*. Aluminium-Verlag, Dusseldorf.

Barlat F, Lian J. (1989): *Plastic behaviour and stretchability of sheet metals. Part I: A yield function for orthotropic sheets under plane stress conditions*. International Journal of Plasticity, 5: 55-66.

Barlat F, Richmond O. (1987): *Prediction of tricomponent plane stress yield surfaces and associated flow and failure behaviour of strongly textured F.C.C. Polycrystalline Sheets.* Material Science and Engineering, 95:15-29.

Bazant ZP, Pijaudier-Gabot G. (1988): *Nonlocal continuum damage, localisation instability and convergence*. Journal of Applied Mechanics, 55:287-293.

Belytschko T, Liu WK, Moran B. (2000): *Nonlinear finite elements for continua and structures*. John Wiley & Sons Ltd, England.

Bressan JD, Williams JA. (1982): *The use of shear instability criterion to predict local necking in sheet metal deformation*. Int J Mech Sci, 25:155-168.

Chan TK and Porter Goff RFD. (2000): *Welded aluminium alloy connections: Test results and BS8118*. Thin-Walled Structures, 36: 265-287.

Cockcroft MG, Latham DJ. (1968): *Ductility and the workability of metals*. Journal of the Institute of Metals, 96: 33-39.

Dieter GE. (1988): *Mechanical metallurgy*. McGraw-Hill, London.

European Committee for Standardisation (CEN) (2004): *Eurocode 9: Design of aluminium structures, Part 1-1: General structural rules*. Brussels.

Hatherly M, Hutchinson WB. (1979): *An introduction to textures in metals*. Institution of metallurgists, London.

Hersey AV, Dahlgen VA. (1954): *The plasticity of an isotropic aggregate of anisotropic face-centered cubic crystals*. J Appl Mech Phys Solids, 76:241.

Hildrum HG and Malo KA (2002): *An introductory FEM study of strain localisation in welded aluminium structures. Part I: Isotropic material*. Techanical report R-22-01, Department of Structural Engineering, NTNU, Trondheim.

Hildrum HG. (2002): *Stiffened aluminium plates subjected to impact loading*. Doctoral thesis. NTNU, Trondheim.

Hildrum HG, Berstad T, Lademo O-G, Malo KA, Hopperstad OS. (2002): *An introductory FEM study of strain localisation in welded aluminium structures. Part II: Fillet weld*. Techanical report R-3-02, Department of Structural Engineering, NTNU, Trondheim.

Hildrum HG, Hopperstad OS. (2002): *Rigid body weld constraint in LS-DYNA for welded aluminium structures: an introductory study*. Technical report R-11-02, Department of Structural Engineering, NTNU, Trondheim.

Hopperstad OS, Berstad T, Lademo O-G, Langseth M. (2005): *Shear instability criterion for plastic anisotropy*. SINTEF Report, Trondheim.

Hopperstad OS, Lademo O-G. (2002): *Classical FLD calculator in Excel/Visual Basic*. SINTEF report, Trondheim.

Hosford WF. (1972): *A generalized isotropic yield criterion*. J Appl Mech 39: 607.

Hosford WF, Caddell RM. (2002): *Metal forming: Mechanics and metallurgy*. PTR Prentice Hall Inc., New Jersey.

Khan AS, Huang S. (1995): *Continuum theory of plasticity*. Canada: John Wiley & Sons Inc., New York.

Lademo O-G, Engler O, Eriksson M, Hopperstad OS, Berstad T. (2005): *An experimental and numerical investigation on the applicability of the STM-2D model for rolled aluminium alloys*. SINTEF report STF24 F04204, Trondheim.

Lademo O-G, Eriksson M, Berstad T, Hopperstad OS, Langseth M. (2005): *Characterisation of failure and identification of failure related parameters*. SINTEF report STF24 F05, Trondheim.

Lademo O-G. (1999): *Engineering models of elastoplasticity and fracture for aluminium alloys*. Doctoral Thesis, NTNU, Trondheim.

Lademo O-G, Berstad T, Hopperstad OS. (2004a): *A numerical tool for formability analysis of aluminium alloys. Part I: theory*. Steel Grips 2, Suppl. Metal Forming 2004: 427-431.

Lademo O-G, Pedersen KO, Hopperstad OS. (2004b): *A numerical tool for formability analysis of aluminium alloys. Part II: experimental validation*. Steel Grips 2, Suppl. Metal Forming 2004: 433-437.

Lademo O-G, Berstad T, Tryland T, Furu T, Hopperstad OS, Langseth M. (2004c): *A model for process-based crash simulation.* 8th International LS-DYNA User's Conference, Detroit

Livermore Software Technology Corporation (LSTC). (2003): *LS-DYNA keyword user's manual, Version 970*. California.

Marciniak K, Kuczynski K, Pokora T. (1973): *Influence of the plastic properties of a material on the forming limit diagram for sheet metals in tension*. Int J Mech Sci, 15: 33-39.

Marciniak Z, Duncan JL, Hu SJ. (2002): *Mechanics of sheet metal forming*. Butterworth-Heinemann, Oxford.

Marciniak Z, Kuczinsky K, Pokora T. (1973): *Influence of the plastic properties of a material on the forming limit diagram for sheet metal in tension*. Int J mech Sci, 15: 789-805.

Marciniak Z, Kuczynski K. (1967): *Limit strains in the processes of stretch-forming sheet metal*. Int J Mech Sci, 9: 609-620.

Matusiak M. (1999): *Strength and ductility of welded structures in aluminium alloys.* Doctor thesis, NTNU, Trondheim.

Mellor BG, Rainey RTC, Kirk NE. (1999): *The static strength of end and T fillet weld connections.* Materials and Design, 20:193-205.

Patrick JD, Peter RK, Graham WO. (1988): *Structural steel design*. Butterworths, London.

Soetens F. (1987): *Welded connections in aluminium alloy structures*. Heron, 32, No. 1, Delft.

Zhang ZL, Odegard J, Myhr OR, Fjær H. (2001): *From microstructure to deformation and fracture behaviour of aluminium welded joints -- a holistic modelling approach.* Computational Material Sciences, 21: 429-435.

Ødegard J, Zhang ZL. (1996): *Prediction of the performance of welded aluminium nodes for car body applications.* Body Design & Engineering, 20: 17-24.

Appendix A Uniaxial tensile test results

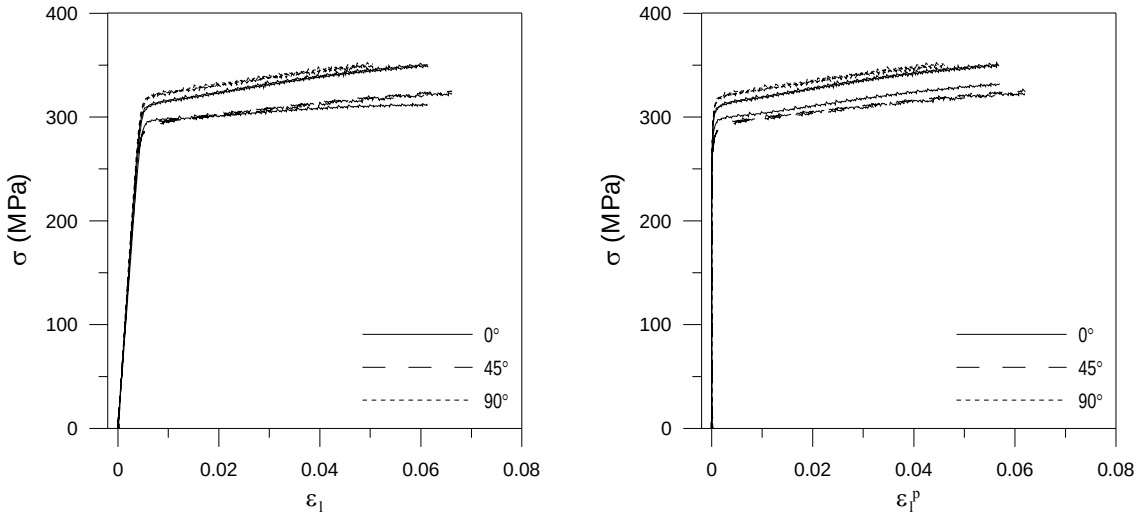

Figure A-1. a) true stress-strain curves, and b) true stress-plastic strain curves.

Table A-1. Hardening parameters

Test	Y_0 [N/mm^2]	Q_1 [N/mm^2]	C_1 [-]	Q_2 [N/mm^2]	C_2 [-]	$Y_0+\Sigma Q$ [N/mm^2]
0-1	256.0	52.3	4605.5	59.5	20.5	367.8
0-2	257.9	39.2	2970.4	332.4	2.1	629.5
0-3	263.8	47.0	3291.4	309.9	2.8	620.7
45-1	261.9	30.9	1450.5	63.5	11.2	356.4
45-2	228.0	60.2	7216.9	47.5	19.9	335.7
45-3	217.9	68.1	7533.5	37.9	37.9	323.9
90-1	217.7	95.1	9764.1	41.5	41.4	354.3
90-2	225.1	86.1	9231.3	36.7	57.7	347.9
90-3	228.6	87.2	9729.4	50.4	25.9	366.3

Table A-2. Measurement and calculation of the R-ratio

Test	Measurement	Before testing			After testing					
		Width [mm]	Thickness [mm]	Area [mm^2]	Width [mm]	Thickness [mm]	Area [mm^2]	ε_w	ε_t	R_α
0-1*	green	7.993	4.819	38.518	7.843	4.590	35.999	-0.019	-0.049	0.389
	red	7.994	4.838	38.675	7.850	4.585	35.992	-0.018	-0.054	0.338
	blue	7.991	4.820	38.517	7.800	4.530	35.334	-0.024	-0.062	0.390
	average	7.993	4.826	38.570	7.831	4.568	35.775	-0.020	-0.055	0.372
0-2	green	7.992	4.950	39.560	7.818	4.680	36.588	-0.022	-0.056	0.392
	red	7.994	4.907	39.227	7.752	4.627	35.869	-0.031	-0.059	0.523
	blue	7.994	4.922	39.346	7.815	4.685	36.613	-0.023	-0.049	0.459
	average	7.993	4.926	39.378	7.795	4.664	36.357	-0.025	-0.055	0.458
0-3	green	7.996	4.779	38.213	7.856	4.558	35.808	-0.018	-0.047	0.373
	red	7.993	4.813	38.470	7.830	4.525	35.431	-0.021	-0.062	0.334
	blue	7.996	4.784	38.253	7.822	4.522	35.371	-0.022	-0.056	0.391
	average	7.995	4.792	38.312	7.836	4.535	35.536	-0.020	-0.055	0.366
45-1*	green	8.010	4.798	38.432	7.399	4.489	33.214	-0.079	-0.067	1.192
	red	7.991	4.815	38.477	7.665	4.661	35.727	-0.042	-0.033	1.281
	blue	7.990	4.842	38.688	7.778	4.725	36.751	-0.027	-0.024	1.099
	average	7.997	4.818	38.532	7.614	4.625	35.231	-0.049	-0.041	1.191
45-2	green	7.993	4.789	38.278	7.670	4.657	35.719	-0.041	-0.028	1.476
	red	7.992	4.827	38.577	7.570	4.615	34.936	-0.054	-0.045	1.208
	blue	8.002	4.765	38.130	7.639	4.609	35.208	-0.046	-0.033	1.395
	average	7.996	4.794	38.328	7.626	4.627	35.288	-0.047	-0.035	1.359
45-3	green	7.989	4.775	38.147						
	red	7.989	4.784	38.219	7.712	4.652	35.876	-0.035	-0.028	1.261
	blue	7.988	4.805	38.382	7.778	4.708	36.619	-0.027	-0.020	1.306
	average	7.989	4.788	38.250	7.745	4.680	36.248	-0.031	-0.024	1.284
90-1	green	7.988	4.831	38.590						
	red	7.990	4.788	38.256	7.785	4.670	36.356	-0.026	-0.025	1.042
	blue	7.989	4.777	38.163	7.635	4.568	34.877	-0.045	-0.045	1.013
	average	7.989	4.799	38.337	7.710	4.619	35.616	-0.036	-0.035	1.027
90-2*	green	7.991	4.843	38.700	7.702	4.658	35.876	-0.037	-0.039	0.946
	red	7.990	4.813	38.456	7.810	4.690	36.629	-0.023	-0.026	0.880
	blue	7.989	4.782	38.203						
	average	7.990	4.813	38.453	7.756	4.674	36.252	-0.030	-0.032	0.913
90-3	green	7.997	4.754	38.018	7.781	4.609	35.863	-0.027	-0.031	0.884
	red	7.991	4.779	38.189	7.816	4.658	36.407	-0.022	-0.026	0.863
	blue	7.991	4.781	38.205						
	average	7.993	4.771	38.137	7.799	4.634	36.135	-0.025	-0.028	0.874

*representative tests for the corresponding directions

Table A-3. The average and standard deviation of the R-ratio.

	0°	45°	90°
average	0.40	1.28	0.94
stdeva	0.05	0.08	0.08

Appendix B Four-point bending tests

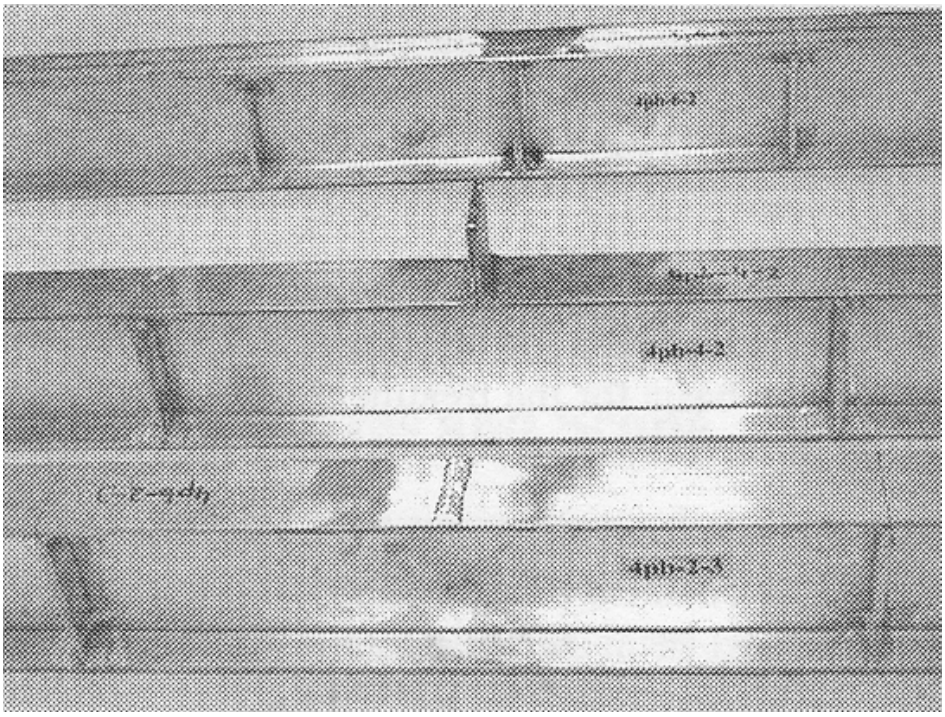

Figure B-1. Welded members (Matusiak 1999).

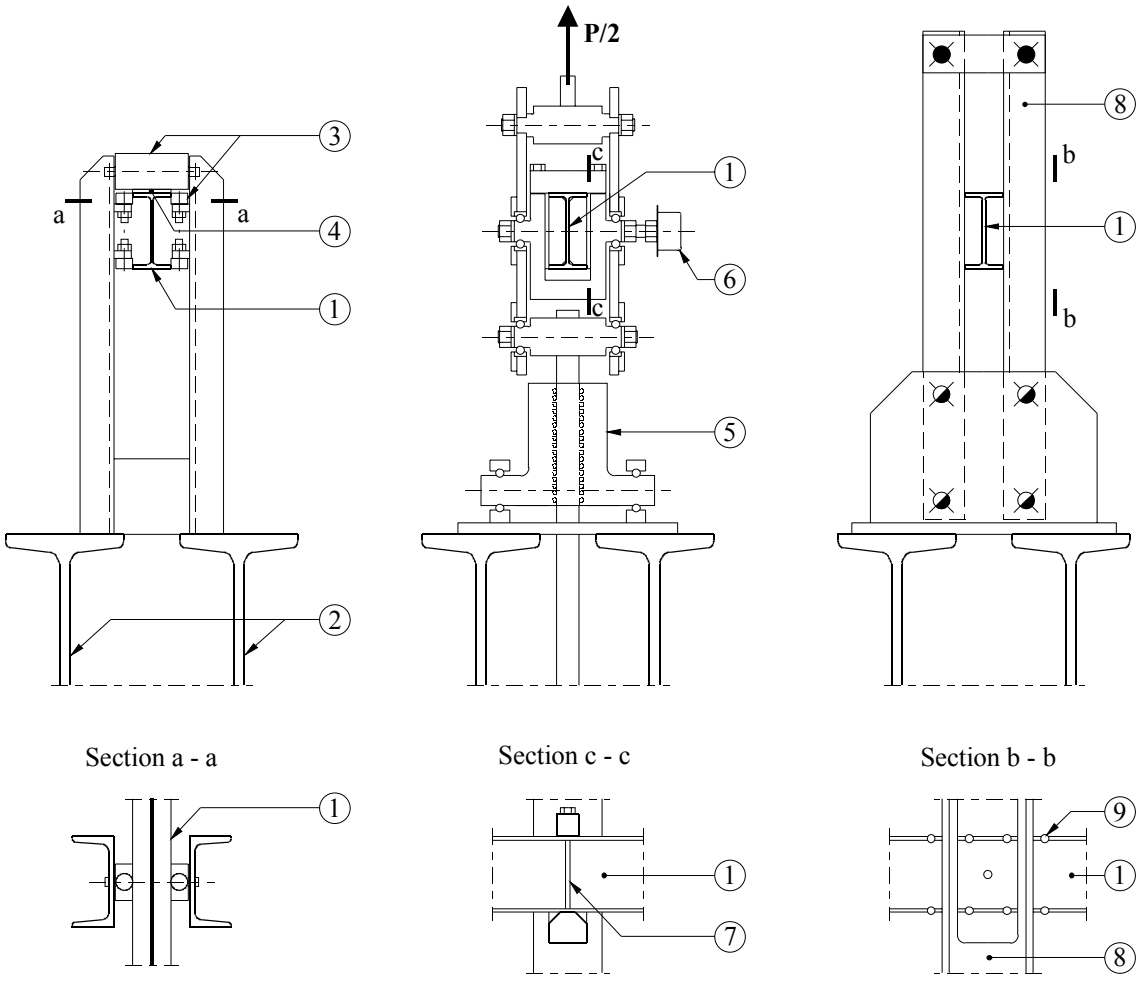

1 Test specimen
2 Girder
3 Rolling bearings
4 Steel plate; t = 5mm
5 Ball bearing
6 Electronic clinometer
7 Stiffener
8 Slip support
9 Target for video extensometer

Figure B-2. Details of support and loading arrangement for four-point bending (Matusiak 1999).

DEPARTMENT OF STRUCTURAL ENGINEERING
NORWEGIAN UNIVERSITY OF SCIENCE AND TECHNOLOGY

N–7491 TRONDHEIM, NORWAY
Telephone: +47 73 59 47 00 Telefax: +47 73 59 47 01

"Reliability Analysis of Structural Systems using Nonlinear Finite Element Methods",
C. A. Holm, 1990:23, ISBN 82-7119-178-0.

"Uniform Stratified Flow Interaction with a Submerged Horizontal Cylinder",
Ø. Arntsen, 1990:32, ISBN 82-7119-188-8.

"Large Displacement Analysis of Flexible and Rigid Systems Considering Displacement-Dependent Loads and Nonlinear Constraints", K. M. Mathisen, 1990:33, ISBN 82-7119-189-6.

"Solid Mechanics and Material Models including Large Deformations",
E. Levold, 1990:56, ISBN 82-7119-214-0, ISSN 0802-3271.

"Inelastic Deformation Capacity of Flexurally-Loaded Aluminium Alloy Structures",
T. Welo, 1990:62, ISBN 82-7119-220-5, ISSN 0802-3271.

"Visualization of Results from Mechanical Engineering Analysis",
K. Aamnes, 1990:63, ISBN 82-7119-221-3, ISSN 0802-3271.

"Object-Oriented Product Modeling for Structural Design",
S. I. Dale, 1991:6, ISBN 82-7119-258-2, ISSN 0802-3271.

"Parallel Techniques for Solving Finite Element Problems on Transputer Networks",
T. H. Hansen, 1991:19, ISBN 82-7119-273-6, ISSN 0802-3271.

"Statistical Description and Estimation of Ocean Drift Ice Environments",
R. Korsnes, 1991:24, ISBN 82-7119-278-7, ISSN 0802-3271.

“Properties of concrete related to fatigue damage: with emphasis on high strength concrete”,
G. Petkovic, 1991:35, ISBN 82-7119-290-6, ISSN 0802-3271.

"Turbidity Current Modelling",
B. Brørs, 1991:38, ISBN 82-7119-293-0, ISSN 0802-3271.

"Zero-Slump Concrete: Rheology, Degree of Compaction and Strength. Effects of Fillers as Part Cement-Replacement",
C. Sørensen, 1992:8, ISBN 82-7119-357-0, ISSN 0802-3271.

"Nonlinear Analysis of Reinforced Concrete Structures Exposed to Transient Loading",
K. V. Høiseth, 1992:15, ISBN 82-7119-364-3, ISSN 0802-3271.

"Finite Element Formulations and Solution Algorithms for Buckling and Collapse Analysis of Thin Shells", R. O. Bjærum, 1992:30, ISBN 82-7119-380-5, ISSN 0802-3271.

"Response Statistics of Nonlinear Dynamic Systems",
J. M. Johnsen, 1992:42, ISBN 82-7119-393-7, ISSN 0802-3271.

"Digital Models in Engineering. A Study on why and how engineers build and operate digital models for decisison support", J. Høyte, 1992:75, ISBN 82-7119-429-1, ISSN 0802-3271.

"Sparse Solution of Finite Element Equations",
A. C. Damhaug, 1992:76, ISBN 82-7119-430-5, ISSN 0802-3271.

"Some Aspects of Floating Ice Related to Sea Surface Operations in the Barents Sea",
S. Løset, 1992:95, ISBN 82-7119-452-6, ISSN 0802-3271.

"Modelling of Cyclic Plasticity with Application to Steel and Aluminium Structures",
O. S. Hopperstad, 1993:7, ISBN 82-7119-461-5, ISSN 0802-3271.

"The Free Formulation: Linear Theory and Extensions with Applications to Tetrahedral Elements
with Rotational Freedoms", G. Skeie, 1993:17, ISBN 82-7119-472-0, ISSN 0802-3271.

"Høyfast betongs motstand mot piggdekkslitasje. Analyse av resultater fra prøving i Veisliter'n",
T. Tveter, 1993:62, ISBN 82-7119-522-0, ISSN 0802-3271.

"A Nonlinear Finite Element Based on Free Formulation Theory for Analysis of Sandwich Structures", O. Aamlid, 1993:72, ISBN 82-7119-534-4, ISSN 0802-3271.

"The Effect of Curing Temperature and Silica Fume on Chloride Migration and Pore Structure of High Strength Concrete", C. J. Hauck, 1993:90, ISBN 82-7119-553-0, ISSN 0802-3271.

"Failure of Concrete under Compressive Strain Gradients",
G. Markeset, 1993:110, ISBN 82-7119-575-1, ISSN 0802-3271.

"An experimental study of internal tidal amphidromes in Vestfjorden",
J. H. Nilsen, 1994:39, ISBN 82-7119-640-5, ISSN 0802-3271.

"Structural analysis of oil wells with emphasis on conductor design",
H. Larsen, 1994:46, ISBN 82-7119-648-0, ISSN 0802-3271.

"Adaptive methods for non-linear finite element analysis of shell structures",
K. M. Okstad, 1994:66, ISBN 82-7119-670-7, ISSN 0802-3271.

"On constitutive modelling in nonlinear analysis of concrete structures",
O. Fyrileiv, 1994:115, ISBN 82-7119-725-8, ISSN 0802-3271.

"Fluctuating wind load and response of a line-like engineering structure with emphasis on motion-induced wind forces",
J. Bogunovic Jakobsen, 1995:62, ISBN 82-7119-809-2, ISSN 0802-3271.

"An experimental study of beam-columns subjected to combined torsion, bending and axial actions", A. Aalberg, 1995:66, ISBN 82-7119-813-0, ISSN 0802-3271.

"Scaling and cracking in unsealed freeze/thaw testing of Portland cement and silica fume concretes", S. Jacobsen, 1995:101, ISBN 82-7119-851-3, ISSN 0802-3271.

"Damping of water waves by submerged vegetation. A case study of laminaria hyperborea", A. M. Dubi, 1995:108, ISBN 82-7119-859-9, ISSN 0802-3271.

"The dynamics of a slope current in the Barents Sea",
Sheng Li, 1995:109, ISBN 82-7119-860-2, ISSN 0802-3271.

"Modellering av delmaterialenes betydning for betongens konsistens",
Ernst Mørtsell, 1996:12, ISBN 82-7119-894-7, ISSN 0802-3271.

"Bending of thin-walled aluminium extrusions",
Birgit Søvik Opheim, 1996:60, ISBN 82-7119-947-1, ISSN 0802-3271.

"Material modelling of aluminium for crashworthiness analysis",
Torodd Berstad, 1996:89, ISBN 82-7119-980-3, ISSN 0802-3271.

"Estimation of structural parameters from response measurements on submerged floating tunnels",
Rolf Magne Larssen, 1996:119, ISBN 82-471-0014-2, ISSN 0802-3271.

“Numerical modelling of plain and reinforced concrete by damage mechanics”,
Mario A. Polanco-Loria, 1997:20, ISBN 82-471-0049-5, ISSN 0802-3271.

“Nonlinear random vibrations - numerical analysis by path integration methods”,
Vibeke Moe, 1997:26, ISBN 82-471-0056-8, ISSN 0802-3271.

“Numerical prediction of vortex-induced vibration by the finite element method”,
Joar Martin Dalheim, 1997:63, ISBN 82-471-0096-7, ISSN 0802-3271.

“Time domain calculations of buffeting response for wind sensitive structures”,
Ketil Aas-Jakobsen, 1997:148, ISBN 82-471-0189-0, ISSN 0802-3271.

"A numerical study of flow about fixed and flexibly mounted circular cylinders",
Trond Stokka Meling, 1998:48, ISBN 82-471-0244-7, ISSN 0802-3271.

“Estimation of chloride penetration into concrete bridges in coastal areas”,
Per Egil Steen, 1998:89, ISBN 82-471-0290-0, ISSN 0802-3271.

“Stress-resultant material models for reinforced concrete plates and shells”,
Jan Arve Øverli, 1998:95, ISBN 82-471-0297-8, ISSN 0802-3271.

“Chloride binding in concrete. Effect of surrounding environment and concrete composition”,
Claus Kenneth Larsen, 1998:101, ISBN 82-471-0337-0, ISSN 0802-3271.

“Rotational capacity of aluminium alloy beams”,
Lars A. Moen, 1999:1, ISBN 82-471-0365-6, ISSN 0802-3271.

“Stretch Bending of Aluminium Extrusions”,
Arild H. Clausen, 1999:29, ISBN 82-471-0396-6, ISSN 0802-3271.

“Aluminium and Steel Beams under Concentrated Loading”,
Tore Tryland, 1999:30, ISBN 82-471-0397-4, ISSN 0802-3271.

"Engineering Models of Elastoplasticity and Fracture for Aluminium Alloys",
Odd-Geir Lademo, 1999:39, ISBN 82-471-0406-7, ISSN 0802-3271.

"Kapasitet og duktilitet av dybelforbindelser i trekonstruksjoner",
Jan Siem, 1999:46, ISBN 82-471-0414-8, ISSN 0802-3271.

“Etablering av distribuert ingeniørarbeid; Teknologiske og organisatoriske erfaringer fra en norsk ingeniørbedrift”, Lars Line, 1999:52, ISBN 82-471-0420-2, ISSN 0802-3271.

“Estimation of Earthquake-Induced Response”,
Símon Ólafsson, 1999:73, ISBN 82-471-0443-1, ISSN 0802-3271.

“Coastal Concrete Bridges: Moisture State, Chloride Permeability and Aging Effects”
Ragnhild Holen Relling, 1999:74, ISBN 82-471-0445-8, ISSN 0802-3271.

”Capacity Assessment of Titanium Pipes Subjected to Bending and External Pressure”,
Arve Bjørset, 1999:100, ISBN 82-471-0473-3, ISSN 0802-3271.

“Validation of Numerical Collapse Behaviour of Thin-Walled Corrugated Panels”,
Håvar Ilstad, 1999:101, ISBN 82-471-0474-1, ISSN 0802-3271.

“Strength and Ductility of Welded Structures in Aluminium Alloys”,
Miroslaw Matusiak, 1999:113, ISBN 82-471-0487-3, ISSN 0802-3271.

“Thermal Dilation and Autogenous Deformation as Driving Forces to Self-Induced Stresses in High Performance Concrete”,
Øyvind Bjøntegaard, 1999:121, ISBN 82-7984-002-8, ISSN 0802-3271.

“Some Aspects of Ski Base Sliding Friction and Ski Base Structure”,
Dag Anders Moldestad, 1999:137, ISBN 82-7984-019-2, ISSN 0802-3271.

"Electrode reactions and corrosion resistance for steel in mortar and concrete",
Roy Antonsen, 2000:10, ISBN 82-7984-030-3, ISSN 0802-3271.

"Hydro-Physical Conditions in Kelp Forests and the Effect on Wave Damping and Dune Erosion. A case study on Laminaria Hyperborea",
Stig Magnar Løvås, 2000:28, ISBN 82-7984-050-8, ISSN 0802-3271.

"Random Vibration and the Path Integral Method",
Christian Skaug, 2000:39, ISBN 82-7984-061-3, ISSN 0802-3271.

"Buckling and geometrical nonlinear beam-type analyses of timber structures",
Trond Even Eggen, 2000:56, ISBN 82-7984-081-8, ISSN 0802-3271.

”Structural Crashworthiness of Aluminium Foam-Based Components”,
Arve Grønsund Hanssen, 2000:76, ISBN 82-7984-102-4, ISSN 0809-103X.

“Measurements and simulations of the consolidation in first-year sea ice ridges, and some aspects of mechanical behaviour”, Knut V. Høyland, 2000:94, ISBN 82-7984-121-0, ISSN 0809-103X.

”Kinematics in Regular and Irregular Waves based on a Lagrangian Formulation”,
Svein Helge Gjøsund, 2000-86, ISBN 82-7984-112-1, ISSN 0809-103X.

”Self-Induced Cracking Problems in Hardening Concrete Structures”,
Daniela Bosnjak, 2000-121, ISBN 82-7984-151-2, ISSN 0809-103X.

"Ballistic Penetration and Perforation of Steel Plates",
Tore Børvik, 2000:124, ISBN 82-7984-154-7, ISSN 0809-103X.

"Freeze-Thaw resistance of Concrete. Effect of: Curing Conditions, Moisture Exchange and Materials", Terje Finnerup Rønning, 2001:14, ISBN 82-7984-165-2, ISSN 0809-103X

Structural behaviour of post tensioned concrete structures. Flat slab. Slabs on ground",
Steinar Trygstad, 2001:52, ISBN 82-471-5314-9, ISSN 0809-103X.

"Slipforming of Vertical Concrete Structures. Friction between concrete and slipform panel",
Kjell Tore Fosså, 2001:61, ISBN 82-471-5325-4, ISSN 0809-103X.

"Some numerical methods for the simulation of laminar and turbulent incompressible flows",
Jens Holmen, 2002:6, ISBN 82-471-5396-3, ISSN 0809-103X.

“Improved Fatigue Performance of Threaded Drillstring Connections by Cold Rolling”,
Steinar Kristoffersen, 2002:11, ISBN: 82-421-5402-1, ISSN 0809-103X.

"Deformations in Concrete Cantilever Bridges: Observations and Theoretical Modelling",
Peter F. Takâcs, 2002:23, ISBN 82-471-5415-3, ISSN 0809-103X.

"Stiffened aluminium plates subjected to impact loading",
Hilde Giæver Hildrum, 2002:69, ISBN 82-471-5467-6, ISSN 0809-103X.

"Full- and model scale study of wind effects on a medium-rise building in a built up area",
Jónas Thór Snæbjørnsson, 2002:95, ISBN82-471-5495-1, ISSN 0809-103X.

“Evaluation of Concepts for Loading of Hydrocarbons in Ice-infested water”,
Arnor Jensen, 2002:114, ISBN 82-417-5506-0, ISSN 0809-103X.

”Numerical and Physical Modelling of Oil Spreading in Broken Ice”,
Janne K. Økland Gjøsteen, 2002:130, ISBN 82-471-5523-0, ISSN 0809-103X.

”Diagnosis and protection of corroding steel in concrete”,
Franz Pruckner, 20002:140, ISBN 82-471-5555-4, ISSN 0809-103X.

“Tensile and Compressive Creep of Young Concrete: Testing and Modelling”,
Dawood Atrushi, 2003:17, ISBN 82-471-5565-6, ISSN 0809-103X.

“Rheology of Particle Suspensions. Fresh Concrete, Mortar and Cement Paste with Various Types of Lignosulfonates”,
Jon Elvar Wallevik, 2003:18, ISBN 82-471-5566-4, ISSN 0809-103X.

“Oblique Loading of Aluminium Crash Components”, Aase Reyes, 2003:15, ISBN 82-471-5562-1, ISSN 0809-103X.

“Utilization of Ethiopian Natural Pozzolans”, Surafel Ketema Desta, 2003:26,
ISSN 82-471-5574-5, ISSN:0809-103X.

“Behaviour and strength prediction of reinforced concrete structures with discontinuity regions”, Helge Brå, 2004:11, ISBN 82-471-6222-9, ISSN 1503-8181.

“High-strength steel plates subjected to projectile impact. An experimental and numerical study”, Sumita Dey, 2004:38, ISBN 82-471-6281-4 (elektr. Utg.), ISBN 82-471-6282-2 (trykt utg.),
ISSN 1503-8181.

“Alkali-reactive and inert fillers in concrete. Rheology of fresh mixtures and expansive reactions.”
Bård M. Pedersen, 2004:92, ISBN 82-471-6401-9 (trykt utg.), ISBN 82-471-6400-0 (elektr. utg.),
ISSN 1503-8181.

“On the Shear Capacity of Steel Girders with Large Web Openings”. Nils Christian Hagen, 2005:9 ISBN 82-471-6878-2 (trykt utg.), ISBN 82-471-6877-4 (elektr. utg.), ISSN 1503-8181.

”Behaviour of aluminium extrusions subjected to axial loading”. Østen Jensen, 2005:7, ISBN 82-471-6872-3 (elektr. utg.) , ISBN 82-471-6873-1 (trykt utg.), ISSN 1503-8181.

”Thermal Aspects of corrosion of Steel in Concrete”. Jan-Magnus Østvik, 2005:5, ISBN 82-471-6869-3 (trykt utg.) ISBN 82-471-6868 (elektr.utg), ISSN 1503-8181.

”Mechanical and adaptive behaviour of bone in relation to hip replacement.” A study of bone remodelling and bone grafting. Sébastien Muller, 2005:34, ISBN 82-471-6933-9 (trykt utg.) (ISBN 82-471-6932-0 (elektr.utg), ISSN 1503-8181.

“Analysis of geometrical nonlinearities with applications to timber structures”. Lars Wollebæk, 2005:74, ISBN 82-471-7050-5 (trykt utg.), ISBN 82-471-7019-1 (elektr. Utg.), ISSN 1503-8181.

“Pedestrian induced lateral vibrations of slender footbridges”, Anders Rönnquist, 2005:102, ISBN 82-471-7082-5 (trykt utg.), ISBN 82-471-7081-7 (elektr.utg.), ISSN 1503-8181.

“Initial Strength Development of Fly Ash and Limestone Blended Cements at Various Temperatures Predicted by Ultrasonic Pulse Velocity”, Tom Ivar Fredvik, 2005:112, ISBN 82-471-7105-8 (trykt utg.), ISBN 82-471-7103-1 (elektr.utg.), ISSN 1503-8181.

“Behaviour and modelling of thin-walled cast components”, Cato Dørum, 2005:128, ISBN 82-471-7140-6 (trykt utg.), ISBN 82-471-7139-2 (elektr. utg.), ISSN 1503-8181.

“Behaviour and modelling of selfpiercing riveted connections”, Raffaele Porcaro, 2005:165, ISBN 82-471-7219-4 (trykt utg.), ISBN 82-471-7218-6 (elektr.utg.), ISSN 1503-8181.

”Behaviour and Modelling og Aluminium Plates subjected to Compressive Load”, Lars Rønning,
2005:154, ISBN 82-471-7169-1 (trykt utg.), ISBN 82-471-7195-3 (elektr.utg.), ISSN 1503-8181

”Bumper beam-longitudinal system subjected to offset impact loading”, Satyanarayana Kokkula, 2005:193, ISBN 82-471-7280-1 (trykt utg.), ISBN 82-471-7279-8 (elektr.utg.), ISSN 1503-8181.

“Control of Chloride Penetration into Concrete Structures at Early Age”, Guofei Liu, 2006:46, ISBN 82-471-7838-9 (trykt utg.), ISBN 82-471-7837-0 (elektr. utgave), ISSN 1503-8181.